INNER SHELL HYDRATION ENERGIES OF ALKALINE EARTH METAL DICATIONS

by

Damon Ryan Carl

A dissertation submitted to the faculty of
The University of Utah
in partial fulfillment of the requirements for the degree of

Doctor of Philosophy

Department of Chemistry

The University of Utah

May 2013

The University of Utah Graduate School

STATEMENT OF DISSERTATION APPROVAL

The dissertation of **Damon Ryan Carl**

has been approved by the following supervisory committee members:

Peter B. Armentrout	, Chair	**10/05/2009** Date Approved
Scott L. Anderson	, Member	**10/05/2009** Date Approved
Joel M. Harris	, Member	**10/05/2009** Date Approved
Peter F. Flynn	, Member	**10/05/2009** Date Approved
David Blair	, Member	**10/05/2009** Date Approved

and by **Henry S. White**, Chair of the Department of **Chemistry**

and by Donna M. White, Interim Dean of The Graduate School.

ABSTRACT

Hydrated alkaline earth metal dications, $M^{2+}(H_2O)_x$, have become the epitome of solvation studies of multiply charged ions in the gas phase ever since the inception of electrospray ionization. Collision-induced dissociation in a guided ion beam mass spectrometer is used to determine the hydration energies of $M^{2+}(H_2O)_x$, where M^{2+} = Mg^{2+}, Ca^{2+} and Sr^{2+} and x = 2 – 10, 1 – 9, and 1 – 6, respectively. The formation of $M^{2+}(H_2O)_x$ complexes, where $x < 6$, is only possible in our electrospray ionization source using an in-source fragmentation technique that takes place in the high pressure region of the hexapole ion guide. These studies comprise the first experimentally determined hydration energies for x = 2 – 4 for Mg^{2+} and x = 1 – 4 for Ca^{2+} and Sr^{2+}, which are found to be in good agreement with theoretical calculations. These results provide evidence that the internal energies of the ions accessed with the fragmentation technique are thermalized at 300 K.

For Elissa and Noah Jameson

TABLE OF CONTENTS

ACKNOWLEDGEMENTS

The work presented here could not be possible without the help and support of so many great people. First and foremost, I would like to thank my advisor, Dr. Peter B. Armentrout, for his support, wisdom, and guidance throughout my graduate career. It has been an honor to work with a scientist of his caliber. Peter has taught me so many things, but most of all I have learned to pay attention to the details. I hope that in the next phase of my life, I am as devoted, passionate, and successful in my own craft as he is with his.

I would also like to thank Dennis Romney and Jeff Welch in the machine shop for many useful discussions in machining, design, science, and life. Dale Heisler and Ron Jones in the electronics shop have both been great friends and extremely helpful when electrical issues manifest themselves in the lab.

I would also like to thank all of the Armentrout group members for their continuous support. Specifically, I would like to Dr. Chris Iceman, Dr. Bob Moision, Dr. Theresa Hofstetter, Dr. Murat Citir, and Mr. Chris Hinton, who have been instrumental in my development as a scientist. You are truly great friends.

I would also like to thank my wife, Elissa, my son, Noah Jameson, my parents, Pam and Dane, and my entire family for their undying love and support throughout these years in success, hardship, and everywhere in between. I couldn't have done it without you.

The National Science Foundation generously provided funding for this work.

CHAPTER 1

INTRODUCTION AND OVERVIEW

Introduction

Metal cations, M^{n+}, play an integral role in numerous physiological processes. Na^+ and K^+ ions are instrumental for propagating the action potential of nerve cells by moving in and out of cells through specific integral membrane proteins called ion channels.[1] Mg^{2+} ions serve as an important structural component in nucleic acid chemistry,[2] Ca^{2+} ions interact with calcium modulated proteins to promote muscle contraction,[3] and Sr^{2+}, in the form of the antiosteoporotic drug strontium ranelate, reduces the incidence of bone fractures in osteroporotic patients.[4] What all biologically relevant M^{n+} have in common is that when they are not interacting with biomolecules (e.g., proteins, nucleic acids), they are extensively solvated by water molecules, $M^{n+}(H_2O)_x$. Water molecules that bind directly to the M^{n+} center are located in the inner hydration shell with additional water molecules are located in outer hydration shells and hydrogen bond to other water molecules. As $M^{n+}(H_2O)_x$ ions move to perform a specific task, such as the binding and subsequent activation of a protein, they undergo extensive dehydration until it is partially hydrated by only those inner shell water molecules. For M^{n+} ions to bind, ligand exchange must occur between these inner shell water molecules and functional groups of the protein binding site in some capacity. Understanding the

complete dehydration of $M^{n+}(H_2O)_x$ complexes is a critical component to understand such ligand exchange processes.

Thermochemical investigations of metal ion-water interactions have been an area of active research in the gas-phase ion-molecule community over the last several decades. Early experimental studies using equilibrium[5-7] and guided ion beam techniques[8-11] have determined the binding energies of the first four to six water molecules for a number of singly charged metal cations, M^+. Singly charged metal ion hydrates, $M^+(H_2O)_x$, can be formed by three-body associative reactions after producing M^+ ions in the gas phase in the presence of water vapor. Doubly charged metal ion hydrates, $M^{2+}(H_2O)_x$, can also be produced by association as long as the second ionization energy of the metal is below the first ionization energy of water (12.6 eV).[12] However, for instances where this is not the case, association leads to the formation of $MOH^+(H_2O)_x$ and $H^+(H_2O)_y$ complexes. The method adopted by most researchers for generating multiply-charged hydrated metal cations is electrospray ionization (ESI), where ions that exist in solution can be transferred directly into the gas phase as a fine spray of charged droplets.[13-15]

Since the development of ESI, hydrated alkaline earth metal dications have become the epitome of ion hydration studies of multiply charge ions. Kebarle and coworkers[15,16] first utilized equilibrium experiments in a high pressure mass spectrometer (HPMS) to determine the hydration energies for $M^{2+}(H_2O)_x$ complexes, where M^{2+} = Mg^{2+}, Ca^{2+}, Sr^{2+}, and Ba^{2+} and x = 6 – 14. Later studies by Williams and coworkers[17,18] determined the hydration energies for $M^{2+}(H_2O)_x$ complexes, where x = 5 – 10 for M^{2+} = Mg^{2+} and Ca^{2+} and x = 5 – 7 for M^{2+} = Sr^{2+} and Ba^{2+}, using kinetics experiments via blackbody infrared radiative dissociation (BIRD) in an Fourier transform ion cyclotron

resonance (FT-ICR) mass spectrometer. Despite gaining a fundamental understanding of the hydration energies for larger $M^{2+}(H_2O)_x$ complexes, neither experimental method can determine the hydration energies of the remaining inner shell water molecules that are tightly bound to the metal cation (x = 1 – 4). HPMS and BIRD are inherently temperature-dependent techniques, such that investigating smaller $M^{2+}(H_2O)_x$ complexes would require accessing temperatures beyond their instrumental capabilities.

Guided ion beam mass spectrometry (GIBMS)[19,20] lends itself to these experimental limitations because the dissociation of $M^{2+}(H_2O)_x$ complexes is investigated as a function of kinetic energy, which can be varied over a broader range than temperature. Therefore, if smaller $M^{2+}(H_2O)_x$ complexes can be formed, their reactivity can be investigated by threshold collision-induced dissociation (TCID) with Xenon (Xe). From TCID experiments, the minimum energy required to lose a single water molecule from a given $M^{2+}(H_2O)_x$ complex, Reaction 1.1, can be determined and related to the binding or hydration energy of the x^{th} water molecule.

$$M^{2+}(H_2O)_x + Xe \rightarrow M^{2+}(H_2O)_{x-1} + H_2O + Xe \qquad (1.1)$$

Here, electrospray ionization of aqueous $MgCl_2$, $CaCl_2$, and $SrCl_2$ solutions produces an initial distribution of $M^{2+}(H_2O)_x$ complexes, where x = 7 – 10, 6 – 9 and 6 – 9, respectively. Smaller $M^{2+}(H_2O)_x$ complexes are formed utilizing an in-source fragmentation technique[21] that takes place within the high pressure region of the hexapole ion guide of a custom-built ESI source.[22] Smaller $M^{2+}(H_2O)_x$ complexes can be formed with this fragmentation technique as long as simple ligand loss, Reaction 1.2, is energetically favored over the charge separation pathway, Reaction 1.3.

$$M^{2+}(H_2O)_x \rightarrow M^{2+}(H_2O)_{x-1} + H_2O \quad (1.2)$$

$$M^{2+}(H_2O)_x \rightarrow MOH^{+}(H_2O)_y + H^{+}(H_2O)_{x-y-1} \quad (1.3)$$

At $Mg^{2+}(H_2O)_3$ and $Ca^{2+}(H_2O)_2$, charge separation becomes the energetically preferred pathway over water loss, which inhibits the direct formation of $Mg^{2+}(H_2O)_2$, $Mg^{2+}(H_2O)$ and $Ca^{2+}(H_2O)$; however, the $Sr^{2+}(H_2O)$ complex can be formed directly using the in-source fragmentation technique. The lowest observable $M^{2+}(H_2O)_x$ species for a particular metal ion provides a qualitative assessment of the critical size structure (x_c), which is defined as the size at which charge separation becomes a lower energy process over water loss.[15,23] The ability to access the smallest $M^{2+}(H_2O)_x$ complexes allows Reactions 1.2 and 1.3 to be investigated by TCID measurements under single collision conditions with Xenon, the results of which provides a more definitive answer as to x_c complex. Despite the energetic limitations, the binding energies of inaccessible $Mg^{2+}(H_2O)_x$ and $Ca^{2+}(H_2O)$ complexes can still be determined from the CID of the lowest accessible $M^{2+}(H_2O)_x$ complexes by sequential analysis of first and second water molecules simultaneously. The hydration energies for $Mg^{2+}(H_2O)_x$, $Ca^{2+}(H_2O)_y$ and $Sr^{2+}(H_2O)_z$, where x = 2 – 10, y = 1 – 9 and z = 1 – 6, respectively, have been determined from CID measurements using GIBMS. This work includes the first experimentally measured binding energies for x = 2 – 4, y = 1 – 4, and z = 1 – 4. Concomitantly, this work also provides the very first experimental measurements of the energetic barriers for those charge separation processes that prevent the formation of the smallest $M^{2+}(H_2O)_x$ complexes for M = Mg and Ca in the source region using the CID data of the smallest accessible $M^{2+}(H_2O)_x$ complexes.

Overview

Chapter 2 presents a brief description of the guided ion beam mass spectrometer and the electrospray ionization source. The protocol for reducing the data into a useable form for thermochemical analysis as well as the methods for analyzing endothermic cross sections from collision-induced dissociation experiments is described for the single channel, competitive, and sequential models. Chapter 3 describes the computational approach taken for all theoretical calculations throughout Chapters 4 and 6 – 9.

Chapter 4 details collision-induced dissociation experiments for $Ca^{2+}(H_2O)_x$ complexes, where x = 5 – 9. The hydration energies for single water molecule loss from these complexes are determined employing an early design of the electrospray ionization source. A detailed theoretical study of the structure and relative energetics of ground state and low-lying $Ca^{2+}(H_2O)_x$ complexes compliments the experimental results.

Chapter 5 describes the implementation of an in-source fragmentation technique for the production of thermalized ions that takes place in the hexapole ion guide of the electrospray source. An inexpensive and effective protocol for generating smaller $Ca^{2+}(H_2O)_x$ complexes, where x = 2 – 5, from an initial distribution of x = 6 – 9, is discussed. Chapter 6 utilizes this fragmentation technique to access the smaller $Ca^{2+}(H_2O)_x$ complexes and study their reactivity by collision-induced dissociation. This chapter encompasses x = 6 – 8 investigated in Chapter 4, but was repeated to ensure the new electrospray source modifications did not adversely affect the resultant thermochemistry. In addition to the first experimental measurements of the hydration energies for x = 1 – 4, the thermodynamic onsets for charge separation of $Ca^{2+}(H_2O)_2$ and $Ca^{2+}(H_2O)_3$ complexes into $CaOH^+(H_2O)/H_3O^+$ and $CaOH^+/H_3O^+$ are measured

experimentally for the first time. The primary and secondary water losses are also analyzed simultaneously for x = 2 – 8 using the sequential model.

Chapter 7 involves a complete experimental and theoretical investigation of the hydration energies of $Sr^{2+}(H_2O)_x$, where x = 1 – 6. Qualitative comparisons are made between $Sr^{2+}(H_2O)_x$ complexes formed using the in-source fragmentation technique and those formed directly from three-body association reactions in a flow tube source. This work show ions generated with the in-source fragmentation technique are internally cooler than those generated by three body association reactions, which allow accurate thermochemical measurements to be made. Chapter 8 describes a comprehensive experimental examination of the collision-induced dissociation of $Mg^{2+}(H_2O)_x$, where x = 3 – 10. The hydration energies for x = 2 – 10 are determined using a combination of in-source fragmentation and sequential modeling. This work determines the first experimental measurements of the hydration energies for x = 2 – 4 and the first thermochemical measurements of the onset for charge separation of $Mg^{2+}(H_2O)_3$ and $Mg^{2+}(H_2O)_4$ complexes into $MgOH^+(H_2O)_2/H_3O^+$ and $MgOH^+(H_2O)/H_3O^+$. A rigorous theoretical investigation of both ground state and low-lying structures for $Mg^{2+}(H_2O)_x$ complexes investigated is provided. The work presented in Chapters 5 – 8 unequivocally establishes the fragmentation technique as a viable experimental tool capable of producing accurate thermochemistry for the smallest $M^{2+}(H_2O)_x$ complexes.

Chapter 9 introduces an infrared multiple photon dissociation (IRMPD) study on the gas phase structures of alkali-metal cations complexed to the amino acid methionine and protonated methionine. A considerable amount of theoretical work was performed to determine low energy structures of all M^+(Met). Comparisons are made between

calculated IR spectra and observed IRMPD action spectra (photodissociation) to determine contributing conformations of the gas phase structure. This work was done in collaboration with Jos Oomens and Jeffrey Steill at the FOM Institute for Plasma Physics "Rijnhuizen" in the Netherlands under the National Science Foundation's Mass Spectrometry Partnership for International Research and Education (MS PIRE).

References

(1) Hille, B. *Ion Channels of Excitable Membranes*, 3rd ed.; Sinauer: Sunderland, Mass, 2001.

(2) Cowan, J. A. *Introduction to the Biological Chemistry of Magnesium*; VCH: New York, 1995.

(3) Lodish, H.; Berk, A.; Matsudaira, P.; Kaiser, C. A.; Krieger, M.; Scott, M. P.; Zipursky, S. L. *Molecular Cell Biology*, 5th ed.; W. H. Freeman and Company: New York, 2004.

(4) Nielsen, S. P. *Bone* **2004**, *35*, 583.

(5) Dzidic, I.; Kebarle, P. *J. Phys. Chem.* **1970**, *74*, 1466.

(6) Searles, S. K.; Kebarle, P. *Can. J. Chem.* **1969**, *47*, 2619.

(7) Holland, P. M.; Castleman, A. W., Jr. *J. Chem. Phys.* **1982**, *76*, 4195.

(8) Dalleska, N. F.; Honma, K.; Sunderlin, L. S.; Armentrout, P. B. *J. Am. Chem. Soc.* **1994**, *116*, 3519.

(9) Dalleska, N. F.; Tjelta, B. L.; Armentrout, P. B. *J. Phys. Chem.* **1994**, *98*, 4191.

(10) Rodgers, M. T.; Armentrout, P. B. *J. Phys. Chem. A* **1997**, *101*, 1238.

(11) Koizumi, H.; Larson, M.; Muntean, F.; Armentrout, P. B. *Int. J. Mass Spectrom.* **2003**, *228*, 221.

(12) *Ion Energetics Data*; Lias, S. G.; Liebman, J. F., Eds. Gaithersburg MD, 2001; Vol. NIST Standard Reference Database Number 69, pp (http://webbook.nist.gov).

(13) Whitehouse, C. M.; Dreyer, R. N.; Yamashita, M.; Fenn, J. B. *Anal. Chem.* **1985**, *57*, 675.

(14) Yamashita, M.; Fenn, J. B. *J. Phys. Chem.* **1984**, *88*, 4451.

(15) Blades, A. T.; Jayaweera, P.; Ikonomou, M. G.; Kebarle, P. *J. Chem. Phys.* **1990**, *92*, 5900.

(16) Peschke, M.; Blades, A. T.; Kebarle, P. *J. Phys. Chem. A* **1998**, *102*, 9978.

(17) Rodriguez-Cruz, S. E.; Jockusch, R. A.; Williams, E. R. *J. Am. Chem. Soc.* **1999**, *121*, 8898.

(18) Wong, R. L.; Paech, K.; Williams, E. R. *Int. J. Mass Spectrom.* **2004**, *232*, 59.

(19) Ervin, K. M.; Armentrout, P. B. *J. Chem. Phys.* **1985**, *83*, 166.

(20) Muntean, F.; Armentrout, P. B. *J. Chem. Phys.* **2001**, *115*, 1213.

(21) Carl, D. R.; Moision, R. M.; Armentrout, P. B. *J. Am. Soc. Mass Spectrom.* **2009**, *20*, 2312.

(22) Moision, R. M.; Armentrout, P. B. *J. Am. Soc. Mass Spectrom.* **2007**, *18*, 1124.

(23) Shvartsburg, A. A.; Siu, K. W. M. *J. Am. Chem. Soc.* **2001**, *123*, 10071.

CHAPTER 2

EXPERIMENTAL TECHNIQUES AND DATA ANALYSIS

Guided Ion Beam Mass Spectrometer

The experiments described in Chapters 4 – 8 were performed using a guided ion beam mass spectrometer (GIBMS), which has been previously described in detail.[1,2] The GIBMS is shown in Figure 2.1 and is comprised of an electrospray ionization (ESI) source,[3] magnetic momentum analyzer, octopole ion guide/reaction cell, and a quadrupole mass filter and Daly detector. A schematic of the ESI source is shown in Figure 2.2. Briefly, $M^{2+}(H_2O)_x$ ions are generated by syringe pumping 10^{-4} M $MgCl_2$, $CaCl_2$ and $SrCl_2$ dissolved in HPLC water through a 35 gauge stainless steel electrospray emitter set to ~ 2000 V with respect to an inlet cap, which serves as the counterelectrode (~ 15 V). Ions then pass through a heated capillary (80 °C) and are transferred into an electrodynamic ion funnel.[4] The ion funnel efficiently transfers ions through the high pressure region of the source (10^{-2} Torr) using a combination of direct current (dc) and radio frequency (rf) voltages.[5] A linear dc voltage drop (~10 V) across the ion funnel plates drags the ions in the axial direction, while opposite phases of rf voltage (~ 15 V peak-to-peak (V_{pp}) at 1.5 MHz) on adjacent plates radially focus the ions into a tight beam. The ion funnel includes an independently controlled dc-only jet disrupter located 20 plates from the entrance of the funnel. The jet disrupter effectively disperses the jet stream emerging from the heated capillary while maintaining ion transmission through

the funnel.[6] The advantage of the jet disrupter within the ion funnel was realized in later versions of the ESI design and was not included for the earliest $Ca^{2+}(H_2O)_x$ investigation (Chapter 4), but was employed for all subsequent chapters. Ions are transferred from the ion funnel and into an rf-only hexapole ion guide (200 – 300 V_{pp} at 5.5 MHz) that spans the high pressure region of the source and the first region of differential pumping (10^{-5} Torr). Multipole ion guides have been used extensively in ion-molecule experiments for effectively transporting ions from high to low pressure regions.[7] In the high pressure region of the hexapole, the ions undergo sufficient ion/neutral collisions with the ambient gas such that they become thermalized. Thermal ions are assumed to be in their ground vibrational and rotational states and can be described by a Maxwell Boltzmann distribution at 300 K. Previous work has shown this source arrangement produces thermalized ions at room temperature for ions formed directly,[3,8-12] as well as those created by in-source fragmentation (Chapter 5 – 8) and elsewhere.[13-21]

In addition to the ESI source used throughout this body of work, a dc discharge flow tube ion source (DC/FT)[22] was used to generate $Sr^{2+}(H_2O)_x$ complexes for x = 1 – 6. However, this data was not originally published, but is incorporated for comparative purposes with the ESI-generated $Sr^{2+}(H_2O)_x$ complexes presented in Chapter 7. In the DC/FT source, strontium dications are generated at the cathode, a tantalum boat filled with strontium metal located at the head of a 1 m long flow tube, by using a continuous dc discharge with typical operating conditions of 1.9 – 2.2 kV and 10 – 20 mA. The metal dications are carried down the flow tube by a buffer gas (~ 10% argon in helium) with normal operating pressures of 0.3 – 0.4 Torr. About 50 cm downstream from the discharge, water vapor is introduced into the flow tube and the complexes of interest are

formed via three-body associative reactions in the flow of the He/Ar carrier gas. For singly-charged species, complex ions formed in the DC/FT source are thermalized to 300 K (the temperature of the flow tube) by undergoing ~10^5 collisions with the buffer gases as they drift along the one-meter long flow tube.[23-30]

Ions are extracted from the source region and focused into and accelerated through a magnetic momentum analyzer, which serves as the initial mass selector. The magnetic field strength is adjusted such that only ions with a specific mass-to-charge ratio (*m/z*) will be deflected through the exit slit. The mass-selected ion beam is then decelerated to desired kinetic energies (collision energies) and focused into an rf octopole ion guide, which radially focuses the ions, but leaves their axial velocities unaffected.[1,7,31] The kinetic energy of the ion beam is controlled by adjusting the dc bias on the octopole with respect to the dc voltage on the hexapole ion guide in the source region. The octopole is surrounded by a static gas cell containing the collision gas, Xenon. Xenon is used for its high polarizability and because it provides efficient kinetic to internal energy transfer upon collision.[32,33] Product ions formed in these collisions and unreacted parent ions drift to the end of the octopole where they are focused, mass selected using a quadrupole mass filter, and detected using a scintillation ion detector capable of single-ion counting.[34]

The collision-induced dissociation (CID) of the $M^{2+}(H_2O)_x$ complex with Xenon is initially carried out at a few collision energies over a sufficiently large mass-to-charge ratio (*m/z*) range to capture all possible dissociation products. Next, the exact masses of the reactant and product ions are determined by scanning the quadrupole mass filter over a short *m/z* window including the ion of interest. In the main experiment, the Xe pressure

in the octopole gas cell is measured at the beginning of the scan, the collision energy of the ion beam is set and the quadrupole mass filter isolates the reactant ion while the detector counts its signal intensity. The quadrupole mass filter isolates each product mass being collected with subsequent detection at the same collision energy. The collision energy then increments and all ions will be isolated and detected again until reaching the maximum collision energy. Data collected with xenon gas in the gas cell is termed a foreground scan. Next, the Xe gas is directed out of the octopole gas cell and into the reaction chamber and a background data scan is collected by incrementing the collision energy in the reverse direction. The background scan determines the product intensities resulting from collisions that place outside of the octopole collision cell. Once the background scan is complete, the pressure is measured again and a new foreground scan begins. Scans continue until the noise of the foreground profiles for each ion has been minimized. Finally, the raw data are reduced into a useable form for thermochemical analysis.

Data Reduction

The absolute zero of energy and the kinetic energy distribution of the reactants are determined using a retarding potential technique.[1] The derivative of the transmission curve of the ion beam is fit to a Gaussian function, which provides a measurement of the kinetic energy distribution of the reactant ion by the full-width at half maximum (FWHM). FWHMs are typically 0.08 – 0.15 eV for these studies.

In the octopole reaction region, ions are accelerated by V_{Lab}, nominally the voltage difference between the dc bias on the octopole ion beam guide and the ion source. Because the ions studied here are doubly charged, their kinetic energy in the laboratory

frame is twice this voltage, $E_{Lab} = 2 \times V_{Lab}$. These laboratory frame energies (E_{Lab}) are converted to center-of-mass (CM) collision energies using Equation 2.1,

$$E_{CM} = E_{Lab} \times m/(m+M) \tag{2.1}$$

where m and M represent the mass of the neutral collision gas and ionic species, respectively. This conversion is necessary to give the reactant $M^{2+}(H_2O)_x$ complexes a frame of reference with respect to its collision partner and provides an energy scale suitable for thermodynamic analysis.

Ion intensities are converted into absolute cross sections using a Beer's law relationship, Equations 2.2 and 2.3,

$$I = I_0 \exp(-\sigma_{tot} nl) \tag{2.2}$$

$$\sigma_P = \sigma_{tot}(I_p / \sum I_P) \tag{2.3}$$

where I is the ion intensity of the transmitted ion beam, I_0 is the sum all ions, σ_{tot} is the total cross section, n is the gas density of xenon in the reaction cell, l is the effective gas cell path length. σ_P is a product cross section with transmitted intensity I_P. Uncertainties in the absolute cross sections are estimated to be ± 20%.

Data Analysis

The kinetic energy dependent cross sections for single water molecule loss from a parent $M^{2+}(H_2O)_x$ complex, Equation 1.1, are modeled using the empirical threshold model shown in Equation 2.4,

$$\sigma(E) = \sigma_0 \sum g_i (E + E_i + E_0)^n / E \tag{2.4}$$

where σ_0 is an energy independent scaling factor, E is the relative translational energy of the ion, E_0 is the reaction threshold at 0 K, and n is an adjustable fitting parameter that describes the efficiency of the energy transfer upon collision.[2] The summation is over the ro-vibrational states of the reactants having excitation energies, E_i, and populations, g_i, where $\Sigma g_i = 1$. Vibrational frequencies and rotational constants are taken from ab initio calculations of the $M^{2+}(H_2O)_x$ complexes. The Beyer-Swinehart-Stein-Rabinovich algorithm is used to evaluate the internal energy distribution for the reactants.[35-38] The relative populations, g_i, are computed for a Maxwell-Boltzmann distribution at 300 K.

To produce accurate thermochemical data from the modeling of the CID process, a number of effects such as those arising from multiple collisions, lifetime effects, and energy distributions must be considered. To insure rigorous single collision conditions, cross sections are obtained at multiple pressures of Xe, typically about 0.20, 0.10, and 0.05 mTorr in these studies, and extrapolated to zero-pressure cross sections.[23,39] As the $M^{2+}(H_2O)_x$ ions become more complex, ions with excess energy of the threshold energy may not have time to dissociate on the timescale of the experiment, $\tau \approx 5 \times 10^{-4}$ s.[2] This leads to a "kinetic shift" in the energy threshold obtained from the modeling. To account for this effect, Rice-Ramsperger-Kassel-Marcus (RRKM) statistical theory[38,40,41] for unimolecular dissociation is incorporated into Equation 2.4, as discussed in detail previously[42-44] and shown in Equation 2.5.

$$\sigma_j(E) = \left(\frac{n\sigma_{0,j}}{E}\right)\sum_i g_i \int_{E_{0,j}-E_i}^{E} [k_j(E^*)/k_{tot}(E^*)][1-e^{-k_{tot}(E^*)\tau}](E-\varepsilon)^{n-1}d(\varepsilon) \qquad (2.5)$$

Here, most parameters are the same as in Equation 2.4. ε is the energy transferred into internal degrees of freedom of the dissociating ion at a relative translational energy, E.

The internal energy of the energized molecule after collision is $E^* = \varepsilon + E_i$ and $k_{tot}(E^*)$ is the total unimolecular dissociation rate coefficient. The rate coefficient is used to calculate the probability of dissociation, P_{D1}, the second term in brackets in Equation 2.5 . The RRKM unimolecular dissociation rate constant is defined by Equation 2.6,

$$k_{tot}(E^*) = \sum_j k_j(E^*) = \sum_j d_j N_j^{\dagger}(E^* - E_{0,j}) / h\rho(E^*) \qquad (2.6)$$

where $k_j(E^*)$ is the rate constant for a single dissociation channel j, d_j is the reaction degeneracy calculated from the ratio of rotational symmetry numbers of the reactants with respect to the products for channel j, $N_j^{\dagger}(E^* - E_{0,j})$ is the sum of the ro-vibrational states of the transition state at an energy $(E^* - E_{0,j})$ above the threshold for channel j, and $\rho(E^*)$ is the density of ro-vibrational states for the energized molecule at the energy available, E^*. When the rate constant is much faster than the average experimental timescale, Equation 2.5 reduces to Equation 2.4. The integration in Equation 2.5 is over the excitation energy distribution, which is related to the impact parameter between the ion and Xenon gas. Equation 2.5 has been shown to accurately describe kinetic shifts in a number of previous CID experiments.[8-11,29,30,45]

The ratio of rate coefficients in Equation 2.6 is utilized to model competition between multiple dissociation pathways from a single energized molecule. The competition between the loss of a single water molecule and charge separation process from $Ca^{2+}(H_2O)_2$ and $Ca^{2+}(H_2O)_3$ (Chapter 6) and $Mg^{2+}(H_2O)_3$ and $Mg^{2+}(H_2O)_4$ (Chapter 8) complexes must be taken into account. Individual dissociation channels are coupled through the $k_{tot}(E^*)$ term. The reason for explicit modeling of the competition between multiple channels is because the formation of the higher energy dissociation pathway can

be inhibited by the lower energy process, such that efficient detection may only be possible at energies higher than the actual threshold, resulting in a "competitive shift."[46]

Modeling of sequential dissociation is used in Chapters 6 and 8 to analyze the cross sections for the loss of the first and second water molecules simultaneously from a given size $M^{2+}(H_2O)_x$ complex, Equation 2.7. The difference in the measured thresholds for the first and second water loss, $E_{0,1}$ and $E_{0,2}$, respectively, provides the binding energy of the x – 1 water

$$M^{2+}(H_2O)_x + Xe \rightarrow M^{2+}(H_2O)_{x-1} + H_2O + Xe \rightarrow M^{2+}(H_2O)_{x-2} + 2\,H_2O + Xe \tag{2.7}$$

molecule for the $M^{2+}(H_2O)_{x-1}$ complex.[47] If the cross sections for high ordered processes are modeled with Equation 2.5 ignoring the initial dissociation, the thresholds measured are typically larger than the sum of the analogous primary dissociation threshold energies for singly charged complexes.[23,33,47] This is because the internal energy of the primary product ion, $M^{2+}(H_2O)_{x-1}$, leading to the higher order products is not well characterized because the energy available to the products of the primary dissociation, $E_1^\dagger = E^* - E_{0,1}$, can be partitioned into the translational energy, T_1, and internal energy, $E_{1,\mathrm{int}}^\dagger$,. The internal energy of the products can be further partitioned into internal energies of the ligand, E_L, and product ion that undergoes further dissociation, E_2^*, Equation 2.8.

$$E_1^\dagger = T_1 + E_{1,\mathrm{int}}^\dagger = T_1 + E_L + E_2^* \tag{2.8}$$

In the sequential model described elsewhere in detail,[47] this partitioning is assumed to be statistically behaved, which provides a prediction of the distribution of energies for each

of these components. This permits the dissociation probability of the primary product, $P_{D2} = 1 - \exp[-k_2(E_2^*)\tau]$, to be evaluated using the same procedure described above for P_{D1}. Multiplication of the primary cross section from Equation 2.5 with P_{D2} provides the cross section for the secondary product and their difference is the cross section for the remaining primary product.

Calculation of the RRKM unimolecular rate constant in Equation 2.6 requires the ro-vibrational states of the energized molecule (EM) and transition state (TS).[38,40,41] The molecular parameters for the EM are taken from quantum chemical calculations of the reactant ion. For water loss, the TS is assumed to be loose with no reverse activation barrier, as is appropriate for the heterolytic bond cleavages studied here.[48] Therefore, the phase-space limit (PSL) TS is product-like using molecular parameters taken from quantum chemical calculations of the $M^{2+}(H_2O)_{x-1}$ and H_2O products. The transitional modes, those that become rotations of the dissociated products, are treated as rotors and calculated from the rotational constants of the separate dissociation products, $M^{2+}(H_2O)_{x-1}$ and H_2O. The external rotational constants and rotational energy of the TS are determined by assuming that the TS is located at the centrifugal barrier for the interaction of $M^{2+}(H_2O)_{x-1}$ and H_2O, and calculated using a variational approach as outlined elsewhere.[44] The data analysis program (CRUNCH) accurately accounts for the charge on the ion in determining the location of the centrifugal barrier. The 2D external rotations are treated adiabatically, but include centrifugal effects.[49] In the present work, the adiabatic 2D external rotational energy of the EM is calculated using a statistical distribution with an explicit summation over the possible values of the rotational quantum number.[44] In contrast, the TS for the charge separation process is tight, because it

requires a structural rearrangement into a rate limiting step. Molecular parameters for the tight TS are taken from quantum chemical calculations described in Chapters 6 and 8.

The model CID cross sections of Equations 2.4, 2.5, and the sequential model are convoluted over the kinetic energy distributions of the $M^{2+}(H_2O)_x$ and Xe reactants before comparison with the experimental cross sections. A nonlinear least squares fitting procedure is used to optimize the fitting parameters, $\sigma_{0,j}$, n, and $E_{0,j}$ in each model. Because all sources of energy are explicitly accounted for in the data analysis, the reaction threshold for water loss represents the 0 K bond dissociation energy (BDE) of the water molecule to the reactant complex. This assumes that there are no activation barriers beyond the endothermicity of the reaction, which is typically the case for heterolytic bond cleavages such as those studied here for water loss.[48] However, for charge separation, the threshold corresponds to the difference between the ground state $M^{2+}(H_2O)_x$ complex and rate limiting TS, located at the Coulomb barrier between the separating singly charged products. The uncertainties (reported as two standard deviations throughout) associated with the fitting parameters, $\sigma_{0,j}$, n, and $E_{0,j}$, are determined by scaling the vibrational frequencies up and down by 10%, varying the best fit n value up and down by about 0.1, and scaling the average experimental time available for dissociation up and down by a factor of two. The absolute uncertainty of the energy scale (0.05 eV lab) is also included in the uncertainty of $E_{0,j}$.

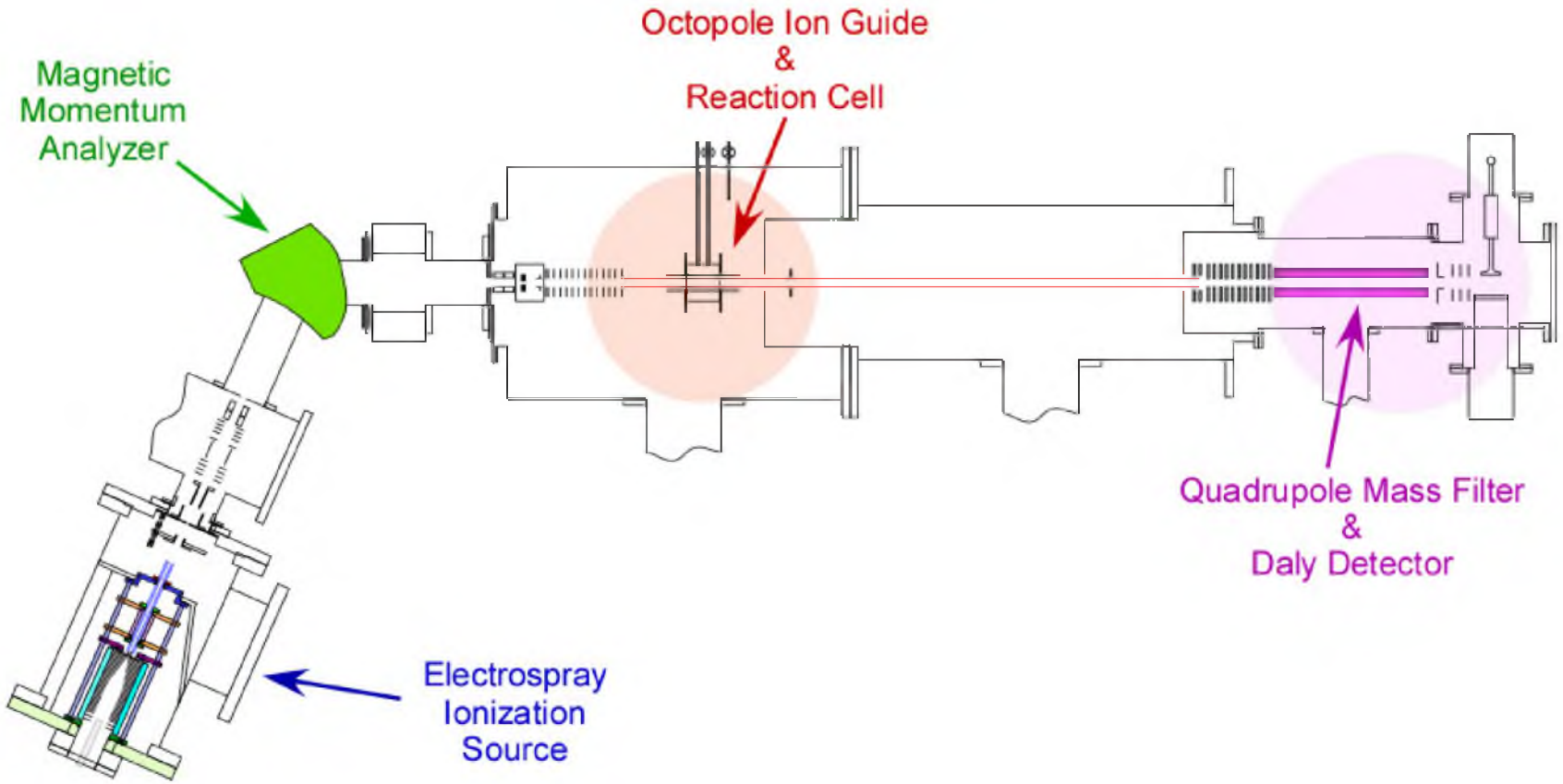

Figure 2.1. Schematic of the guided ion beam mass spectrometer.

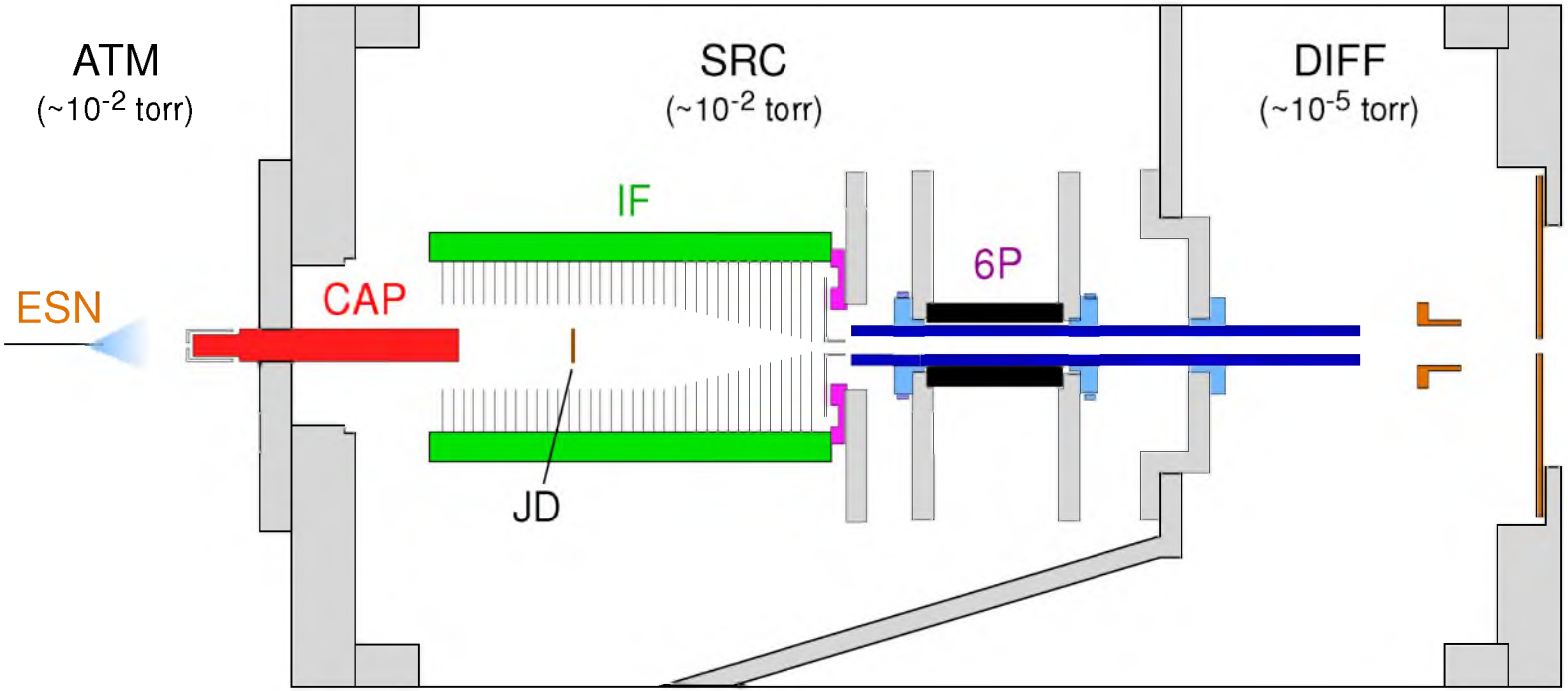

Figure 2.2. Schematic of the electrospray ionization (ESI) source. The electrospray needle (ESN) is located at atmospheric pressure (ATM). Ions are introduced into the source region (SRC) of the instrument through a heated capillary (CAP). Ions are collected in an ion funnel (IF), which includes a jet disrupter (JD). Ions are then transferred into the hexapole ion guide (6P). The 6P passes through a high pressure SRC region (~10^{-2} Torr) and low pressure differential region (DIFF, ~10^{-5} Torr).

References

(1) Ervin, K. M.; Armentrout, P. B. *J. Chem. Phys.* **1985**, *83*, 166.

(2) Muntean, F.; Armentrout, P. B. *J. Chem. Phys.* **2001**, *115*, 1213.

(3) Moision, R. M.; Armentrout, P. B. *J. Am. Soc. Mass Spectrom.* **2007**, *18*, 1124.

(4) Kim, T.; Tolmachev, A. V.; Harkewicz, R.; Prior, D. C.; Anderson, G.; Udseth, H. R.; Smith, R. D. *Anal. Chem* **2000**, *72*, 2247.

(5) Belov, M. E.; Gorshkov, M. V.; Udseth, H. R.; Anderson, G. A.; Smith, R. D. *Anal. Chem.* **2000**, *72*, 2271.

(6) Kim, T.; Tang, K.; Udseth, H. R.; Smith, R. D. *Anal. Chem.* **2001**, *73*, 4162.

(7) Gerlich, D. *Adv. Chem. Phys.* **1992**, *82*, 1.

(8) Carl, D. R.; Moision, R. M.; Armentrout, P. B. *Int. J. Mass Spectrom.* **2007**, *265*, 308.

(9) Heaton, A. L.; Armentrout, P. B. *J. Phys. Chem. A* **2008**, *112*, 10156.

(10) Heaton, A. L.; Armentrout, P. B. *J. Phys. Chem. B* **2008**, *112*, 12056.

(11) Heaton, A. L.; Moision, R. M.; Armentrout, P. B. *J. Phys. Chem. A* **2008**, *112*, 3319.

(12) Ye, S. J.; Armentrout, P. B. *J. Phys. Chem. A* **2008**, *112*, 3587.

(13) Carl, D. R.; Armentrout, P. B. *J. Phys. Chem. A* **2012**, *116*, 3802.

(14) Carl, D. R.; Armentrout, P. B. *Chem. Phys. Chem.* **2013**, in press.

(15) Carl, D. R.; Chatterjee, B. K.; Armentrout, P. B. *J. Chem. Phys.* **2010**, *132*, 44303.

(16) Cooper, T. E.; Armentrout, P. B. *J. Phys. Chem. A* **2009**, *113*, 13742.

(17) Cooper, T. E.; Armentrout, P. B. *Chem. Phys. Lett.* **2010**, *486*, 1.

(18) Cooper, T. E.; Armentrout, P. B. *J. Chem. Phys.* **2011**, *134*, 114308.

(19) Cooper, T. E.; Carl, D. R.; Armentrout, P. B. *J. Phys. Chem. A* **2009**, *113*, 13727.

(20) Hofstetter, T. E.; Armentrout, P. B. *J. Chem. Phys.* **2013**, in press.

(21) Armentrout, P. B.; Clark, A. A. *Int. J. Mass Spectrom.* **2012**, *316-318*, 182.

(22) Schultz, R. H.; Armentrout, P. B. *Int. J. Mass Spectrom. Ion Proc.* **1991**, *107*, 29.

(23) Schultz, R. H.; Crellin, K. C.; Armentrout, P. B. *J. Am. Chem. Soc.* **1991**, *113*, 8590.

(24) Fisher, E. R.; Armentrout, P. B. *J. Chem. Phys.* **1991**, *94*, 1150.

(25) Fisher, E. R.; Kickel, B. L.; Armentrout, P. B. *J. Chem. Phys.* **1992**, *97*, 4859.

(26) Rodgers, M. T.; Armentrout, P. B. *J. Phys. Chem. A* **1997**, *101*, 1238.

(27) Rodgers, M. T.; Armentrout, P. B. *Int. J. Mass Spectrom.* **1999**, *185/186/187*, 359.

(28) Rodgers, M. T.; Armentrout, P. B. *J. Phys. Chem. A* **1999**, *103*, 4955.

(29) Moision, R. M.; Armentrout, P. B. *Phys. Chem. Chem. Phys.* **2004**, *6*, 2588.

(30) Moision, R. M.; Armentrout, P. B. *J. Phys. Chem. A.* **2006**, *110*, 3933.

(31) Teloy, E.; Gerlich, D. *Chem. Phys.* **1974**, *4*, 417.

(32) Aristov, N.; Armentrout, P. B. *J. Phys. Chem.* **1986**, *90*, 5135.

(33) Dalleska, N. F.; Honma, K.; Sunderlin, L. S.; Armentrout, P. B. *J. Am. Chem. Soc.* **1994**, *116*, 3519.

(34) Daly, N. R. *Rev. Sci. Instrum.* **1960**, *31*, 264.

(35) Stein, S. E.; Rabinovich, B. S. *Chem. Phys. Lett.* **1977**, *49*, 1883.

(36) Beyer, T. S.; Swinehart, D. F. *Comm. Assoc. Comp. Mach.* **1973**, *16*, 379.

(37) Stein, S. E.; Rabinovich, B. S. *J. Chem. Phys.* **1973**, *58*, 2438.

(38) Gilbert, R. G.; Smith, S. C. *Theory of Unimolecular and Recombination Reactions*; Blackwell Scientific: London, 1990.

(39) Hales, D. A.; Lian, L.; Armentrout, P. B. *Int. J. Mass Spectrom. Ion Proc.* **1990**, *102*, 269.

(40) Holbrook, K. A.; Pilling, M. J.; Robertson, S. H. *Unimolecular Reactions*, 2nd ed.; Wiley: New York, 1996.

(41) Truhlar, D. G.; Garrett, B. C.; Klippenstein, S. J. *J. Phys. Chem.* **1996**, *100*, 12771.

(42) Loh, S. K.; Hales, D. A.; Lian, L.; Armentrout, P. B. *J. Chem. Phys.* **1989**, *90*, 5466.

(43) Khan, F. A.; Clemmer, D. E.; Schultz, R. H.; Armentrout, P. B. *J. Phys. Chem.* **1993**, *97*, 7978.

(44) Rodgers, M. T.; Ervin, K. M.; Armentrout, P. B. *J. Chem. Phys.* **1997**, *106*, 4499.

(45) Moision, R. M.; Armentrout, P. B. *J. Phys. Chem. A.* **2002**, *106*, 10350.

(46) Muntean, F.; Armentrout, P. B. *J. Phys. Chem. A* **2003**, *107*, 7413.

(47) Armentrout, P. B. *J. Chem. Phys.* **2007**, *126*, 234302.

(48) Armentrout, P. B.; Simons, J. *J. Am. Chem. Soc.* **1992**, *114*, 8627.

(49) Waage, E. V.; Rabinovitch, B. S. *Chem. Rev.* **1970**, *70*, 377.

CHAPTER 3

THEORETICAL CALCULATIONS

Structural and Energetic Calculations of $M^{2+}(H_2O)_x$

The theoretical approaches used throughout Chapters 4 and 6 – 8 are quite similar. The main objective is to identify the lowest energy or ground-state (GS) conformation for a given sized $M^{2+}(H_2O)_x$ complex and any other low-lying structures utilizing computational chemistry software. Water molecules that bind directly to the metal ion center are located in the inner solvent shell of the hydrated complex. The number of water molecules making up the inner shell can increase with larger ionic radii of the metal center. Once the inner shell is satisfied, additional water molecules of a $M^{2+}(H_2O)_x$ complex will bind in the secondary solvent shell through hydrogen-bonding interactions with the inner shell water molecules. Assuming a complete inner shell of six water molecules, the approximate location of the oxygen atoms of the water molecules with respect to the metal ion center can be easily predicted using valence-shell electron pair repulsion (VSEPR) theory.[1,2] If the hydrogen atoms are now included, the structure will optimize the position of the water molecules about the metal ion center to minimize hydrogen-hydrogen repulsions. Identifying ground state and low-lying structures for $M^{2+}(H_2O)_x$ complexes containing secondary solvent shell water molecules with a number of different inner shell sizes becomes less intuitive and requires more sophisticated computational procedures. Theoretical binding energies of the x^{th} water molecule of a

given $M^{2+}(H_2O)_x$ complex are determined by calculating the energetic difference between the sum of the individual optimized $M^{2+}(H_2O)_{x-1}$ and H_2O products with respect to the optimized $M^{2+}(H_2O)_x$ reactant and subsequently compared to experimentally determined binding energies.

All theoretical calculations were performed using Gaussian03 unless noted otherwise.[3] Geometry optimizations for the $M^{2+}(H_2O)_x$ complexes, where M = Mg and Ca, are calculated using density functional theory (DFT) with Becke's three parameter (B3) functional[4] and the correlation functionals of Lee, Yang, and Parr (LYP)[5] with a 6-311+G(d,p) basis set. The opt = CalcAll keyword is specified to ensure structure convergence upon optimization. Vibrational frequencies and rotational constants used in the modeling procedures were obtained at this same level of theory. Zero-point energy (ZPE) and thermal corrections for a given complex are calculated from vibrational frequencies scaled by 0.989. B3LYP, B3P86,[6] and MP2(full)[7] single point energies are calculated with a 6-311+G(2d,2p) basis set from the B3LYP/6-311+G(d,p) geometries. ZPE and thermal corrections were calculated for the reactants and products using the scaled frequencies. Basis set superposition error (BSSE) corrections were also calculated using the full counterpoise (CP) method, which is commonplace for metal-ligand systems utilizing finite basis sets.[8,9] For the earliest hydration studies for $Ca^{2+}(H_2O)_x$ complexes, Chapter 4, single point energies calculated from MP2(full)/6-311+G(d,p) geometries resulted in theoretical binding energies that differed less than 1 kJ/mol compared to analogous single point energies of B3LYP/6-311+G(d,p) gometries. With minimal energetic differences between the two optimization procedures and the MP2(full) optimizations requiring significantly more computational resources because of electron-

electron correlation, all subsequent geometry optimizations were performed using the B3LYP level of theory.

As the $M^{2+}(H_2O)_x$ complexes become more complex by having various inner shell sizes and water molecules located in the secondary solvent shell, more sophisticated computational procedures are necessary to determine all possible low-energy conformations. Simulated annealing in combination with quantum-chemical calculations[10] were employed for $M^{2+}(H_2O)_x$ complexes where M = Mg and Ca. Briefly, the AMBER molecular dynamics package with the AMBER force field[11] was used to search for possible stable structures in each system's conformational space. At the end of each annealing cycle, the structure was optimized using NWChem[12] at the HF/3-21G level. Unique structures for each system within ~ 50 kJ/mol of the lowest energy structure were further optimized at the B3LYP/6-31G(d) level of theory,[4,13] specifying the "loose" keyword in Gaussian03, which utilizes a large step size (0.01 au) and root mean squared (rms) force constant (0.0017) to ensure a rapid geometry convergence. Unique structures obtained from these optimizations were then chosen for higher-level geometry optimization and frequency calculations using B3LYP/6-311+G(d,p) with subsequent B3LYP, B3P86 and MP2(full) single point energies calculated with the 6-311+G(2d,2p) basis set. Simulated annealing calculations for $Ca^{2+}(H_2O)_x$ and $Mg^{2+}(H_2O)_x$ complexes were carried out for four, five, and six water inner shells for x = 5 – 7 complexes and a five and six water inner shell for x = 8 and larger.

All calculations described up until now have exclusively utilized all-electron Pople-style basis sets, however, the initial theoretical investigations of $Ca^{2+}(H_2O)_x$ complexes, Chapter 4, also considered a split-basis set approach. B3LYP geometry

optimizations and subsequent B3LYP, B3P86, MP2(full) and MP2(frozen core) single point energy calculations were performed with calcium maintaining the Pople-style basis sets and with water molecules treated with Dunning's correlation consistent basis set, aug-cc-pVTZ.[14] This split-basis set approach is referred to as pVTZ(Ca-G). In Chapter 6, additional split-basis set calculations were also performed for calcium treated with correlational consistent cc-pVTZ, cc-pCVTZ, and cc-pwCVTZ basis sets for B3LYP geometry optimizations and B3LYP, B3P86, BH&HLYP,[68] and MP2(full) single point energies while water molecules utilized the aug-cc-pVTZ basis set. These calculations are further identified as pVTZ, pCVTZ, and pwCVTZ, respectively. The cc-pCVTZ (correlation consistent polarized core/valence triple zeta) basis set includes extra functions designed for core-core and core-valence correlation, with the cc-pwCVTZ basis set weighting the core-valence contributions in order to achieve faster convergence.[15] BSSE corrections were also calculated using the same split-level basis set treatments from the optimized geometries. Thermal corrections (298 K) calculated from B3LYP/6-311+G(d,p) frequency calculations were applied all calculations utilizing these additional split-level basis sets. pCVTZ calculations were the only split-level basis set approach utilized for the investigations of $Mg^{2+}(H_2O)_x$ complexes, Chapter 8.

Previous theoretical calculations by Iceman and Armentrout[17] on $K^+(NH_3)_x$ complexes, which are isoelectronic with $Ca^{2+}(H_2O)_x$ complexes, have shown that the use of relativistic Hay-Wadt[18] and Stuttgart-Dresden[19] effective core potentials (ECPs) for potassium underestimates the metal-ligand binding energies. As a result, such pseudopotential calculations were not considered for $Ca^{2+}(H_2O)_x$ complexes. However, Sr is not parameterized by the all-electron Pople-style basis sets utilized for calcium and

magnesium. Therefore, geometry optimizations for $Sr^{2+}(H_2O)_x$ complexes were performed at the B3LYP/HW*/6-311+G(d,p) level of theory where the HW* indicates that Sr was described using an effective core potential and valence basis set from Hay and Wadt[18] with a single d polarization function (exponent of 0.40) added.[20] Water molecules are still treated with the 6-311+G(d,p) basis set. For comparison of $Sr^{2+}(H_2O)_x$ binding energies described in Chapter 7, geometry optimizations were performed with three additional levels of theory: B3LYP/SD/6-311+G(d,p), B3LYP/Def2TZVP, and BH&HLYP/Def2TZVPP. The former uses the Stuttgart-Dresden (SD) ECP and basis set for Sr developed by Kaupp et al.[21] and the 6-311+G(d,p) basis set for water, whereas in the latter, all atoms are represented by the Def2TZVP basis set,[22] a balanced set of triple zeta + polarization functions quality that also uses the SD ECP for Sr. Both ECPs for $Sr^{2+}(H2O)_x$ utilize a small core of 28 electrons. Vibrational frequencies and rotational constants were also calculated with these three basis set treatments and frequencies were scaled by 0.989 to calculate zero-point energy and thermal corrections.[23] Single point energies were calculated at the B3LYP, B3P86,[6] MP2(full),[7] and M06[24] levels using the HW*/6-311+G(2d,2p), SD/6-311+G(2d,2p), and Def2TZVPP basis sets. These basis set treatments are further identified as HW*, SD, and Def2. The Def2TZVPP basis set includes extra valence functions for Sr and H atoms compared to the Def2TZVP basis set, but no difference for O atoms. M06 single point energies were calculated using NWChem instead of Gaussian03.[12] BSSE corrections in the binding energies were calculated using the full counterpoise (cp) method.[8,9]

The reaction coordinates for charge separation from $M^{2+}(H_2O)_x$, where x = 2 (M = Sr and Ca), x = 3, (M = Ca and Mg) and x = 4 (M = Mg), were mapped out utilizing a

combination of relaxed potential energy surface scans and quadratic synchronous transit (QST3) calculations[25] to locate all transition state and intermediate complexes. This was accomplished using the B3LYP/6-311+G(d,p) level of theory for magnesium and calcium calculation whereas strontium calculations utilized the B3LYP/HW*/6-311+G(d,p), B3LYP/SD/6-311+G(d,p), and B3LYP/Def2TZVP levels of theory. For magnesium and calcium studies, single point energies of the transition state and intermediate structures were calculated using B3LYP/, B3P86/, and MP2(full)/6-311+G(2d,2p) levels of theory with the B3LYP/6-311+G(d,p) geometries whereas single point energies of transition state and intermediate structures from the $Sr^{2+}(H_2O)_2$ charge separation process were calculated at the B3LYP and MP2(full) levels with the HW*/6-311+G(2d,2p), SD/6-311+G(2d,2p), and Def2TZVPP basis sets for the B3LYP/HW*/6-311+G(d,p), B3LYP/SD/6-311+G(d,p), and B3LYP/Def2TZVP geometries. All energies include ZPE corrections with vibrational frequencies scaled by 0.989.

$M^{2+}(H_2O)_x$ structures are designated throughout this thesis with an (x,y,z) notation to distinguish water molecules in the first (x), second (y), and third (z) solvent shells. Inner shell water molecules are simply designated as either single (D) or double (DD) donor water molecules whereas outer shell water molecules are identified as single (A) or double (AA) acceptor water molecules. In some structures, secondary solvent shell water molecules can also be identified as single acceptor-single donor (AD) or double acceptor-single donor (AAD). In these instances, this second solvent shell water molecule specifies that the structure either contains a third solvent shell water molecule (z) or a water molecule that binds to both an inner and second solvent shell water molecule (identified by half-integers in y and z and an A_1A_2 designation).

Structural Investigations of M^+(Met) Complexes

In collision-induced dissociation studies of M^+(Met), where M = Li, Na, and K and Met = Methionine, a sulfur-containing amino cid,[26] conducted by Armentrout et al., all likely conformers for examined using the simulated annealing procedure described in the previous section. The same procedure is used for H^+(Met) complexes. Geometry calculations were initially optimized using B3LYP/6-311G(d,p), but were reoptimized at the B3LYP/6-311+G(d,p) level of theory for the studies presented in Chapter 9. Bond lengths typically changed by < 0.03 Å, bond angles by < 1°, and relative energies of different conformers were within 3 kJ/mol when diffuse functions (designated by a "+") were included into the basis set. Single point energy calculations were carried out for the 6 – 10 most stable structures at the B3LYP, B3P86, and MP2(full) levels using the 6-311+G(2d,2p) basis set.[27] Zero-point vibrational energy (ZPE) corrections were determined using vibrational frequencies calculated at the B3LYP/6-311+G(d,p) level scaled by a factor of 0.9804.[28]

For the Rb^+(Met) and Cs^+(Met) complexes, all conformations considered previously for K^+(Met) were used as starting points for geometry and vibrational frequency calculations optimized at the B3LYP/HW*/6-311+G(d,p) level where HW* indicates Rb^+ and Cs^+ were described using the effective core potentials and valence basis sets of Hay and Wadt[18] with a single d polarization function (exponents of 0.24 and 0.19, respectively) included.[29] Relative energies are determined using single point energies at the B3LYP, B3P86, and MP2(full) levels using the HW*/6-311+G(2d,2p) basis set. Additionally, geometry optimizations, frequency calculations, and single point energy calculations were performed using the Def2TZVP basis sets of triple zeta valence quality

for all elements of the Rb^+(Met) and Cs^+(Met) complexes.[30] These basis sets for Rb and Cs are designed to be used with ECPs developed by Leininger et al.[31]

Calculated vibrational frequencies and intensities were calculated for optimized M^+(Met) complexes using the harmonic oscillator approximation and analytical derivatives of the energy-minimized Hessian calculated at the levels of theory noted above. Frequencies were scaled by 0.975 as this scaling factor leads to good agreement between calculated and experimentally well-resolved peaks and is in accord with comparisons with previous infrared multiple photon dissociation spectral.[32-35] Calculated vibrational frequencies are broadened using a 20 cm^{-1} full width at half maximum Gaussian line shape for comparison to experimental IRPMD spectra.

References

(1) Gillespie, R. J. *J. Chem. Educ.* **1970**, *47*, 18.

(2) Gillespie, R. J.; Nyholm, R. S. *Quart. Rev.* **1957**, *11*, 339.

(3) Frisch, M. J.; Trucks, G. W.; Schlegel, H. B.; Scuseria, G. E.; Robb, M. A.; Cheeseman, J. R.; Montgomery, J., J. A. ; Vreven, T.; Kudin, K. N.; Burant, J. C.; Millam, J. M.; Iyengar, S. S.; Tomasi, J.; Barone, V.; Mennucci, B.; Cossi, M.; Scalmani, G.; Rega, N.; Petersson, G. A.; Nakatsuji, H.; Hada, M.; Ehara, M.; Toyota, K.; Fukuda, R.; Hasegawa, J.; Ishida, M.; Nakajima, T.; Honda, Y.; Kitao, O.; Nakai, H.; Klene, M.; Li, X.; Knox, J. E.; Hratchian, H. P.; Cross, J. B.; Adamo, C.; Jaramillo, J.; Gomperts, R.; Stratmann, R. E.; Yazyev, O.; Austin, A. J.; Cammi, R.; Pomelli, C.; Ochterski, J. W.; Ayala, P. Y.; Morokuma, K.; Voth, G. A.; Salvador, P.; Dannenberg, J. J.; Zakrzewski, V. G.; Dapprich, S.; Daniels, A. D.; Strain, M. C.; Farkas, O.; Malick, D. K.; Rabuck, A. D.; Raghavachari, K.; Foresman, J. B.; Ortiz, J. V.; Cui, Q.; Baboul, A. G.; Clifford, S.; Cioslowski, J.; Stefanov, B. B.; Liu, G.; Liashenko, A.; Piskorz, P.; Komaromi, I.; Martin, R. L.; Fox, D. J.; Keith, T.; Al-Laham, M. A.; Peng, C. Y.; Nanayakkara, A.; Challacombe, M.; Gill, P. M. W.; Johnson, B.; Chen, W.; Wong, M. W.; Gonzalez, C.; Pople, J. A. Gaussian 03, Revision B.02; Gaussian, Inc.: Pittsburgh, PA, 2003.

(4) Becke, A. D. *J. Chem. Phys.* **1993**, *98*, 5648.

(5) Lee, C.; Yang, W.; Parr, R. G. *Phys. Rev. B* **1988**, *37*, 785.

(6) Perdew, J. P. *Phys. Rev. B* **1986**, *33*, 8822.

(7) Möller, C.; Plesset, M. S. *Phys. Rev.* **1934**, *46*, 618.

(8) Boys, S. F.; Bernardi, R. *Molec. Phys.* **1970**, *19*, 553.

(9) van Duijneveldt, F. B.; van Duijneveldt de Rijdt, J. G. C. M.; van Lenthe, J. H. *Chem. Rev.* **1994**, *94*, 1873.

(10) Moision, R. M.; Armentrout, P. B. *J. Phys. Chem. A.* **2002**, *106*, 10350.

(11) Pearlman, D. A.; Case, D. A.; Caldwell, J. W.; Ross, W. R.; Cheatham, T. E.; DeBolt, S.; Ferguson, D.; Seibel, G.; Kollman, P. *Comp. Phys. Commun.* **1995**, *91*, 1.

(12) Bylaska, E. J.; Jong, W. A. d.; Govind, N.; Kowalski, K.; Straatsma, T. P.; Valiev, M.; Wang, D.; Apra, E.; Windus, T. L.; Hammond, J.; Nichols, P.; Hirata, S.; Hackler, M. T.; Zhao, Y.; Fan, P. D.; Harrison, R. J.; Dupuis, M.; Smith, D. M. A.; Nieplocha, J.; Tipparaju, V.; Krishnan, M.; Wu, Q.; Voorhis, T. V.; Auer, A. A.; Nooijen, M.; Brown, E.; Cisneros, G.; Fann, G. I.; Fruchtl, H.; Garza, J.; Hirao, K.; Kendall, R.; Nichols, J. A.; Tsemekhman, K.; Wolinski, K.; Anchell,

J.; Bernholdt, D.; Borowski, P.; Clark, T.; Clerc, D.; Dachsel, H.; Deegan, M.; Dyall, K.; Elwood, D.; Glendening, E.; Gutowski, M.; Hess, A.; Jaffe, J.; Johnson, B.; Ju, J.; Kobayashi, R.; Kutteh, R.; Lin, Z.; Littlefield, R.; Long, X.; Meng, B.; Nakajima, T.; Niu, S.; Pollack, L.; Rosing, M.; Sandrone, G.; Stave, M.; Taylor, H.; G. Thomas, J. v. L.; Wong, A.; Zhang, Z. NWChem, A Computational Chemistry Package for Parallel Computers; Version 5.1 ed.; Pacific Northwest National Laboratory: Richland, Washington 99352, 2007.

(13) Ditchfield, R.; Hehre, W. J.; Pople, J. A. *J. Chem. Phys.* **1971**, *54*, 724.

(14) Woon, D. E.; Dunning, T. H. *J. Chem. Phys.* **1993**, *98*, 1358.

(15) Koput, J.; Peterson, K. A. *J. Phys. Chem. A.* **2002**, *106*, 9595.

(16) Rodgers, M. T.; Armentrout, P. B. *Int. J. Mass Spectrom.* **2007**, *267*, 167.

(17) Iceman, C.; Armentrout, P. B. *Int. J. Mass Spectrom.* **2003**, *222*, 329.

(18) Hay, P. J.; Wadt, W. R. *J. Chem. Phys.* **1985**, *82*, 299.

(19) Andrae, D.; Haeussermann, U.; Dolg, M.; Stoll, H.; Preuss, H. *Theor. Chim. Acta* **1990**, *77*, 123.

(20) Glendening, E. D.; Feller, D. *J. Phys. Chem.* **1996**, *100*, 4790.

(21) Kaupp, M.; Schleyer, P. v. R.; Stoll, H.; Preuss, J. *J. Chem. Phys.* **1991**, *94*, 1360.

(22) Weigend, F.; Ahlrichs, R. *Phys. Chem. Chem. Phys* **2005**, *7*, 3297.

(23) Bauschlicher, J., C. W.; Partridge, H. *J. Chem. Phys.* **1995**, *103*, 1788.

(24) Zhao, Y.; Truhlar, D. G. *Theor. Chem. Acc.* **2008**, *120*, 215.

(25) Peng, C. Y.; Schlegel, H. B. *Israel J. Chem.* **1994**, *33*, 449.

(26) Armentrout, P. B.; Gabriel, A.; Moision, R. M. *Int. J. Mass Spectrom.* **2009**, *283*, 56.

(27) McLean, A. D.; Chandler, G. S. *J. Chem. Phys.* **1980**, *72*, 5639.

(28) Foresman, J. B.; Frisch, A. E. *Exploring Chemistry with Electronic Structure Methods*, 2nd ed.; Gaussian, Inc.: Pittsburgh, PA, 1996.

(29) Glendening, E. D.; Feller, D.; Thompson, M. A. *J. Am. Chem. Soc.* **1994**, *116*, 10657.

(30) Weigend, F.; Ahlrichs, R. *Phys. Chem. Chem. Phys.* **2005**, *7*, 3297.

(31) Leininger, T.; Nicklass, A.; Kuechle, W.; Stoll, H.; Dolg, M.; Bergner, A. *Chem. Phys. Lett.* **1996**, *255*, 274.

(32) Heaton, A. L.; Bowman, V. N.; Oomens, J.; Steill, J. D.; Armentrout, P. B. *J. Phys. Chem. A* **2009**, *113*, 5519.

(33) Polfer, N. C.; Oomens, J.; Dunbar, R. C. *Phys. Chem. Chem. Phys.* **2006**, *8*, 2744.

(34) Bush, M. F.; Oomens, J.; Saykally, R. J.; Williams, E. R. *J. Am. Chem. Soc.* **2008**, *130*, 6463.

(35) Bush, M. F.; Oomens, J.; Saykally, R. J.; Williams, E. R. *J. Phys. Chem. A* **2008**, *112*, 8578.

CHAPTER 4

BINDING ENERGIES FOR THE INNER HYDRATION SHELL OF CALCIUM DICATIONS: AN EXPERIMENTAL AND THEORETICAL INVESTIGATION OF $Ca^{2+}(H_2O)_x$ COMPLEXES (x = 5 – 9)

Abstract

The sequential bond energies of $Ca^{2+}(H_2O)_x$ complexes, where x = 5 – 9, are determined by collision-induced dissociation (CID) using a guided ion beam tandem mass spectrometer equipped with an electrospray ionization source. This work constitutes the first quantitative threshold CID study of multiply charged ions. The kinetic energy dependent cross sections are determined over a wide energy range to monitor all possible dissociation products and are modeled to obtain 0 and 298 K binding energies for loss of a single water molecule. These binding energies decrease monotonically for the $Ca^{2+}(H_2O)_5$ complex to $Ca^{2+}(H_2O)_7$ and plateau for $Ca^{2+}(H_2O)_7$, $Ca^{2+}(H_2O)_8$, and $Ca^{2+}(H_2O)_9$. This suggests that six water molecules bind directly to the calcium ion and that three outer shell water molecules bind to inner shell water molecules through similar binding motifs. These experimental results agree well with previous literature results obtained thermochemical experimental techniques. A comprehensive theoretical investigation of the structures and energetics of the $Ca^{2+}(H_2O)_x$ systems employing several levels of theory accompany the experimental work.

Introduction

Calcium ions play a significant role in a number of physiological processes. As an example, the concentration of free calcium ions within the cytosol of a muscle cell must be maintained between 10^{-6} and 10^{-7} M to induce muscle contraction.[1] Intracellular calcium concentrations are governed by ions coming in and out of the cell via ATP driven calcium ion channels within the cellular membrane, in and out of internal storage facilities (sarcoplasmic reticulum), or regulated by calmodulin, a calcium-regulating protein. For these calcium ions to bind to calmodulin, they must go from an extensively hydrated state to one that is partially hydrated, at which point ligand exchange occurs between the remaining water molecules and oxygen containing side chains of the protein molecule. Studying the complete dehydration of the calcium ion is a critical building block for a detailed understanding of such ligand exchange reactions.

The stepwise dehydration of a number of singly charged metal ion (M^+) hydrates has been previously investigated experimentally using equilibrium[2-4] and guided ion beam techniques.[5-8] These metal ion hydrates are formed by three-body associative reactions after generating M^+ in the gas phase in the presence of water vapor. Using this type of approach to study doubly charged ion hydrates is troublesome because the second ionization energy of most metals exceeds the first ionization energy of water (12.6 eV).[9] Thus, association reactions may not lead to $M^{2+}(H_2O)_x$, but rather to two singly charged species, $MOH^+(H_2O)_{x-y-1}$ and $H^+(H_2O)_y$.[10,11] As a result, alternative sources for efficiently generating such $M^{n+}(H_2O)_x$ species are desirable. One attractive possibility is to use electrospray ionization (ESI) where ions that exist in solution can be transferred directly into the gas phase.[12,13]

This chapter presents results obtained using the ESI source discussed in Chapter 2, which enables the formation of $Ca^{2+}(H_2O)_x$ complexes. In the present work, the energetics for single water molecule loss from the $Ca^{2+}(H_2O)_x$ system, where x = 5 – 9, are investigated using threshold collision-induced dissociation (TCID). TCID studies are well established means of acquiring accurate bond energies of ligated metal systems, but quantitative TCID studies have never been performed on multiply charged metal-ligand systems. Therefore, the hydration of doubly charged calcium ions is also of interest because comparisons between experimental binding energies of the $Ca^{2+}(H_2O)_x$ complexes with those in the literature can test the accuracy of our experimental approach. Ca^{2+} hydration has been studied previously by a number of experimental methods. Kebarle and coworkers have investigated the stepwise dehydration of $Ca^{2+}(H_2O)_x$ where x = 6 – 14, using high pressure mass spectrometry (HPMS) equilibrium experiments.[10,14] Williams and coworkers have also studied the $Ca^{2+}(H_2O)_x$ systems (x = 5 – 10) using kinetic experiments of blackbody infrared radiative dissociation (BIRD).[15,16] In addition to these quantitative studies, Shvartsburg and Siu have qualitatively studied the critical size for the $Ca^{2+}(H_2O)_x$ systems, i.e., the size at which a proton transfer/charge separation process becomes competitive with single ligand loss.[11]

Because experimentalists have yet to determine the binding of water molecules making up the inner hydration shell of calcium, much theoretical work has been done to fill this void. Theoretical calculations employing a diverse group of basis sets and levels of theory have been used to study these tightly bound water molecules, whereas larger $Ca^{2+}(H_2O)_x$ complexes that involve a second solvent shell have generally not been included.[17-20] As the data analysis requires reliable molecular parameters, the present

study provides an in-depth theoretical look at the structures and energetics of the $Ca^{2+}(H_2O)_x$ systems (x = 1 – 9), including those where second shell water molecules hydrogen bond to the inner hydration shell. By comparing these experimental results with theoretical calculations, we provide a more extensive understanding of the geometric structures of the inner and outer hydration shells.

Results

Cross sections for collision-induced dissociation. The CID cross sections for $Ca^{2+}(H_2O)_x$ (x = 5 – 9) are shown in Figure 4.1. A broad energy range was set to observe all possible dissociation products for each reactant complex. In all cases, the dominant process is the loss of a single water molecule from the parent species, Reaction 4.1.

$$Ca^{2+}(H_2O)_x + Xe \rightarrow Ca^{2+}(H_2O)_{x-1} + H_2O + Xe \qquad (4.1)$$

Once the first water molecule dissociates, additional water molecules dissociate sequentially as the collision energy increases until all water molecules are lost to form the bare metal ion. A proton transfer/charge separation process, Reaction 4.2, is also observed within the sequential dissociation of $Ca^{2+}(H_2O)_{5-7}$, Figure 4.1. Reaction 4.2 is observed once the

$$Ca^{2+}(H_2O)_2 + Xe \rightarrow CaOH^+ + H_3O^+ + Xe \qquad (4.2)$$

$Ca^{2+}(H_2O)_2$ complex is formed. The apparent threshold for this process is close to the apparent threshold for losing an additional water molecule giving $Ca^{2+}(H_2O)$. The energy ranges for the CID of $Ca^{2+}(H_2O)_8$ and $Ca^{2+}(H_2O)_9$ complexes were not sufficiently broad enough to observe the charge separation products.

The cross sections in Figure 4.1 do not show the second singly charged ion, $CaOH^+$ (m/z 57), because the mass overlap with the much more intense $Ca^{2+}(H_2O)_4$ product (m/z 56) obscures this minor product. Interestingly, no other calcium hydroxide product ions, $CaOH^+(H_2O)_{x-y-1}$, or proton-bound water clusters, $H^+(H_2O)_y$, were observed in the CID of any other reactant complex. As a result, the $Ca^{2+}(H_2O)_2$ complex represents a critical size for the calcium water system in which simple ligand loss becomes a competitive process with the proton transfer/charge separation process, in agreement with observations of Shvartsburg and Siu.[11] No other processes besides reaction 4.2 and sequential water losses were observed in these studies.

The H_3O^+ product channels in the CID spectra for $Ca^{2+}(H_2O)_5$ and $Ca^{2+}(H_2O)_6$ exhibit a noticeable break in the data, near 12.5 eV in the lab frame. This occurs because these light product ions can backscatter in the laboratory frame and can either be lost or reflected by the final lens that focuses ions into the octopole ion guide. Above 12.5 eV, the backscattered ions are reflected and thus collected by the detector, enhancing the observed signal. This lens does not affect the collection of heavier product ions, which are generally forward scattered in the laboratory frame, and thus has no impact on the threshold modeling.

Pressure dependence. One interesting observation made in the present studies was the sensitivity of the cross sections to the pressure of the collision gas. In CID studies, we routinely measure the pressure dependence of our product cross sections in order to extrapolate the cross sections to single collision conditions (zero pressure),[21,22] thereby ensuring that the collision energy is well-defined. Because the pressures used here are fairly low, 0.02 – 0.13 mTorr, such that single collision conditions generally

prevail, these extrapolations are usually linear in pressure. In the present work, it was found that this typical procedure led to primary product cross sections of $Ca^{2+}(H_2O)_x$, x = 6 and 7, being negative at the lowest energies. This result indicates that secondary collisions are contributing to the dissociations observed such that a linear extrapolation over corrects for the pressure effect. For x = 5, the threshold is high enough that secondary collisions are not influential, and for x = 8 and 9, the thresholds are sufficiently low that single collision events dominate the cross section at all energies. This sensitivity to pressure is a direct result of the double charge on these species, thereby increasing the collision cross section above those usually observed for singly charged ions. To properly account for this behavior, a quadratic pressure dependence can be used to extrapolate the cross sections to zero pressure conditions or the highest pressure can be removed from a linear extrapolation. Both methods gave similar extrapolated cross sections that fall to zero at the lowest energies, as shown in Figure 4.2.

Thermochemical results. The total reaction cross sections for water dissociation were modeled using Equations 2.4 and 2.5 for all $Ca^{2+}(H_2O)_x$ complexes because the overall shape of the cross sections is influenced by the cross sections for sequential dissociation of additional water molecules. In all threshold analyses, the reactant isomer corresponds to the 298 K GS, which comprises the largest population at thermal energies and the product ion corresponds to the 0 K GS because our threshold analysis is dominated by the lowest 0 K enthalpy species.[23] It might be noted that the cross sections for x = 7 and 8 could not be reproduced accurately at the lowest energies when using Equation 2.4, which demonstrates the need to include lifetime effects in modeling the data. The optimum modeling parameters obtained are listed in Table 4.1 and the models

of Equation 2.5 are compared to zero pressure-extrapolated cross sections in Figure 4.2. From Table 4.1, the kinetic shifts between the E_0 values obtained with and without lifetime effects accounted for in the modeling increase from 0.13 eV for x = 5 to 0.33 for x = 9.

Reaction thresholds for loss of a single water molecule from a reactant species decrease monotonically as the complex size increases from the $Ca^{2+}(H_2O)_5$ complex to the $Ca^{2+}(H_2O)_7$ complex. The $Ca^{2+}(H_2O)_7$, $Ca^{2+}(H_2O)_8$, and $Ca^{2+}(H_2O)_9$ complexes have nearly identical bond energies. These observations suggest two conclusions. First, it seems likely that six water molecules bind directly to the calcium ion and thus reside in the inner solvent shell. Second, because the larger calcium ion hydrates have similar bond energies, their hydrogen bonding interactions to the inner shell water molecules are likely to be similar.

The transition state for water loss from the reactant complex is considered to be loose. A useful measure of the looseness of these transition states is the entropies of activation, $\Delta S^{\dagger}$, which are also shown in Table 4.1 and derived from analyses of the data at a temperature of 1000 K. In all cases, these values are positive and relatively large, consistent with a loose transition state. These values increase from the $Ca^{2+}(H_2O)_5$ to the $Ca^{2+}(H_2O)_6$ complex, decrease for the $Ca^{2+}(H_2O)_7$, and then increase again for the larger complexes. This behavior also points to a change in the $Ca^{2+}(H_2O)_7$ structure upon addition of the seventh water molecule, consistent with the hypothesis of six inner shell water molecules.

Theoretical geometries and structural details for ground states of x = 1 – 6. The geometry optimizations and frequency calculations for each system studied here are

calculated using the B3LYP/6-311+G(d,p) level of theory. Structures for x = 1 – 6 were optimized without any explicit constraints, but all converged to symmetric structures. These ground-state (GS) structures have all water molecules bound directly to calcium with their dipole moments directed towards the metal ion center, in agreement with previous theoretical studies.[17-20] Ground state structures for $Ca^{2+}(H_2O)_x$ (x = 1 – 4) are shown in Figure 4.3. As expected, the single water complex has C_{2v} symmetry. One might expect a O–Ca–O linear configuration for the $Ca^{2+}(H_2O)_2$ complex because Ca^{2+} has no valence electrons, however, the B3LYP/6-311+G(d,p) geometry optimization predicts a bent geometry with a O–Ca–O angle of 124.7°. The orientation of the hydrogen atoms gives this structure C_2 symmetry. Such a bent structure has been calculated before for $Ca^{2+}(H_2O)_2$ and $Sr^{2+}(H_2O)_2$, but $Mg^{2+}(H_2O)_2$ optimizes to a linear configuration.[24] This behavior is attributed to the core polarization of these alkaline earth metal ions, which can compensate for the increased ligand repulsion in the bent structure.[24] The MP2(full)/6-311+G(d,p) geometry optimization also converged to a bent structure with a O–Ca–O angle of 125.8° and has C_s symmetry (i.e., one of the water molecules is in the same plane as O–Ca–O and the other is perpendicular to this plane). This small structural disparity for $Ca^{2+}(H_2O)_2$ at the two levels of theory has a negligible effect on the hydration enthalpies for water loss from $Ca^{2+}(H_2O)_2$ or $Ca^{2+}(H_2O)_3$ which differ by less than 1 kJ/mol. The $Ca^{2+}(H_2O)_3$ complex has all heavy atoms in the same plane with O–Ca–O angles of 120°. The hydrogen atoms lie above and below this plane such that the complex exhibits D_3 symmetry and the HOCaO dihedral angle, where the second oxygen atom refers to the oxygen atom that the hydrogen atom points toward, is 37.0°. The $Ca^{2+}(H_2O)_4$ complex exhibits S_4 symmetry.

Ground-state structures for $Ca^{2+}(H_2O)_x$ (x = 5 and 6) are shown in Figures 4.4 and 4.5, respectively. The five water complex is pseudo square-pyramidal with the base having two sets of unique water molecules, such that the (5,0) structure has C_{2v} symmetry. The addition of the sixth water molecule to the five water complex puts the base of the pyramid in the same plane as the calcium ion, giving a highly symmetrical (6,0) complex with T_h symmetry (including hydrogen atoms). The structures of the (5,0) and (6,0) complexes are clearly influenced by inner shell hydrogen bonding interactions, which are shown by dashed lines in Figures 4.4 and 4.5. Examining the orientation of the hydrogen atoms in $Ca^{2+}(H_2O)_6$, each hydrogen atom points towards the oxygen atom on an adjacent ligand, giving the complex T_h symmetry. Removal of one of the water molecules from this complex gives the pseudo-square pyramid structure of the (5,0) structure, Figure 4.4. Because of this inner shell hydrogen bonding, the O–Ca–O bond angles in the base of the pyramid are unequal: 161.6° for the two water molecules with hydrogen atoms pointed at the apex water molecule such that the O–Ca–O bond angles to the apex oxygen are 99.2°, and 149.0° for the two water molecules with hydrogen atoms parallel with the base such that the O–Ca–O bond angles to the apex oxygen are 105.5°. The four water molecules at the base have O–Ca–O angles of 87.6° with respect to each other. The hydrogen bonding is further indicated by asymmetric Ca–O–H angles for the water molecules having a 161.6° O–Ca–O angle. Here, the hydrogen atoms pointing directly towards the apex oxygen atom have Ca–O–H angles of 126.4° whereas the hydrogen atoms not participating in the inner shell hydrogen bonding have Ca–O–H angles of 128.7°.

Relevant structural details of the $Ca^{2+}(H_2O)_x$ complexes, where x = 1 – 6, are listed in Table 4.2. The Ca–O bond distances increase by about 0.03 ± 0.01 angstroms (Å) as each additional water molecule is added to the $Ca^{2+}(H_2O)_x$ complex consistent with the gradually decreasing bond energies, Table 4.1. At the same time, the O–H bond distances decrease from 0.977 Å for $Ca^{2+}(H_2O)$ to 0.967 Å for $Ca^{2+}(H_2O)_6$, approaching the O–H distance of 0.962 Å for a free water molecule. The H–O–H angles increase as more water molecules surround the ion, increasing from 104.3° for $Ca^{2+}(H_2O)$ to 104.7° for $Ca^{2+}(H_2O)_4$. The (5,0) and (6,0) structures have comparable H–O–H angles (105.0° – 105.4°) with respect to a free water molecule (105.1°).

Low-lying structures for x = 5 and 6. Additional low-lying structures for $Ca^{2+}(H_2O)_5$ and $Ca^{2+}(H_2O)_6$ having inner shells consisting of four and four or five water molecules, respectively, were located using the simulated annealing procedure described in Chapter 3. These structures are also shown in Figures 4.4 and 4.5 with relative 0K enthalpies and 298 K free energies with respect to the (5,0) and (6,0) GS structures provided in Table 4.3. Relative B3LYP/6-311+G(2d,2p), B3P86/6-311+G(2d,2p), and MP2(full)/6-311+G(2d,2p) single point energies are calculated from B3LYP/6-311+G(d,p) geometries. B3LYP and B3P86 energies are further designated as DFT energies.

If four water molecules reside in the inner solvent shell with a fifth water molecule hydrogen bonded to two of the inner shell water molecules, this results in the (4,1)_2D_AA structure having 0 K enthalpies [298 K free energies] 19 – 30 [21 – 31] kJ/mol above the (5,0) GS. For $Ca^{2+}(H_2O)_6$, four additional structures besides the (6,0) GS are worth further descriptions. Two additional low-lying structures have a five water

inner shell with the sixth water molecule participating in either two or one hydration bonds with the inner shell water molecules, resulting in the (5,1)_2D_A_aA_b or (5,1)_D_A_b structures, respectively. The "a" and "b" subscripts for acceptor water molecules designate binding to the apex and base water molecules for $Ca^{2+}(H_2O)_x$ complexes with a five water inner shell. The (5,1)_2D_A_aA_b or (5,1)_D_A_b structures lie 13 – 26 [3 – 16] and 22 – 37 [8 – 23] kJ/mol above the (6,0) GS. The (4,2)_4D_2AA and (4,2)_3D_AA,A structures build off the (4,1)_2D_AA structure and adds a sixth water molecule by hydrogen bonding to either two or one of the remaining inner shell water molecules. Both (4,2) structures exceed the (6,0) GS structure by more than 31 [26] kJ/mol, but the 2AA structure lies lower than the AA,A structure at 0 K by 6 – 10 kJ/mol, but the AA,A structure is preferred at 298 K by 0 – 4. The AA,A 298 K free energy lies 12 kJ/mol below its relative enthalpy because of a large entropic contribution due to the single acceptor water molecule behaving as a free rotor.

Theoretical geometries of ground state and low-lying structures for x = 7 – 9. Ground-state and low-lying structures for $Ca^{2+}(H_2O)_x$ complexes (x = 7 – 9) were obtained using the simulated annealing program detailed in Chapter 3 and are shown in Figures 4.6 – 4.8. Relative 0 K enthalpies and 298 K free energies are also provided in Table 4.3. GS (6,*y*) structures are preferred over (5,*y*) structures for DFT and MP2 levels of theory for a given $M^{2+}(H_2O)_x$ complex by 4 – 15 [9 – 15] and 17 – 32 [22 – 27] kJ/mol. B3P86 energies are 2 – 3 kJ/mol lower in energy than corresponding B3LYP energies for a specific conformer. The $Ca^{2+}(H_2O)_7$ GS structure forms when two adjacent inner shell water molecules from the (6,0) complex orient in the same plane and each donates a hydrogen bond to the outer shell water molecules resulting in a (6,1)_2D_AA

structure, Figure 4.6. Additional $Ca^{2+}(H_2O)_7$ structures were located with four, five and seven water molecules in the inner solvent shell. The lowest energy five water inner shell complexes are the (5,2)_4D_2A_bA_b and (5,2)_DD,2D_2A_aA_b structures at 4 – 22 [9 – 22] kJ/mol above the (6,1)_2D_AA GS. For the (5,2)_4D_2A_bA_b complex, each base water molecule of the inner shell participates in a single hydrogen bond such that the two A_bA_b water molecules lie directly across from one another whereas in the (5,2)_DD,2D_2A_aA_b structure, the apex water molecule serves as a double donor such that the A_aA_b water molecules reside next to each other. Interestingly, for DFT energies, the (7,0) structure lies [19 – 20] 17 – 18 kJ/mol above the (6,1)_2D_AA GS and 12 – 16 [6 – 10] kJ/mol above the (5,2)_4D_2A_bA_b complex, but MP2(full) calculates the (7,0) complex lies within 7 [5] kJ/mol above the (6,1)_2D_AA GS, but 10 [16] kJ/mol below the (5,2)_4D_2A_bA_b complex. The lowest energy (4,3) complexes lie more than 34 [29] above the (6,1)_2D_AA GS structure.

The eighth water molecule can hydrogen bond to the inner shell water molecules of the (6,1)_2D_AA complex in a number of ways. Rotation around a Ca–O bond adjacent to the first Ca–O rotation leads to the 0 K and 298 K ground state $Ca^{2+}(H_2O)_8$ (6,2)_4D_2AA (1) complex with C_2 symmetry, Figure 4.7. The initial 90° rotation around any one Ca–O bond in the $Ca^{2+}(H_2O)_6$ (6,0) complex puts three inner shell water molecules into the same plane allowing the middle water molecule to serve as a double donor water molecule for two outer shell water molecules. This (6,2)_DD,2D_2AA (1) structure lies 2 [2] kJ/mol higher above the (6,2)_4D_2AA (1). Alternatively, rotation around the Ca–O bond directly across from the initial Ca–O rotation in the (6,0) complex puts the two AA water molecules directly across from one another. This (6,2)_4D_2AA

(2) structure lies 4 [4] kJ/mol higher in energy than the (6,2)_4D_2AA (1) GS. Other high energy (6,2) complexes were located where the eighth water molecule hydrogen bonds in a sterically crowded (6,2)_DD,2D_2AA (2) complex, in the third solvent shell, (6,1,1)_2D_AAD_A, or binds to both inner and outer solvent shell water molecules, (6,1.5,0.5)_3D_AAD_A_1A_2. These structures lie 11 – 17 [6 – 13] kJ/mol above the (6,2)_4D_2AA (1) GS structure. Low-lying $Ca^{2+}(H_2O)_8$ complexes were also located with a five water inner shell. The (5,3)_DD,4D_2A_bA_b,A_aA_b, (5,3)_2DD,2D_3A_bA_b, and (5,3)_DD,3D_2A_aA_b,A_b structures lie [9 – 31] 10 – 26 kJ/mol above the (6,2)_4D_2AA (1) GS. Like the relative energies of the (7,0), DFT energies for the (8,0) structure lie 37 – 39 [35 – 37] kJ/mol above the (6,2)_4D_2AA (1) and 19 – 23 [23 – 27] kJ/mol above the lowest five water inner shell complex, (5,3)_DD,3D_2A_aA_b,A_b. However, for MP2(full), the (8,0) energy lies 12 [10] kJ/mol above the (6,2)_4D_2AA (1) GS, but 19 [15] kJ/mol below the (5,3)_DD,3D_2A_aA_b,A_b energy.

The ninth water molecule hydrogen bonds to the two remaining unbound inner shell water molecules of the (6,2)_4D_2AA (1) $Ca^{2+}(H_2O)_8$ complex. This $Ca^{2+}(H_2O)_9$ (6,3)_6D_3AA GS complex has D_3 symmetry with a C_3 axis such that each hydrogen bound second shell water molecule can rotate into one another as well as three C_2 axes around each outer shell oxygen – calcium ion bond, Figure 4.8. Another low-lying $Ca^{2+}(H_2O)_9$ complex, (6,3)_DD,4D_3AA (1), builds off the low energy (6,2)_DD,2D_2AA (1) structure such that the ninth water molecule can hydrogen bond to two of the three remaining inner shell water molecules that have yet to participate in any hydrogen bonding interactions. The (6,3)_DD,4D_3AA (1) structure lies 3 [2] kJ/mol above the (6,3)_6D_3AA GS at 298 K. A number of other unique six water inner shell

complex for x = 9 were also located, but these lie 10 – 17 kJ/mol above the (6,3)_6D_3AA GS at all levels of theory. The five water inner shell structures, (5,4)_2DD,3D_3A_bA_b,A_a, (5,4)_3DD,2D_2A_bA_b,2A_aA_b, and (5,4)_4DD_4A_bA_b structures were located and lie 20 – 34 [12 – 33] kJ/mol above the (6,3)_6D_3AA GS complex.

The small relative energetic differences between the (6,2)_4D_2AA (1) GS and (6,2)_DD,2D_2AA (1) conformers at x = 8 and the (6,3)_6D_3AA GS and (6,3)_DD,4D_3AA (1) conformers at x = 9 likely result in a distribution of these structures produced by the ESI source. Because the energetics are virtually identical, this will not affect the data analysis or the final bond enthalpies measured. Using molecular parameters for the alternate structures, the data analysis did not change parameters of Equation 2.5 listed in Table 4.1.

Conversion from 0 to 298 K. $\Delta H_{298} - \Delta H_0$ and $T\Delta S_{298}$ values, Table 4.4, are calculated with a rigid rotor/harmonic oscillator approximation using the vibrational frequencies and rotational constants calculated at the B3LYP/6-311+G(d,p) level of theory. The uncertainties for these values are found by scaling the vibrational frequencies up and down by 10%. These conversion factors are used to determine the ΔH_{298} and ΔG_{298} values listed in Table 4.4.

The $T\Delta S_{298}$ values increase going from $Ca^{2+}(H_2O)_5$ to $Ca^{2+}(H_2O)_6$, decrease for $Ca^{2+}(H_2O)_7$, and increase once again for the larger $Ca^{2+}(H_2O)_8$ and $Ca^{2+}(H_2O)_9$ complexes. This is a clear indication of the formation of a second solvent shell. Like the hydration enthalpies, ΔH_{298}, the free energies of hydration, ΔG_{298}, decrease as the size of the $Ca^{2+}(H_2O)_x$ complex increases. The $\Delta\Delta G_{298}$ (difference between ΔG_{298} of $Ca^{2+}(H_2O)_x$

and $Ca^{2+}(H_2O)_{x-1}$) values decrease monotonically from $Ca^{2+}(H_2O)_5$ to $Ca^{2+}(H_2O)_9$, but the free energies do not exhibit the same large decrease between $Ca^{2+}(H_2O)_6$ and $Ca^{2+}(H_2O)_7$ as the enthalpy values. This change occurs because of the large entropy change between the $Ca^{2+}(H_2O)_6$ and $Ca^{2+}(H_2O)_7$ complexes.

Theoretical bond enthalpies. Theoretical bond enthalpies for losing a single water molecule from all $Ca^{2+}(H_2O)_x$ complexes are listed in Table 4.5. These enthalpies include ZPE and thermal corrections to 298 K both with and without BSSE corrections and are calculated for the GS structures described above. B3LYP, B3P86, and MP2(full) single point energies were calculated with a 6-311+G(2d,2p) basis set using B3LYP/ and MP2(full)/6-311+G(d,p) geometries. Results for the MP2(full) geometries are provided in Table 4.5 only for the B3LYP bond energies because the two geometries produced nearly identical bond enthalpies for x = 1 – 9 with differences less than 1 kJ/mol. Single point energies calculated from MP2(full) geometries will not be discussed further. The B3LYP and B3P86 single point calculations produced almost identical binding enthalpies for $Ca^{2+}(H_2O)_x$, where x = 1 – 6, but B3LYP values are 2 – 3 kJ/mol lower than B3P86 binding enthalpies for x = 7 – 9. MP2(full) energies are lower for x = 1 – 3, higher values for x = 5 and 6, and slightly lower values for x = 7 – 9 compared with B3LYP single point enthalpies. The BSSE corrections are 1 – 3 kJ/mol for DFT bond energies, but 4 – 9 kJ/mol for MP2(full) bond energies.

Binding enthalpies calculated at the B3LYP and B3P86 levels with the pVTZ(Ca-G) basis set produce very similar results to values calculated using the 6-311+G(2d,2p) basis set. Values for x = 3 – 9 are essentially identical and values for the smallest complexes are slightly larger (3 – 5 kJ/mol) for the pVTZ(Ca-G) basis set. Somewhat

larger differences occur for the MP2(full)/pVTZ(Ca-G)//B3LYP/pVTZ(Ca-G) calculations compared with the MP2(full)/6-311+G(2d,2p)//B3LYP/6-311+G(d,p) results, Table 4.5. Bond energies using the pVTZ(Ca-G) basis set yielded BSSE corrections less than 1 kJ/mol for DFT bond energies. BSSE corrections at the MP2(full)/pVTZ(Ca-G) and MP2(FC)/pVTZ(Ca-G) levels of theory are larger, 4 – 9 and 2 – 5 kJ/mol, respectively.

It is useful to provide one additional observation regarding the calculations using frozen core MP2, MP2(FC) calculations, performed using the pVTZ(Ca-G) basis set. For MP2(FC) calculations of Ca^{2+}, the Gaussian03 default uses a small 10-electron core corresponding to the 1s, 2s, and 2p electrons, but switches to an 18-electron core when calcium complexes to any number of water molecules. The MP2(FreezeG2) command, which freezes the 10-electron core of Ca^{2+} and the 1s electrons of the oxygen atoms, should be used to avoid the switch in the default conditions.

The deviations among the various theoretical methods listed in Table 4.5 can be compared succinctly using the calculated mean absolute deviation (MAD) with respect to the B3LYP6-311+G(2d,2p)//B3LYP/6-311+G(d,p) binding energies. Very small differences are found between the results obtained using the 6-311+G(2d,2p) and pVTZ(Ca-G) basis sets and between B3LYP and B3P86 single point energies. Somewhat larger deviations are found for the MP2 methods, with lack of BSSE corrections yielding the biggest differences. Given these comparisons, the B3LYP/6-311+G(2d,2p)//B3LYP/6-311+G(d,p) (B3LYP//B3LYP) binding energies are representative of our calculated theoretical results.

Literature calculations. Table 4.5 also includes results from a number of theoretical studies in the literature, which employ a diverse group of basis sets and levels of theories in determining their binding enthalpies. All of these studies treat the calcium ion basis set in some special way compared to the light atoms. Katz and coworkers[20] performed single point energy calculations for $Ca^{2+}(H_2O)_x$, x = 1 – 9, where all water molecules were bound directly to the Ca^{2+} ion using a MP2(full)/HUZSP*(p,d)//RHF/HUZSP*(p) level with ZPE and thermal corrections taken from the RHF/HUZSP*(p) frequency calculations. This basis set comprises a standard 6-31G(d) basis set for the light atoms and a split-valence Huzinaga basis set for the calcium ion, but no diffuse functions are included. This study also computed relative energies for the $Ca^{2+}(H_2O)_x$ complexes where x = 6 – 8 with varying number of water molecules bound directly to the calcium ion, but these calculations included diffuse functions on all of the atoms. Glendening and Feller[18] calculated hydration energies for $Ca^{2+}(H_2O)_x$, x = 1 – 6, employing a MP2(FC)/6-31+G(d)//RHF/6-31+G(d) level of theory. For the geometry optimization and single point energy calculations, a Hay/Wadt ECP treatment of the calcium atom (10 core electrons) was used and correlation of the 1s electrons on oxygen was neglected. ZPE, thermal, and BSSE corrections were included in this study.

Merrill and coworkers[19] have utilized an effective fragment potential approach for $Ca^{2+}(H_2O)_x$, x = 1 – 6 where only the metal cation is treated with an ab initio wavefunction. This approach is used to reproduce Hartree-Fock binding energies with the 6-31+G(d) basis set. The energies include ZPE and thermal corrections, but no BSSE correction because the water molecules have no basis functions. Pavlov et al.[17] have studied $Ca^{2+}(H_2O)_x$ complexes where x = 1 – 8 with density functional theory (B3LYP)

that includes a Hay/Wadt ECP treatment for calcium and a LANL2DZ basis set for the smaller atoms in the geometry optimization. Their $Ca^{2+}(H_2O)_7$ structure is identical to the (6,1)_2D_AA structure described previously, but the binding energy for the $Ca^{2+}(H_2O)_8$ complex is calculated for an (8,0) structure. B3LYP/6-311+G(2d,2p) was used for subsequent single point energy calculations that include ZPE corrections. In this case, the values listed in Table 4.5 have been adjusted to 298 K using thermal corrections taken from our calculations. Their procedure for optimizing $Ca^{2+}(H_2O)_x$ structures and calculating their single point energies closely resembles our theoretical approach.

Discussion

Comparison between present and literature experimental values. Kebarle and coworkers[10,14] and Williams and coworkers[15,16] have previously reported hydration enthalpies at 298 K for the $Ca^{2+}(H_2O)_x$ systems where x = 6 – 14 and x = 5 – 10, respectively. Figure 4.9 shows that our experimental results agree within experimental uncertainty with these previous experimental results and that the same qualitative trends are observed. A more quantitative comparison shows that our experimental numbers agree best with those of the BIRD experiments of Williams and coworkers for the inner shell complexes, $Ca^{2+}(H_2O)_5$ and $Ca^{2+}(H_2O)_6$ complex, Table 4.5. For the larger complexes, $Ca^{2+}(H_2O)_7$ and $Ca^{2+}(H_2O)_8$, our experimental results agree within the combined experimental uncertainties with the HPMS results of Kebarle and coworkers, whereas the BIRD results, which are slightly higher, are at the edge of the combined experimental uncertainties. For $Ca^{2+}(H_2O)_9$, all three experimental bond enthalpies agree well. It is possible that our experimental numbers for the $Ca^{2+}(H_2O)_7$, $Ca^{2+}(H_2O)_8$, and $Ca^{2+}(H_2O)_9$ complexes are slightly low because the ions are not completely thermalized,

which would shift the thresholds for CID to lower energies. For instance, it may be the ions have reached equilibrium at the capillary temperature used for these larger systems, 80° C, although recent experiments suggest that thermalization of the ions occurs primarily in the hexapole ion trap, which is at room temperature.[25] If the data are analyzed using 80° C as the reactant temperature, the binding enthalpies increase by 4 kJ/mol for the $Ca^{2+}(H_2O)_7$, $Ca^{2+}(H_2O)_8$, and $Ca^{2+}(H_2O)_9$ complexes. Ideally, such a temperature increase could be evaluated by examining these CID processes at multiple capillary temperatures, however, the range of capillary temperatures providing stable and sufficiently intense ion beams is limited with this ESI source design.

Comparison between theory and experiment. Table 4.5 also compares the experimental 298 K bond enthalpies with B3LYP//B3LYP values computed here, which we've deemed representative of the many theoretical calculations performed in this chapter, Table 4.5. Our experimental values agree best with the B3LYP//B3LYP hydration enthalpies when BSSE corrections are included, as evidenced by a MAD decrease from 12 ± 6 kJ/mol without BSSE corrections to 9 ± 4 kJ/mol with BSSE corrections. Likewise, BSSE corrections always improved the agreement between experiment and theory for other levels of theory considered here.

The B3LYP//B3LYP hydration enthalpies show similar qualitative trends as the experimental results, Figure 4.9. The enthalpies decrease monotonically from the $Ca^{2+}(H_2O)_5$ to the $Ca^{2+}(H_2O)_7$ complex. Binding enthalpies for the seventh, eighth, and ninth water molecules differ from one another by less than 5 kJ/mol at all levels of theory. Calculated hydration enthalpies from theory are 2 – 4 kJ/mol higher for the $Ca^{2+}(H_2O)_8$ complex compared with the $Ca^{2+}(H_2O)_7$ complex, but the $Ca^{2+}(H_2O)_9$

complex is 3 – 5 kJ/mol lower in energy than the $Ca^{2+}(H_2O)_8$ complex. Therefore, the $Ca^{2+}(H_2O)_7$ and $Ca^{2+}(H_2O)_9$ complexes have theoretical hydration enthalpies that are within 1 – 2 kJ/mol of one another. These theoretical trends in the x = 7 – 9 bond enthalpies agree somewhat better with our results, where the values change little, compared to the HPMS and BIRD results where the bond enthalpies decrease systematically by 7 – 9 kJ/mol from $Ca^{2+}(H_2O)_7$ to $Ca^{2+}(H_2O)_9$.

From a quantitative standpoint, our experimental values for the x = 5 – 9 complexes are consistently lower than B3LYP//B3LYP theoretical calculations, except for x = 5. The experimental value x = 6 is within 9 kJ/mol of the theory values. Experimental second shell complexes have hydration enthalpies 11 – 14 kJ/mol lower than the calculations. Because the HPMS and BIRD values are slightly larger than our experimental values, the agreement with theory is better. The MADs for these literature results are 7 ± 3 and 4 ± 4 kJ/mol, respectively, with respect to the B3LYP//B3LYP results..

Comparison with theoretical results from the literature. A host of theoretical studies of the $Ca^{2+}(H_2O)_x$ system, where x = 1 – 7, can be found in the literature. The results from four theoretical studies are provided in Table 4.5. The hydration enthalpies calculated by Pavlov et al.[17] do not include BSSE corrections, and therefore resemble our B3LYP//B3LYP energies without BSSE corrections as evidenced by a MAD of 1 ± 1 kJ/mol, Table 4.5, although these results are systematically higher than our B3LYP//B3LYP values. The MAD excludes the value for the $Ca^{2+}(H_2O)_8$ complex because the literature value refers to the (8,0) geometry.

BSSE corrected single point energies calculated by Glendening and Feller[18] have a MAD of 9 ± 4 kJ/mol with respect to our B3LYP//B3LYP energies and are systematically higher. It seems likely that the bond energies of Glendening and Feller would decrease if a more advanced level of theory that accounts for electron correlation was used for the geometry optimization and larger basis sets with additional polarization functions were employed for subsequent single point energies. Single point energy calculations determined by Merrill et al.[19] using the effective fragment potential produces comparable single point energies with those from Glendening and Feller[18] with a MAD of 9 ± 6 kJ/mol with respect to our B3LYP//B3LYP energies without BSSE corrections included. Finally, the theoretical results taken from Katz et al.[20] are much higher than all other theoretical approaches with a MAD of 22 ± 11 kJ/mol compared to B3LYP//B3LYP results. Their results suggest the absence of diffuse functions into their basis sets for geometry optimizations or single point energy calculationsr0 result in significantly larger binding energies.

Katz et al.[20] also calculated the relative 298 K enthalpies for x = 6 – 8 to determine the number of water molecules that prefer to bind directly to the calcium ion. Even with their single point energy basis set now augmented by diffuse functions, their calculated relative MP2(full) energies for the $Ca^{2+}(H_2O)_6$ (5,1)_2D_AA and (4,2)_4D_2AA structures lie 34 and 63 kJ/mol higher in energy than the ground state (6,0) structure, which is roughly 1.2 – 1.5 times larger than our MP2(full)/6-311+G(2d,2p)//B3LYP/6-311+G(d,p) (MP2//B3LYP) single point energies of 23 and 52 kJ/mol. In agreement with the present results, Katz et al. determined that six water molecules preferentially bind directly to the calcium ion with additional water molecules

hydrogen bonding to inner shell water molecules for the $Ca^{2+}(H_2O)_7$ and $Ca^{2+}(H_2O)_8$ complexes. Katz et al. determined relative energies for the (7,0) and (8,0) structures were 6 and 2 kJ/mol higher than the (6,1)_2D_AA and (6,2)_4D_2AA (1) GSs. Our MP2//B3LYP results suggest that overcrowding the inner shell leads to single point energies of 5 and 10 kJ/mol higher than the (6,1)_2D_AA and (6,2)_4D_2AA ground states, respectively. The overestimation of the relative single point energies for the $Ca^{2+}(H_2O)_6$ structure and underestimation of the $Ca^{2+}(H_2O)_7$ and $Ca^{2+}(H_2O)_8$ structures likely results from the restricted Hartree-Fock treatment for the geometry optimizations used by Katz et al.

Conclusions

The kinetic energy dependent cross sections for $Ca^{2+}(H_2O)_x$ complexes where x = 5 – 9 are determined by collision-induced dissociation using a guided ion beam tandem mass spectrometer with an electrospray ionization source described in Chapter 2. The results reported here represent the first comprehensive study of multiply charged ions with this new source. The dominant process taking place in all systems studied here is the loss of a single water molecule from the parent species. An additional proton transfer/charge separation process is also observed once the $Ca^{2+}(H_2O)_2$ complex forms from sequential dissociation of the larger complexes. At this point, the $Ca^{2+}(H_2O)_2$ complex can lose one of its water molecules or form two singly charged particles, $CaOH^+$ and H_3O^+. Chapter 6 discusses the CID of the smallest $Ca^{2+}(H_2O)_x$ complexes and the competition between water loss and charge separation processes.

Our experimental results for the $Ca^{2+}(H_2O)_x$ (x = 5 – 9) system agree well with other experimental techniques found in the literature.[10,14-16] Binding energies decrease

monotonically from $Ca^{2+}(H_2O)_5$ to $Ca^{2+}(H_2O)_7$. The binding energies for the $Ca^{2+}(H_2O)_7$, $Ca^{2+}(H_2O)_8$, and $Ca^{2+}(H_2O)_9$ complexes differ by less than 2 kJ/mol, suggesting the binding motifs of these three water molecules are very similar. This suggests that six water molecules bind directly to the calcium ion, in agreement with theory. Binding energies obtained for these second shell complexes tend to be a bit lower than HPMS[10,14] and BIRD[15,16] studies, but still fall within experimental uncertainties.

Our theoretical calculations of the structures and energetics for the $Ca^{2+}(H_2O)_x$ (x = 1 – 9) system represent the first comprehensive study of the ion's hydration throughout this range. We find that six water molecules bind directly to the calcium ion in agreement with previous work.[17-20] For the $Ca^{2+}(H_2O)_x$ complexes (x = 7 – 9), the additional outer shell water molecules hydrogen bond to pairs of the six inner shell water molecules using the same structural motif. Alternate structures for $Ca^{2+}(H_2O)_7$, $Ca^{2+}(H_2O)_8$, and $Ca^{2+}(H_2O)_9$ complexes have been qualitatively and quantitatively discussed in detail with respect to the lowest energy structures. The present results demonstrate that accurate calculations of the binding energies must include diffuse functions for the geometry optimization, single point energy calculations, and BSSE corrections. From this theoretical study of the $Ca^{2+}(H_2O)_x$ complexes where x = 1 – 9, it appears that B3LYP/6-311+G(d,p) geometry optimizations and subsequent B3LYP/6-311+G(2d,2p) single point energies provide reasonable agreement with experiment and should be sufficient for future hydration studies.

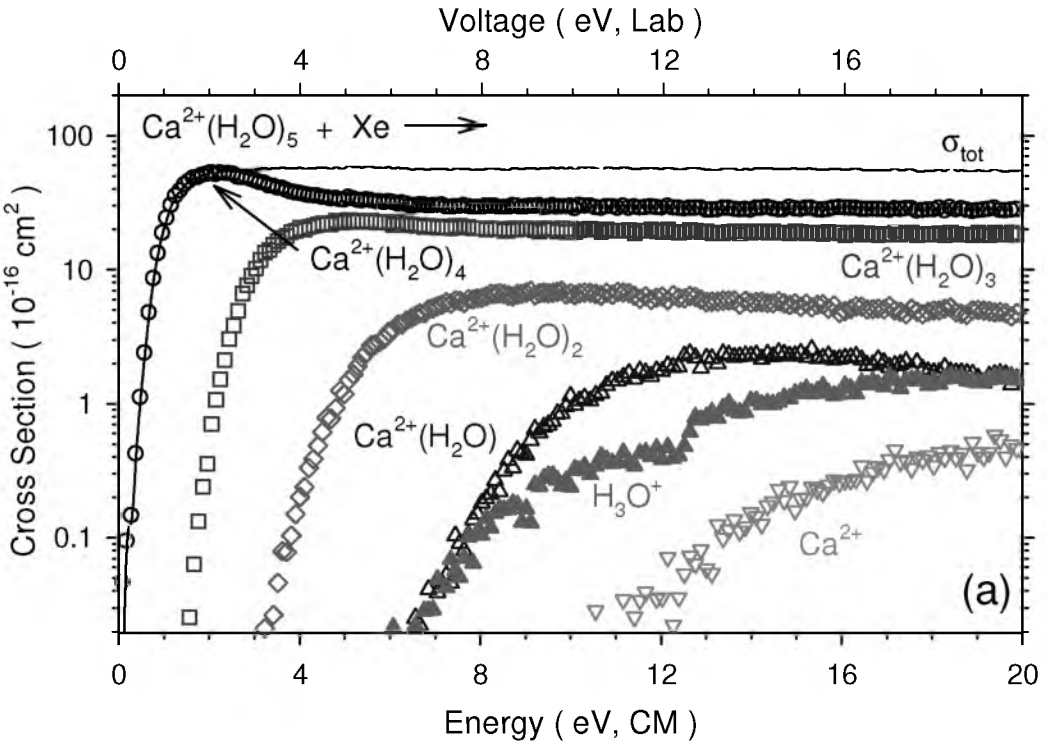

Figure. 4.1. Cross sections for collision-induced dissociation of $Ca^{2+}(H_2O)_x$, where x = 5 – 9 (parts a – e, respectively) with Xenon as a function of kinetic energy in the center-of-mass frame (lower x-axis) and the applied laboratory frame voltage (upper x-axis).

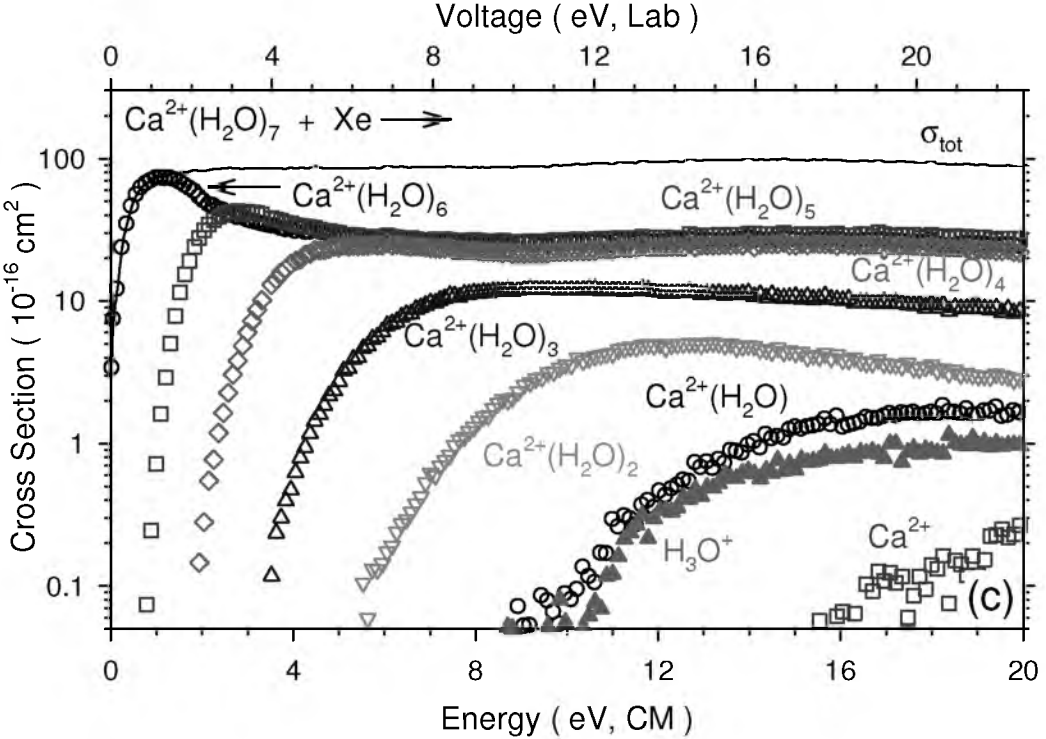

Figure 4.1. continued

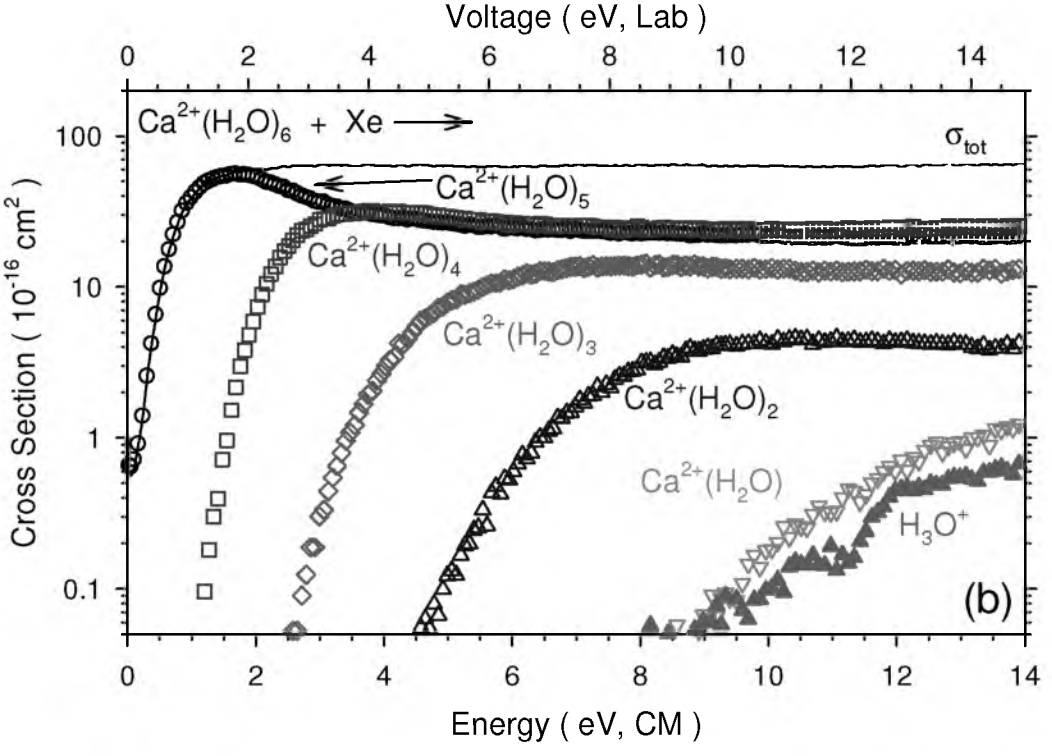
Voltage (eV, Lab)
0
2
4
6
8
10
12
14
$Ca^{2+}(H_2O)_6$ + Xe
σ_{tot}
$Ca^{2+}(H_2O)_5$
$Ca^{2+}(H_2O)_4$
$Ca^{2+}(H_2O)_3$
$Ca^{2+}(H_2O)_2$
$Ca^{2+}(H_2O)$
H_3O^+
(b)
Cross Section (10^{-16} cm^2)
100
10
1
0.1
Energy (eV, CM)

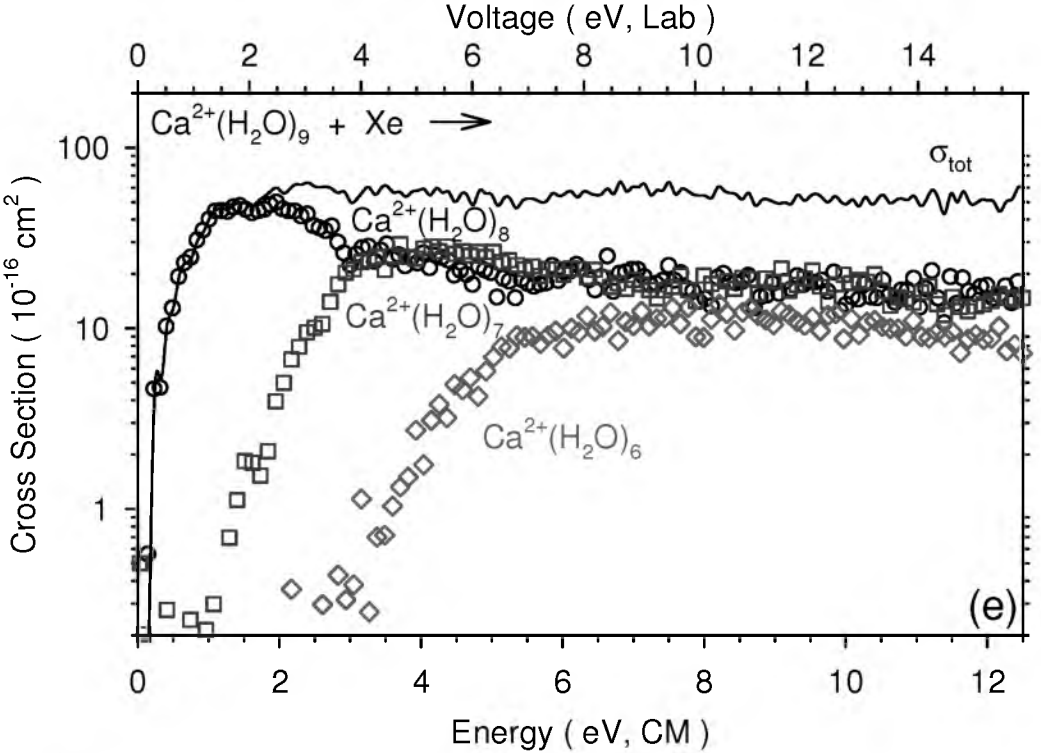

Figure 4.1. continued

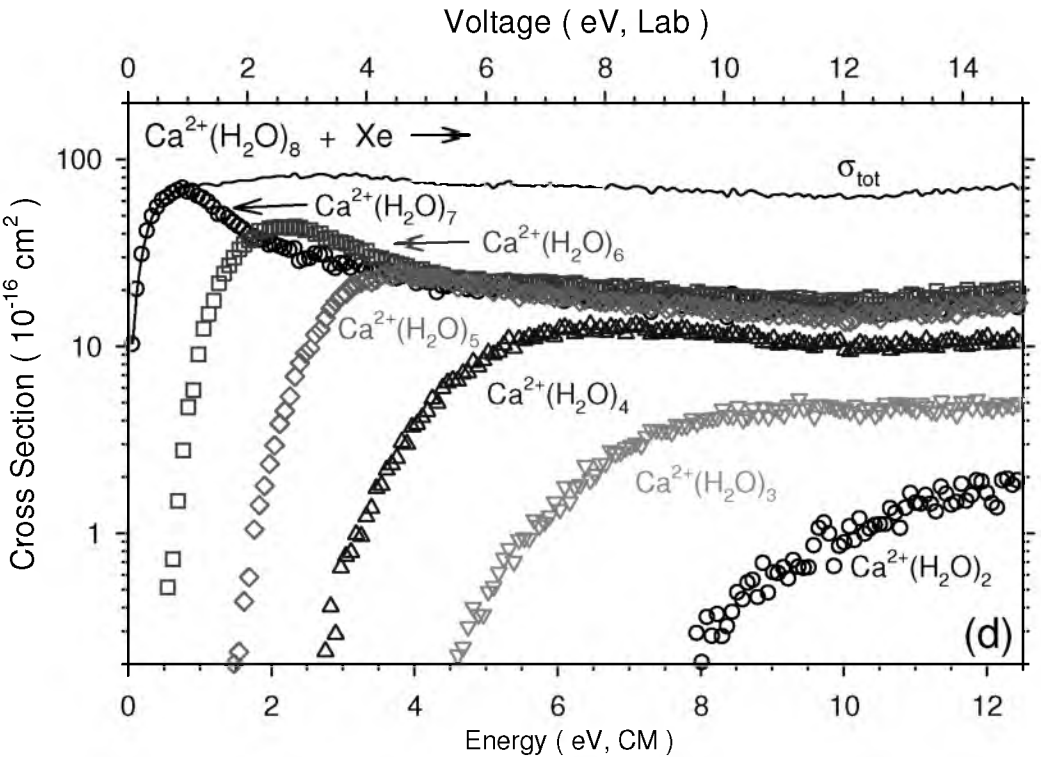
Voltage (eV, Lab)
0
2
4
6
8
10
12
14
$Ca^{2+}(H_2O)_8$ + Xe
σ_{tot}
$Ca^{2+}(H_2O)_7$
$Ca^{2+}(H_2O)_6$
$Ca^{2+}(H_2O)_5$
$Ca^{2+}(H_2O)_4$
$Ca^{2+}(H_2O)_3$
$Ca^{2+}(H_2O)_2$
(d)
Cross Section (10^{-16} cm^2)
100
10
1
Energy (eV, CM)

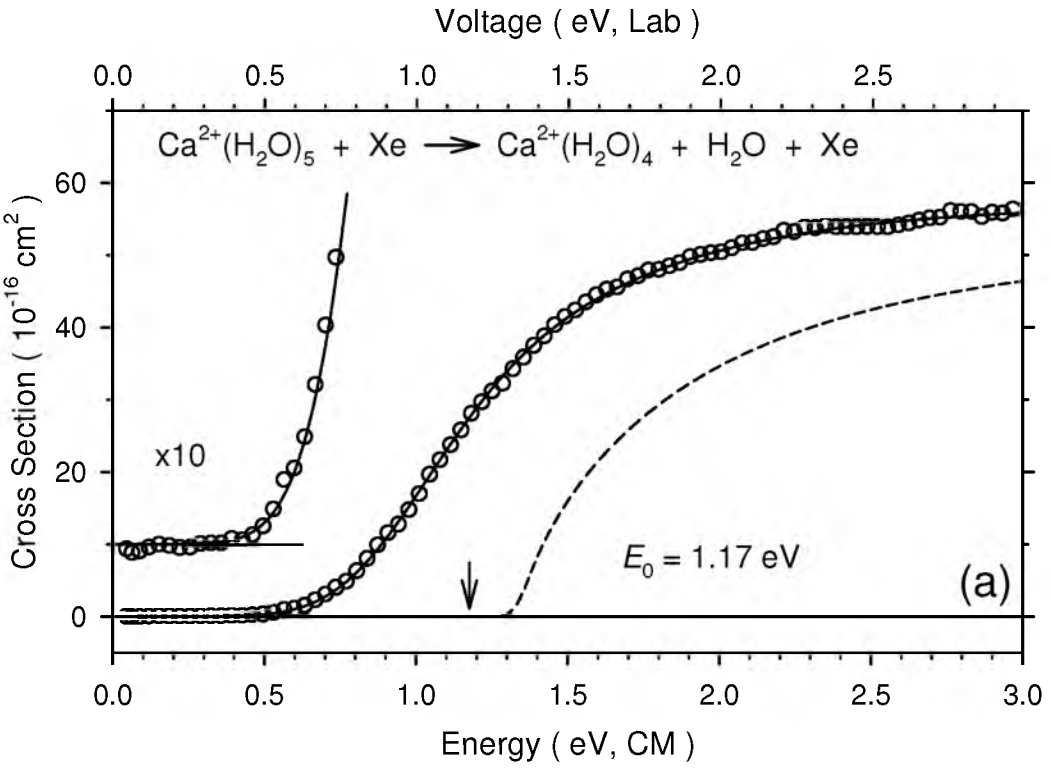

Figure 4.2. Zero pressure extrapolated cross sections for collision-induced dissociation of $Ca^{2+}(H_2O)_x$ where x = 5 – 9 (parts a – e, respectively) with Xenon in the threshold region as a function of kinetic energy in the center-of-mass frame (lower x-axis) and the applied laboratory frame voltage (upper x-axis). The solid lines show the best fit to the data using the model of Equation 2.5 convoluted over the neutral and ion kinetic and internal energy distributions. The dashed lines show the model cross sections in the absence of experimental kinetic energy broadening for reactions with an internal energy of 0 K. The arrow indicates the threshold energy, E_0.

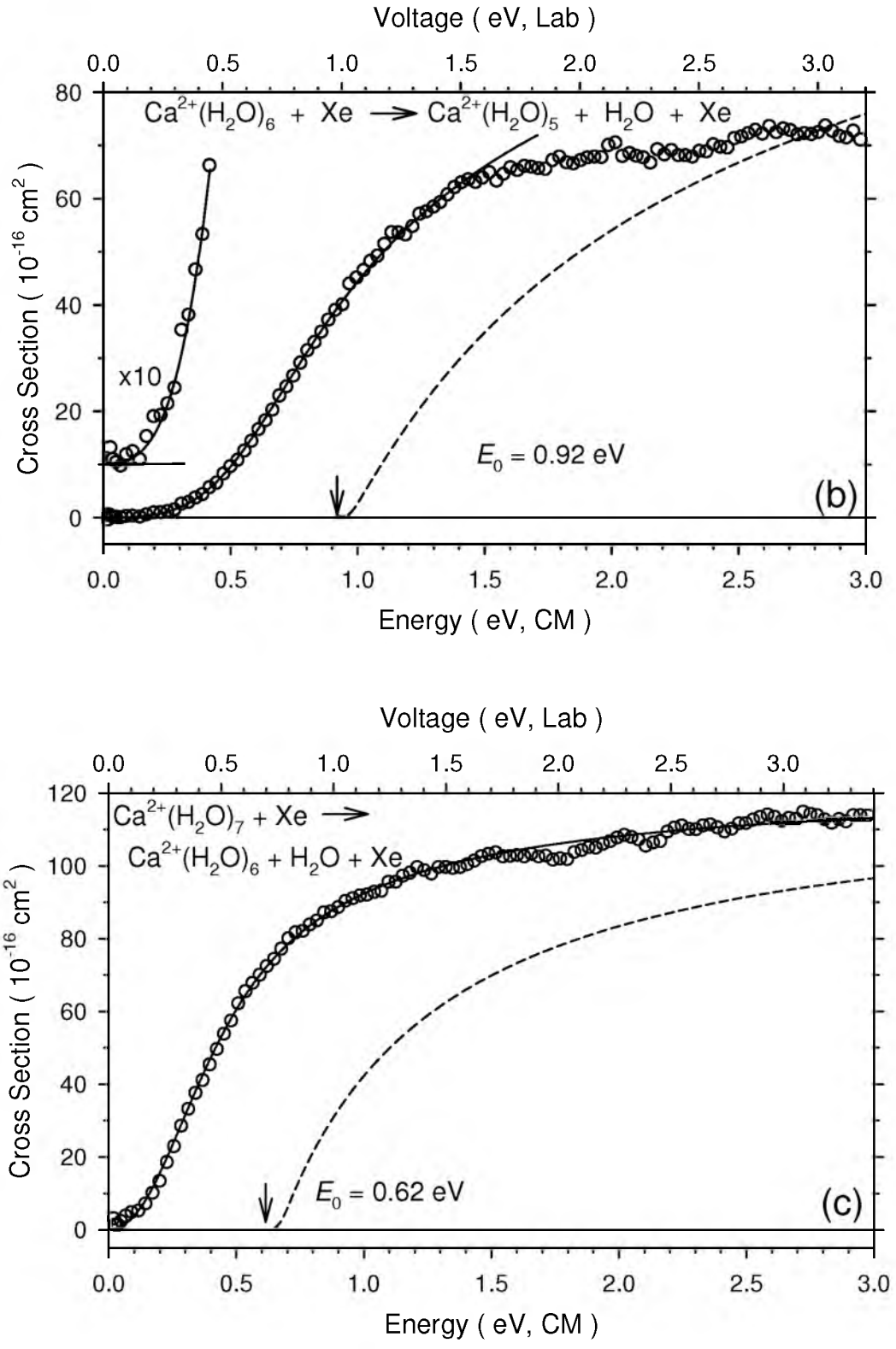

Figure 4.2. continued

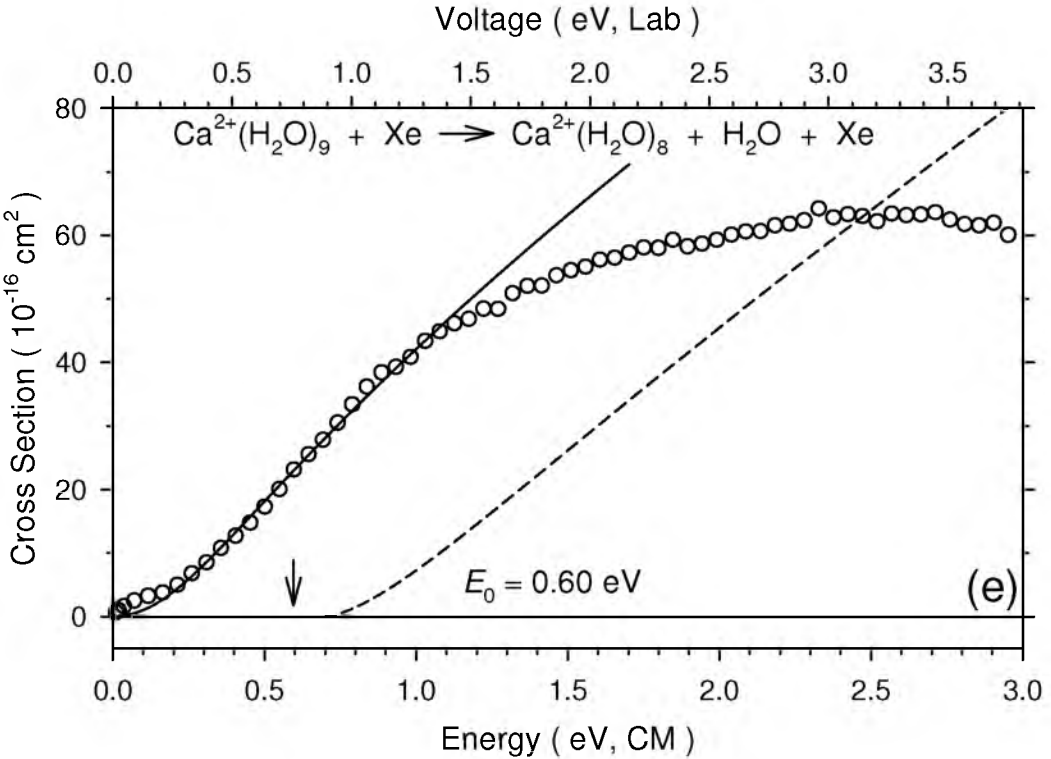

Figure 4.2. continued

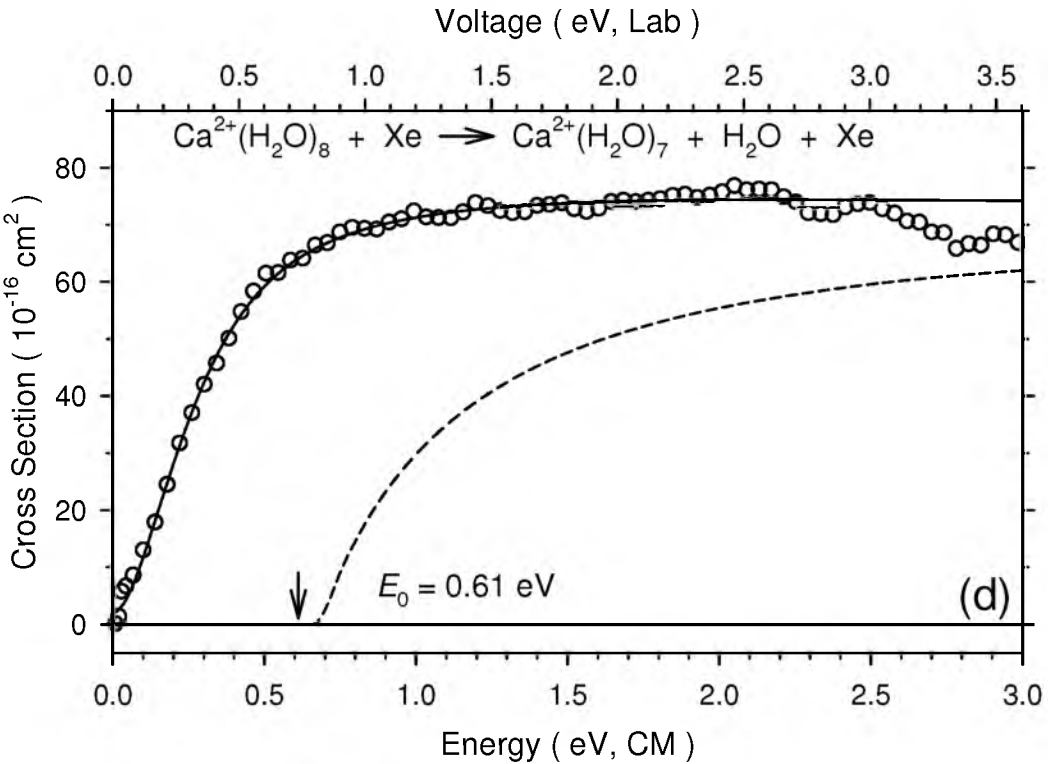
Voltage (eV, Lab)
0.0
0.5
1.0
1.5
2.0
2.5
3.0
3.5
$Ca^{2+}(H_2O)_8$ + Xe → $Ca^{2+}(H_2O)_7$ + H_2O + Xe
Cross Section (10^{-16} cm^2)
80
60
40
20
0
E_0 = 0.61 eV
(d)
0.0
0.5
1.0
1.5
2.0
2.5
3.0
Energy (eV, CM)

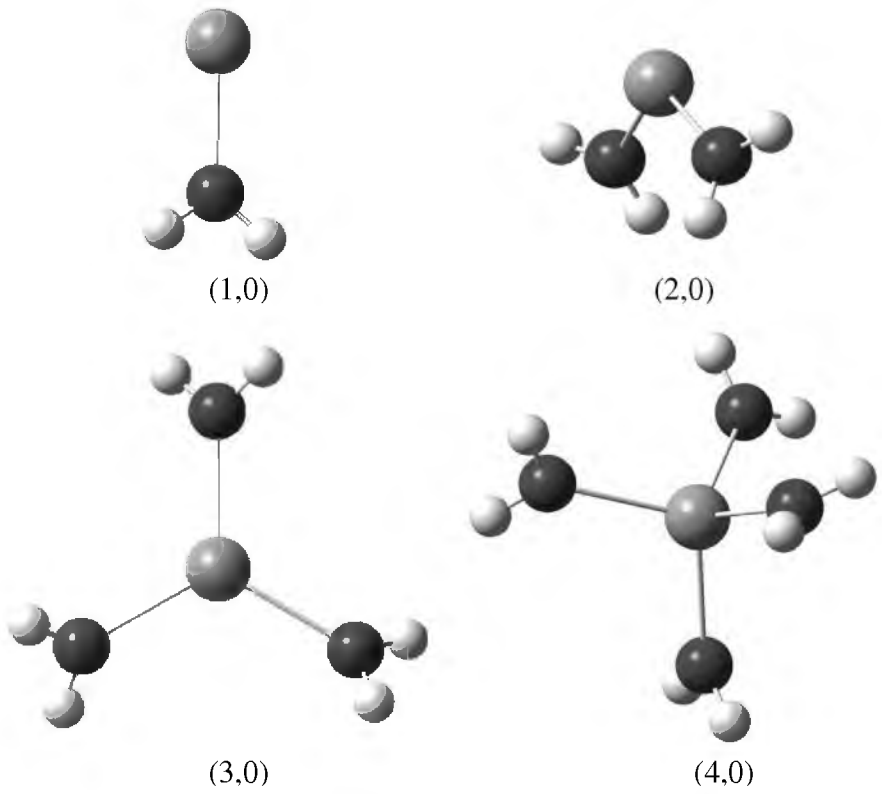

Figure 4.3. Ground-state geometries of $Ca^{2+}(H_2O)_{1-4}$.

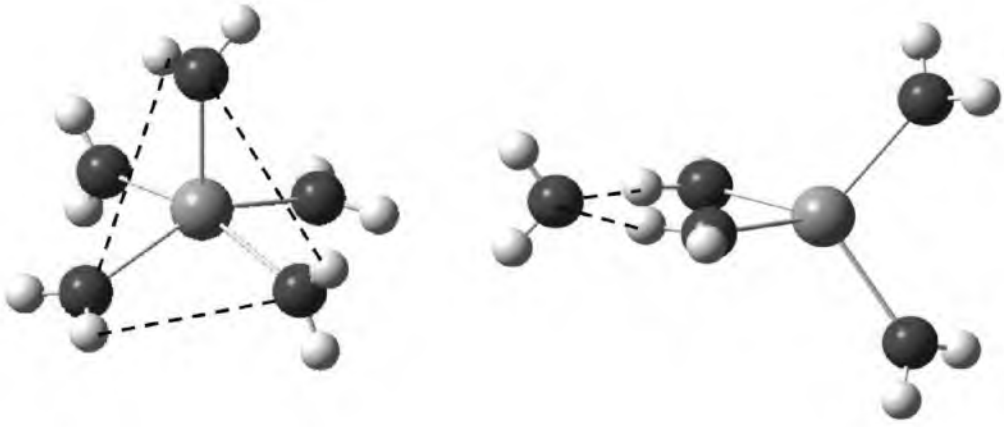

Figure 4.4. Ground-state and low-lying geometries of $Ca^{2+}(H_2O)_5$. Hydrogen bonds are shown as dashed lines. The relative B3LYP/6-311+G(2d,2p)//B3LYP/6-311+G(d,p) (roman) and MP2(full)/6-311+G(2d,2p)//B3LYP/6-311+G(d,p) (**bold**) 298 K free energies (kJ/mol) from Table 4.1 are provided.

(6,0), 0.0, **0.0**

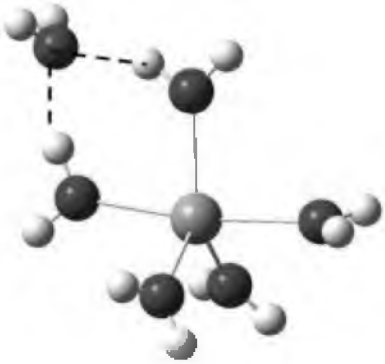

(5,1)_2D_A_aA_b, 5.9, **15.6**

(5,1)_D_A_b, 10.5, **23.0**

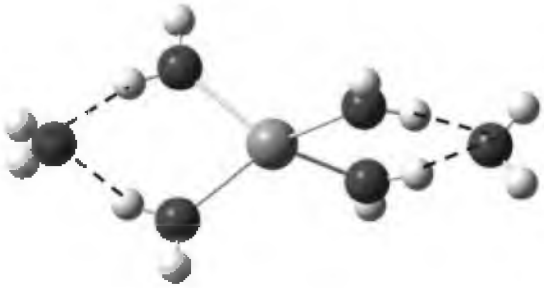

(4,2)_4D_2AA, 36.1, **52.2**

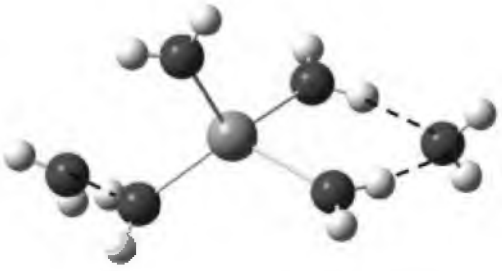

(4,2)_3D_AA,A, 32.2, **52.1**

Figure 4.5. Ground-state and low-lying geometries of $Ca^{2+}(H_2O)_6$. Hydrogen bonds are shown as dashed lines. The relative B3LYP/6-311+G(2d,2p)//B3LYP/6-311+G(d,p) (roman) and MP2(full)/6-311+G(2d,2p)//B3LYP/6-311+G(d,p) (**bold**) 298 K free energies (kJ/mol) from Table 4.1 are provided.

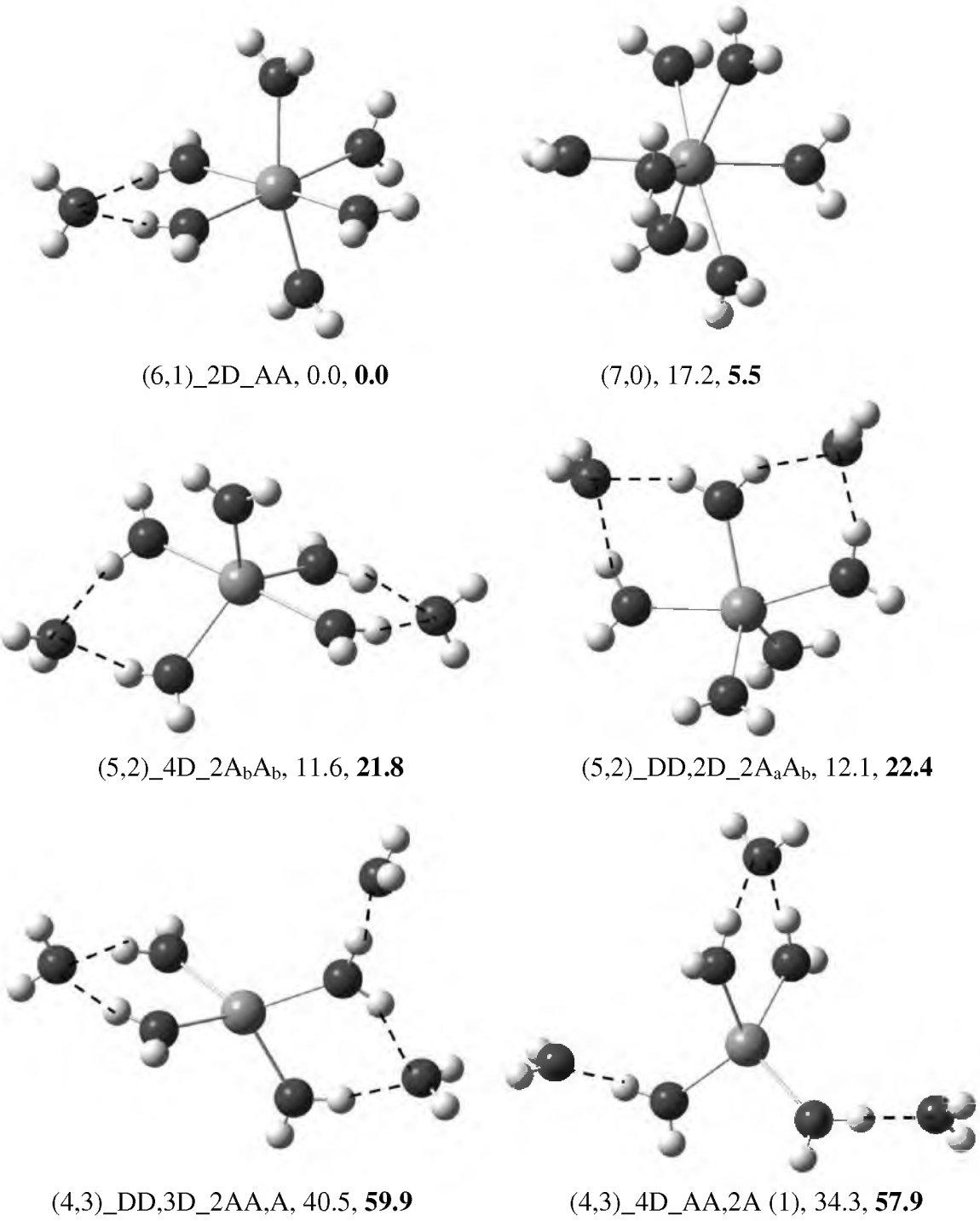

Figure 4.6. Ground-state and low-lying geometries of $Ca^{2+}(H_2O)_7$. Hydrogen bonds are shown as dashed lines. The relative B3LYP/6-311+G(2d,2p)//B3LYP/6-311+G(d,p) (roman) and MP2(full)/6-311+G(2d,2p)//B3LYP/6-311+G(d,p) (**bold**) 298 K free energies (kJ/mol) from Table 4.1 are provided.

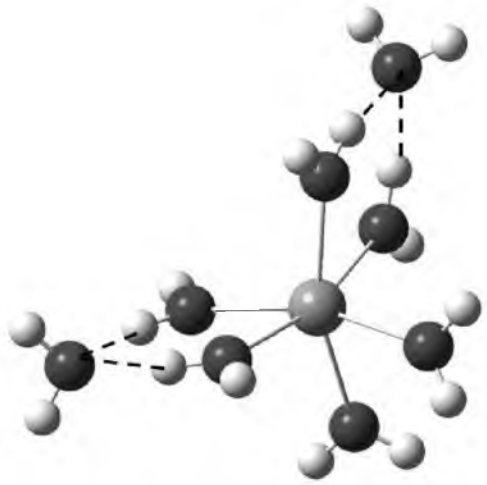

(6,2)_4D_2AA (1), 0.0, **0.0**

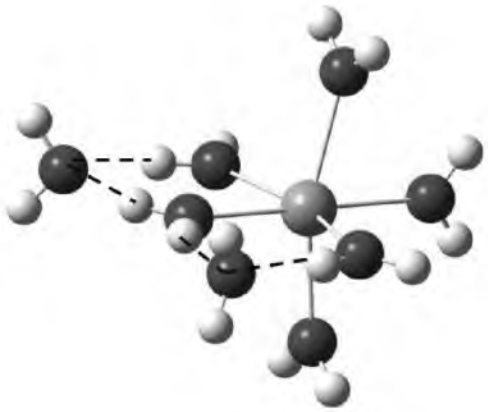

(6,2)_DD,2D_2AA (1), 1.7, **2.1**

(6,2)_4D_2AA (2), 3.7, **3.8**

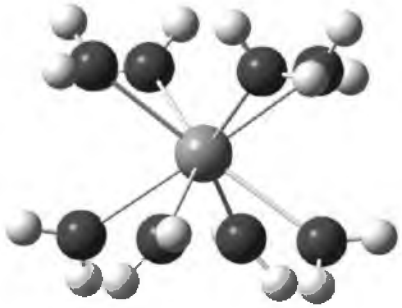

(8,0), 35.1, **10.4**

(5,3)_DD,4D_2A_bA_b,A_aA_b, 14.6, **24.5**

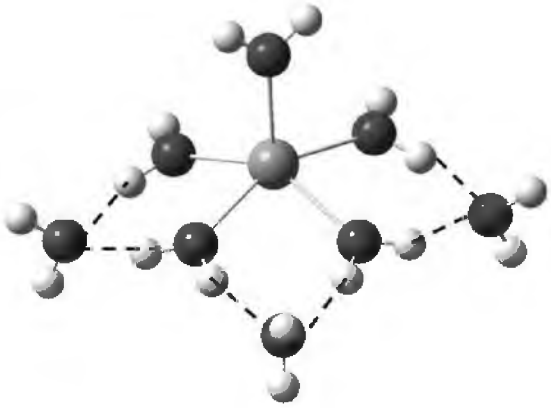

(5,3)_2DD,2D_3A_bA_b, 13.6, **23.6**

Figure 4.7. Ground-state and low-lying geometries of $Ca^{2+}(H_2O)_8$. Hydrogen bonds are shown as dashed lines. The relative B3LYP/6-311+G(2d,2p)//B3LYP/6-311+G(d,p) (roman) and MP2(full)/6-311+G(2d,2p)//B3LYP/6-311+G(d,p) (**bold**) 298 K free energies (kJ/mol) from Table 4.1 are provided.

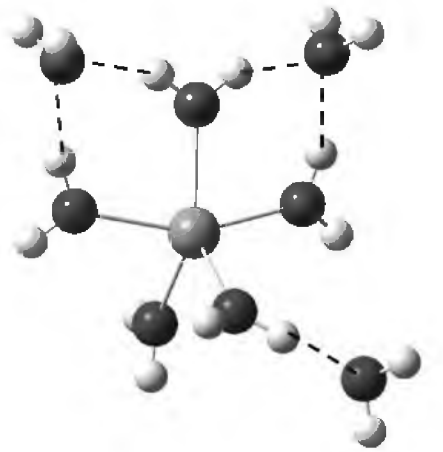

(5,3)_DD,3D_2A_aA_b,A_b, 12.5, **25.5**

Figure 4.7. continued

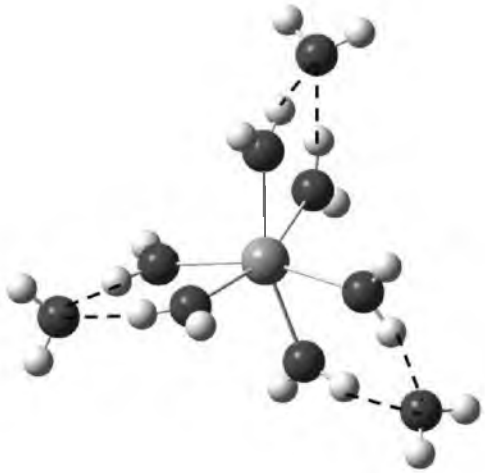

(6,3)_6D_3AA, 0.0, **0.0**

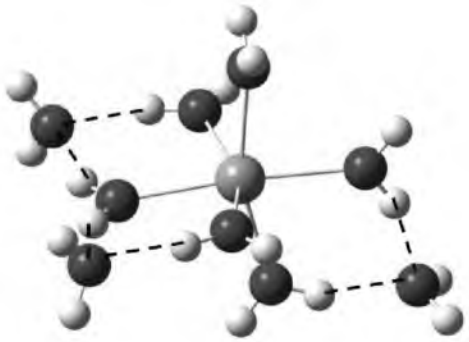

(6,3)_DD,4D_3AA, 2.0, **1.7**

(5,4)_2DD,3D_3A_bA_b,A_a, 14.5, **27.1**

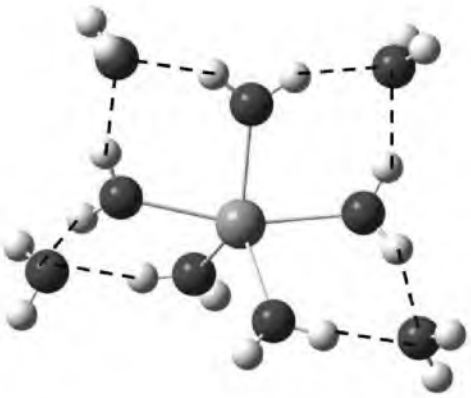

(5,4)_3DD,2D_2A_bA_b,2A_aA_b, 23.0, **32.7**

(5,4)_4DD_4A_bA_b, 19.8, **30.8**

Figure 4.8. Ground-state and low-lying geometries of $Ca^{2+}(H_2O)_9$. Hydrogen bonds are shown as dashed lines. The relative B3LYP/6-311+G(2d,2p)//B3LYP/6-311+G(d,p) (roman) and MP2(full)/6-311+G(2d,2p)//B3LYP/6-311+G(d,p) (**bold**) 298 K free energies (kJ/mol) from Table 4.1 are provided.

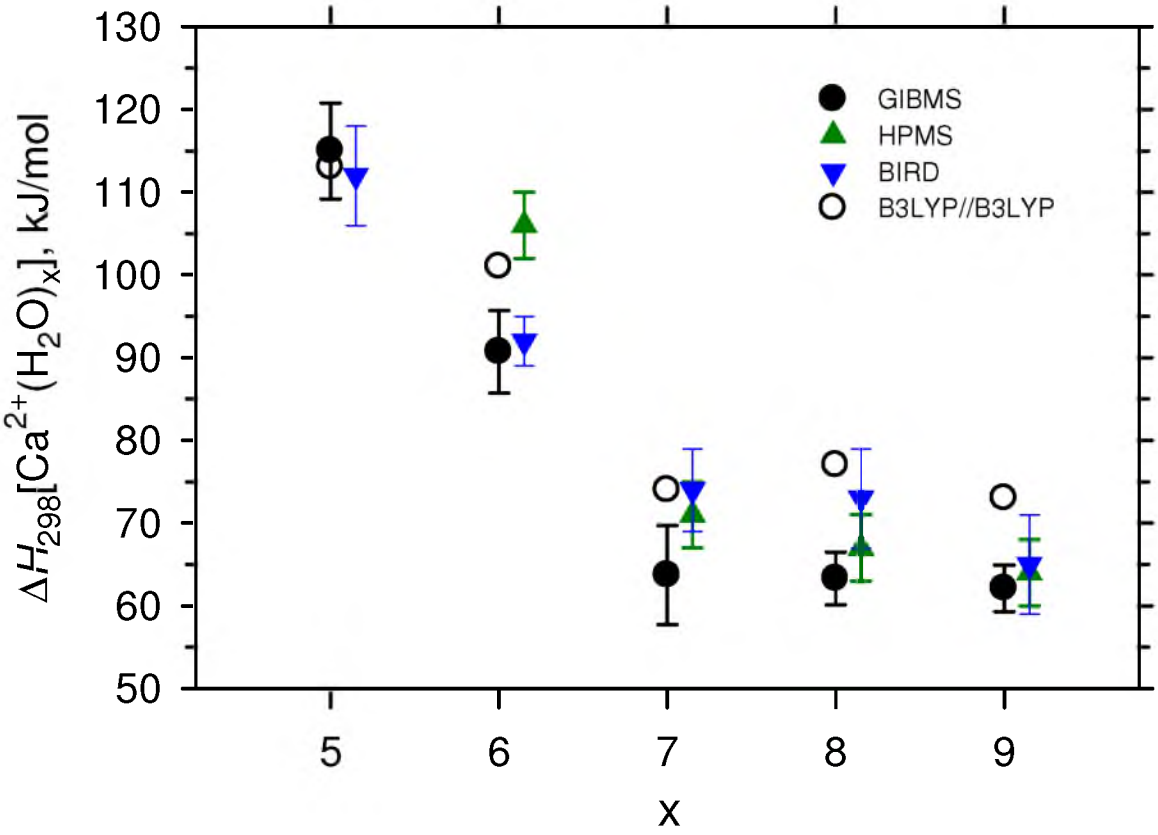

Figure 4.9. Comparison of experimental (solid black circles) and B3LYP//B3LYP (open circles) bond enthalpies at 298 K. HPMS results (green triangles) from reference 10 and BIRD results (blue inverted triangles) from references 15 and 16 are included for comparison and offset to the right of the experimental results (this work) and theoretical results.

Table 4.1. Parameters from Equation 2.5 used to model the data for collision-induced dissociation of $Ca^{2+}(H_2O)_x$ (x = 5 – 9)[a]

Complex	σ_0[b]	n[b]	E_0, eV[c]	E_0 (PSL), eV[b]	$\Delta S^{\ddagger}_{1000}$, J/mol K
$Ca^{2+}(H_2O)_5$	95 (3)	0.8 (0.2)	1.30 (0.07)	1.17 (0.06)	50 (5)
$Ca^{2+}(H_2O)_6$	102 (2)	1.1 (0.2)	1.02 (0.06)	0.92 (0.05)	71 (5)
$Ca^{2+}(H_2O)_7$	123 (6)	1.0 (0.1)	0.89 (0.05)	0.62 (0.06)	30 (5)
$Ca^{2+}(H_2O)_8$	85 (2)	0.9 (0.1)	0.85 (0.06)	0.61 (0.03)	72 (5)
$Ca^{2+}(H_2O)_9$	56 (2)	1.7 (0.1)	0.93 (0.04)	0.60 (0.03)	75 (5)

[a] Uncertainties are in parentheses.
[b] Parameters from modeling with Equation 2.5, where lifetime effects are taken into account. [c] Thresholds from modeling with Equation 2.4, where no lifetime affects are included.

Table 4.2. B3LYP/6-311+G(d,p) geometry optimized structures for ground state $Ca^{2+}(H_2O)_{1-6}$[a]

Complex	Symmetry	r(CaO), Å	∠OCaO, °	∠CaOH, °	r(OH), Å	∠HOH, °
H_2O	C_{2v}				0.962	105.1
$Ca^{2+}(H_2O)$	C_{2v}	2.244		127.9 (2)	0.977 (2)	104.3
$Ca^{2+}(H_2O)_2$	C_2	2.282 (2)	124.7	127.7 (2)	0.974 (4)	104.4 (2)
				127.9 (2)		
$Ca^{2+}(H_2O)_3$	D_3	2.313 (3)	120.0 (3)	127.7 (6)	0.972 (6)	104.5 (3)
$Ca^{2+}(H_2O)_4$	S_4	2.340 (4)	106.6 (2)	127.4 (4)	0.970 (8)	104.7 (4)
			110.9 (4)	127.9 (4)		
$Ca^{2+}(H_2O)_5$	C_{2v}	2.364 (1)	87.6 (4)	126.4 (2)	0.968 (4)	105.0 (2)
		2.365 (2)	99.2 (2)	127.4 (6)	0.969 (6)	105.1
		2.393 (2)	105.5 (2)	128.7 (2)		105.3 (2)
			149.0			
			161.6			
$Ca^{2+}(H_2O)_6$	T_h	2.405 (6)	90.0 (12)	127.3 (12)	0.967	105.4 (6)
			180.0 (3)		(12)	

[a] Numbers in parentheses denote degeneracies.

Table 4.3. Relative calculated enthalpies (ΔH_0) and free energies (ΔG_{298}) in kJ/mol for $Ca^{2+}(H_2O)_x$ isomers[a]

x	Complex name	B3LYP[b]	B3P86[b]	MP2(full)[b]
5	(5,0)	**0.0 (0.0)**	**0.0 (0.0)**	**0.0 (0.0)**
	(4,1)_2D_AA	22.5 (24.3)	19.1 (20.9)	29.6 (31.4)
6	(6,0)	**0.0 (0.0)**	**0.0 (0.0)**	**0.0 (0.0)**
	(5,1)_2D_A_aA_b	15.9 (5.9)	12.8 (2.8)	25.5 (15.6)
	(5,1)_D_A_b	24.4 (10.5)	21.7 (7.8)	36.9 (23.0)
	(4,2)_4D_2AA	37.6 (36.1)	31.0 (29.5)	53.7 (52.2)
	(4,2)_3D_AA,A	43.7 (32.2)	37.5 (26.0)	63.6 (52.1)
	(4,2)_DD,2D_2AA	47.9 (45.1)	41.7 (38.8)	62.8 (59.9)
	(4,2)_DD,D_AA,A	48.7 (36.2)	42.9 (30.5)	68.4 (56.0)
	(4,1,1)_2D_AAD_A	54.8 (42.1)	47.3 (34.7)	75.0 (62.3)
7	**(6,1)_2D_AA**	**0.0 (0.0)**	**0.0 (0.0)**	**0.0 (0.0)**
	(5,2)_4D_2A_bA_b	7.0 (11.6)	4.0 (8.6)	17.3 (21.8)
	(5,2)_DD,2D_2A_aA_b	11.4 (12.1)	8.6 (9.4)	21.6 (22.4)
	(5,2)_DD,2D_2A_bA_b	11.5 (13.6)	8.6 (10.7)	21.5 (23.6)
	(5,2)_3D_A_aA_b,A_b	16.6 (13.1)	13.7 (10.3)	29.5 (26.0)
	(7,0)	19.1 (17.2)	20.0 (18.1)	7.5 (5.5)
	(4,3)_DD,3D_2AA,A	39.3 (40.5)	34.4 (34.7)	58.7 (59.9)
	(4,3)_4D_AA,2A (1)	41.9 (35.3)	36.1 (28.5)	65.4 (57.9)
	(4,3)_4D_AA,2A (2)	42.0 (34.1)	36.2 (29.3)	65.5 (58.6)
	(4,2,1)_3D_A,AAD_A	50.2 (42.8)	43.0 (35.6)	74.2 (66.7)
8	**(6,2)_4D_2AA (1)**	**0.0 (0.0)**	**0.0 (0.0)**	**0.0 (0.0)**
	(6,2)_DD,2D_2AA (1)	1.7 (1.7)	2.1 (2.1)	2.0 (2.1)
	(6,2)_4D_2AA (2)	4.4 (3.7)	4.3 (3.6)	4.5 (3.8)
	(5,3)_DD,4D_2A_bA_b,A_aA_b	11.5 (14.6)	8.7 (11.8)	21.4 (24.5)
	(6,2)_DD,2D_2AA (2)	11.8 (10.0)	11.7 (9.9)	11.5 (9.7)
	(6,1.5,0.5)_3D_AAD,A_1A_2	12.4 (12.9)	12.8 (13.3)	11.3 (11.8)
	(6,2)_2D_AAD_A	13.7 (6.9)	12.8 (6.1)	17.4 (10.7)
	(5,3)_2DD,2D_3A_bA_b	14.3 (13.6)	12.0 (11.3)	24.3 (23.6)

Table 4.3. continued

	Complex name	B3LYP[b]	B3P86[b]	MP2(full)[b]
8	(5,3)_DD,3D_2A_aA_b,A_b	18.1 (12.5)	15.7 (10.2)	31.1 (25.5)
	(5,2,1)_DD,2D_A_aA_b,A_aA_bD_A	25.6 (15.5)	22.3 (12.2)	39.7 (29.6)
	(8,0)	36.7 (35.1)	39.0 (37.4)	12.0 (10.4)
9	**(6,3)_6D_3AA**	**0.0 (0.0)**	**0.0 (0.0)**	**0.0 (0.0)**
	(6,3)_DD,4D_3AA (1)	3.3 (2.0)	3.5 (2.1)	3.1 (1.7)
	(6,3)_2DD,2D_3AA (1)	11.0 (8.3)	10.7 (8.0)	10.6 (7.9)
	(6,2.5,0.5)_5D_AA,AAD,A_1A_2 (1)	12.5 (12.6)	12.8 (12.9)	11.1 (11.1)
	(6,3)_2DD,2D_3AA (2)	12.9 (10.7)	13.1 (10.8)	12.7 (10.4)
	(6,2.5,0.5)_5D_AA,AAD,A_1A_2 (2)	14.8 (12.0)	14.8 (12.0)	13.3 (10.4)
	(6,3)_DD,4D_3AA (2)	15.0 (12.8)	14.8 (12.6)	14.3 (12.1)
	(6,2.5,0.5)_DD,3D_AA,AAD,A_1A_2 (1)	16.9 (16.2)	17.6 (17.0)	15.3 (14.6)
	(6,2.5,0.5)_DD,3D_AA,AAD,A_1A_2 (2)	17.5 (16.0)	17.9 (16.4)	15.6 (14.1)
	(5,4)_2DD,3D_3A_bA_b,A_a	21.7 (14.5)	19.6 (12.4)	34.3 (27.1)
	(5,4)_3DD,2D_2A_bA_b,2A_aA_b	21.8 (23.0)	19.5 (20.7)	31.5 (32.7)
	(5,4)_4DD_4A_bA_b	23.4 (19.8)	23.2 (19.7)	34.4 (30.8)
	(5,3,1)_DD,4D_A_aA_b,A_bA_b,AbA_bD_A	24.9 (20.3)	21.3 (16.7)	38.2 (33.6)
	(5,4.5,0.5)_2DD,3D_2A_bA_b,A_bA_bD _A_aA_2	26.0 (28.3)	24.1 (26.4)	34.2 (36.5)
	(5,4.5,0.5)_DD,4D_A_aA_b,A_bA_b,A_bD _A_bA_2	30.0 (26.6)	28.3 (24.9)	41.8 (38.5)

[a] Relative ΔG_{298} are in parentheses. **Bold** structures represent ground-state structures.
[b] Single point energies calculated with 6-311+G(2d,2p) basis set from B3LYP/6-311+G(d,p) geometries include zero-point energy corrections.

Table 4.4. Conversion between 0 K enthalpies for H_2O loss from ground state $Ca^{2+}(H_2O)_x$ (x = 5 – 9) to enthalpies and free energies at 298 K in kJ/mol[a]

Complex	ΔH_0 [b]	$\Delta H_{298} - \Delta H_0$ [c]	ΔH_{298}	$T\Delta S_{298}$ [c]	ΔG_{298}
$Ca^{2+}(H_2O)_5$	112.8 (5.8)	2.2 (0.5)	115.0 (5.8)	40.5 (1.3)	70.7 (5.9)
$Ca^{2+}(H_2O)_6$	88.9 (5.0)	1.8 (0.5)	90.7 (5.0)	47.1 (1.4)	44.6 (5.2)
$Ca^{2+}(H_2O)_7$	60.0 (6.0)	4.7 (0.4)	64.7 (6.0)	33.0 (1.0)	30.7 (6.1)
$Ca^{2+}(H_2O)_8$	58.9 (4.2)	4.4 (0.5)	64.3 (4.2)	46.4 (1.0)	16.9 (4.4)
$Ca^{2+}(H_2O)_9$	57.8 (2.8)	4.3 (0.5)	62.1 (2.8)	47.2 (1.0)	15.2 (3.0)

[a] Uncertainties are in parentheses.
[b] Experimental values from this work (Table 4.1).
[c] Values were calculated using standard formulae and molecular constants calculated at the B3LYP/6-311+G(d,p) level. Uncertainties correspond to scaling the vibrational frequencies up and down by 10%.

Table 4.5. Experimental and theoretical 298 K bond enthalpies for H_2O loss from ground state $Ca^{2+}(H_2O)_x$ (x = 1 – 9) in kJ/mol[a]

Expt[b] or Geom.[c]	Single pt.[d]	x = 1	2	3	4	5	6
GIBMS[e]						115 (6)	91 (5)
HPMS[f]							106 (4)
BIRD[g]						112 (6)	92 (3)
MP2(full)[h]	B3LYP	235 (236)	197 (199)	172 (174)	148 (149)	114 (115)	102 (104)
B3LYP[h]	B3LYP	235 (236)	197 (199)	172 (174)	147 (149)	113 (116)	101 (104)
	B3P86	235 (236)	196 (198)	171 (173)	146 (148)	114 (116)	101 (104)
	MP2(full)	218 (222)	188 (194)	168 (174)	147 (152)	120 (127)	108 (117)
B3LYP/	B3LYP	240 (240)	200 (200)	173 (173)	147 (148)	113 (113)	101 (102)
pVTZ(Ca-G)	B3P86	240 (241)	199 (200)	172 (173)	147 (147)	113 (113)	101 (102)
	MP2(full)	226 (230)	193 (198)	171 (175)	149 (155)	120 (126)	109 (117)
	MP2(FC)	226 (228)	193 (196)	171 (173)	149 (152)	120 (124)	109 (113)
Pavlov et al.[i]		(236)	(200)	(177)	(151)	(118)	(105)
GF[j]		224	198	179	157	126	114
Merrill et al.[k]		(220)	(196)	(177)	(157)	(129)	(117)
Katz et al.[l]		(235)	(216)	(200)	(179)	(143)	(133)

Table 4.5. continued[a]

Expt[b] or Geom.[c]	Single pt.[d]	7	8	9	MAD[m]
GIBMS[e]		64 (6)	63 (3)	62 (3)	9±4
HPMS[f]		71 (4)	67 (4)	64 (4)	7±3
BIRD[g]		74 (5)	73 (6)	65 (6)	4±4
MP2(full)[h]	B3LYP	74 (77)	77 (80)	73 (76)	0±0 (0±0)
B3LYP[h]	B3LYP	74 (77)	77 (80)	73 (76)	
	B3P86	77 (80)	79 (82)	75 (78)	1±1 (1±1)
	MP2(full)	73 (82)	76 (85)	72 (81)	5±5 (7±5)
B3LYP/	B3LYP	74 (75)	77 (78)	73 (74)	1±2 (2±1)
pVTZ(Ca-G)	B3P86	77 (78)	78 (80)	75 (76)	2±2 (2±1)
	MP2(full)	77 (86)	79 (88)	75 (84)	4±3 (7±4)
	MP2(FC)	77 (82)	80 (84)	76 (80)	4±3 (5±3)
Pavlov et al.[i]		(77)	(39)		(1±1)
GF[j]					9±4
Merrill et al.[k]					(9±6)
Katz et al.[l]		(90)	(85)	(57)	(22±11)

Table 4.5. continued.

[a] Values in parentheses for theoretical binding energies do not include BSSE corrections.
[b] Experimental binding energies in top of table.
[c] Level of theory used for geometry optimization.
[d] Level of theory used for single point energy calculations using either 6-311+G(2d,2p) or pVTZ (Ca-G) basis set.
[e] Results from Table 4.4
[f] Reference 10. Uncertainties assigned in reference 16.
[g] Values taken from reference 15 and 16.
[h] 6-311+G(d,p) basis set used for optimization.
[i] Reference 17.
[j] Reference 18, GF = Glendening and Feller.
[k] Reference 19.
[l] Reference 20.
[m] Mean absolute deviation from the B3LYP/6-311+G(2d,2p)//B3LYP/6-311+G(d,p) results. Uncertainties are one standard deviation of the absolute deviations.

References

(1) Lodish, H.; Berk, A.; Matsudaira, P.; Kaiser, C. A.; Krieger, M.; Scott, M. P.; Zipursky, S. L. *Molecular Cell Biology*, 5th ed.; W. H. Freeman and Company: New York, 2004.

(2) Dzidic, I.; Kebarle, P. *J. Phys. Chem.* **1970**, *74*, 1466.

(3) Searles, S. K.; Kebarle, P. *Can. J. Chem.* **1969**, *47*, 2619.

(4) Holland, P. M.; Castleman, A. W., Jr. *J. Chem. Phys.* **1982**, *76*, 4195.

(5) Dalleska, N. F.; Tjelta, B. L.; Armentrout, P. B. *J. Phys. Chem.* **1994**, *98*, 4191.

(6) Dalleska, N. F.; Honma, K.; Sunderlin, L. S.; Armentrout, P. B. *J. Am. Chem. Soc.* **1994**, *116*, 3519.

(7) Koizumi, H.; Larson, M.; Muntean, F.; Armentrout, P. B. *Int. J. Mass Spectrom.* **2003**, *228*, 221.

(8) Rodgers, M. T.; Armentrout, P. B. *J. Phys. Chem. A* **1997**, *101*, 1238.

(9) *Ionization Energy Evaluation*; Lias, S. G., Ed.; National Institute of Standards and Technology: Gaithersburg MD, 20899, June 2005; Vol. NIST Standard Reference Database Number 69, pp (http://webbook.nist.gov).

(10) Peschke, M.; Blades, A. T.; Kebarle, P. *J. Phys. Chem. A* **1998**, *102*, 9978.

(11) Shvartsburg, A. A.; Siu, K. W. M. *J. Am. Chem. Soc.* **2001**, *123*, 10071.

(12) Yamashita, M.; Fenn, J. B. *J. Phys. Chem.* **1984**, *88*, 4451.

(13) Whitehouse, C. M.; Dreyer, R. N.; Yamashita, M.; Fenn, J. B. *Anal. Chem.* **1985**, *57*, 675.

(14) Blades, A. T.; Jayaweera, P.; Ikonomou, M. G.; Kebarle, P. *J. Chem. Phys.* **1990**, *92*, 5900.

(15) Rodriguez-Cruz, S. E.; Jockusch, R. A.; Williams, E. R. *J. Am. Chem. Soc.* **1999**, *121*, 8898.

(16) Wong, R. L.; Paech, K.; Williams, E. R. *Int. J. Mass Spectrom.* **2004**, *232*, 59.

(17) Pavlov, M.; Siegbahn, P. E. M.; Sandstrom, M. *J. Phys. Chem. A* **1998**, *102*, 219.

(18) Glendening, E. D.; Feller, D. *J. Phys. Chem.* **1996**, *100*, 4790.

(19) Merrill, G. N.; Webb, S. P.; Bivin, D. B. *J. Phys. Chem. A* **2003**, *107*, 386.

(20) Katz, A. K.; Glusker, J. P.; Beebe, S. A.; Bock, C. W. *J. Am. Chem. Soc.* **1996**, *118*, 5752.

(21) Hales, D. A.; Lian, L.; Armentrout, P. B. *Int. J. Mass Spectrom. Ion Proc.* **1990**, *102*, 269.

(22) Schultz, R. H.; Crellin, K. C.; Armentrout, P. B. *J. Am. Chem. Soc.* **1991**, *113*, 8590.

(23) Cooper, T. E.; Carl, D. R.; Armentrout, P. B. *J. Phys. Chem. A* **2009**, *113*, 13727.

(24) Bauschlicher, C. W.; Sodupe, M.; Partridge, H. *J. Chem. Phys.* **1992**, *96*, 4453.

(25) Moision, R. M.; Armentrout, P. B. *J. Am. Soc. Mass Spectrom.* **2007**, *18*, 1124.

CHAPTER 5

IN-SOURCE FRAGMENTION TECHNIQUE FOR THE PRODUCTION OF THERMALIZED IONS

Abstract

The electrospray ionization – ion funnel – rf hexapole source is designed to produce ions for threshold collision-induced dissociation (TCID) studies in a guided ion beam mass spectrometer. The ion source, described in Chapter 2, forms an initial distribution of $Ca^{2+}(H_2O)_x$ ions where x is 6 – 9. A new in-source fragmentation technique within the hexapole ion guide of the source is described, which is easy to implement and of modest machining and electrical costs, and is able to generate smaller $Ca^{2+}(H_2O)_x$ complexes, where x = 2 – 5. Fragmentation is achieved by biasing an assembly of six 0.25" long electrodes that are inserted between the hexapole rods. The assembly is positioned in the high pressure region of the source such that newly formed $Ca^{2+}(H_2O)_x$ ions undergo enough collisions to become thermalized, as verified by TCID studies presented in Chapter 6. From the initial distribution of ions, fragmentation proceeds along the lowest energy pathway, which corresponds to sequential water loss for most complexes. However, the $Ca^{2+}(H_2O)$ complex cannot be formed directly using this method because charge separation into $CaOH^+$ and H_3O^+ becomes the lowest energy pathway from the $Ca^{2+}(H_2O)_2$ complex. Therefore, this fragmentation technique can be used to potentially identify the critical size (x_c) complex for $M^{2+}(H_2O)_x$ systems, which is

defined as the complex size at which charge separation becomes a lower energy pathway compared to simple ligand loss.

Introduction

In-source fragmentation techniques are pervasive within the field of proteomics for top-down sequencing that provides structural information. Cone-skimmer and nozzle-skimmer dissociation are well-known fragmentation techniques that accelerate ions between static lenses in the high pressure region of a mass spectrometer, thereby providing additional internal energy into ion complexes to induce dissociation.[1,2] Consecutive steps of nozzle-skimmer activation[3] in an electrospray ionization Fourier transform ion cyclotron resonance mass spectrometer (ESI-FTICR) have been shown to increase the number of backbone fragmentation pairs of $8^+ - 11^+$ ubiquitin ions compared to activation in the FTICR cell by sustained off-resonance irradiation collision-activated dissociation (SORI-CAD)[4] and infrared multiphoton dissociation (IRMPD).[5]

Fragmentation can also take place in accumulation radio frequency (rf) multipole ion guides external to the analysis region of the mass spectrometer. Fragmentation techniques include multipole-storage-assisted dissociation (MSAD),[6] ion "threshing,"[7] and external infrared multiple photon dissociation (IRMPD).[8] MSAD involves trapping ions within a hexapole by creating an axial well using a hexapole offset voltage with respect to entrance and exit cap plates. The degree of fragmentation depends on the depth of the axial well and the amount of time the ions spend in the multipole.[9] Ion "threshing" utilizes an axial potential gradient within an octopole ion guide by placing tilted wires between octopole rods. Switching the wires between positive and negative direct current (DC) voltages multiple times over a millisecond timescale induces

energetic ion–neutral collisions and leads to fragmentation. The extent of fragmentation depends on the frequency, amplitude, and number of field reversals of the applied static potential.[7] Fragmentation can also be induced via dipolar resonant excitation in a quadrupole ion guide that acts as a mass filtering linear ion trap by supplying a small supplementary dipolar rf voltage at the secular frequency of the ion of interest to a pair of opposite rods.[10,11] In combination with dipolar excitation, the efficiency of fragmentation has been shown to increase within the linear ion trap by placing DC-only auxiliary electrodes between the quadrupole rods, which creates higher order fields within the trap.[12] In this implementation, the electrodes span the entire length of the quadrupole. Extensive fragmentation can also occur with broadband resonant excitation waveforms in quadrupole ion guides prior to an ICR cell.[13] Even though the current techniques for fragmentation have been predominantly investigated for large macromolecules, they can also be utilized for much smaller ion complexes, such as those studied in this body of work.

In this chapter, the implementation of a new in-source fragmentation technique that utilizes DC electrodes set between the hexapole ion guide rods in our ESI-ion funnel-rf hexapole (ESI-IF-6P) source is described.[14] This approach is illustrated by applying it to $Ca^{2+}(H_2O)_x$ complexes.[15] Here, $x = 2 - 5$ complexes are formed from an initial distribution where x is always ≥ 6. The $Ca^{2+}(H_2O)_x$ complexes formed in this way are subjected to threshold collision-induced dissociation (TCID) in a guided ion beam tandem mass spectrometer (GIBMS). These studies indicate that the reactant ions are thermalized, but only when the electrodes are located in the high pressure region of the hexapole ion guide and only when modest electrode voltages are utilized.

In-Source Fragmentation

The ESI-IF-6P source, shown in Figure 5.1, produces an initial distribution of $Ca^{2+}(H_2O)_x$ complexes, where x = 6 – 9. Fragmentation of larger $Ca^{2+}(H_2O)_x$ complexes to form the smaller $Ca^{2+}(H_2O)_x$ ions is achieved by placing six 0.25" long brass electrodes (0.032" thickness) between the 6.0" long hexapole rods. The electrodes or "fins", as we've termed them, each get the same DC bias. For most of the work described here, the fins are located in the high pressure region of the source chamber, ~ 3.5" from the entrance to the hexapole ion guide and before the conductance limiting aperture that separates the source region (~ 10^{-2} Torr) from the differential region (~ 10^{-5} Torr) spanned by the hexapole ion guide, Position 2. Positioning the fins further upstream in the high pressure region of the hexapole (Position 1) as well as downstream in the second pumping region of the hexapole (position 3) was also tested. A custom assembly holds the fins in place insuring that they remain electrically isolated from the hexapole rods. The inner edges of the electrodes are located 0.140" from the central axis of the hexapole and are designed such that they do not extend into the trapping volume of the hexapole ion guide.

Results and Discussion

In-source fragmentation can occur with either positive or negative DC voltages applied to the fin electrodes, but the degree of fragmentation is greater for negative voltages. Figure 5.2 shows the distribution of $Ca^{2+}(H_2O)_x$ complexes as a function of the negative DC fin voltage for a the peak-to-peak rf voltage (V_{pp}) on the hexapole rods of 250 V_{pp}. At zero volts on the fins, the initial distribution of x = 6 – 9 complexes is present with $Ca^{2+}(H_2O)_7$ and $Ca^{2+}(H_2O)_8$ having the largest intensity and much smaller

intensities of $Ca^{2+}(H_2O)_6$ and $Ca^{2+}(H_2O)_9$. As the fin voltage becomes more negative, the $Ca^{2+}(H_2O)_9$, $Ca^{2+}(H_2O)_8$, and $Ca^{2+}(H_2O)_7$ complexes fragment to produce the $Ca^{2+}(H_2O)_6$ species, which reaches a maximum intensity near -10 V. As the fin voltage is decreased further, $Ca^{2+}(H_2O)_6$ begins to fragment giving way to $Ca^{2+}(H_2O)_5$, which reaches a maximum intensity near -15 V. Sequential water loss continues until $Ca^{2+}(H_2O)_2$ reaches a maximum intensity at -21 V. It is clear that the dissociation process is not heavily mass dependent, as complexes ranging over a factor of about three in mass are effectively dissociated. The fin voltage required to induce a specific amount of fragmentation is coupled to the peak-to-peak voltage (V_{pp}) on the hexapole rods. Compared to the results shown in Figure 5.2 for 250 V_{pp}, the fin voltage required for maximum fragmentation is reduced when there is 200 V_{pp} on the hexapole, whereas 300 V_{pp} increases the required fin voltage.

The total $Ca^{2+}(H_2O)_x$ ion intensity, where x = 2 – 9, decreases slowly by about 25% in going from 0 to -17.5 V on the fin electrodes. At more negative voltages, the intensity of the hydrated calcium complexes decreases more rapidly retaining only 25% of the original intensity at the highest fin voltage examined, -21.6 V. However, the total ion intensity, which includes a $CaOH^+$ fragment, retains 50% of the original overall ion intensity. The $CaOH^+$ ion is the result of a charge separation process forming $CaOH^+$ and H_3O^+ ions from $Ca^{2+}(H_2O)_2$, which is lower in energy than simple H_2O loss.[15,16] Thus, the $Ca^{2+}(H_2O)$ complex does not form in the source region, which demonstrates that x = 2 likely represents the critical size structure where charge separation is a lower energy pathway for the $Ca^{2+}(H_2O)_x$ systems. However, a quantitative assessment of such

processes under single- collision conditions such as those described in Chapter 6 are necessary to confidently assess the critical size structure.

The $Ca^{2+}(H_2O)_6$ complex is the only ion present from the initial distribution that increases in intensity with increasingly negative fin voltages. If this ion is investigated by TCID with Xe in the GIBMS, the product cross sections for losing a water molecule from the $Ca^{2+}(H_2O)_6$ complex are identical within experimental uncertainty at fin voltages of 0 and -5 V, Figure 5.3a. Furthermore, data analysis of these two cross sections using the modeling procedures described in Chapter 2 yields identical threshold energies. Given that the ESI-IF-6P source generates thermalized ions at room temperature,[14] this result indicates that $Ca^{2+}(H_2O)_6$ complexes formed from dissociation of higher solvated complexes, x = 7 – 9, are able to undergo sufficient collisions within the source region and emerge from the hexapole thermalized at 300 K when the fin voltage is on the low voltage side of the distribution profile maximum shown in Figure 5.2. However, TCID results for $Ca^{2+}(H_2O)_6$ complexes begin to change for more negative fin voltages, Figure 5.3, clearly indicating a change in the ion population. It can be noted that the changes in the TCID cross sections observed as a function of fin voltage are reproducible within the overall experimental uncertainties in the cross section magnitudes of 20% over a time period exceeding two years. These changes could either be the result of an increase in the ion temperature (leading to lower thresholds for water loss) or to the appearance of alternate isomers that would have lower water binding energies.

The origins of these changes become more obvious when smaller complexes are examined. Figure 5.3b shows the changes in the TCID cross sections observed as a

function of fin voltage for $Ca^{2+}(H_2O)_4$ losing a single water molecule. When $Ca^{2+}(H_2O)_4$ is generated with -15.5 V on the fins (low voltage side of the distribution of Figure 5.2, solid circles), the CID cross section shows only a rapid rise from an apparent threshold of ~ 0.7 eV. Increasing the fin voltage to -17.5 V produces the largest ion intensity for the $Ca^{2+}(H_2O)_4$ mass (Figure 5.2, solid squares), however, the $Ca^{2+}(H_2O)_3$ product cross section contains a low energy feature below ~ 0.8 eV along with a high energy feature that matches the cross section observed at -15.5 V. At -18.8 V on the fins (on the high voltage side of the distribution of Figure 5.2, solid diamonds), the low energy feature increases in intensity by a factor of 15 while the high energy feature remains at a similar magnitude. Note that the shape of the low energy feature (from 0.1 to 0.7 eV) does not change as a function of the fin voltage as shown in Figure 5.3. Therefore, the high energy feature is attributed to dissociation from the ground state structure of the $Ca^{2+}(H_2O)_4$ complex in which all four water molecules are bound directly to the metal ion.[15] The low energy feature can then be associated with a small percentage of $Ca^{2+}(H_2O)_3(H_2O)$ present in which one water molecule is located in the second solvent shell and much more weakly bound than an inner shell water molecule. Similar observations are made for the x = 5 and 6 complexes where a comparison with experimental and theoretical results from Chapter 4 demonstrate that the high energy features correspond to ions that are thermalized at room temperature and have the ground state structure.[15]

The assignment of the low energy feature to a different isomer arises from several considerations. It is clear, especially for Figure 5.3 and the comparable data for x = 5, that the low energy feature cannot be attributed to simply raising the temperature of the

parent ions. In this case, the product cross section would broaden to lower energies rather than yielding a distinct low-energy feature. In addition, for a fin voltage that gives the maximum intensity of a given sized $Ca^{2+}(H_2O)_x$ ion, Figure 5.2, there is an appreciable amount of the $Ca^{2+}(H_2O)_{x-1}$ and $Ca^{2+}(H_2O)_{x+1}$ ions also produced (on the order of 20%). Most of the gas load in the source region of the apparatus is the electrospray solvent (here H_2O). Thus, thermalization of the ions occurs by collisions with water, such that the presence of $Ca^{2+}(H_2O)_{x-1}$ ions under these conditions allows rehydration of these complexes to occur. As the rehydration need not form an equilibrium distribution of the $Ca^{2+}(H_2O)_x$ complexes, higher energy isomers can be formed. The fact that shapes of the low energy features in the TCID cross section do not change with fin voltage indicates that these ions are also thermalized. Therefore, the source can be used to form high energy isomers that are still thermalized.

For the purpose of generating thermalized ions for quantitative CID studies presented in Chapters 6 - 8, the optimum position of the fins was determined to be located in the high pressure region of the source (Position 2 in Figure 5.1). Placing the electrodes closer to the entrance of the ion guide (Position 1) did not produce as extensive fragmentation. This is attributed to the higher local pressure in the front of the hexapole ion guide such that the ions are not accelerated by the fin voltage appreciably before undergoing a collision and because the ions have significantly more hexapole length to rehydrate and re-equilibrate.

With the fin electrodes located towards the end of the ion guide (Position 3) in the low pressure region ($P_{DIFF} \sim 10^{-5}$ Torr), the amount of fragmentation was extensive and rehydration was avoided. However, the low pressure of position 3 means that there is

little collisional cooling, such that the ions formed are internally hotter. This is shown in Figure 5.4. With -16.0 V on the fins in Position 3, the $Ca^{2+}(H_2O)_4$ ion signal has a maximum intensity. Upon TCID, these ions yield a $Ca^{2+}(H_2O)_3$ product cross section that is shifted to lower kinetic energies compared to complexes formed with -15.5 V on the fins at Position 2 in the high pressure region. A higher negative fin voltage furthers shifts the CID onset to lower energies. The data for single water molecule loss from $Ca^{2+}(H_2O)_4$ ions formed with the fins in Position 3 at voltages of -16.0 and -17.5 V can be reproduced (using the same parameters needed to reproduce the thermalized data) if the temperature of the $Ca^{2+}(H_2O)_4$ reactant ions is set to 402 and 453 K, respectively. Note that under these conditions, distinctive low-energy features attributable to alternate isomers of the ion beam are absent. This demonstrates that rehydration no longer occurs efficiently. Similar observations are found for the x = 5 and 6 complexes.

Conclusions

An in-source fragmentation technique has been described for implementation within a hexapole ion guide of an electrospray ionization-ion funnel-rf hexapole source that is able to produce smaller $Ca^{2+}(H_2O)_x$ complexes, where x = 2 – 5, from an initial distribution that always consists of complexes where x = 6 – 9. When the electrodes are properly placed and modest voltages applied, product cross sections for single water molecule loss from $Ca^{2+}(H_2O)_x$ complexes formed in this way indicate that the ions have a single ground-state isomer that is thermalized at 300 K. The newly accessed $Ca^{2+}(H_2O)_x$ complexes are transmitted to the reaction region as a continuous ion beam and require no intricate pulsing schemes out of the hexapole ion guide. Other in-source fragmentation techniques that take place in ion guides external to FTICR mass

spectrometers inherently require the ions to be stored in the external linear ion trap, fragmented, and pulsed into the ICR cell for detection,[6,7] whereas other techniques are amenable to continuous operation.[8,13] The present technique could prove useful for systems operating in continuous transmission mode, such as a source region multipole ion guide before the first quadrupole within a triple quadrupole apparatus. A significant advantage of the fin electrodes is their implementation into an ion guide is relatively straightforward with respect to other methods and can be done at modest machining and electrical costs. The versatility of the present method can be illustrated by the applications of the in-source fragmentation technique to generate $M^{2+}(H_2O)_x$ complexes, where M = Ca (Chapter 6)[17], Sr (Chapter 7)[18], Mg (Chapter 8)[19], Ba,[20] Cd,[21,22] and Fe[23] with x values lying between the critical size and the complexes making up the initial distribution of the $M^{2+}(H_2O)_x$ system. Additionally, this fragmentation technique could generate Li^+(amino acid) complexes by electrospray ionization, which are otherwise formed in low abundance under normal operating source conditions because these complexes are easily solvated with electrospray solvent.

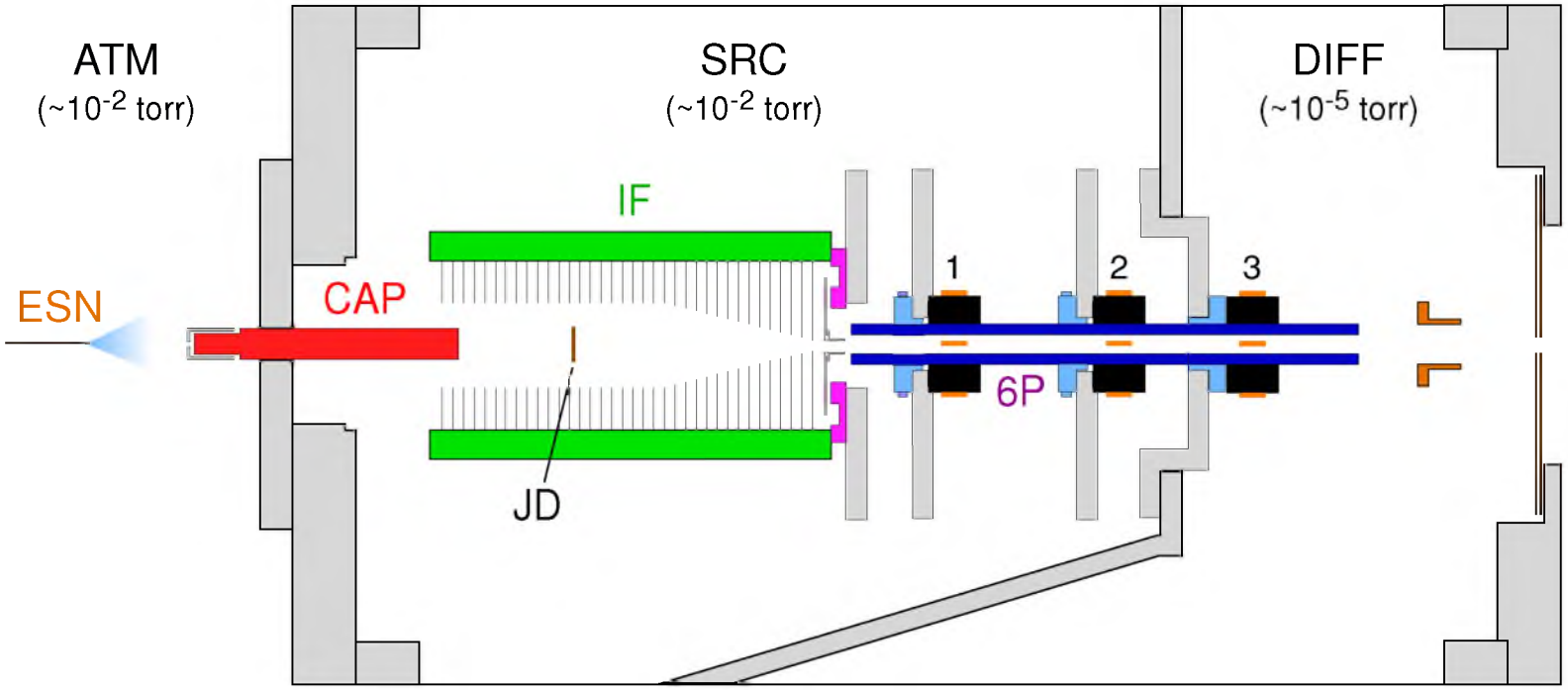

Figure 5.1. Electrospray ionization – ion funnel – rf hexapole (ESI-IF-6P) source schematic depicting three possible locations of fin electrode assembly. Fin electrodes located at positions 1 and 2 are in the high pressure source (SRC) region. Position 3 of the fin electrodes is in the low pressure differential (DIFF) region. The electrospray needle (ESN) is located at atmosphere (ATM).

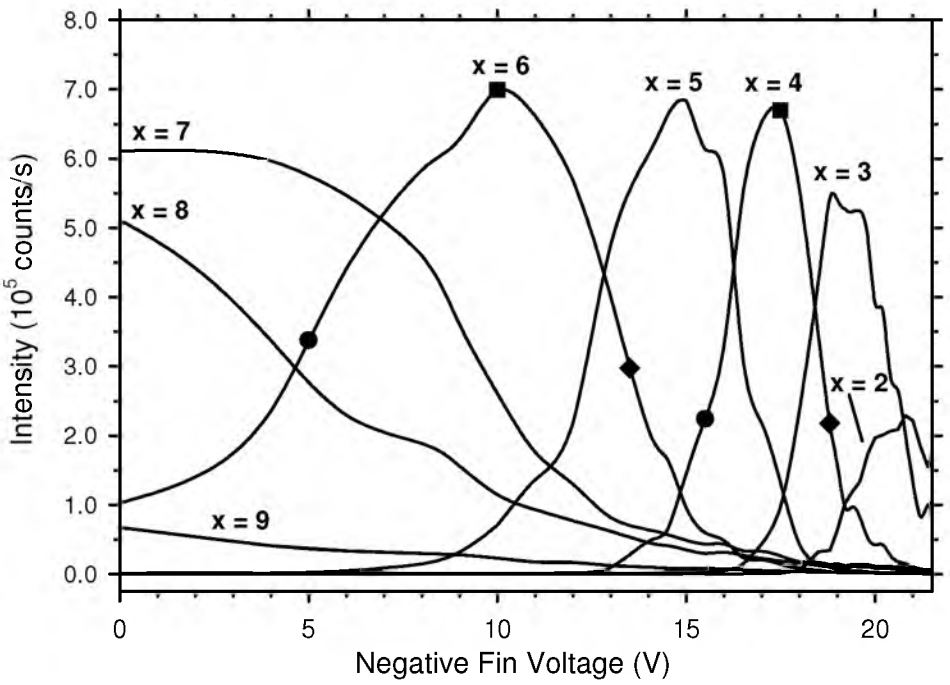

Figure 5.2. Distribution of $Ca^{2+}(H_2O)_x$ complexes as a function of negative fin voltage. The filled symbols on the $Ca^{2+}(H_2O)_6$ and $Ca^{2+}(H_2O)_4$ intensity profiles correspond to specific fin voltages used to select a specific reactant ion as described further in Figure 5.3.

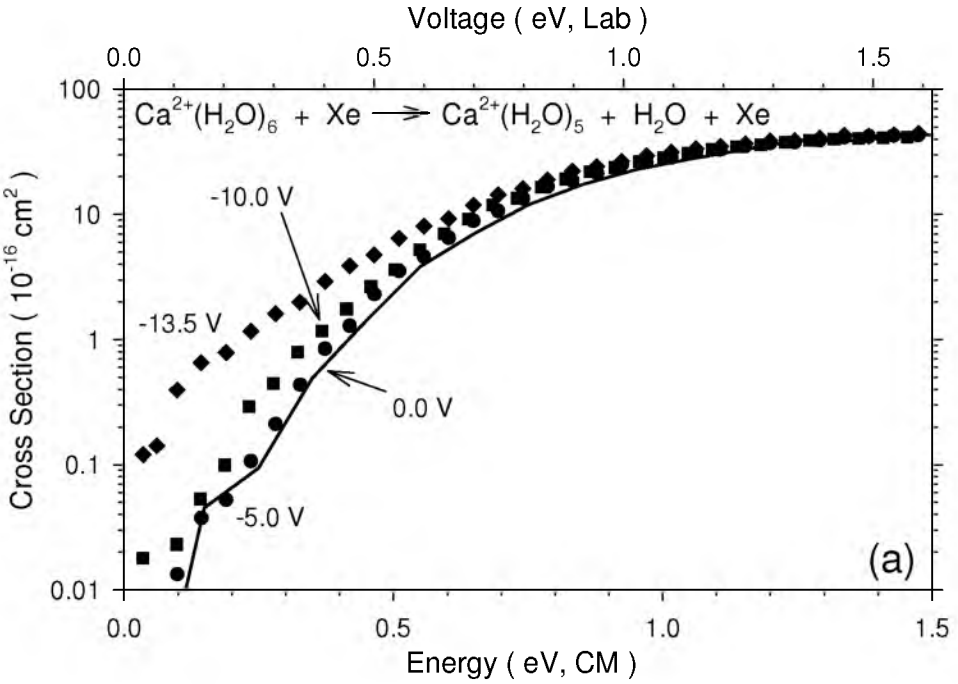

Figure 5.3. $Ca^{2+}(H_2O)_{x-1}$ product cross sections from the collision-induced dissociation of $Ca^{2+}(H_2O)_6$ (a) and $Ca^{2+}(H_2O)_4$ (b) with Xe with fin electrodes in high pressure region (position 2). In part a, the solid line represents the product cross section for losing a single water molecule with a fin voltage of 0.0 V. Filled circles, squares, and diamonds correspond to fin voltages of -5.0, -10.0, and -13.5 V, respectively. In part b, filled circles, squares, and diamonds correspond to fin voltages of -15.5, -17.5, and -18.8 V, respectively. The solid line represents low energy data for -17.5 V scaled up by a factor of 15.

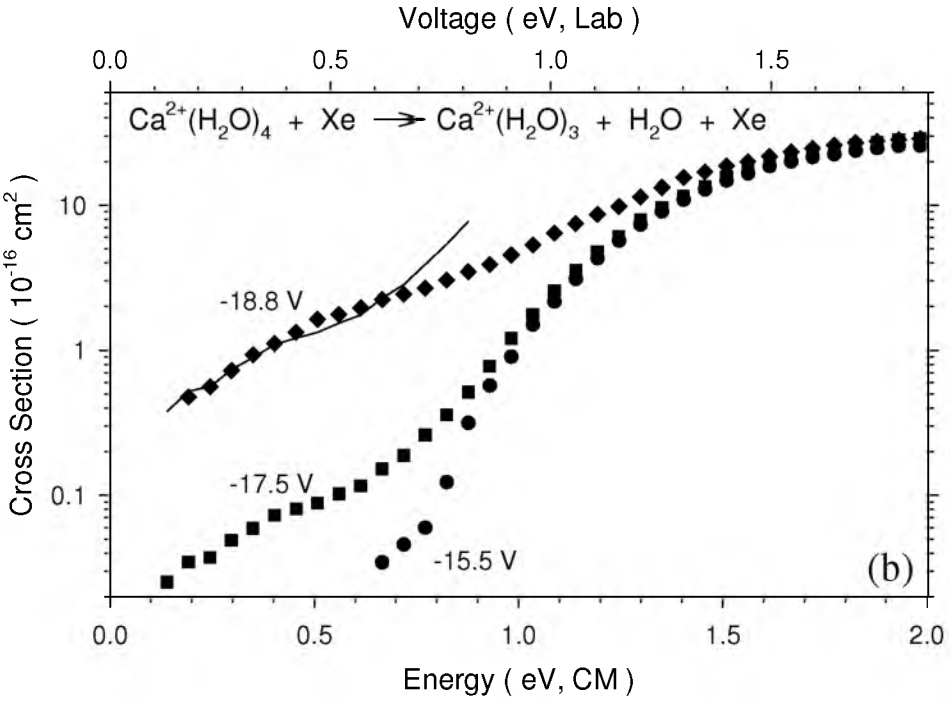

Figure 5.3. continued

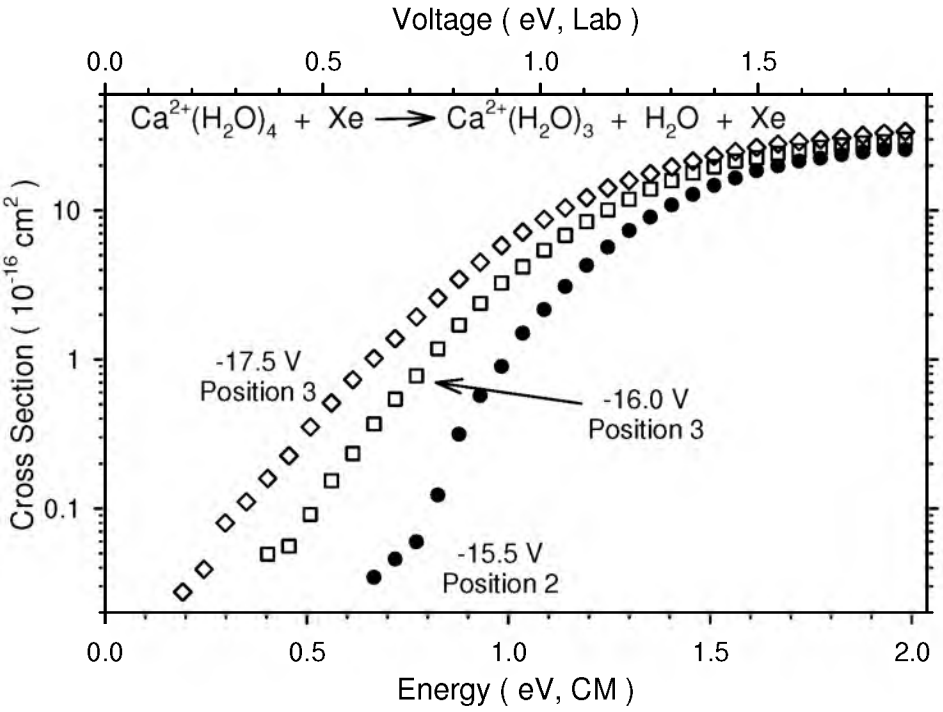

Figure 5.4. $Ca^{2+}(H_2O)_3$ product cross sections from the collision-induced dissociation of $Ca^{2+}(H_2O)_4$ with Xe. Filled circles correspond to a fin voltage of -15.5 V and the electrodes at position 2 in the high pressure region (10^{-2} Torr). Open squares and diamonds correspond to fin voltages of -16.0 and -17.5 V, respectively, with fin electrodes in the low pressure region (10^{-5} Torr) at position 3.

References

(1) Loo, J. A.; Edmonds, C. G.; Smith, R. D. *Science* **1990**, *248*, 201.

(2) Loo, J. A.; Edmonds, C. G.; Smith, R. D. *Anal. Chem.* **1991**, *63*, 2488.

(3) Zhai, H.; Han, X.; Breuker, K.; McLafferty, F. W. *Anal. Chem.* **2005**, *77*, 5777.

(4) Gauthier, J. W.; Trautman, T. R.; Jacobson, D. B. *Anal. Chim. Acta* **1991**, *246*, 211.

(5) Little, D. P.; Speir, J. P.; Senko, M. W.; O'Connor, P. B.; McLafferty, F. W. *Anal. Chem.* **1994**, *66*, 2809.

(6) Sannes-Lowery, K.; Griffey, R. H.; Kruppa, G. H.; Speir, J. P.; Hofstadler, S. *Rapid Commun. Mass Spectrom.* **1998**, *12*, 1957.

(7) McFarland, M. A.; Hendrickson, C. L.; Marshall, A. G. *Anal. Chem.* **2004**, *76*, 1545.

(8) Hofstadler, S. A.; Sannes-Lowery, K. A.; Griffey, R. H. *Anal. Chem.* **1999**, *71*, 2067.

(9) Pan, C.; Hettich, R. L. *Anal. Chem.* **2005**, *77*, 3072.

(10) Collings, B. A.; Stott, W. R.; Londry, F. A. *J. Am. Soc. Mass Spectrom.* **2003**, *14*, 622.

(11) Campbell, J. M.; Collings, B. A.; Douglas, D. J. *Rapid Commun. in Mass Spectrom.* **1998**, *12*, 1463.

(12) Collings, B. A. *J. Am. Soc. Mass Spectrom.* **2005**, *16*, 1342.

(13) Vilkov, A. N.; Bogdanov, B.; Paša-Tolić, L.; Prior, D. C.; Anderson, G. A.; Masselson, C. D.; Moore, R. J.; Smith, R. D. *Rapid. Comm. Mass Spectrom.* **2004**, *18*, 2682.

(14) Moision, R. M.; Armentrout, P. B. *J. Am. Soc. Mass Spectrom.* **2007**, *18*, 1124.

(15) Carl, D. R.; Moision, R. M.; Armentrout, P. B. *Int. J. Mass Spectrom.* **2007**, *265*, 308.

(16) Beyer, M.; Williams, E. R.; Bondybey, V. E. *J. Am. Chem. Soc.* **1999**, *121*, 1565.

(17) Carl, D. R.; Armentrout, P. B. *J. Phys. Chem. A* **2012**, *116*, 3802.

(18) Carl, D. R.; Chatterjee, B. K.; Armentrout, P. B. *J. Chem. Phys.* **2010**, *132*, 44303.

(19) Carl, D. R.; Armentrout, P. B. *Chem. Phys. Chem.* **2013**, in press.

(20) Wheeler, O.; Armentrout, P. B., work in progress.

(21) Cooper, T. E.; Armentrout, P. B. *Chem. Phys. Lett.* **2010**, *486*, 1.

(22) Cooper, T. E.; Armentrout, P. B. *J. Chem. Phys.* **2011**, *134*, 114308.

(23) Hofstetter, T. E.; Armentrout, P. B. *J. Chem. Phys.* **2013**, in press.

CHAPTER 6

EXPERIMENTAL INVESTIGATION OF THE COMPLETE INNER SHELL HYDRATION ENERGIES OF CALCIUM

Abstract

The sequential bond energies of $Ca^{2+}(H_2O)_x$ complexes, where x = 1 – 8, are measured by threshold collision-induced dissociation in a guided ion beam tandem mass spectrometer. From an electrospray ionization source that produces an initial distribution of $Ca^{2+}(H_2O)_x$ complexes where x = 6 – 9, complexes down to x = 2 are formed using the in-source fragmentation technique described in the previous chapter. $Ca^{2+}(H_2O)$ cannot be formed in this source because charge separation into $CaOH^+$ and H_3O^+ is a lower energy pathway than simple water loss from $Ca^{2+}(H_2O)_2$. The kinetic energy dependent cross sections for dissociation of $Ca^{2+}(H_2O)_x$ complexes, where x = 2 – 9, are examined over a wide energy range to monitor all dissociation products and are modeled to obtain 0 and 298 K binding energies. Analysis of both primary and secondary water molecule losses from each sized complex provides thermochemistry for the sequential hydration energies of Ca^{2+} for x = 1 – 8 and the first experimental values for x = 1 – 4. Additionally, the thermodynamic onsets leading to the charge separation products from $Ca^{2+}(H_2O)_2$ and $Ca^{2+}(H_2O)_3$ are determined for the first time. Our experimental results agree well with previously calculated B3LYP//B3LYP binding enthalpies (Chapter 4) for x = 1 – 6 as well as new quantum chemical calculations in which calcium is treated with

the cc-pCVTZ basis set. This new treatment, which includes core polarization for the calcium ion, results in calculated bond energies that are 7 and 4 kJ/mol higher for x = 1 and 2 complexes, respectively, compared to B3LYP//B3LYP energies.

Introduction

Gas-phase multiply charged hydrated metal ions, $M^{2+}(H_2O)_x$, for which the alkaline earth metals are model systems, are complexes of considerable interest in understanding solvation phenomena. Studies of such systems have been greatly aided by their facile generation using electrospray ionization (ESI).[1-6] In Chapter 4, the sequential bond dissociation energies (BDEs) of water loss from $Ca^{2+}(H_2O)_x$, x = 5 – 9, were measured using threshold collision-induced dissociation (TCID) in a guided ion beam tandem mass spectrometer (GIBMS).[7] These values were found to be in good agreement with previous equilibrium results from Kebarle and coworkers, who used high pressure mass spectrometry (HPMS),[3,4] and kinetic measurements from the Williams group, who used blackbody infrared dissociation (BIRD).[5,6] From these three experimental studies, the bond dissociation energies (BDEs) for $Ca^{2+}(H_2O)_x$, x = 5 – 15, have now been determined, leaving theoretical calculations to determine the bond energies for the remaining inner shell complexes (x = 1 – 4). $Ca^{2+}(H_2O)_x$ complexes, x = 4 – 69, have also been investigated via infrared multiple photon dissociation (IRMPD) in a Fourier transform ion cyclotron resonance (FT-ICR) mass spectrometer by Bush et al.[8,9] The structures of these ions were characterized by comparison of their photodissociation spectra from 3000 to 3800 cm^{-1} with theoretical spectra. These spectroscopic studies indicate that six water molecules bind directly to calcium and the next several second solvent shell water molecules bind to two inner shell water molecules that each donate a

single hydrogen bond in agreement with the results of Chapter 4.[7,8] However, once $Ca^{2+}(H_2O)_{11}$ is reached, the size of the inner shell transitions from six to eight water molecules.[9]

Smaller $Ca^{2+}(H_2O)_x$ complexes, x = 1 – 6, have been investigated by theoretical calculations using a variety of basis set treatments and different levels of theory.[7,10-13] Details from these studies were previously described in Chapter 4 along with our rigorous theoretical assessment for x = 1 – 9 complexes specifically focusing on the ground-state and low-lying structures for x = 5 – 9 complexes. From our calculations, we determined B3LYP/6-311+G(2d,2p)//B3LYP/6-311+G(d,p) bond energies were representative for all calculations as they showed the best overall agreement to the experimental results. A recent theoretical investigation by Rao et al. for x = 1 – 6 complexes has calculated sequential BDEs at the B3LYP/6-311++G(3d,3p), MP2(full)/6-311++G(3d,3p) and CCSD(T)/6-311++G(d,p) levels of theory using B3LYP/6-311++G(d,p) geometry optimizations along with Gaussian-3 (G3) theory BDEs.[14] Unlike the abundance of calculated bond energies for the inner shell $Ca^{2+}(H_2O)_x$ complexes, only one theoretical study exploring the reaction coordinate for the charge separation pathway from $Ca^{2+}(H_2O)_2$ to produce $CaOH^+$ and H_3O^+, has been conducted.[15]

In this chapter, threshold collision-induced dissociation in a GIBMS equipped with a second generation ESI source is employed to determine the binding enthalpies for the complete inner shell of calcium ions for the first time. These determinations require the use of a combination of in-source fragmentation[16] and a statistical model for sequential dissociation.[17] The current study is an extension of the work presented in Chapter 4 for the $Ca^{2+}(H_2O)_x$, x = 5 – 9, systems.[7] The ESI source now consistently

produces an initial distribution of $Ca^{2+}(H_2O)_x$ complexes with x = 6 – 9 rather than x = 5 – 9 described in Chapter 4. Smaller $Ca^{2+}(H_2O)_x$ complexes, x = 2 – 5, are generated via in-source fragmentation, described in Chapter 5.[16] This fragmentation procedure does not form the $Ca^{2+}(H_2O)$ complex because $Ca^{2+}(H_2O)_2$ preferentially charge separates into $CaOH^+ + H_3O^+$ ions instead of losing a water ligand. Therefore, sequential modeling of the primary and secondary water losses from the TCID of $Ca^{2+}(H_2O)_2$ serves as the only means available to determine the binding enthalpy for $Ca^{2+}(H_2O)$. Sequential modeling has been shown to be a viable tool for extracting BDEs for $K^+(NH_3)_x$, where x = 1 – 4,[17] which have also been determined directly by TCID[18] and HPMS.[19] For doubly charged solvated metal ions, Cooper et al. utilized sequential modeling to determine bond dissociation energies for $Zn^{2+}(H_2O)_x$ and $Cd^{2+}(H_2O)_y$, where x = 6 – 10 and y = 4 – 11, respectively.[20-23] In addition to the dominant water loss channels, charge separation from the $Ca^{2+}(H_2O)_2$ and $Ca^{2+}(H_2O)_3$ species into $CaOH^+ + H_3O^+$ and $CaOH^+(H_2O) + H_3O^+$, respectively, are examined experimentally as a function of kinetic energy for the first time with their respective rate-limiting transition states measured and compared to theoretical calculations.

Results

Cross sections for collision-induced dissociation. The CID cross sections for $Ca^{2+}(H_2O)_x$, where x = 2 – 4, are shown in Figure 6.1. Even though the results for x = 5 – 9 were reported in Chapter 4,[7] TCID experiments were repeated for x = 5 – 8 to assess whether any quantitative changes had occurred since the implementing the jet disruptor into the ion funnel and the in-source fragmentation capabilities within the hexapole ion guide. Qualitatively, these results are the same as in Chapter 4; however, small

differences in the quantitative results obtained between these results and the previous (Chapter 4) are noted below.

The primary dissociation process for all complexes studied is the loss of a single water molecule, Reaction 6.1. Sequential water loss occurs at higher kinetic energies until the bare metal ion is formed, Figure 6.1.

$$Ca^{2+}(H_2O)_x + Xe \rightarrow Ca^{2+}(H_2O)_{x-1} + H_2O + Xe \qquad (6.1)$$

In addition, a proton transfer/charge separation process from the $Ca^{2+}(H_2O)_2$ complex, Reaction 6.2, is observed for all CID cross sections in Figure 6.1. The product cross sections of $CaOH^+$ and H_3O^+ ions are nearly identical, as they must be, and have lower apparent thresholds than the $Ca^{2+}(H_2O)$ product cross section, as can be observed in the results for both $Ca^{2+}(H_2O)_2$ and $Ca^{2+}(H_2O)_3$.

$$Ca^{2+}(H_2O)_2 + Xe \rightarrow CaOH^+ + H_3O^+ + Xe \qquad (6.2)$$

The $CaOH^+$ (57 m/z) product was not collected in the CID of $Ca^{2+}(H_2O)_4$ because mass overlap with the ion beam (56 m/z) obscures this minor product. A second proton transfer/charge separation process from the $Ca^{2+}(H_2O)_3$ ion into $CaOH^+(H_2O)$ and H_3O^+ ions, Reaction 6.1, is also observed in the CID of $Ca^{2+}(H_2O)_3$ and $Ca^{2+}(H_2O)_4$. This process clearly has a threshold much higher than H_2O loss to form $Ca^{2+}(H_2O)_2$, and therefore, is very inefficient.

$$Ca^{2+}(H_2O)_3 + Xe \rightarrow CaOH^+(H_2O) + H_3O^+ + Xe \qquad (6.3)$$

The CID product cross sections for x = 3 and 4 shown in Figure 6.1b and 6.1c utilize in-source fragmentation conditions that produced the largest reactant ion signal

intensity. For the primary product ions produced in Reaction 6.1, cross sections obtained using lower in-source fragmentation voltages (dotted circles) are also shown. It can be seen that these cross sections increase sharply with increasing collision energy and do not exhibit the low energy tail evident in the other cross sections (open circles). These low energy features are not the result of any pressure dependent effects, as verified by comparison of product cross sections obtained at ~0.05, 0.10, and 0.20 mTorr of Xe collision gas. Therefore, these low energy features are attributed to single water loss from a population of higher energy species present in the reactant ion beam. Compared with the main part of the cross section, the absolute magnitudes of these tails suggest that the population of these high energy isomers is less than 1% in both systems. Thus, even at the higher in-source fragmentation voltages, the majority of the ion beam consists of isomers in which all water molecules are bound directly to the Ca^{2+} ion, designated $Ca^{2+}(H_2O)_3$ and $Ca^{2+}(H_2O)_4$ or more simply as (3,0) and (4,0), respectively. Because the parent signal intensity for the lowest energy isomer is enhanced by the higher in-source fragmentation voltages,[16] high quality data for the low intensity product ions, such as $CaOH^+(H_2O)$, can be collected. We verified that all these minor product channels were also present at the lower in-source voltages, indicating that the $CaOH^+(H_2O)$ product does indeed originate from a $Ca^{2+}(H_2O)_3$ precursor. Importantly, the source conditions that generate such high energy isomers cannot be used to elucidate accurate thermochemical information for the ground state isomers where water molecules are bound directly to Ca^{2+}. Therefore, all thermochemical information discussed below is acquired from analysis of cross sections taken with the lower in-source fragmentation voltages, where excited isomers are not present.

The high energy isomers correspond to structures in which one water molecule is located in the second solvent shell, $Ca^{2+}(H_2O)_2(H_2O)$ and $Ca^{2+}(H_2O)_3(H_2O)$ or (2,1) and (3,1), respectively. Although there is little direct evidence for this identification, the higher in-source fragmentation voltages used for each system also produce appreciable amounts of $Ca^{2+}(H_2O)_2$ and $Ca^{2+}(H_2O)_3$, respectively, whereas at the lower voltages, little of these complexes are produced as discussed in Chapter 5.[16] It seems plausible that when water molecules (present in the source region as the solvent used in the ESI source) interact with these smaller complexes, they can attach in both the inner and outer solvent shell. Thermalization of the latter species yields the distinct low-energy tails observed in the cross sections.

Thermochemical results for primary water loss from $Ca^{2+}(H_2O)_x$ complexes, x = 2 – 8. The total cross sections for water dissociation, Reaction 6.1, were modeled using Equations 2.4 and 2.5 for all $Ca^{2+}(H_2O)_x$ complexes. The total cross section is modeled because the overall shape of the cross sections for Reaction 6.1 is influenced by sequential dissociation of additional water molecules. The optimum fitting parameters for modeling the primary water loss from the $Ca^{2+}(H_2O)_x$ complexes, where x = 2 – 8, are listed in Table 6.1. The models of Equation 2.5 are compared to the zero pressure-extrapolated cross sections for x = 2 – 4 shown in Figure 6.2. In all cases, the models reproduce the data from threshold to 7 eV. The kinetic shift, the difference between threshold values obtained with (Equation 2.5) and without (Equation 2.4) consideration of lifetime effects, is negligible for x = 2 and gradually increases from 0.05 eV for x = 3 to 0.38 eV for x = 8, Table 6.1. This progression is expected as dissociation rates should

decline as the size of the $Ca^{2+}(H_2O)_x$ complex increases. These kinetic shifts are similar to the results presented in Chapter 4.1 for thermochemical results for x = 5 – 9.

E_0 values for x = 5 – 9 from Chapter 4 are also included in Table 6.1 and agree well with the current results. The only notable difference between these two studies is that the current threshold value for water loss from x = 6 is larger by 0.10 eV, a difference that is very clear in a direct comparison of the zero pressure-extrapolated total cross sections shown in Figure 6.3. This comparison indicates the $Ca^{2+}(H_2O)_6$ ions in the previous study were not completely thermalized to 300 K. Indeed, reproduction of these older data using the 0 K threshold value of 1.02 eV in Equation 2.5 can be achieved by setting the reactant temperature to 350 K. We believe this is because our previous source arrangement allowed charged droplets from the ESI capillary to deposit in the hexapole, creating a sufficiently large electrostatic charge that ions could be accelerated and collisionally heated. This hypothesis led to the creation of the in-source fragmentation electrodes that allow us to manipulate this process directly.[16] The extent of this heating effect depended on when the source was last cleaned and therefore could vary appreciably from experiment to experiment. The present source arrangement shows no signs of similar instabilities.

Reaction thresholds for losing a single water molecule decrease monotonically with increasing size of the $Ca^{2+}(H_2O)_x$ complex for x = 2 – 7. x = 7 and 8 complexes have similar E_0 values which indicates that water molecules are located in the second solvent shell and hydrogen bond to the inner shell water molecules in a similar manner. The 0.39 eV difference between the threshold values for x = 6 and 7 is larger than any other subsequent pair of complexes indicating the closing of the complete inner solvent

shell at x = 6. This conclusion is consistent with Chapter 4 theoretical calculations,[7] experimental thermochemical studies,[4,5,7] and IR action spectroscopy results of $Ca^{2+}(H_2O)_x$ complexes, which suggest an inner shell of six water molecules for $x < 11$.[8]

Thermochemical results for competitive modeling of $Ca^{2+}(H_2O)_2$ and $Ca^{2+}(H_2O)_3$. In addition to the inner shell hydration energies of the $Ca^{2+}(H_2O)_x$ system, it is of interest to determine the thermodynamic onset for the rate-limiting transition state (TS) for the charge separation process from $Ca^{2+}(H_2O)_2$, Reaction 6.2. The zero pressure-extrapolated cross section for the average of the charge separation products ($CaOH^+$ and H_3O^+) was modeled independently and in competition with water loss using Equation 2.5. The latter analysis is shown in Figure 6.4 and optimum fitting parameters for modeling these dissociation channels are presented in Table 6.1.

Independent analysis of the water loss and charge separation pathways produce 0 K reaction thresholds of 2.15 ± 0.18 eV and 1.57 ± 0.13 eV, respectively. In the competitive model, it was determined that if the computed vibrational frequencies for the rate-limiting TS of the charge separation pathway are used, the charge separation cross section is reproduced with a 0 K reaction threshold of 1.05 – 1.15 eV, a significant departure from the single channel analysis, and required a scaling factor, $\sigma_{0,j}$ in Equation 2.5, that optimizes between 10^{-6} and 10^{-7}. We have previously suggested that such a nonphysical result indicates inaccurate frequencies.[21,24] In this case, the scaling factor indicates that the calculated rate-limiting transition state for charge separation, TS (CS), is too loose. To produce a more physically realistic representation of the competition, the vibrational frequencies below 800 cm^{-1} of TS (CS) (those most likely to be inaccurately determined) are scaled up. When these frequencies are increased by a factor of 10, a

scaling factor near unity is obtained and the 0 K reaction threshold for the charge separation pathway is determined as 1.46 ± 0.14 eV, which corresponds to the first direct experimental determination of this pathway. In this competitive analysis, the 0 K threshold for water loss decreases to 2.05 ± 0.18 eV, corresponding to a competitive shift of 0.10 eV from the independently modeled threshold of 2.15 ± 0.18 eV, Table 6.1. The competitive model reproduces the cross sections for both channels from threshold to 4 eV, including the slow decline in the charge separation cross section, Figure 6.4. Overall, the modeling correctly captures the competition between the energetically favored charge separation channel, which is kinetically disfavored because it involves a tight TS, and the water loss channel involving a loose TS.

The zero-pressure extrapolated cross section for the charge separation process from $Ca^{2+}(H_2O)_3$ into $CaOH^+(H_2O)$ and H_3O^+ ions, Reaction 6.3, was not modeled competitively because the $CaOH^+(H_2O)$ cross section could only be observed clearly at high Xe pressures (~0.2 mTorr) and when the in-source fragmentation electrodes were set to maximize the ion intensity of the $Ca^{2+}(H_2O)_3$ signal. When the fragmentation electrode voltage is turned to conditions needed for accurate thermodynamic information, the $CaOH^+(H_2O)$ cross section was too small, especially at low Xe pressures, to allow for an accurate zero-pressure extrapolated cross section to be obtained. However, if the $Ca^{2+}(H_2O)_2$ and $CaOH^+(H_2O)$ product cross sections shown in Figure 6.1b are analyzed competitively at the largest Xe pressure, the threshold values for water loss and charge separation optimize to 1.68 ± 0.08 and 1.63 ± 0.09 eV, respectively, Table 6.1. Here, the threshold for water loss is lower than that for the independent fit of zero-pressure extrapolated data, 1.76 ± 0.09 eV, because of the pressure effect. In this analysis, the

vibrational frequencies less than 800 cm^{-1} for the rate-limiting TS of the charge separation pathway from $Ca^{2+}(H_2O)_3$ were scaled by 1.3. We consider the 1.63 ± 0.09 eV threshold to be a rough estimate and a likely lower limit to the true thermodynamic value. Because the difference in thresholds for Reactions 4.1 and 6.1 (0.05 ± 0.12 eV) may be more accurate, our best estimate for the true TS energy is 1.71 ± 0.15 eV. Notably, this analysis indicates that charge separation has a slightly lower threshold than water loss, a result that has implications on the assignment for the critical size complex.

Thermochemical results for sequential modeling. Thermochemical results utilizing the sequential model for x = 2 – 8 are presented in Table 6.2. Examples of the sequential model are shown in Figure 6.5 for the smallest $Ca^{2+}(H_2O)_x$ complexes investigated, x = 2 – 4. The sequential modeling of the primary and secondary water losses in the dissociation of $Ca^{2+}(H_2O)_4$, Figure 6.5c is representative of the results for the x = 5 – 8 systems. Here, the model reproduces both product cross sections from the initial onsets to energies near 6 eV. For $Ca^{2+}(H_2O)_2$ and $Ca^{2+}(H_2O)_3$, competition between the charge separation pathway and water loss as a primary and secondary process is incorporated into the sequential model analysis in Figures 6.5a and 6.5b, respectively. The difference between the primary and secondary thresholds, shown in brackets in Table 6.2, provides a second independent measurement of the BDE for $Ca^{2+}(H_2O)_{x-1}$ dissociating to $Ca^{2+}(H_2O)_{x-2} + H_2O$ and is referred to as a secondary BDE. The secondary BDEs have low uncertainties (0.05 – 0.08 eV for x = 3 – 8) despite utilizing results from multiple data sets because many systematic uncertainties in the measurements cancel for these relative thresholds. Table 6.2 also includes primary BDEs from Table 6.1 for comparison to these secondary BDEs. The σ_0, E_0, and n values from

modeling the total cross sections for $Ca^{2+}(H_2O)_x$ complexes, Table 6.1, are nearly identical to those in Table 6.2, with analogous E_0 values within 0.02 eV. Secondary BDEs for x = 6 and 7 agree with primary values, but differ by about 0.1 eV for x = 3 – 5 complexes with the secondary BDEs being consistently larger.

For x = 3, the combined sequential/competitive analysis reproduces all three product cross sections reasonably well in Figure 6.5b, although the thresholds for the small secondary reactions appear somewhat elevated compared to the data. For dissociation of $Ca^{2+}(H_2O)_3$, the secondary BDE of 2.40 ± 0.08 eV is 0.25 ± 0.20 eV higher than the primary BDE of 2.15 ± 0.18 eV, a difference outside of experimental uncertainty. If competition with the charge separation pathway is included in the sequential analysis of $Ca^{2+}(H_2O)_3$ dissociation, the secondary BDE (2.36 ± 0.07 eV) remains ~0.3 eV larger than the analogous primary BDE (2.05 ± 0.18 eV, Table 6.1) that also includes competition from charge separation. Additionally, by including the competition for x = 3, a secondary measurement of the rate-limiting for the charge separation pathway is measured using the combined sequential/competitive model as 2.03 ± 0.13 eV, Table 6.2. However, this value is significantly larger than the primary measurement of 1.46 ± 0.14 eV.

As noted above, our source does not produce $Ca^{2+}(H_2O)$ because the $Ca^{2+}(H_2O)_2$ complex dissociates preferentially by charge separation. Therefore, analyzing the $Ca^{2+}(H_2O)_2$ data for the secondary BDE is our only means to ascertain the BDE of the most tightly bound water molecule. The analysis of the zero-pressure extrapolated cross sections for the primary and secondary water losses (excluding competition) results in absolute values of 2.16 ± 0.20 eV and 4.83 eV ± 0.39 eV, respectively, and a secondary

BDE of 2.68 ± 0.32 eV, Table 6.2. The substantial uncertainty in the analysis of the secondary water loss cross section (Ca^{2+}) is attributed to its small cross section, which leads to a relatively noisy zero-pressure cross section. Alternatively, data for individual pressures (duplicates at each of three pressures) can be analyzed utilizing the sequential model and yields less scattered results. If these thresholds are plotted as a function of pressure and linearly extrapolated to a zero-pressure value, a BDE of 2.52 ± 0.06 eV is obtained for the $Ca^{2+}(H_2O)$ complex, within experimental error of the less precise 2.68 ± 0.32 eV value. Additionally, if the competition between the water loss and charge separation pathway is included in the sequential model, both the primary and secondary thresholds are observed to shift to lower energies by ~0.07 eV, which agrees with the 0.10 eV competitive shift determined for zero-pressure extrapolated cross sections of the primary dissociation processes, Table 6.1. Therefore, competition with the charge separation channel does not affect the difference in the primary and secondary reaction thresholds for water loss. An example of the combined competitive/sequential model analysis for a low pressure dissociation of $Ca^{2+}(H_2O)_2$ is shown in Figure 6.5a. The model reproduces the primary water loss from the onset up to 6 eV and the second water loss from the onset to 7 eV. The larger fitting range required to reproduce the onset of the secondary water loss results in a somewhat less robust fit of the onset of the charge separation pathway compared to competitive analysis of the primary dissociation pathways analyzed only up to 4.5 eV, Figure 6.4. Overall, we believe the best value for the BDE of $Ca^{2+}(H_2O)$ is given by the values obtained from threshold extrapolation and fitting, 2.52 ± 0.06 and 2.68 ± 0.32 eV, with the former being our most precise value.

Charge separation channels. $Ca^{2+}(H_2O)_2$ undergoes charge separation to form the $CaOH^+$ and H_3O^+ products, which have lower apparent thresholds than the $Ca^{2+}(H_2O)$ product cross section, Figure 6.1a. This result is consistent with previous observations of Reaction 6.4 at room temperature.[25,26]

$$Ca^{2+}(H_2O) + H_2O \rightarrow CaOH^+ + H_3O^+ \qquad (6.4)$$

Charge separation also takes place from the $Ca^{2+}(H_2O)_3$ complex to form $CaOH^+(H_2O)$ and H_3O^+ products, however, the $CaOH^+(H_2O)$ product cross section has a higher apparent threshold than the $Ca^{2+}(H_2O)_2$ product cross section and is smaller by nearly three orders of magnitude, Figure 6.1b and 6.1c. We have previously defined the critical size (x_c) for a $M^{2+}(H_2O)_x$ system as the complex size at which charge separation becomes the lower energy pathway compared to simple ligand loss.[16] Thus, these observations assign the critical size for hydrated calcium complexes as $x_c = 2$. However, our approximate analysis of the charge separation process for $x = 3$ indicates it has a slightly lower threshold (by 0.05 eV) than water loss. Therefore, a critical size of $x_c = 3$ for the $Ca^{2+}(H_2O)_2$ system cannot be discounted. This latter assignment agrees with that of Shvartsburg and Siu on the basis of the smallest complex they observed to dissociate not solely by simple ligand evaporation.[27]

The theoretical reaction coordinates for charge separation from $Ca^{2+}(H_2O)_2$ and $Ca^{2+}(H_2O)_3$ are calculated at the B3LYP/6-311+G(d,p) level of theory and are shown in Figure 6.6 for B3LYP/6-311+G(2d,2p) single point energies. The charge separation process involves transferring a water molecule from the inner solvent shell through TS1 to the second solvent shell, where it binds through a single hydrogen bond forming the (x-1,1) intermediate (INT). As the products separate, a proton is transferred to the second

solvent shell water molecule, thereby allowing formation of two singly charged ions that separate from one another over a large Coulombic barrier at TS[x-2+1].[15] Table 6.3 provides relative energies for the TSs, intermediates, and products of the charge separation and water loss pathways for the $Ca^{2+}(H_2O)_2$ and $Ca^{2+}(H_2O)_3$ ground state structures calculated at the B3LYP, B3P86, and MP2(full) levels with a 6-311+G(2d,2p) basis set. For $Ca^{2+}(H_2O)_2$, all levels of theory predict charge separation over TS[0+1] is favored over water loss by 32 – 65 kJ/mol, which agrees nicely with the measured difference of 57 ± 11 kJ/mol (0.59 ± 0.11 eV), Table 6.1. For $Ca^{2+}(H_2O)_3$, charge separation over TS[1+1] is slightly favored by B3LYP and B3P86 results by 5 – 7 kJ/mol, whereas MP2(full) calculations indicate that water loss is the favored pathway by 17 kJ/mol. The former results agree with the approximate analysis yielding an experimental difference of 5 ± 12 kJ/mol. For charge separation from $Ca^{2+}(H_2O)_2$, the $CaOH^+$ and H_3O^+ products are more stable than the dihydrated complex by 24 – 64 kJ/mol at all levels of theory. MP2(full) calculations predict the trihydrate lies 29 kJ/mol below the $CaOH^+(H_2O)$ and H_3O^+ products, whereas B3LYP and B3P86 (DFT) energies predict the $Ca^{2+}(H_2O)_3$ complex and its charge separated products are more comparable in energy, the latter being preferred by 1 – 5 kJ/mol.

On the basis of our thermodynamic criterion for defining the critical size, DFT calculations of the charge separation dissociation pathway from the $Ca^{2+}(H_2O)_3$ complex suggest a critical size of $x_c = 3$, whereas MP2(full) calculations predict the critical size is $x_c = 2$. The latter results agree with the $x_c = 2$ based on the inability to see the $Ca^{2+}(H_2O)$ complex from the in-source fragmentation procedure, Chapter 5. Because of the very small magnitude of the $CaOH^+(H_2O)$ cross section, no definitive threshold information is

obtained although our rough analysis agrees better with the density functional theory (DFT) predictions. Certainly, the mere observation of the entropically disfavored $CaOH^+(H_2O)$ product ion indicates that the threshold for Reaction 6.3 must be close to that for Reaction 6.1. The relative magnitudes of product cross sections for water loss and the charge separation product ions from the $Ca^{2+}(H_2O)_3$ complex, Figure 6.1b, are consistent with our ability to generate the $Ca^{2+}(H_2O)_2$ complex in the ESI source by fragmenting the $Ca^{2+}(H_2O)_3$ complex.

Conversion of 0 K hydration energies to 298 K. To convert the 0 K hydration energies to enthalpies and free energies at 298 K, H_{298} - H_0 and $T\Delta S_{298}$ values are calculated with a rigid rotor/harmonic oscillator approximation using the rotational constants and vibrational frequencies calculated at the B3LYP/6-311+G(d,p) level of theory.[7] The uncertainties in these values are determined by scaling the vibrational frequencies up and down by 10%. These conversion factors are used to calculate ΔH_{298} and ΔG_{298} values for primary and secondary BDEs in Table 6.4, which are compared below to previous theoretical calculations and experimental results. It should be realized that some of the low-lying vibrational frequencies correspond to torsional motions of the water ligands (hindered rotations) such that their treatment as harmonic oscillators may not be completely accurate.

Literature calculations. A rigorous theoretical analysis of ground state and low-lying structures for $Ca^{2+}(H_2O)_x$ complexes, x = 1 – 9, was presented in Chapter 4.[7] B3LYP/6-311+G(2d,2p)//B3LYP/6-311+G(d,p) [B3LYP//B3LYP] binding enthalpies were considered representative of all theoretical calculation because they agreed best with the experimental results for the x = 5 – 9 primary BDEs.[7] These values are listed in

Table 6.5 for x = 1 – 6. The B3LYP/pVTZ (Ca-G) energies agreed quite nicely with B3LYP//B3LYP results, except for x = 1 and 2, which were higher by 5 and 3 kJ/mol for the split-level basis set treatment (former). Additional split-lvel basis set calculations with the calcium atom described with the correlation consistent cc-pVTZ, cc-pCVTZ, and cc-pwCVTZ basis sets are also considered in the present chapter. These new split basis sets are denoted as pVTZ, pCVTZ, and pwCVTZ, respectively. Only the pCVTZ results are included in Table 6.5 for x = 1 – 6 for split-level basis set treatment. DFT (B3LYP and B3P86) with the pVTZ and pwCVTZ basis sets differ less than 1 kJ/mol compared to the analogous DFT/pCVTZ enthalpies. MP2(full)/pVTZ and MP2(full)/pwCVTZ binding enthalpies are 0 to 3 kJ/mol smaller and 0 to 2 kJ/mol larger than the corresponding MP2(full)/pCVTZ enthalpies for x = 1 – 6, respectively. Minimal differences (< 2 kJ/mol) were found between B3LYP/6-311+G(2d,2p), B3LYP/pVTZ (Ca-G), and B3LYP/pCVTZ binding enthalpies for x = 3 – 9, however, larger differences, up to 6 and 4 kJ/mol, were found for x = 1 and 2, respectively. In addition to B3LYP/pCVTZ energies, B3P86/pCVTZ, MP2(full)/pCVTZ, and BH&HLYP/pCVTZ results are also included in Table 6.5. These three levels of theory have MADs (with respect to B3LYP/pCVTZ binding enthalpies) of 1 ± 1, 5 ± 3, and 4 ± 2 kJ/mol for x = 1 – 9. Even though B3LYP/6-311+G(2d,2p)//B3LYP/6-311+G(d,p) binding enthalpies were considered as our representative calculations for comparison to experimental results presented in Chapter 4, adding core correlation may be important for the x = 1 and 2 complexes.

Theoretical calculations by Rao et al. have also determined sequential BDEs of $Ca^{2+}(H_2O)_x$ complexes, where x = 1 – 6.[14] Geometry optimizations and frequency

calculations were first performed at the B3LYP/6-31G(d) level of theory to locate minimum energy conformations. These lowest energy conformations were subjected to further optimizations at the B3LYP/6-311++G(d,p) level of theory followed by single point energies calculated the B3LYP/6-311++G(3d,3p), MP2(full)/6-311++G(3d,3p), and CCSD(T)/6-311++G(d,p) levels of theory. G3 calculations were also reported in this study. Oddly, although all these BDEs were corrected for BSSE, these authors did not include either ZPE or thermal corrections. As a result, additional geometry and frequency calculations (scaled by 0.989) were performed at the B3LYP/6-311++G(d,p) level of theory and adjusted their BDEs to 298 K to allow for comparison to our theoretical calculations.

The reaction pathway for the charge separation process from $Ca^{2+}(H_2O)_2$ has been calculated previously by Beyer et al.[15] In this work, calcium ions were treated with the Stuttgart/Dresden relativistic effective core potential for all calculations. Oxygen and hydrogen atoms utilized the 6-311G(d,p) for geometry optimizations and frequency calculations and the 6-311+G(3df,2pd) basis set for single point energies. Zero-point energy corrections were calculated from vibrational frequencies scaled by 0.90.

Discussion

In the following discussion, we generally focus on a comparison of experimental and theoretical results for the inner shell hydration enthalpies of the calcium dication. This is because the present values for x = 1 – 4 are the first experimental values and the result for x = 6 has been revised from the work presented in Chapter 4. In contrast, values obtained with the newer ESI source design remain essentially the same as the

results for x = 7 – 9 presented in Chapter 4, where such a detailed comparison has already been made.[7]

Comparison between present and literature experimental values. The binding enthalpies for $Ca^{2+}(H_2O)_x$ complexes have previously been reported for x = 6 – 14, x = 5 – 10, and x = 5 – 9 using equilibrium,[3,4] kinetic,[5,6] and TCID measurements,[7] respectively. Results from the two former experimental techniques are included in Table 6.5 and Figure 6.7 along with present experimental primary and secondary binding enthalpies. For x = 5, our primary bond enthalpy is comparable to the BIRD result. Our primary binding enthalpy for x = 6 falls in between the BIRD and HPMS results. Our second solvent shell BDEs (x = 7 – 9) are on the low end compared to the results from the other two experimental studies with nearly constant values of 61 – 63 kJ/mol. The binding enthalpies from HPMS decrease by ~4 kJ/mol with each additional water molecule added whereas BIRD results are virtually identical for x = 7 and 8 with an 8 kJ/mol drop to x = 9. All three experimental studies yield x = 9 binding enthalpies in good agreement with one another. We observe a relatively large decrease in binding enthalpies between x = 6 and 7 of 37 [36] kJ/mol from primary [secondary] modeling. Our difference is nearly identical to the difference determined by HPMS at 35 kJ/mol and twice that from BIRD (18 kJ/mol) experiments.

Comparison between present primary and secondary experimental values. The secondary binding enthalpies are consistently larger than the corresponding primary BDEs for x = 2 – 6, with a MAD of 12 ± 10 kJ/mol, decreasing to 7 ± 2 kJ/mol if x = 2 is excluded. Primary and secondary binding enthalpies agree within experimental uncertainty for x = 3 – 7 and deviate substantially (30 kJ/mol) for x = 2. Similarly large

differences between the primary and secondary binding enthalpies have been observed in previous studies of $Zn^{2+}(H_2O)_x$ and $Cd^{2+}(H_2O)_x$, where values for x = 9 (Zn^{2+}) and 10 (Cd^{2+}) differed by 17 and 15 kJ/mol, respectively.[20,23] For Cd^{2+}, the average deviation for x = 4 – 10 was 8 ± 5 kJ/mol, comparable to the differences observed here. Overall, the primary BDEs are believed to be inherently more reliable than the secondary BDEs because the kinetic and internal energy distributions of the reactants are well known, whereas a statistical model is needed to provide this information in the analysis for the secondary dissociation processes. Conservatively, the secondary bond enthalpies represent upper limits for the binding enthalpies for x = 1 – 7, but the threshold extrapolated secondary value for x = 1 appears to provide a useful determination of this BDE.

Comparison between present experimental and theoretical values for x = 1 – 6. The primary and secondary bond enthalpies are compared with B3LYP/6-311+G(2d,2p) [B3LYP/pCVTZ] energies in Table 6.5 and Figure 6.7. For the inner shell complexes, x = 2 – 6, the agreement between the primary binding enthalpies and the calculated BDEs is excellent with a MAD of 2 ± 2 [3 ± 2] kJ/mol. Primary bond enthalpies for x = 7 – 9 are lower than calculated energies by 11 – 16 kJ/mol and increase the MAD to 6 ± 6 [7 ± 6] kJ/mol when they are taken into account. The MAD of the secondary BDEs with respect to B3LYP/6-311+G(2d,2p) [B3LYP/pCVTZ] results for x = 1 – 6 is larger, 11 ± 11 [9 ± 10] kJ/mol, but decreases to 7 ± 4 [5 ± 2] kJ/mol if the secondary BDE for x = 2 is excluded from the MAD comparison. These deviations are 9 [6] kJ/mol larger than those calculated for the primary binding enthalpies. The secondary BDEs for x = 1 and 2, which include the competition with charge separation in the

analysis, are 12 and 32 [5 and 28] kJ/mol higher than their respective B3LYP/6-311+G(2d,2p) [B3LYP/pCVTZ] energies. The final secondary BDE for x = 1, 247 ± 6 kJ/mol, was obtained from extrapolation of threshold data from individual pressures, rather than extrapolation of pressures to zero pressure and subsequent analysis. This value is in good agreement with theoretical calculations that include core polarization on the calcium ion, 241 – 243 kJ/mol, except for the MP2(full)/pCVTZ value of 230 kJ/mol. Because of the very strong binding of the first two water ligands, Pauli repulsion between the core electrons on Ca^{2+} and the water ligands likely occurs. By including core polarization functions, the core electrons are permitted to polarize away from the ligands, thereby allowing shorter bonds and higher binding water molecules. This is also illustrated by the Ca-O bond lengths, which are shorter at the B3LYP/pCVTZ level compared to those at the calculated at the B3LYP/6-311+G(d,p) level, with differences between the two methods increasing from 0.013 Å for x = 4 to 0.025 Å for x = 1. Overall, the various levels of theory considered here provide comparable agreement with the inner shell hydration enthalpies, although the MP2(full) and BH&HLYP approaches consistently overbind by about 6 kJ/mol. B3LYP with a triple-zeta basis set provides good agreement, with the addition of core polarization yielding better agreement for the $Ca^{2+}(H_2O)$ complex.

Comparison of theoretical results from the literature. The theoretical binding enthalpies for x = 1 – 6 calculated by Rao et al.[14] using G3 theory and the CCSD(T)/6-311++G(d,p)//B3LYP/6-311++G(d,p) level of theory are included in Table 6.5. Their B3LYP/6-311++G(3d,3p)//B3LYP/6-311++(d,p) and MP2(full)/6-311++G(3d,3p)// B3LYP/6-311++(d,p) energies are essentially identical to calculations at similar levels of

theory in Chapter 4, and are excluded from Table 6.5. The geometries determined by Rao et al. were found to be identical to the geometries in Chapter 4, except for the $Ca^{2+}(H_2O)_2$ and $Ca^{2+}(H_2O)_6$ structures. For $Ca^{2+}(H_2O)_2$, the lowest energy conformation calculated at the B3LYP/6-31G(d) level of theory[14] is a linear structure having D_{2d} symmetry, however geometry optimizations employing 6-311++G(d,p) or 6-311+G(d,p)[7] basis sets find the lowest energy structure is a bent geometry with C_2 symmetry. Frequency calculations using these larger basis sets determine the D_{2d} structure has two imaginary frequencies. As such, the C_2 structure is 1.8 kJ/mol lower in energy than the D_{2d} structure when calculated at the B3LYP/6-311++G(d,p) level of theory (including ZPE). For $Ca^{2+}(H_2O)_6$, we've determined the lowest energy structure has a highly symmetric T_h geometry that maximizes inner shell hydrogen bonding such that hydrogen atoms of all water molecules are directed towards oxygen atoms on adjacent water molecules. The $Ca^{2+}(H_2O)_6$ structure optimized by Rao et al. has D_3 symmetry that allows hydrogen-hydrogen repulsions. At the B3LYP/6-311++G(d,p) level, the T_h structure is 9.8 kJ/mol lower in energy (0 K) than the D_3 structure. These structural differences lead to changes in the BDEs reported by Rao et al. compared to our B3LYP/6-311+G(2d,2p) energies. Once the differences in the BDEs for x = 2, 3, and 6 are reconciled, the only noticeable difference between our results and those of Rao et al. is that the BDE for the $Ca^{2+}(H_2O)$ and $Ca^{2+}(H_2O)_2$ complexes are larger by 3 and 2 kJ/mol, respectively, for the B3LYP/6-311++G(3d,3p) level of theory. Overall, these comparisons reinforce that the B3LYP/6-311+G(2d,2p)//B3LYP/6-311+G(d,p) level of theory is sufficient for calculating inner shell BDEs, although for the smallest complexes (x = 1 and 2), core correlation and larger basis sets cumulatively increase the calculated

bond energies by 6 and 3 kJ/mol, respectively. Theoretical binding enthalpies calculated with G3 theory are 7 – 12 kJ/mol larger than the CCSD(T)/6-311++G(d,p)//B3LYP/6-311++G(d,p) level of theory. Compared to the B3LYP/6-311+G(2d,2p) [B3LYP/pCVTZ] hydration enthalpies, G3 and CCSD(T) energies have MADs of 10 ± 7 [10 ± 7] and 7 ± 6 [9 ± 9] kJ/mol, respectively. Compared to our primary experimental binding enthalpies, the MADs for CCSD(T) and G3, 6 ± 3 and 11 ± 8 kJ/mol, respectively, are higher than those for most of the approaches used here. Both G3 and CCSD(T) approaches overbind for the larger complexes, x = 4 – 6, and underbind for x = 1, with good agreement at x = 2 for G3 theory and at x = 3 for CCSD(T).

Comparison of values for charge separation. The thermodynamic onset associated with the rate limiting transition state, TS[0+1] for charge separation was determined by modeling the average charge separation product cross sections in competition with water loss from the $Ca^{2+}(H_2O)_2$ complex. This analysis resulted in a primary 0 K threshold for water loss of 197 ± 17 kJ/mol whereas the onset for charge separation is 140 ± 14 kJ/mol, Table 6.3. The latter value is within experimental uncertainty of the 0 K B3LYP and B3P86 energies, respectively, but ~20 kJ/mol below the 0 K MP2(full) energy, Table 6.3. Beyer et al. calculated a comparable value for the TS[0+1] of 139 kJ/mol above the ground state $Ca^{2+}(H_2O)_2$ complex using B3LYP with a similar basis set. The relative difference between 0 K experimental thresholds for water loss and charge separation is 57 kJ/mol, which is consistent with calculated differences at the B3LYP (62 kJ/mol) and B3P86 (65 kJ/mol) levels of theory. For the $Ca^{2+}(H_2O)_3$ complex, we get an approximate threshold for TS[1+1] of 165 ± 15 kJ/mol, which agrees well with the DFT results, Table 6.3, but is 24 kJ/mol below the MP2(full) result.

Conclusions

The kinetic energy dependent cross sections for $Ca^{2+}(H_2O)_x$ where x = 2 – 8 are measured by threshold collision-induced dissociation using a guided ion beam mass spectrometer equipped with a second generation electrospray ionization source. The ESI source produces an initial distribution of $Ca^{2+}(H_2O)_x$ ions, where x = 6 – 9, having suitable ion intensities for TCID studies. Smaller $Ca^{2+}(H_2O)_x$ complexes, where x = 2 – 5, are accessed using an in-source fragmentation technique that takes place in the high pressure region of the rf-only hexapole ion guide.[16] The $Ca^{2+}(H_2O)$ complex cannot be produced in this manner because the charge separation process that forms $CaOH^+$ and H_3O^+ ions is a lower energy process compared to water loss from $Ca^{2+}(H_2O)_2$. Experimental results confirm this observation and demonstrate that the critical size complex is likely $x_c = 2$ for the $Ca^{2+}(H_2O)_x$ system, although $x_c = 3$ cannot be unequivocally discounted.

The dominant process taking place for all $Ca^{2+}(H_2O)_x$ complexes is the loss of a single water molecule. Charge separation processes are observed once the $Ca^{2+}(H_2O)_3$ and $Ca^{2+}(H_2O)_2$ complexes are reached. For $Ca^{2+}(H_2O)_3$, the magnitude of the product cross section for charge separation is over three orders of magnitude smaller than the $Ca^{2+}(H_2O)_2$ product cross section. Theoretical calculations indicate these processes are energetically similar, but charge separation is entropically disfavored, which explains why the $Ca^{2+}(H_2O)_2$ complex can be generated with the in-source fragmentation technique. Theoretical calculations of the charge separation process from $Ca^{2+}(H_2O)_2$ indicate that charge separation is energetically favored over water loss, which is consistent with the relative apparent thresholds of the charge separated products with

respect to water loss in the CID of $Ca^{2+}(H_2O)_2$. These cross sections only differ an order of magnitude, with the entropically favored water loss channel dominating again.

In an attempt to determine the hydration energies for the complete inner shell of the $Ca^{2+}(H_2O)_x$ system, secondary binding enthalpies for $Ca^{2+}(H_2O)_x$ complexes, where x = 1 – 7, were determined by analyzing the primary and secondary water losses in the CID of x = 2 – 8 using the sequential model. These secondary results are consistently larger than corresponding primary results for all x, suggesting they are most conservatively regarded as upper limits. As the BDE for x = 1 is available only from analysis of the secondary dissociation, an alternative method to determining this value was also pursued. This approach yields a lower experimental value, in reasonable agreement with theory.

The present TCID work determines the first experimental hydration energies for $Ca^{2+}(H_2O)$ to $Ca^{2+}(H_2O)_4$. The experimental hydration energies for $Ca^{2+}(H_2O)_5$ to $Ca^{2+}(H_2O)_8$ are in good agreement with available thermochemistry from HPMS[3,4] and BIRD[5,6] studies. Experimental hydration energies for the inner shell complexes, where x = 1 – 6, are in particularly good agreement with theoretical bond enthalpies calculated at the B3LYP/6-311+G(2d,2p)//B3LYP/6-311+G(d,p) and B3LYP/pCVTZ levels of theory.[7] The best agreement between theory and experiment for the smallest complexes, x = 1 and 2, is obtained when core-core and core-polarization is included in the basis set, a consequence of the very tight binding found in these complexes. The agreement between theoretical and experimental binding enthalpies provides further evidence that TCID studies provide accurate thermodynamic information for multiply-charged ions and that the in-source fragmentation technique produces thermalized $Ca^{2+}(H_2O)_x$ ions at 300 K. Additionally, the thermodynamic onsets of the rate limiting TSs for charge separation

from $Ca^{2+}(H_2O)_2$ and $Ca^{2+}(H_2O)_3$ have been measured experimentally for the first time and are comparable to B3LYP/ and B3P86/6-311+G(2d,2p)//B3LYP/6-311+G(d,p) single point energies and the comparable theoretical value from Beyer et al. for x = 2.[15]

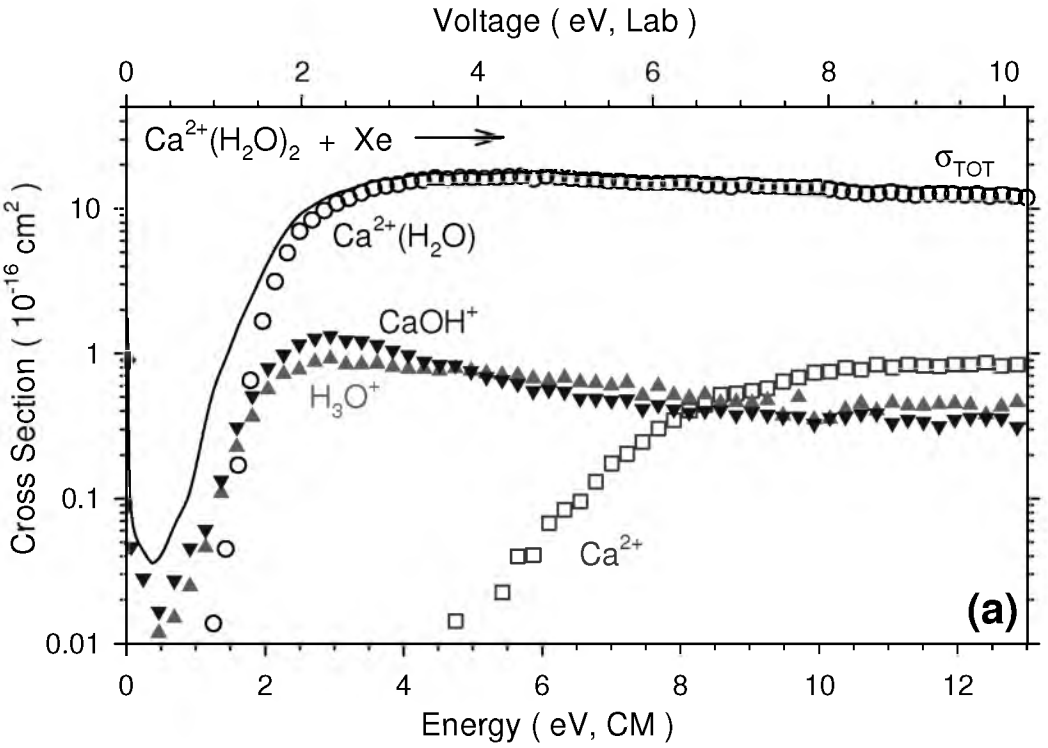

Figure 6.1. Cross sections for collision-induced dissociation of $Ca^{2+}(H_2O)_x$, where x = 2 – 4 (a – c, respectively) with Xenon (~0.2 mTorr) as a function of kinetic energy in the center-of-mass frame (lower x-axis) and applied voltage in the laboratory frame (top x-axis). Dotted circles (b and c) indicate data taken using a lower in-source fragmentation voltage designed for accurate thermochemical determinations.

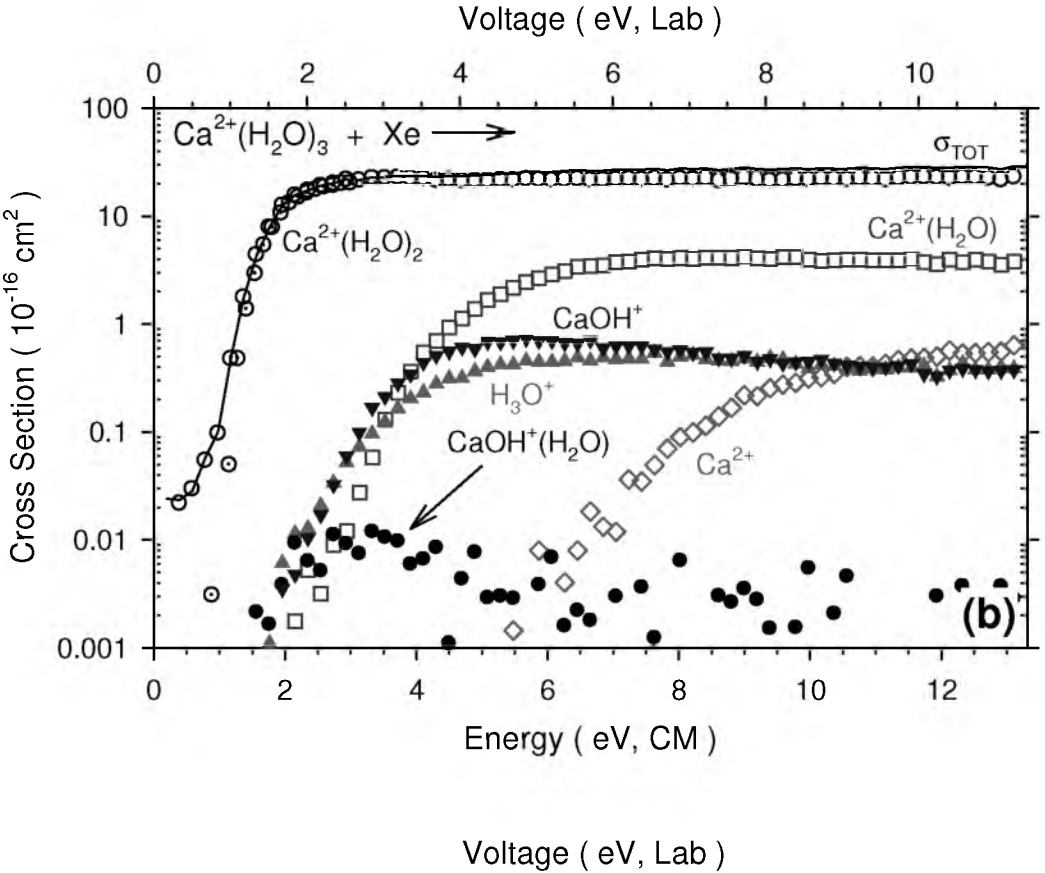
Voltage (eV, Lab)
0
2
4
6
8
10
100
10
1
0.1
0.01
0.001
Cross Section (10^{-16} cm^2)
$Ca^{2+}(H_2O)_3$ + Xe
σ_{TOT}
$Ca^{2+}(H_2O)_2$
$Ca^{2+}(H_2O)$
$CaOH^+$
H_3O^+
$CaOH^+(H_2O)$
Ca^{2+}
(b)
0
2
4
6
8
10
12
Energy (eV, CM)
Voltage (eV, Lab)

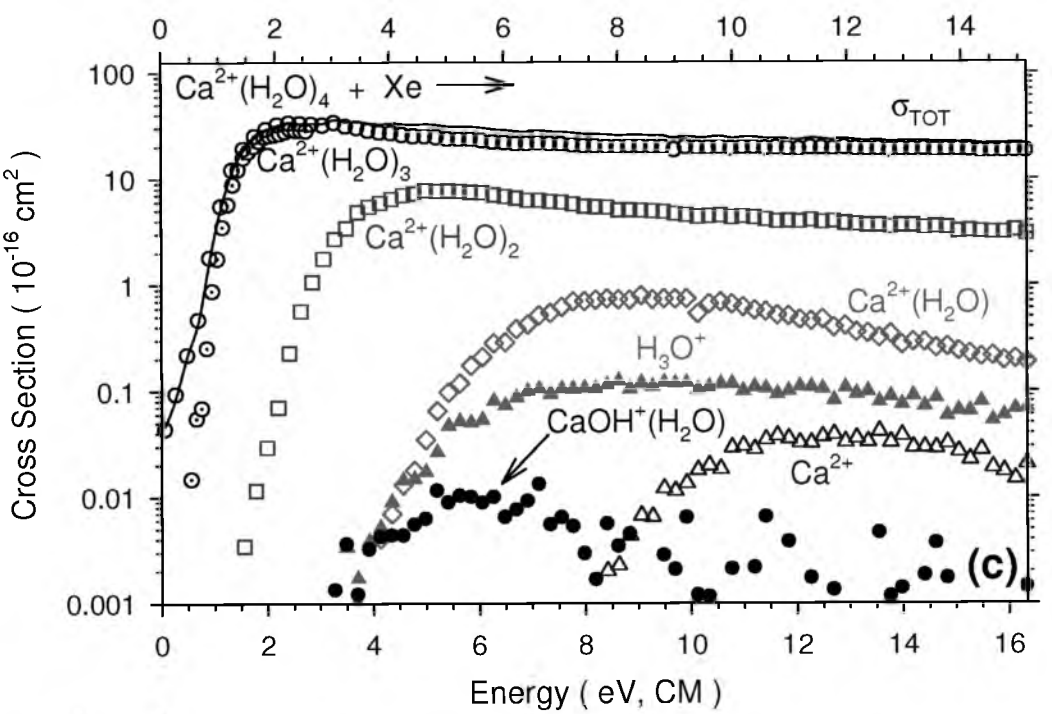

Figure 6.1. continued

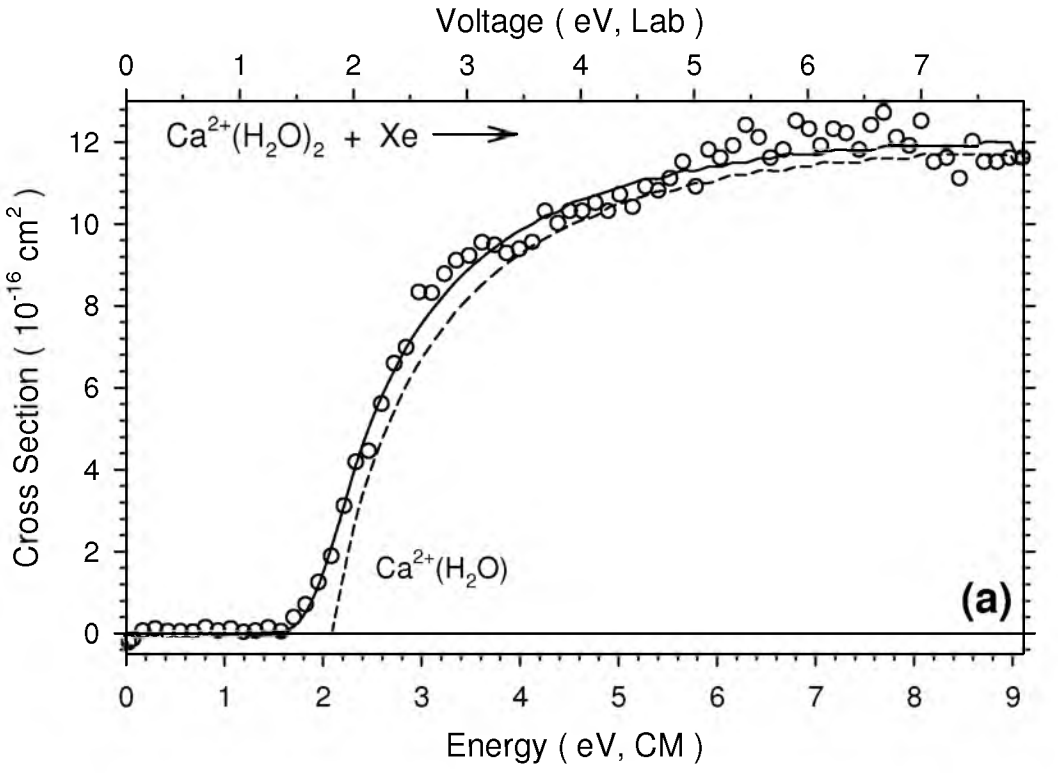

Figure 6.2. Analysis of the zero-pressure extrapolated product cross sections for the primary water loss from the collision-induced dissociation of $Ca^{2+}(H_2O)_x$, where x = 2 – 4 with xenon as a function of kinetic energy in the center-of-mass frame (lower x-axis) and applied laboratory frame voltage (upper x-axis). The solid lines show the best fit to the data modeled with equation 2.5 convoluted over the neutral and ion kinetic and internal energy distributions. The dashed lines show the model cross sections in the absence of experimental kinetic energy broadening for reactions with an internal energy of 0 K.

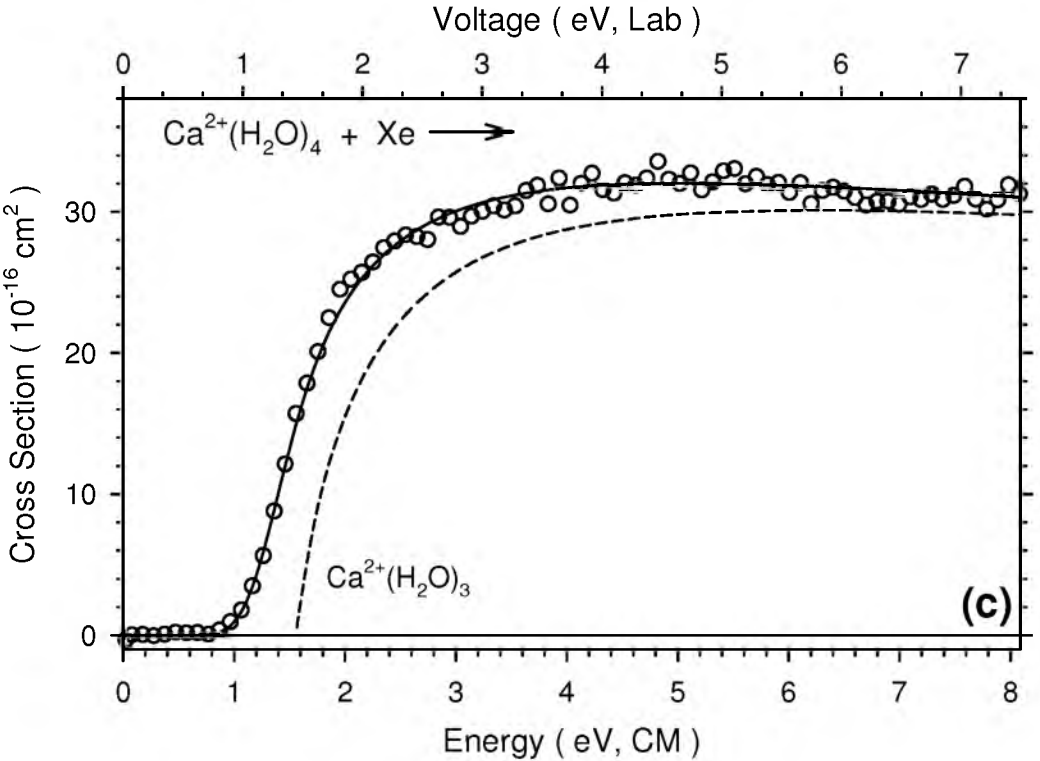

Figure 6.2. continued

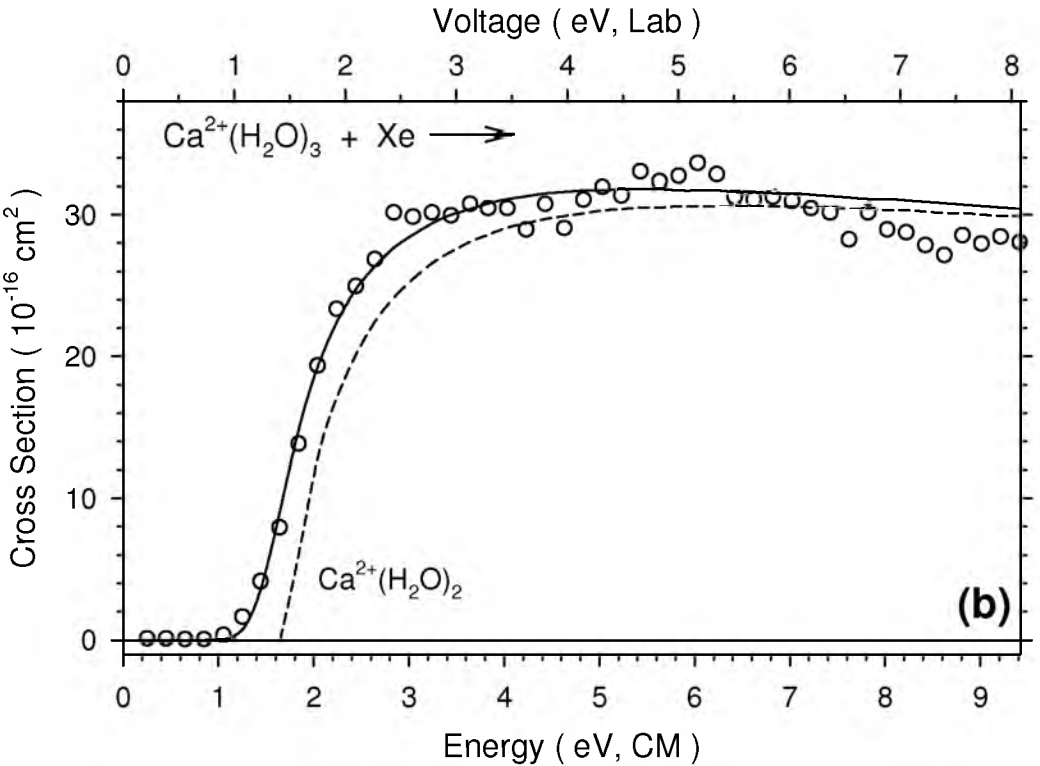
Voltage (eV, Lab)
0
1
2
3
4
5
6
7
8
$Ca^{2+}(H_2O)_3$ + Xe
Cross Section (10^{-16} cm^2)
30
20
10
0
$Ca^{2+}(H_2O)_2$
(b)
0
1
2
3
4
5
6
7
8
9
Energy (eV, CM)

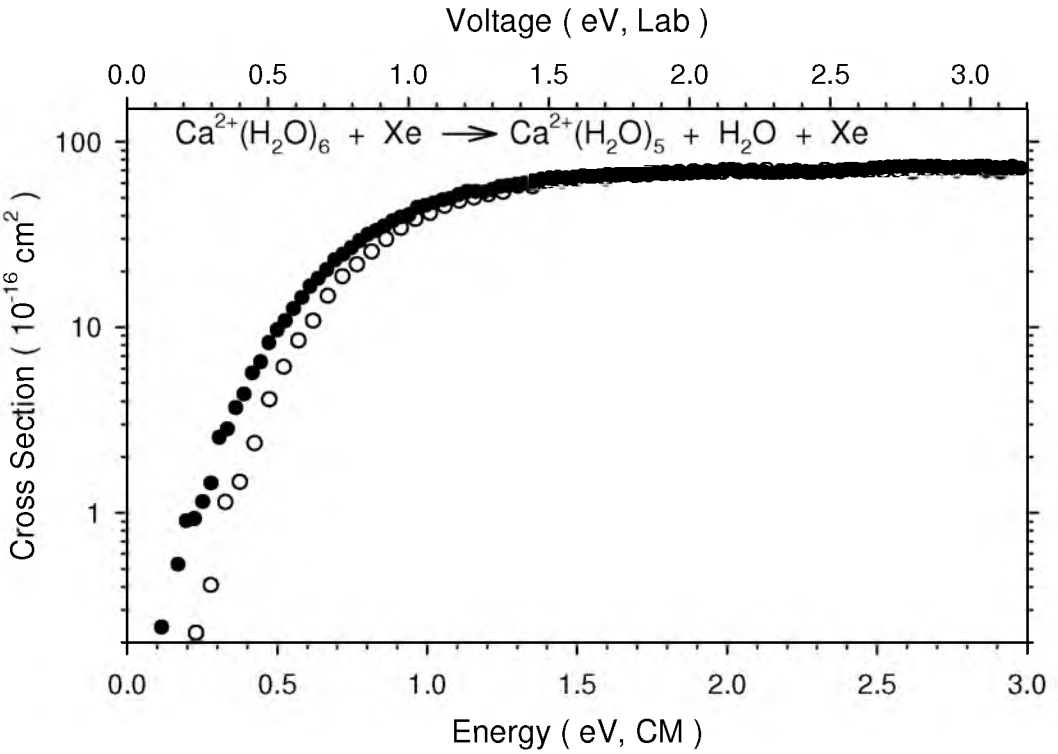

Figure 6.3. Comparison of the total cross sections for collision-induced dissociation of $Ca^{2+}(H_2O)_6$ with Xenon for ions generated with the 1st generation ESI source design used for Chapter 4 studies (solid symbols) and the 2nd generation ESI source desgin utilized in the current chapter (open symbols).

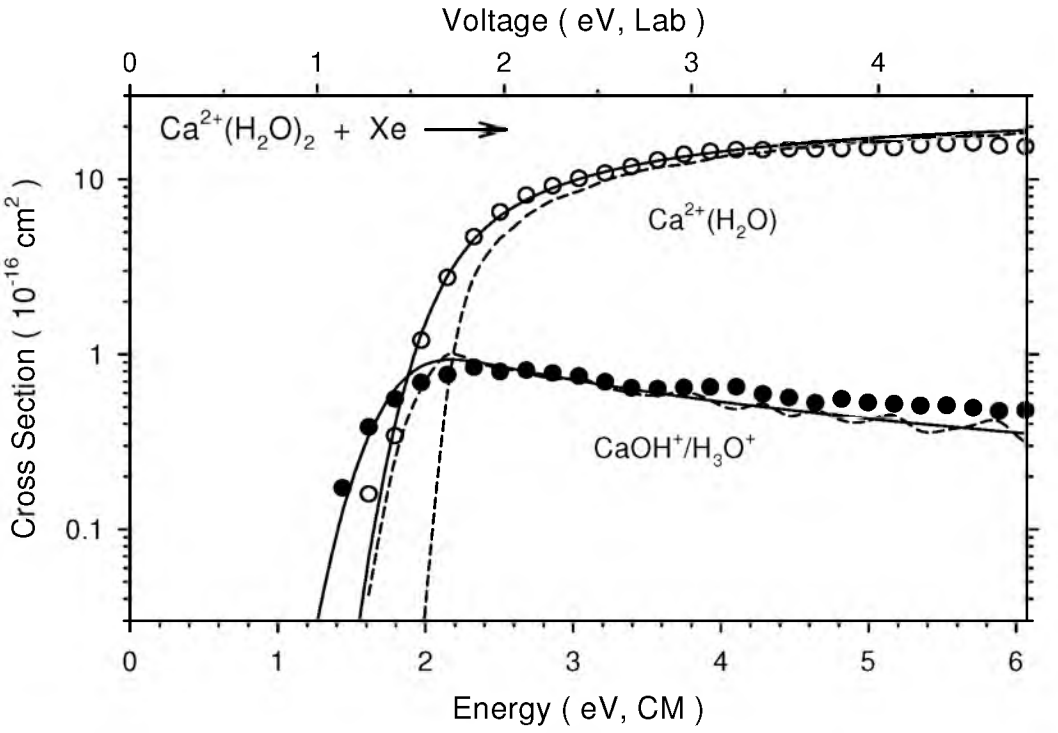

Figure 6.4. Competitive analysis of the zero-pressure cross sections for primary water loss (open circles) and charge separation pathway (closed circles) for the collision-induced dissociation of $Ca^{2+}(H_2O)_2$ with Xenon as a function of kinetic energy in the center-of-mass frame (lower x-axis) and applied laboratory frame voltage (upper x-axis). The solid lines show the best fit to the data using the using the competitive model convoluted over the neutral and ion kinetic and internal energy distributions. The dashed lines show the model cross sections in the absence of experimental kinetic energy broadening for reactions with an internal energy of 0 K.

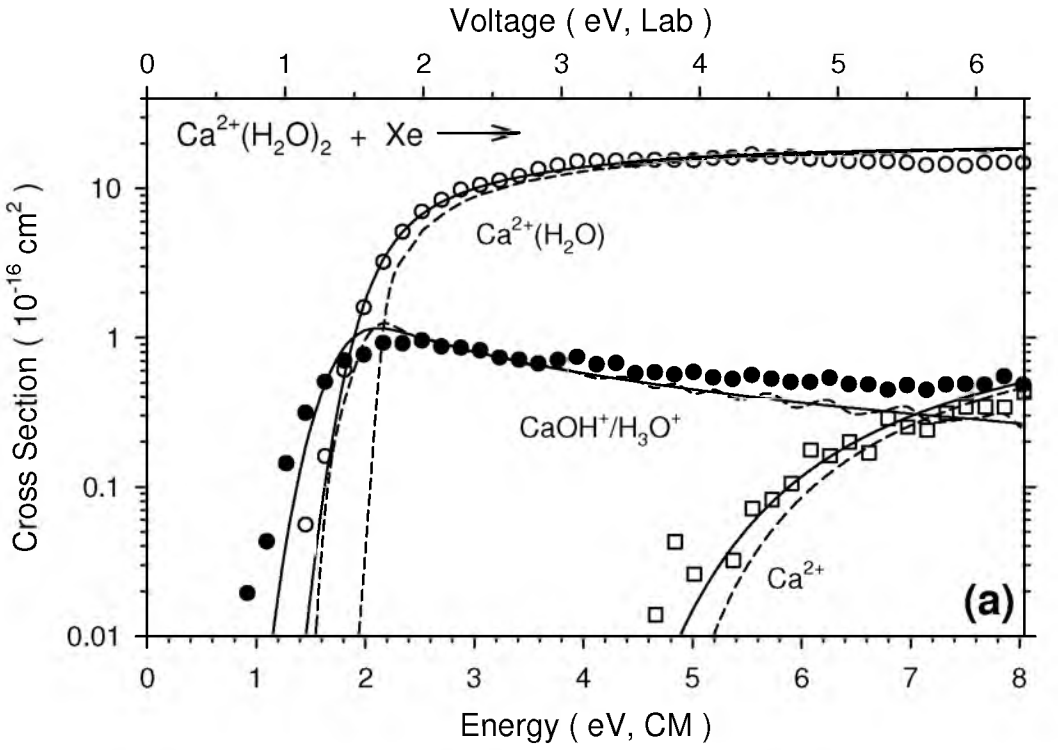

Figure 6.5. Analysis of the low pressure (x = 2) and zero-pressure extrapolated (x = 3 and 4) product cross sections for the primary water loss (open circles), secondary water loss (open squares), and charge separation pathway (closed circles) modeled with a combination of the competitive (where applicable) and sequential models from the collision-induced dissociation of $Ca^{2+}(H_2O)_x$, where x = 2 – 4 (parts a – c, respectively), with Xenon as a function of kinetic energy in the center-of-mass frame (lower x-axis) and applied laboratory frame voltage (upper x-axis). The solid lines show the best fit to the data using the sequential/competitive model convoluted over the neutral and ion kinetic and internal energy distributions. The dashed lines show the model cross sections in the absence of experimental kinetic energy broadening for reactions with an internal energy of 0 K.

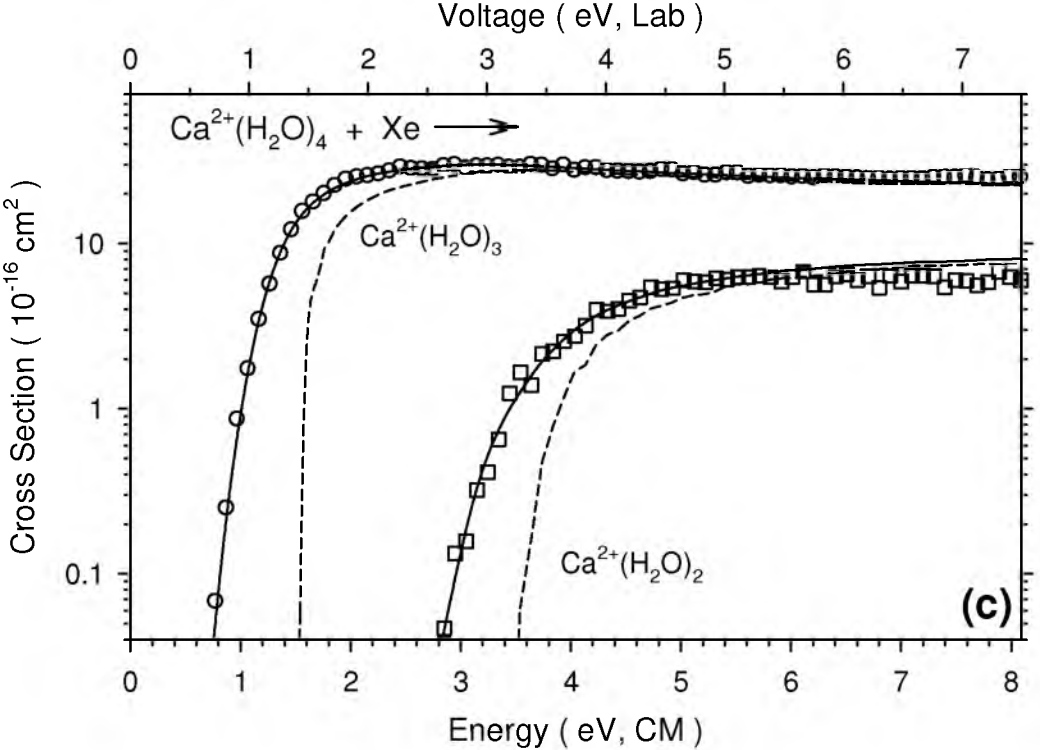

Figure 6.5. continued

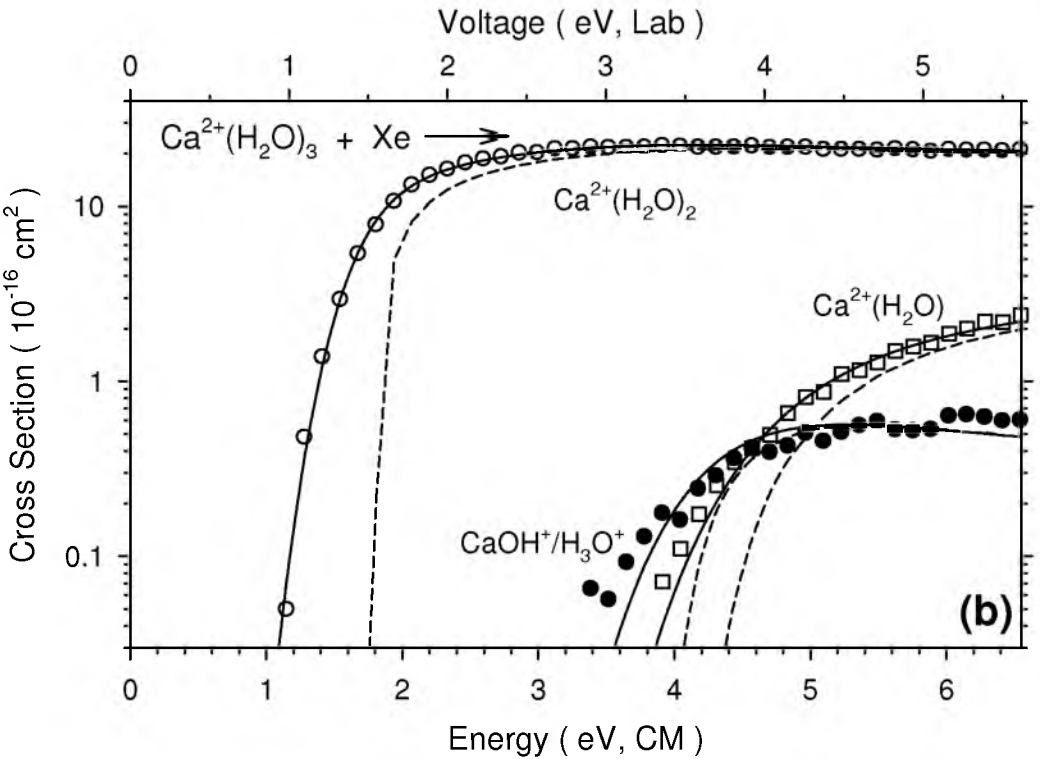
Voltage (eV, Lab)
0
1
2
3
4
5
$Ca^{2+}(H_2O)_3$ + Xe
$Ca^{2+}(H_2O)_2$
$Ca^{2+}(H_2O)$
$CaOH^+/H_3O^+$
(b)
Cross Section (10^{-16} cm^2)
10
1
0.1
0
1
2
3
4
5
6
Energy (eV, CM)

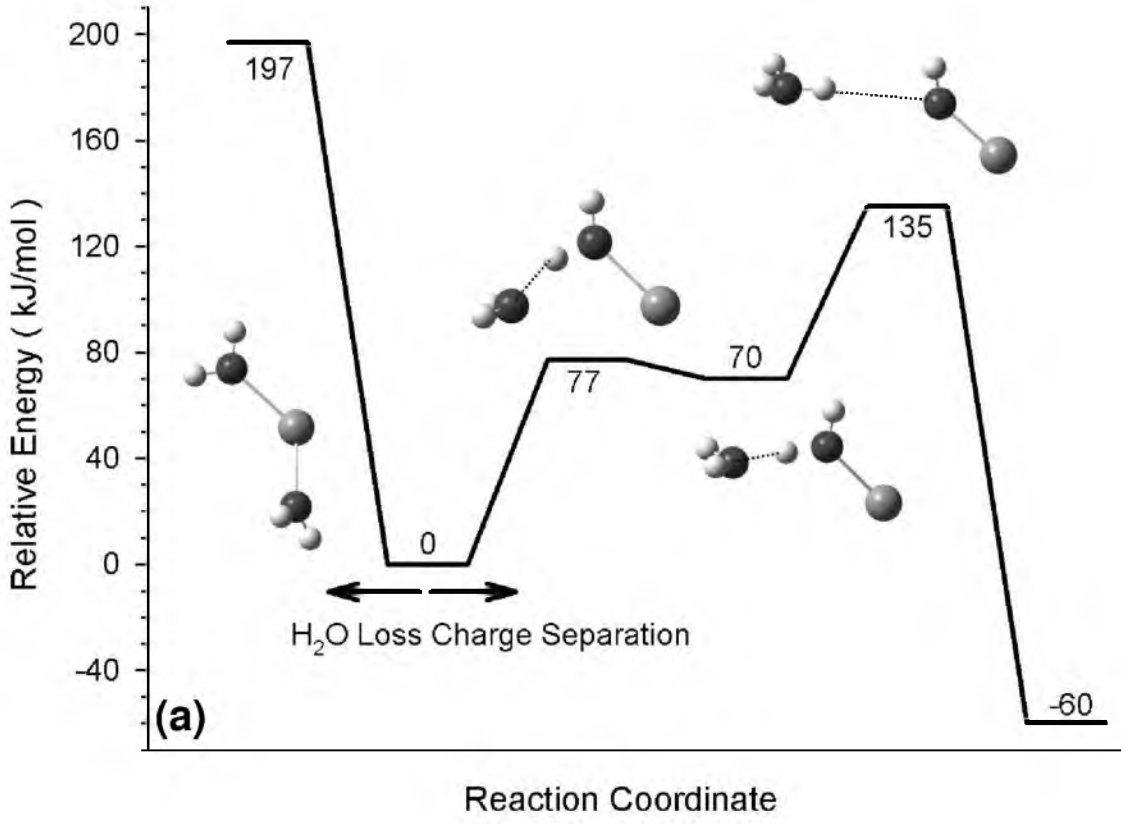

Figure 6.6. Reaction coordinates for water loss and charge separation pathways for $Ca^{2+}(H_2O)_2$ and $Ca^{2+}(H_2O)_3$ calculated at the B3LYP/6-311+G(2d,2p) level of theory (parts a and b, respectively). Relative energies (kJ/mol) include zero-point energy corrections for all stationary structures. Hydrogen bonds shown as dashed lines.

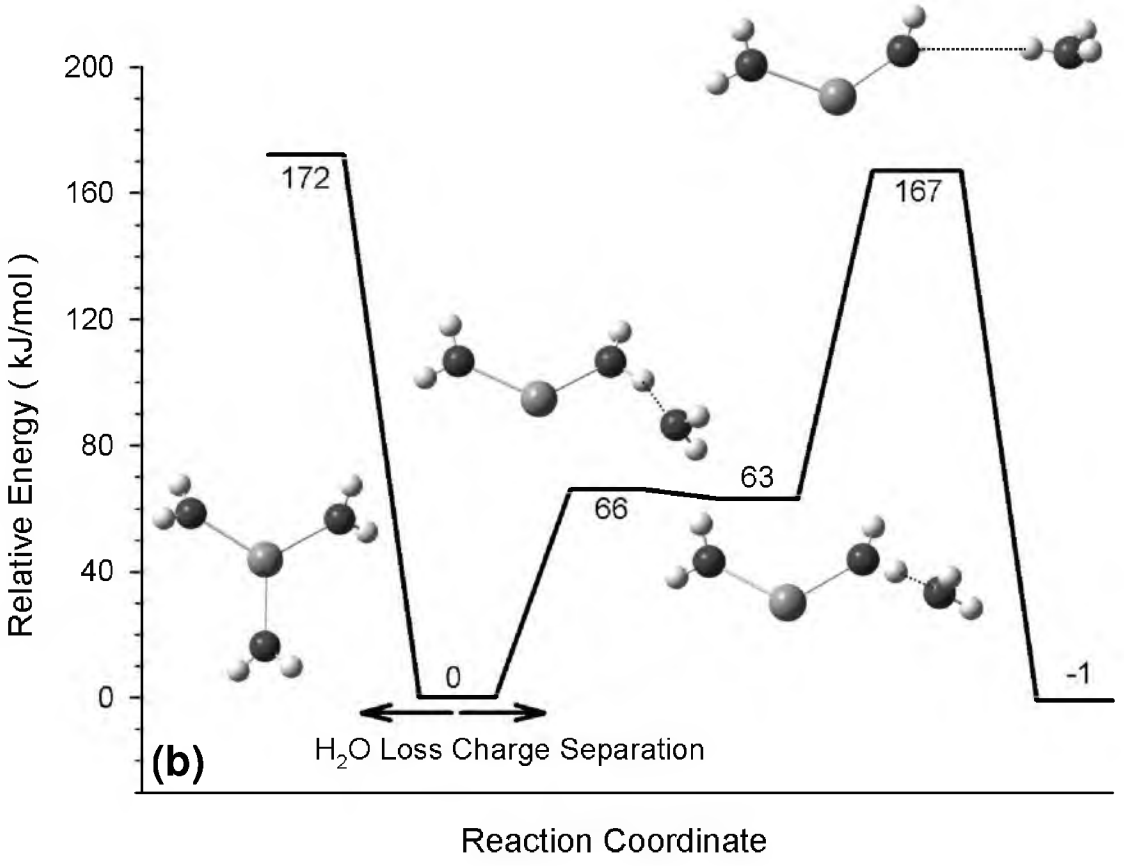

Figure 6.6. continued

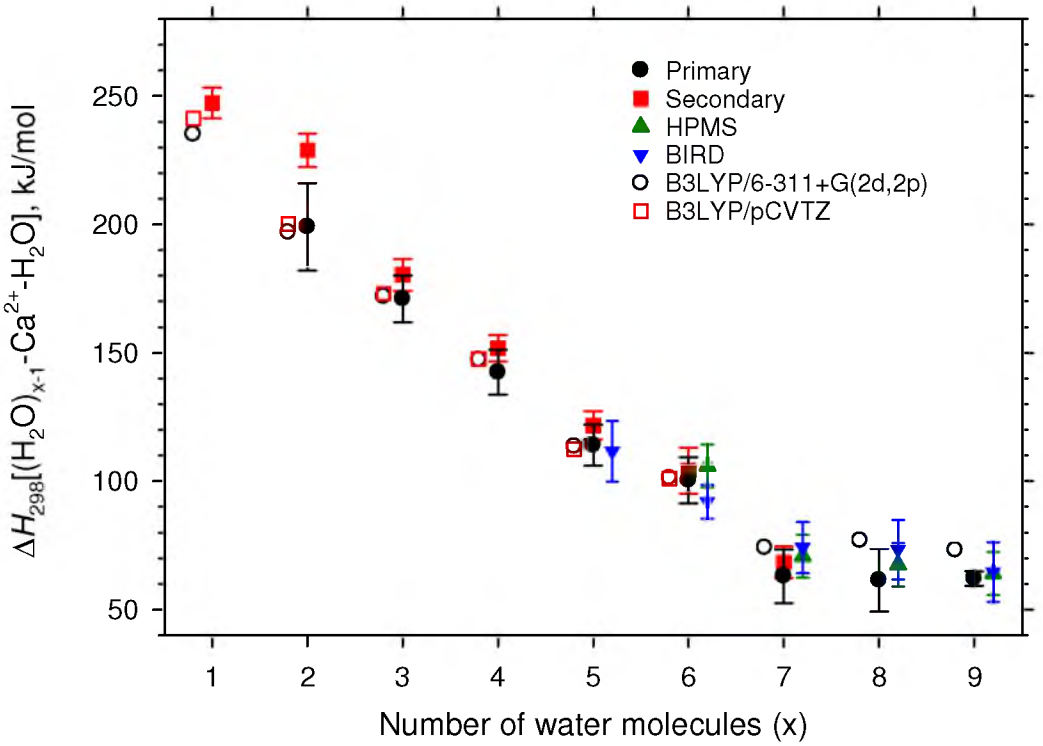

Figure 6.7. Comparison of experimental primary (filled circles) and secondary (filled squares) and theoretical B3LYP/6-311+G(2d,2p)//B3LYP/6-311+G(d,p) (open circles) and B3LYP/pCVTZ (open squares) bond enthalpies in kJ/mol at 298 K. HPMS results from reference 4 (solid green triangles) and BIRD results from references 5 and 6 (solid inverted triangles) are also included.

Table 6.1. Parameters of Equations 2.4 and 2.5 used to model primary dissociation pathways for collision-induced dissociation of $Ca^{2+}(H_2O)_x$, x = 2 – 8[a]

Reactant	Product	σ_0[b]	n[b]	E_0 (eV)[c]	E_0 (PSL) (eV)[b]
$Ca^{2+}(H_2O)_2$	$Ca^{2+}(H_2O)$	28 (13)	0.8 (0.1)	2.16 (0.17)	2.15 (0.18)
$Ca^{2+}(H_2O)_2$	TS[0+1]	2.1 (0.5)	0.4 (0.2)	1.67 (0.16)	1.57 (0.13)
$Ca^{2+}(H_2O)_2$[d]	$Ca^{2+}(H_2O)$	24 (12)	1.0 (0.2)		2.05 (0.18)
	TS[0+1]	6 (13)			1.46 (0.14)
$Ca^{2+}(H_2O)_3$	$Ca^{2+}(H_2O)_2$	45 (10)	0.7 (0.1)	1.81 (0.09)	1.76 (0.09)
$Ca^{2+}(H_2O)_3$[e]	$Ca^{2+}(H_2O)_2$	47 (6)	0.8 (0.2)		1.68 (0.08)
	TS[1+1]	42 (37)			1.63 (0.09)
$Ca^{2+}(H_2O)_4$	$Ca^{2+}(H_2O)_3$	67 (13)	0.8 (0.1)	1.60 (0.09)	1.46 (0.09)
$Ca^{2+}(H_2O)_5$	$Ca^{2+}(H_2O)_4$	90 (25)	0.8 (0.1)	1.31 (0.11)	1.16 (0.08)
					1.17 (0.12)[f]
$Ca^{2+}(H_2O)_6$	$Ca^{2+}(H_2O)_5$	74 (15)	0.8 (0.3)	1.16 (0.11)	1.02 (0.09)
					0.92 (0.10)[f]
$Ca^{2+}(H_2O)_7$	$Ca^{2+}(H_2O)_6$	76 (19)	1.0 (0.2)	0.95 (0.07)	0.62 (0.11)
					0.62 (0.12)[f]
$Ca^{2+}(H_2O)_8$	$Ca^{2+}(H_2O)_7$	81 (22)	0.9 (0.2)	0.97 (0.10)	0.59 (0.13)
					0.61 (0.06)[f]

[a] Uncertainties, in parentheses, are reported to two standard deviations (95% confidence interval).
[b] Parameters from modeling with Equation 2.5, where lifetime effects are taken into account. Values in italics are from Reference 7.
[c] Threshold values from modeling with Equation 2.4, where lifetimes effects are excluded.
[d] Competitive fit. Vibrational frequencies below 800 cm^{-1} for the charge separation pathway transition state are scaled by factor of 10.
[e] Competitive fit of cross sections acquired at high pressure (~0.2 mTorr Xe). Vibrational frequencies below 800 cm^{-1} were scaled by a factor of 1.3.
[f] Results from Chapter 4.

Table 6.2. Parameters for sequential model used to fit primary and secondary water losses simultaneously for collision-induced dissociation of $Ca^{2+}(H_2O)_x$, x = 2 – 8[a]

Reactant	Product	σ_0	n	E_0 (PSL) (eV)[b]	E_0 (PSL) (eV)[c]
$Ca^{2+}(H_2O)_2$	$Ca^{2+}(H_2O)$	28 (14)	0.8 (0.2)	2.16 (0.20)	2.15 (0.18)
	Ca^{2+}	2 (1)		4.83 (0.39)	
				[2.68 (0.32)]	
$Ca^{2+}(H_2O)_3$	$Ca^{2+}(H_2O)_2$	45 (10)	0.7 (0.1)	1.75 (0.09)	1.76 (0.09)
	$Ca^{2+}(H_2O)$	9 (2)		4.15 (0.09)	3.91 (0.20)
				[2.40 (0.08)]	[2.15 (0.18)]
$Ca^{2+}(H_2O)_3$	$Ca^{2+}(H_2O)_2$	45 (10)	0.7 (0.1)	1.74 (0.09)	1.76 (0.09)
	$Ca^{2+}(H_2O)$	9 (2)		4.10 (0.09)	3.81 (0.20)
				[2.36 (0.07)]	[2.05 (0.18)]
	$CaOH^+/H_3O^+$	12 (6)		3.77 (0.14)	3.22 (0.17)
				[2.03 (0.13)]	[1.46 (0.14)]
$Ca^{2+}(H_2O)_4$	$Ca^{2+}(H_2O)_3$	69 (13)	0.8 (0.1)	1.45 (0.11)	1.46 (0.09)
	$Ca^{2+}(H_2O)_2$	25 (6)		3.30 (0.12)	3.20 (0.12)
				[1.86 (0.06)]	[1.76 (0.09)]
$Ca^{2+}(H_2O)_5$	$Ca^{2+}(H_2O)_4$	88 (18)	0.8 (0.1)	1.15 (0.08)	1.16 (0.08)
	$Ca^{2+}(H_2O)_3$	55 (14)		2.71 (0.08)	2.62 (0.12)
				[1.56 (0.05)]	[1.46 (0.09)]
$Ca^{2+}(H_2O)_6$	$Ca^{2+}(H_2O)_5$	74 (15)	0.8 (0.2)	1.03 (0.08)	1.02 (0.09)
	$Ca^{2+}(H_2O)_4$	57 (8)		2.27 (0.09)	2.18 (0.14)
				[1.24 (0.06)]	[1.16 (0.08)]
$Ca^{2+}(H_2O)_7$	$Ca^{2+}(H_2O)_6$	77 (15)	0.9 (0.2)	0.62 (0.09)	0.62 (0.11)
	$Ca^{2+}(H_2O)_5$	67 (21)		1.68 (0.16)	1.64 (0.17)
				[1.06 (0.08)]	[1.02 (0.09)]
$Ca^{2+}(H_2O)_8$	$Ca^{2+}(H_2O)_7$	79 (10)	0.9 (0.1)	0.59 (0.09)	0.59 (0.13)
	$Ca^{2+}(H_2O)_6$	61 (14)		1.26 (0.09)	1.21 (0.13)
				[0.67 (0.06)]	[0.62 (0.11)]

[a] Uncertainties, in parentheses, are reported to two standard deviations.
[b] Values in brackets are the differences between primary and secondary thresholds, with uncertainties determined directly from the sequential models.

Table 6.2. continued

[c] Experimental values from Table 6.1.

Table 6.3. Relative 0 K energies of transition states, intermediates, and products for charge separation and water loss from $Ca^{2+}(H_2O)_2$ and $Ca^{2+}(H_2O)_3$[a]

Complex	B3LYP	B3P86	MP2(full)	Lit./Expt.
$Ca^{2+}(H_2O) + H_2O$	197	197	192	197 ± 17[c]
$Ca^{2+}(H_2O)_2$	0	0	0	
TS1	77	73	78	
INT (1,1)	70	64	74	
TS[0+1]	135, 139[b]	132	160	140 ± 14[c]
$CaOH^+ + H_3O^+$	-60	-64	-24	
$Ca^{2+}(H_2O)_2 + H_2O$	172	172	172	170 ± 9[c]
$Ca^{2+}(H_2O)_3$	0	0	0	
TS1	66	62	69	
INT (2,1)	63	58	67	
TS[1+1]	167	165	189	165 ± 15[d]
$CaOH^+(H_2O) + H_3O^+$	-1	-5	29	

[a] Single point energies calculated with the 6-311+G(2d,2p) basis set using B3LYP/6-311+G(d,p) geometries and ZPE corrections.
[b] B3LYP/6-311+G(3df,2pd)//B3LYP/6-311G(d,p) value from reference 15.
[c] Best value from Table 6.1.
[d] Value determined by applying difference in thresholds for water loss and charge separation from single high pressure CID data (5 ± 12 kJ/mol) to zero pressure extrapolated value for water loss, Table 6.1.

Table 6.4. Conversion between 0 K primary and secondary binding energies for H_2O loss from $Ca^{2+}(H_2O)_x$ (x = 1 – 8) to enthalpies and free energies at 298 K in kJ/mol[a]

Complex	ΔH_0[b]	$H_{298} - H_0$[c]	ΔH_{298}	$T\Delta S_{298}$[c]	ΔG_{298}
$Ca^{2+}(H_2O)$	242.7 (6.0)[d,e] 258.3 (31.1)[e]	4.6 (0.2)	247.3 (6.0) 262.9 (31.1)	29.0 (0.9)	218.3 (6.1) 233.9 (31.1)
$Ca^{2+}(H_2O)_2$	197.4 (17.0)[e] 227.3 (6.5)[e]	1.6 (0.2)	199.0 (17.0) 228.9 (6.5)	29.5 (2.5)	169.5 (17.2) 199.4 (7.0)
$Ca^{2+}(H_2O)_3$	169.7 (9.1) 179.1 (6.2)	1.3 (0.2)	171.0 (9.1) 180.4 (6.2)	32.7 (2.6)	138.3 (9.5) 147.7 (6.7)
$Ca^{2+}(H_2O)_4$	140.6 (8.7) 150.0 (5.2)	1.8 (0.3)	142.4 (8.7) 151.8 (5.2)	36.7 (2.6)	105.7 (9.1) 115.1 (5.7)
$Ca^{2+}(H_2O)_5$	111.8 (8.1) 119.5 (5.5)	2.2 (0.5)	114.0 (8.1) 121.7 (5.5)	40.5 (1.3)	73.5 (8.2) 81.2 (5.7)
$Ca^{2+}(H_2O)_6$	98.8 (9.0) 102.3 (9.0)	1.8 (0.5)	100.3 (9.0) 104.1 (9.0)	47.1 (1.4)	53.5 (9.1) 57.0 (9.1)
$Ca^{2+}(H_2O)_7$	59.3 (10.5) 64.7 (6.2)	3.7 (0.4)	63.0 (10.5) 68.4 (6.2)	33.0 (1.0)	30.0 (10.6) 35.4 (6.3)
$Ca^{2+}(H_2O)_8$	57.0 (12.3)	4.4 (0.5)	61.4 (12.3)	46.4 (1.0)	15.0 (12.4)

[a] Uncertainties, in parentheses, are reported to two standard deviations (95% confidence interval).
[b] 0 K primary (top) and secondary (bottom) binding energies taken from Tables 6.1 and 6.2.
[c] Values were calculated from standard formulae and molecular constants (vibrational frequencies and rotational constants) calculated at the B3LYP/6-311+G(d,p) level of theory. Uncertainties correspond to scaling the vibrational frequencies up and down by 10%.
[d] Threshold energy obtained by extrapolation of threshold energies to zero pressure.
[e] Includes competition from the charge separation process.

Table 6.5. Experimental[a] and theoretical[b] 298 K binding enthalpies for H_2O loss from $Ca^{2+}(H_2O)_x$ (x = 1 – 6)

x	1	2	3	4	5	6
Primary[f]		199 (17)	171 (9)	142 (9)	114 (8)	101 (9)
Secondary[f]	247 (6)	229 (7)	180 (6)	152 (5)	122 (6)	104 (9)
HPMS[g]						106 (4)
BIRD[h]					112 (6)	92 (3)
B3LYP/6-311+G(2d,2p)[i]	235	197	172	147	113	101
B3LYP/pCVTZ[j]	242	201	174	148	113	102
B3P86/pCVTZ[j]	243	201	173	147	113	102
MP2(full)/pCVTZ[j]	230	196	173	152	120	109
BH&HLYP/pCVTZ[j]	241	204	178	153	119	108
CCSD(T)[k]	217	189	169	148	119	108
G3[k]	228	199	176	156	130	120

Table 6.5. continued

MAD[c]	Primary	Secondary	B3LYP//B3LYP[d]	B3LYP/pCVTZ[e]
Primary[f]		12 (10)	2 (2)	3 (2)
Secondary[f]	12 (10)		11 (11)	9 (10)
HPMS[g]	6	2	5	4
BIRD[h]	5 (4)	11 (1)	6 (5)	6 (6)
B3LYP/6-311+G(2d,2p)[i]	2 (2)	11 (11)		2 (2)
B3LYP/pCVTZ[j]	3 (2)	9 (10)	2 (2)	
B3P86/pCVTZ[j]	2 (1)	9 (10)	2 (3)	1 (1)
MP2(full)/pCVTZ[j]	6 (3)	11 (13)	5 (3)	6 (4)
BH&HLYP/pCVTZ[j]	7 (2)	7 (9)	6 (1)	4 (2)
CCSD(T)[k]	6 (3)	15 (16)	7 (6)	9 (9)
G3[k]	11 (8)	14 (10)	10 (7)	10 (7)

Table 6.5. continued

[a] Uncertainties, in parentheses, are reported to two standard deviations (95% confidence interval).
[b] Theoretical calculations include counterpoise corrections.
[c] Mean absolute deviations.
[d] MADs with respect to B3LYP/6-311+G(2d,2p)//B3LYP/6-311+G(d,p) results.
[e] MADs with respect to B3LYP/pCVTZ results.
[f] Primary and secondary BDEs from Table 6.4.
[g] Values taken from reference 4. Uncertainties were assigned in reference 6.
[h] Values taken from references 5 and 6.
[i] B3LYP/6-311+G(2d,2p)//B3LYP/6-311+G(d,p) from Chapter 4.
[j] Single point energies calculated from B3LYP/pCVTZ geometries.
[k] Values taken from reference 14.

References

(1) Whitehouse, C. M.; Dreyer, R. N.; Yamashita, M.; Fenn, J. B. *Anal. Chem.* **1985**, *57*, 675.

(2) Yamashita, M.; Fenn, J. B. *J. Phys. Chem.* **1984**, *88*, 4451.

(3) Blades, A. T.; Jayaweera, P.; Ikonomou, M. G.; Kebarle, P. *J. Chem. Phys.* **1990**, *92*, 5900.

(4) Peschke, M.; Blades, A. T.; Kebarle, P. *J. Phys. Chem. A* **1998**, *102*, 9978.

(5) Rodriguez-Cruz, S. E.; Jockusch, R. A.; Williams, E. R. *J. Am. Chem. Soc.* **1999**, *121*, 8898.

(6) Wong, R. L.; Paech, K.; Williams, E. R. *Int. J. Mass Spectrom.* **2004**, *232*, 59.

(7) Carl, D. R.; Moision, R. M.; Armentrout, P. B. *Int. J. Mass Spectrom.* **2007**, *265*, 308.

(8) Bush, M. F.; Saykally, R. J.; Williams, E. R. *ChemPhysChem* **2007**, 2245.

(9) Bush, M. F.; Saykally, R. J.; Williams, E. R. *J. Am. Chem. Soc.* **2008**, 15482.

(10) Pavlov, M.; Siegbahn, P. E. M.; Sandstrom, M. *J. Phys. Chem. A* **1998**, *102*, 219.

(11) Glendening, E. D.; Feller, D. *J. Phys. Chem.* **1996**, *100*, 4790.

(12) Merrill, G. N.; Webb, S. P.; Bivin, D. B. *J. Phys. Chem. A* **2003**, *107*, 386.

(13) Katz, A. K.; Glusker, J. P.; Beebe, S. A.; Bock, C. W. *J. Am. Chem. Soc.* **1996**, *118*, 5752.

(14) Rao, J. S.; Dinadayalane, T. C.; Leszczynski, J.; Sastry, G. N. *J. Phys. Chem. A* **2008**, *112*, 12944.

(15) Beyer, M.; Williams, E. R.; Bondybey, V. E. *J. Am. Chem. Soc.* **1999**, *121*, 1565.

(16) Carl, D. R.; Moision, R. M.; Armentrout, P. B. *J. Am. Soc. Mass Spectrom.* **2009**, *20*, 2312.

(17) Armentrout, P. B. *J. Chem. Phys.* **2007**, *126*, 234302.

(18) Iceman, C.; Armentrout, P. B. *Int. J. Mass Spectrom.* **2003**, *222*, 329.

(19) Castleman Jr., A. W. *Chem. Phys. Lett.* **1978**, *53*, 560.

(20) Cooper, T. E.; Carl, D. R.; Armentrout, P. B. *J. Phys. Chem. A* **2009**, *113*, 13727.

(21) Cooper, T. E.; Armentrout, P. B. *J. Phys. Chem. A* **2009**, *113*, 13742.

(22) Cooper, T. E.; Armentrout, P. B. *Chem. Phys. Lett.* **2010**, *486*, 1.

(23) Cooper, T. E.; Armentrout, P. B. *J. Chem. Phys.* **2011**, *134*, 114308.

(24) Heaton, A. L.; Armentrout, P. B. *J. Am. Soc. Mass Spectrom.* **2009**, *20*, 852.

(25) Spears, K. G.; Fehsenfeld, F. C. *J. Chem. Phys.* **1972**, *56*, 5698.

(26) Feil, S.; Koyanagi, G. K.; Bohme, D. K. *Int. J. Mass Spectrom.* **2009**, *280*, 38.

(27) Shvartsburg, A. A.; Siu, K. W. M. *J. Am. Chem. Soc.* **2001**, *123*, 10071.

CHAPTER 7

AN EXPERIMENTAL AND THEORETICAL INVESTIGATION OF THE COMPLETE INNER SHELL HYDRATION ENERGIES OF STRONTIUM DICATIONS

Abstract

The sequential bond energies of $Sr^{2+}(H_2O)_x$ complexes, where x = 1 – 6, are determined by threshold collision-induced dissociation (TCID) using a guided ion beam tandem mass spectrometer equipped with an electrospray ionization source. The electrospray source produces an initial distribution of $Sr^{2+}(H_2O)_x$ complexes, where x = 6 – 9. Smaller $Sr^{2+}(H_2O)_x$ complexes, where x = 1 – 5, are accessed using a recently developed in-source fragmentation technique that takes place in the high pressure region of an rf-only hexapole ion guide. The kinetic energy dependent cross sections are determined over a wide energy range to monitor all possible dissociation products and are modeled to obtain 0 and 298 K binding energies for loss of a single water molecule. These binding energies decrease monotonically for the $Sr^{2+}(H_2O)$ complex to $Sr^{2+}(H_2O)_6$. Our experimental results agree well with previous literature results obtained by equilibrium and kinetic studies for x = 5 and 6. With limited theory for the hydration of Sr^{2+} present in the literature, an in-depth theoretical study on the energetics of the $Sr^{2+}(H_2O)_x$ systems for x = 1 – 6 is presented employing several levels of theory with multiple effective core potentials for Sr and different basis sets for the water molecules.

Introduction

Water is an essential component in all forms of life. Bulk water forms an intricate hydrogen bonding network that becomes disrupted in the presence of metal cations as the electronegative oxygen atoms are directed towards the positively-charged metal center. The ionic radius of the metal cation determines the number of water molecules that coordinate directly to the metal cation in the inner hydration shell as well as the binding affinities of those water molecules. Once the inner shell is filled, additional water molecules interact with these inner shell water molecules through hydrogen bonds. Investigating metal ion hydration in the gas-phase provides a suitable environment to acquire fundamental thermodynamic information of these important metal ion-water interactions, which cannot be determined in the liquid phase.

Gas-phase studies of hydrated alkaline earth metal dications have become attractive systems for experimentalists as these ions can be generated readily with electrospray ionization (ESI).[1-7] The hydration energies for $Sr^{2+}(H_2O)_x$, where x = 5 – 14, have been determined previously by equilibrium experiments using high pressure mass spectrometry (HPMS) and kinetic studies using blackbody infrared dissociation (BIRD).[3,5] The thermodynamics for the more tightly bound water molecules (x = 1 – 4) have not been determined as these smaller complexes pose a significant experimental challenge to such temperature-dependent techniques.

This chapter comprises a complete experimental investigation of the hydration energies of $Sr^{2+}(H_2O)_x$, where x = 1 – 6, using threshold collision-induced dissociation (TCID). $Sr^{2+}(H_2O)_x$ ions are formed readily using electrospray ionization (ESI), but can also be generated in a dc discharge flow tube ion source (DC/FT).[8] This is possible

because strontium's second ionization energy (11.0 eV) lies below the first ionization energy of water (12.6 eV).[9] Qualitative comparisons are made between TCID results from $Sr^{2+}(H_2O)_x$ complexes generated with both the ESI and DC/FT sources, which demonstrates that the ESI source provides more reliable quantitative results.

Compared to the number of theoretical studies of $Mg^{2+}(H_2O)_x$ and $Ca^{2+}(H_2O)_x$ complexes, relatively little has been done for the $Sr^{2+}(H_2O)_x$ complexes. Glendening and Feller[10] have performed geometry optimizations and single point energies on $Sr^{2+}(H_2O)_x$ complexes, where x = 1 – 6. Independent studies by Klobukowski,[11] Bauschlicher and coworkers,[12] and Kaupp and Schleyer[13] have determined binding energies for Sr^{2+} bound to x = 1 – 4, x = 1 – 3, and x = 1 – 2 water molecules, respectively, using a variety of basis set treatments. The present work includes a detailed theoretical assessment of the binding enthalpies of all $Sr^{2+}(H_2O)_x$ complexes investigated experimentally (x = 1 – 6) utilizing two different effective core potentials (ECPs) on Sr. By employing multiple levels of theory with different basis set treatments for the $Sr^{2+}(H_2O)_x$ system, we are able to determine specific combinations that are capable of reproducing our experimental hydration energies for these tightly bound water molecules. Such agreement provides additional support for the successful application of TCID studies for such multiply charged systems as well as confirmation that the ESI source produces thermalized ions.

Results

Cross sections for collision-induced dissociation. The CID cross sections for $Sr^{2+}(H_2O)_x$, where x = 1 – 6, are shown in Figure 7.1. In all cases, the dominant reaction is the loss of a single water molecule in Reaction 7.1.

$$Sr^{2+}(H_2O)_x + Xe \rightarrow Sr^{2+}(H_2O)_{x-1} + H_2O \qquad (7.1)$$

At higher kinetic energies, water molecules are sequentially lost until the bare metal ion appears. For the CID of $Sr^{2+}(H_2O)_4$, $Sr^{2+}(H_2O)_5$, and $Sr^{2+}(H_2O)_6$, the energy range was not large enough to observe the Sr^{2+} ion with appreciable intensity. A proton transfer/charge separation process from the $Sr^{2+}(H_2O)_2$ complex, Reaction 7.2, is observed in the CID of $Sr^{2+}(H_2O)_2$ and $Sr^{2+}(H_2O)_3$,

$$Sr^{2+}(H_2O)_2 + Xe \rightarrow SrOH^+ + H_3O^+ + Xe \qquad (7.2)$$

but no other complexes are observed to undergo such a process. The product cross sections of $SrOH^+$ and H_3O^+ ions have a higher apparent threshold than the $Sr^{2+}(H_2O)$ product cross section (~0.5 eV) with amplitudes that are smaller by two over orders of magnitude. These charge separation products could only be observed efficiently at Xenon pressures somewhat higher than those normally used (~0.25 mTorr for x = 2 and ~0.40 mTorr for x = 3). These qualitative results are strikingly similar to those for $Ca^{2+}(H_2O)_3$. No other products were observed besides those described above.

Comparison of CID cross sections for ions generated with ESI and DC/FT sources. In addition to the CID of $Sr^{2+}(H_2O)_x$ complexes generated by the ESI source, CID studies of $Sr^{2+}(H_2O)_x$ ions, where x = 1 – 6, were carried out for ions generated with a dc discharge flow tube source (DC/FT).[8] Intensities for x = 4 – 6 were reasonably large and decreased appreciably for smaller complexes. Comparisons of the total CID cross sections obtained using these two sources are shown in Figure 7.2 for x = 1 – 6. In general, the CID cross sections for ions generated with the ESI source are considerably more well defined than those generated with the DC/FT source and rise sharply from zero. For x = 1, the DC/FT product cross section is shifted to lower kinetic energies (0.5

eV at 0.1Å^2) with respect to the ESI product cross section, which indicates dissociation proceeds from $Sr^{2+}(H_2O)$ complexes that could not dissipate excess internal energy acquired in the association process upon ion formation. Like x = 1, the DC/FT total cross section for x = 2 is shifted to lower energies with respect to the ESI cross section but also includes a low energy feature from 0.0 to 1.2 eV. Such low energy features may indicate the presence of a small population of high energy conformers within the ion beam. With only two water molecules complexed to Sr^{2+}, this high energy conformer can only correspond to a structure in which the second water molecule is located in the second solvent shell and hydrogen bonds to the inner shell water molecule. These low energy tails closely resemble features that can be purposely introduced using the in-source fragmentation technique described in Chapter 5.[14] For x = 3, the low energy feature persists, but the DC/FT and ESI total cross sections are comparable from 1.3 to 5.0 eV. Assuming the low energy feature is attributed to a high energy conformer in the ion beam, the agreement in the two cross sections indicates that the low energy conformer in the ion beam has an internal energy distribution similar to that for ions generated with ESI. The DC/FT and ESI cross sections for the $Sr^{2+}(H_2O)_4$ complex are similar, Figure 7.2, although the DC/FT cross section magnitude is about half that of the ESI cross section. For x = 5 and 6, the DC/FT and ESI cross sections are comparable in magnitude but the former have low energy tails that could either be hot ions or alternate high energy conformations. Overall, these comparisons indicate that the ESI source generates $Sr^{2+}(H_2O)_x$ complexes consisting of single conformations that are well thermalized. The flow tube source, which generally has been found to produce well-thermalized singly-

charged ions,[15-20] is apparently limited in its ability to dissipate the association energies of doubly-charged ions during ion formation.

Thermochemical results. The total dissociation cross sections from ESI generated ions were modeled using Equations 2.4 and 2.5 for all $Sr^{2+}(H_2O)_x$ complexes. The total cross sections are modeled because the overall shapes of the cross sections for reactions 7.1 are influenced by sequential dissociation of additional water molecules. The optimum modeling parameters obtained are listed in Table 7.1 and the models of Equation 2.5 are compared to zero pressure-extrapolated cross sections in Figure 7.3 for $Sr^{2+}(H_2O)_x$, where x = 1 – 6. The model of Equation 2.5 reproduces the experimental data well from threshold to 10.0, 7.0, 5.0, 4.0, 3.5, and 2.0 eV for x = 1 – 6, respectively. For $Sr^{2+}(H_2O)$ to $Sr^{2+}(H_2O)_6$, the kinetic shift between E_0 values modeled with and without consideration of lifetime effects (Equations 2.5 and 2.4, respectively) gradually increases from 0.00 to 0.17 eV, which agrees nicely with the kinetic shifts for the analogous $Ca^{2+}(H_2O)_x$ complexes in Chapter 6. The size of these kinetic shifts agree nicely with the results for $Ca^{2+}(H_2O)_x$ for x = 2 – 6 in Chapter 6. In Figure 7.3, the solid lines represent the model of Equation 2.5 convoluted over the kinetic and internal energy distribution of the reactants, whereas the dashed lines represent the model without kinetic energy broadening or internal energy of the reactants. The energy difference between these two lines is largely a measure of the internal energy of the reactant complex at 300 K. It can be seen that the internal energy of the $Sr^{2+}(H_2O)$ complex is small, but systematically increases for larger $Sr^{2+}(H_2O)_x$ complexes. This is attributable to the relatively floppy motions in such metal-ligand donor-acceptor bonding.

Theoretical geometries of ground state x = 1 – 6 structures. As described in Chapter 3, geometry optimizations and frequency calculations were performed at B3LYP/HW*/6-311+G(d,p), B3LYP/SD/6-311+G(d,p), B3LYP/Def2TZVP, and BH&HLYP/Def2TZVPP levels of theory for $Sr^{2+}(H_2O)_x$ complexes. Here, $Ca^{2+}(H_2O)_x$ complexes served as starting structures. Geometrical parameters do not change significantly between these four levels of theory, e.g., the Sr-O distances for a specific $Sr^{2+}(H_2O)_x$ complex are within 0.005 Å of one another at all levels. The structures for x = 1 – 6 are shown in Figure 7.4 for B3LYP/Def2TZVP optimized structures. The Sr-O distances increase systematically by 0.033 ± 0.003 Å in going from x = 1 to x = 6, Figure 7.4.

The $Sr^{2+}(H_2O)$ complex has C_{2v} symmetry as expected. The $Sr^{2+}(H_2O)_2$ complex has C_2 symmetry and is bent with an O-Sr-O angle between 117.0° to 119.5° depending on the level of theory. A bent geometry has also been calculated for the lowest energy $Ca^{2+}(H_2O)_2$ structure (Chapter 4) with O-Ca-O angles of 124.7° and 125.8° at the B3LYP/6-311+G(d,p) and MP2(full)/6-311+G(d,p) levels of theory, respectively,[7] whereas $Mg^{2+}(H_2O)_2$ complexes prefer a linear geometry with D_{2d} symmetry.[10-12] This structural difference is attributed to the larger core polarization of Sr^{2+} and Ca^{2+}, which compensates for the larger ligand-ligand repulsions in the bent geometry.[12] We find the lowest energy $Sr^{2+}(H_2O)_3$ complex has C_3 symmetry, whereas the lowest energy $Ca^{2+}(H_2O)_3$ and $Mg^{2+}(H_2O)_3$ complexes, adopt D_3 symmetries, in which all heavy atoms are located in the same plane.[10,12] In the C_3 geometry, the Sr^{2+} ion is located above a plane containing the oxygen atoms of the three water molecules with O-Sr-O angles between 113° and 118°. This pyramidal structure has also been attributed to the larger

core polarization of Sr^{2+}.[12] The structures of $Sr^{2+}(H_2O)_4$, $Sr^{2+}(H_2O)_5$, and $Sr^{2+}(H_2O)_6$ have S_4, C_{2v}, and T_h symmetries and geometries similar to their calcium analogues.[7] In all cases, ligands are placed to minimize ligand-ligand repulsion but also to take advantage of weak hydrogen bonding between adjacent ligands.

Conversion from 0 K to 298 K. $\Delta H_{298} - \Delta H_0$ and $T\Delta S_{298}$ values, Table 7.2, are calculated with a rigid rotor/harmonic oscillator approximation using the vibrational frequencies and rotational constants calculated at the B3LYP/HW*/6-311+G(d,p) level of theory. The uncertainties for these values are found by scaling the vibrational frequencies up and down by 10%. These conversion factors are used to determine the ΔH_{298} and ΔG_{298} values listed in Table 7.3, which are used for comparison to available literature results and calculated theoretical values.

Theoretical bond enthalpies. Theoretical bond enthalpies for losing a single water molecule from all $Sr^{2+}(H_2O)_x$ complexes are listed in Table 7.3. These enthalpies include ZPE and thermal corrections to 298 K both with and without counterpoise corrections. Single point energies were calculated at the B3LYP, B3P86, MP2(full), and M06 levels with HW*, SD, and Def2TZVPP basis sets from geometry optimizations using B3LYP/HW*/6-311+G(d,p), B3LYP/SD/6-311+G(d,p), and B3LYP/Def2TZVP levels of theory. Regardless of the basis set treatment, the B3LYP and B3P86 single point calculations produce almost identical binding enthalpies, differing by no more than 2 kJ/mol. MP2(full) results provide lower binding enthalpies for x = 1 – 4 for HW* (by 2 – 11 kJ/mol) and x = 1 – 3 for SD (3 – 10 kJ/mol) and Def2TZVPP (2 – 9 kJ/mol) basis sets with respect to B3LYP single point energies, but higher enthalpies by 4 – 7 kJ/mol for x = 5 and 6 for all basis sets. For x = 1 – 4, the M06 energies are 1 – 3 kJ/mol higher

than B3LYP energies calculated with the HW*, SD, and Def2TZVPP basis sets. The M06 energies for x = 5 and 6 are most similar to the MP2(full) energies. Overall, B3LYP and B3P86 energies calculated with the HW* or SD treatment are noticeably smaller than B3LYP/Def2TZVPP energies by 3 – 5, 4 – 6, 2 – 3, and 0 – 2 for x = 1, 2, 3, and 4 – 6, respectively. All M06 energies are smaller for x = 1 – 4 by 0 – 4 kJ/mol, but 5 – 7 kJ/mol higher for x = 5 and 6 compared to B3LYP/Def2TZVPP energies. The mean absolute deviation for MP2(full) SD energies is slightly lower (2 kJ/mol) than MP2(full) HW* energies with respect the MP2(full)/Def2TZVPP energies. Counterpoise corrections for DFT (B3LYP, B3P86, and M06) calculations are 1 – 2 kJ/mol for the HW* or SD basis sets and 3 – 5 kJ/mol for the Def2TZVPP basis set, whereas for MP2(full) calculations, they are 5 – 12, 5 – 9, and 6 – 10 kJ/mol for the HW*, SD, and Def2TZVPP basis set treatments.

Charge separation channel. We have previously defined the critical size for a $M^{2+}(H_2O)_x$ system as the complex size (x) at which charge separation becomes the lower energy pathway compared to simple ligand loss.[14] $Sr^{2+}(H_2O)_2$ is the only complex that undergoes charge separation, leading to the $SrOH^+$ and H_3O^+ products. The apparent thresholds of the charge separation product cross sections lie above the apparent threshold for the $Sr^{2+}(H_2O)$ product cross sections, Figures 7.1b and 7.1c. We attempted to analyze the cross sections for this process using Equation 2.5, but because they are only observed at high Xe pressures, no reliable zero-pressure extrapolated cross sections suitable for thermodynamic analysis could be obtained.

The theoretical reaction coordinate for charge separation from $Sr^{2+}(H_2O)_2$ is shown in Figure 7.5 as calculated at the B3LYP/Def2TZVPP level of theory. Charge

separation involves transferring a water molecule from the inner solvent shell to the second solvent shell, where it binds through a single hydrogen bond. As the products separate, a proton is transferred to the second solvent shell water molecule, thereby forming two singly charged ions that separate from one another over a large Coulombic barrier.[21] Table 7.4 provides relative energies of the transition states, intermediates, and products for the charge separation and water loss pathways from $Sr^{2+}(H_2O)_2$ calculated at the B3LYP and MP2(full) levels with the HW*, SD, and Def2TZVPP basis sets. The calculations indicate that ~ 60 kJ/mol of energy is required to transfer a water molecule into the second solvent shell (TS1) and that this alternate structure (INT) is less stable than the dihydrated ground state by 56 – 60 kJ/mol. Relative B3LYP energies predict that charge separation over TS[0+1] is favored over water loss by 19, 6, and 0 kJ/mol for Def2, SD, and HW*, respectively. However, MP2(full) results predict water loss the favored pathway by 0, 16, and 24 kJ/mol for these three basis sets. Overall, the $Sr^{2+}(H_2O)_2$ ground state is calculated to be metastable at the B3LYP level of theory by 13 – 34 kJ/mol, whereas MP2(full) calculations yield higher relative energies of –14 to +13 kJ/mol, Table 6.4.

Previous work has assigned a critical size of x = 2 for hydrated strontium dications on the basis that this was the only complex to exhibit charge separation.[22] Using our thermodynamic criterion for defining the critical size, the B3LYP calculations indicate that the critical size complex for the $Sr^{2+}(H_2O)_x$ system is x = 2, whereas the MP2(full) calculations suggest there is no critical size for strontium hydrates. In this regard, the apparent relative thresholds for Reactions 7.1 and 7.2 agree better with the MP2(full) results, although the observation of the entropically disfavored charge

separation reaction indicates its threshold must be close to that for Reaction 7.1, in agreement with theory. The relative magnitudes of the water loss and charge separation cross sections, Figure 7.1, is consistent with our ability to form the $Sr^{2+}(H_2O)$ complex in the ESI source by fragmentation of the larger $Sr^{2+}(H_2O)_2$ complex.

Literature calculations. Table 7.3 includes results from four theoretical studies in the literature. Glendening and Feller[10] calculated geometries and single point energies for $Sr^{2+}(H_2O)_x$, where x = 1 – 6, using the MP2(full)/6-31+G(d)//RHF/6-31+G(d) level of theory. The Hay-Wadt ECP and basis set described the Sr^{2+} ion and correlation of the 1s electrons of the oxygen atoms was neglected in the frozen-core MP2 treatment. Klobukowski[11] calculated Hartree-Fock binding energies for x = 1 – 4 using the Hay-Wadt ECP and basis set for the Sr^{2+} ion and Huzinaga basis sets of triple-zeta quality for the water molecules. Bauschlicher and coworkers[12] also calculated Hartree-Fock binding energies for x = 1 – 3 utilizing the Hay-Wadt ECP and basis set for Sr^{2+}, while treating the water molecules with Dunning basis sets of triple zeta plus polarization quality. Finally, Kaupp and Schleyer[13] calculated MP2 geometries and binding energies for $Sr^{2+}(H_2O)$ and $Sr^{2+}(H_2O)_2$ utilizing a 10 valence-electron quasirelativistic energy-adjusted pseudopotential for Sr^{2+}, single-electron-fit pseudopotentials for oxygen atoms, and a Dunning and Hay basis for hydrogen atoms. In all cases, the $Sr^{2+}(H_2O)_x$ optimized geometries of these literature studies are similar to those presented in Figure 7.4, except that Klobukowski considered only quasi-linear D_{2d} and D_{2h} geometries for x = 2. Glendening and Feller included ZPE, thermal, and BSSE corrections in their calculations of the sequential hydration energies, but the latter three studies did not. Therefore, these literature values are corrected for ZPE and thermal corrections using values calculated

here at the B3LYP/HW*/6-311+G(d,p) level to facilitate comparisons discussed below. The corrections applied here are 3 kJ/mol for $Sr^{2+}(H_2O)$ and 7 kJ/mol for the $Sr^{2+}(H_2O)_2$, $Sr^{2+}(H_2O)_3$, and $Sr^{2+}(H_2O)_4$ complexes.

Discussion

Comparison between experimental and literature experimental values. Available results from other experimental studies found in the literature are included in Table 7.3 and Figure 7.6. For x = 6, our experimental value is identical to the result from high pressure mass spectrometry (HPMS) studies of Kebarle and coworkers.[3] For x = 5 and 6, our results are 4 and 8 kJ/mol higher than those from blackbody infrared dissociation (BIRD) studies of Williams and coworkers.[5] The latter difference is slightly outside the range of the combined uncertainties.

Comparison between present experiment and theory. The present theoretical results of Table 7.3 can be compared to the experimental binding enthalpies by determining the mean absolute deviations (MADs). Our experimental binding enthalpies agree best with the counterpoise-corrected B3LYP/Def2TZVPP energies with a MAD of 4 ± 3 kJ/mol, whereas a MAD of 6 ± 3 kJ/mol is found for B3LYP/Def2TZVPP energies without counterpoise corrections. MADs for the B3LYP/HW*, B3P86/HW*, B3LYP/SD, and B3P86/SD energies are slightly higher at 5 ± 5, 5 ± 4, 5 ± 5, and 5 ± 4 kJ/mol. M06 energies have MADs of 6 ± 3, 6 ± 2, and 6 ± 3 kJ/mol for HW*, SD, and Def2 energies with respect to the experimental binding enthalpies. MP2(full) energies have MADs that are consistently 4 kJ/mol higher than the MADs for B3LYP energies for a specific basis set treatment. For B3LYP and B3P86 calculations with the HW* and SD basis set treatments, the MADs with and without counterpoise corrections do not

significantly change because the corrections are small (1 – 2 kJ/mol). The MADs from the B3LYP and B3P86 levels with the Def2TZVPP basis set decrease slightly (by 1 – 2 kJ/mol) when counterpoise corrections are included because the deviations for x = 3 – 6 are reduced. A more noticeable difference is seen for the MP2(full) binding enthalpies, which have larger BSSEs (5 – 12 kJ/mol) and lead to a MAD decrease of 2 – 3 kJ/mol when counterpoise corrections are included.

The most significant difference between the theoretical calculations and experimental results is for the $Sr^{2+}(H_2O)$ complex. MADs would decrease by 0 – 4 kJ/mol for all calculations if the deviations for the monohydrate binding energy were excluded. Regardless of the ECP chosen, DFT and MP2(full) energies predict a value 4 – 14 and 12 – 25 kJ/mol lower, respectively, than the experimental hydration energy of 206 ± 6 kJ/mol. A possible explanation for this is that core polarization of the Sr is not adequately handled for this complex, in part because an ECP is used. If such polarization were included properly, the water molecule could pull closer to the metal center, thereby resulting in a larger calculated binding energy. Experimental binding energies for x = 2 – 6 are reproduced quite well by B3LYP and B3P86 energies for all basis set treatments. B3LYP and B3P86 energies with the HW* and SD basis set treatments are 6 – 8 kJ/mol lower than the experimental binding enthalpy of 173 ± 5 kJ/mol for $Sr^{2+}(H_2O)_2$, whereas the Def2TZVPP energies fall within experimental uncertainty. For $Sr^{2+}(H_2O)_4$, the experimental binding enthalpy of 125 ± 4 kJ/mol is slightly below the 130 – 132 kJ/mol range predicted by most levels of theory, whereas the experimental results for x = 3, 5, and 6 agree with the B3LYP and B3P86 calculations regardless of the basis set treatment.

Overall, the levels of theory giving the best agreement with experiment are DFT approaches (excluding M06) using the Def2TZVPP basis set.

Comparison between experimental and literature theoretical values. The results from four theoretical studies are also provided in Table 7.3. Counterpoise-corrected MP2 single point energies calculated by Glendening and Feller[10] have a MAD of 10 ± 5 kJ/mol with respect to our experimental binding energies. Their calculated binding energies agree reasonably well with our experimental results for x = 1 and 2, but the binding energies for x = 3 – 6 are systematically higher by 10 – 16 kJ/mol. This is similar to previous results on the analogous calcium complexes.[7] There, our B3LYP/6-311+G(2d,2p)//B3LYP/6-311+G(d,p) binding enthalpies were comparable to those calculated by Glendening and Feller for x = 1 and 2, but their values were higher than our results by 7 – 13 kJ/mol for x = 3 – 6. These bond energies would likely decrease if electron correlation was included in the geometry optimization and if the basis sets in the single point energies included extra polarization functions. 298 K binding enthalpies for $Sr^{2+}(H_2O)_x$ from Klobukowski,[11] Bauschlicher and coworkers (BSP),[12] and Kaupp and Schleyer (KS)[13] have MADs of 12 ± 5, 8 ± 4, and 3 ± 3 kJ/mol with respect to our experimental results, respectively. Compared to our experimental results, the binding enthalpies for x = 1 and 2 of Klobukowski are smaller by 25 and 7 kJ/mol, but larger for x = 3 and 4 by 8 and 12 kJ/mol, respectively. BSP binding enthalpies are similar to Klobukowski's results for x = 2 and 3, differing by only 2 kJ/mol, whereas the binding for x = 1 is now 6 kJ/mol higher. For KS, the values for x = 1 and 2 are in good agreement with our experimental results. More useful comparisons could be made here if

these latter three theoretical studies determined binding enthalpies for all of the inner shell complexes and included corrections for BSSEs.

Conclusions

The kinetic energy dependent cross sections for $Sr^{2+}(H_2O)_x$ where x = 1 – 6 are determined by threshold collision-induced dissociation using a guided ion beam mass spectrometer equipped with an electrospray ionization source. Qualitative comparisons between the CID cross sections for $Sr^{2+}(H_2O)_x$ ions generated with the ESI source and DC/FT source indicate that the ESI source produces ions that are better thermalized than ions generated with the flow tube source. The electrospray source produces an initial distribution of $Sr^{2+}(H_2O)_x$ complexes where x = 6 – 9. Smaller $Sr^{2+}(H_2O)_x$ complexes, where x = 1 – 5, are accessed with an in-source fragmentation technique that takes place in the high pressure region of the rf-only hexapole ion guide.[14] This source can successfully generate reactant complexes in which all water molecules are bound directly to the ion. The dominant process taking place in all systems is the loss of a single water molecule. A charge separation process is observed once the $Sr^{2+}(H_2O)_2$ complex is reached, but the product cross sections for charge separation have magnitudes that are significantly smaller than those for the $Sr^{2+}(H_2O)$ product cross section. Theoretical calculations indicate that water loss and the charge separation process are similar energetically, but the latter process is entropically disfavored. This explains why the formation of the $Sr^{2+}(H_2O)$ complex is possible with the in-source fragmentation technique.

The present work determines the first experimental hydration energies for $Sr^{2+}(H_2O)$ to $Sr^{2+}(H_2O)_4$. Our experimental results for $Sr^{2+}(H_2O)_5$ and $Sr^{2+}(H_2O)_6$ agree

well with available thermochemistry from HPMS and BIRD studies.[3,5] Our experimental hydration energies are in very good agreement with binding enthalpies calculated at the B3LYP, B3P86, and BH&HLYP levels of theory with the Def2TZVPP basis sets, although the HW*/6-311+G(2d,2p) and SD/6-311+G(2d,2p) basis sets are only marginally worse. For $Sr^{2+}(H_2O)$ and $Sr^{2+}(H_2O)_2$, the Def2TZVPP basis set calculates binding enthalpies that are slightly higher than those utilizing the HW* or SD treatment and are in better agreement with experimental binding enthalpies. These theoretical results are also in accord with lower level theoretical results in the literature. The good agreement between theoretical and experimental binding energies provides confidence that the TCID approach provides accurate thermodynamic information for multiply charged ions and that the ESI source produces thermalized ions of multiply charged complexes such as $M^{2+}(H_2O)_x$.

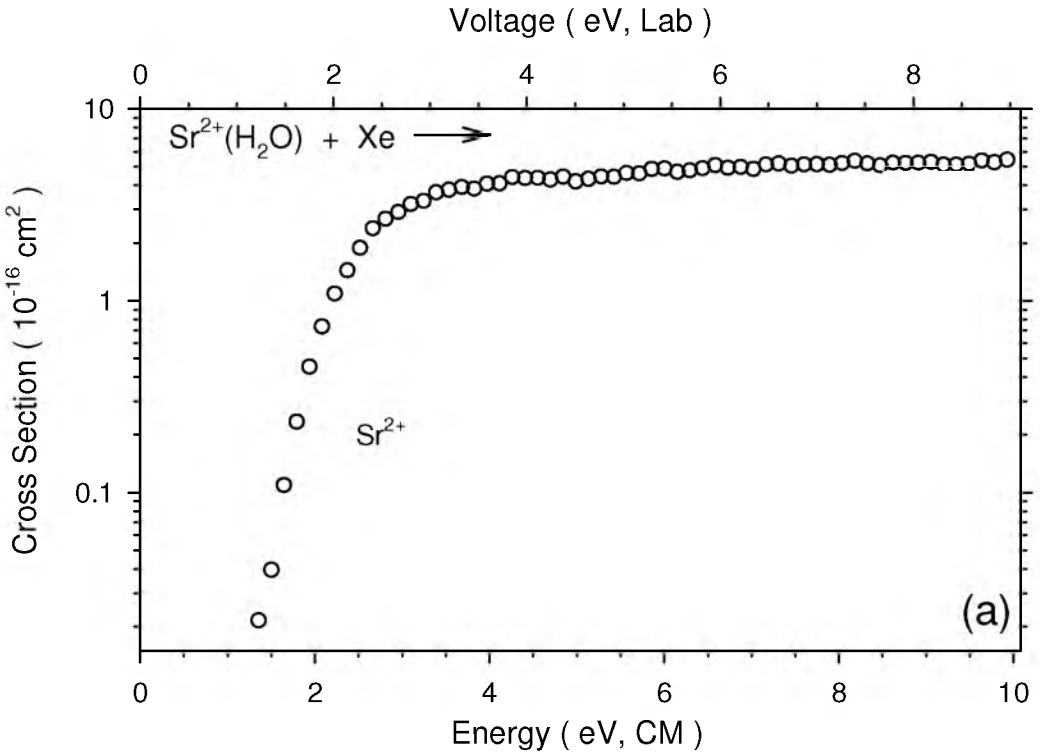

Figure 7.1. Cross sections for collision-induced dissociation of $Sr^{2+}(H_2O)_x$ where x = 1 – 6 (parts a – f, respectively) with Xenon (~ 0.2 mTorr) as a function of kinetic energy in the center-of-mass frame (lower x-axis) and the applied laboratory frame voltage (upper x-axis). Xenon pressures for the CID of $Sr^{2+}(H_2O)_2$ and $Sr^{2+}(H_2O)_3$ were 0.25 and 0.40 mTorr, respectively.

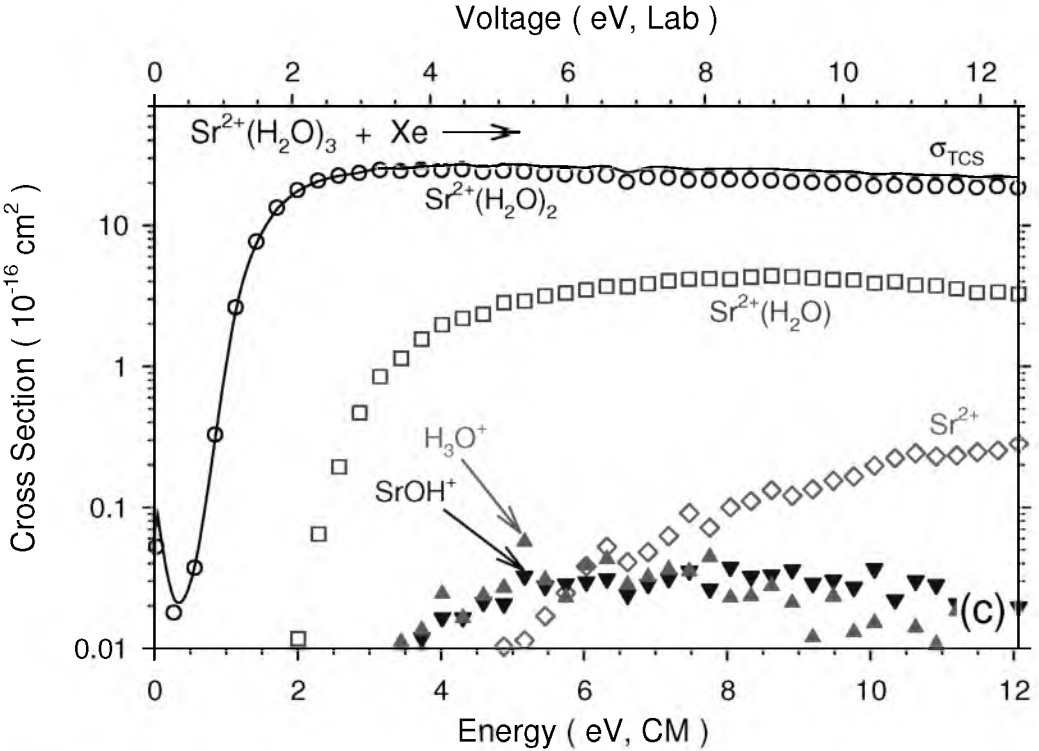

Figure 7.1. continued

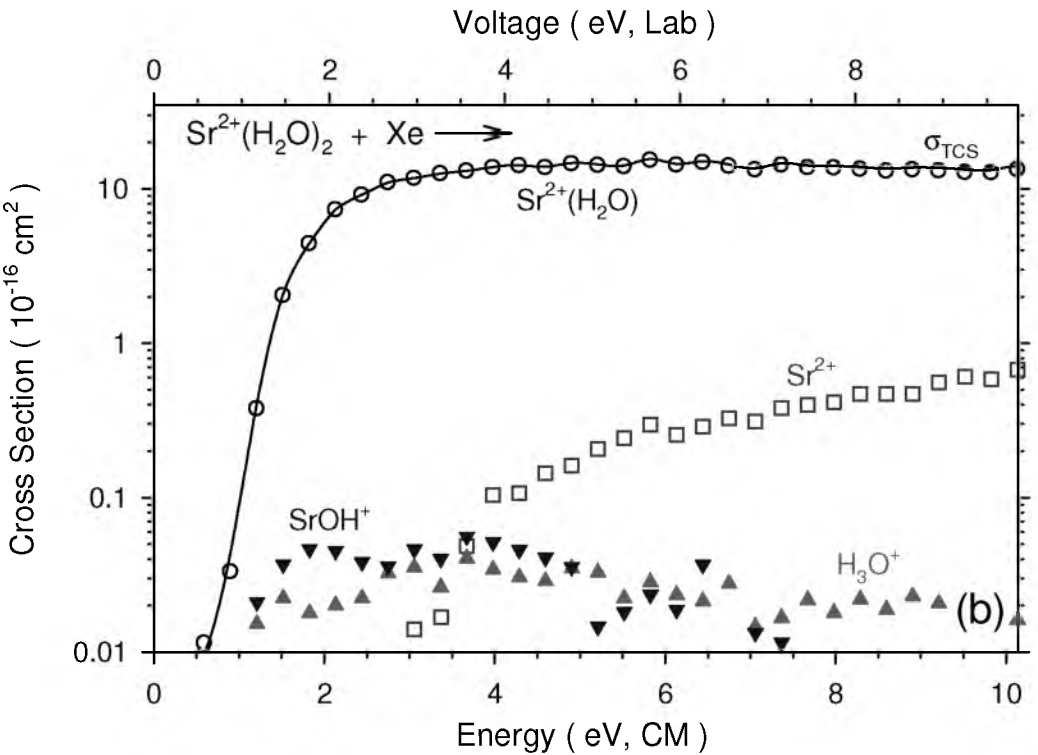
Voltage (eV, Lab)
0
2
4
6
8
$Sr^{2+}(H_2O)_2$ + Xe
σ_{TCS}
$Sr^{2+}(H_2O)$
Sr^{2+}
$SrOH^+$
H_3O^+
(b)
Cross Section (10^{-16} cm^2)
10
1
0.1
0.01
0
2
4
6
8
10
Energy (eV, CM)

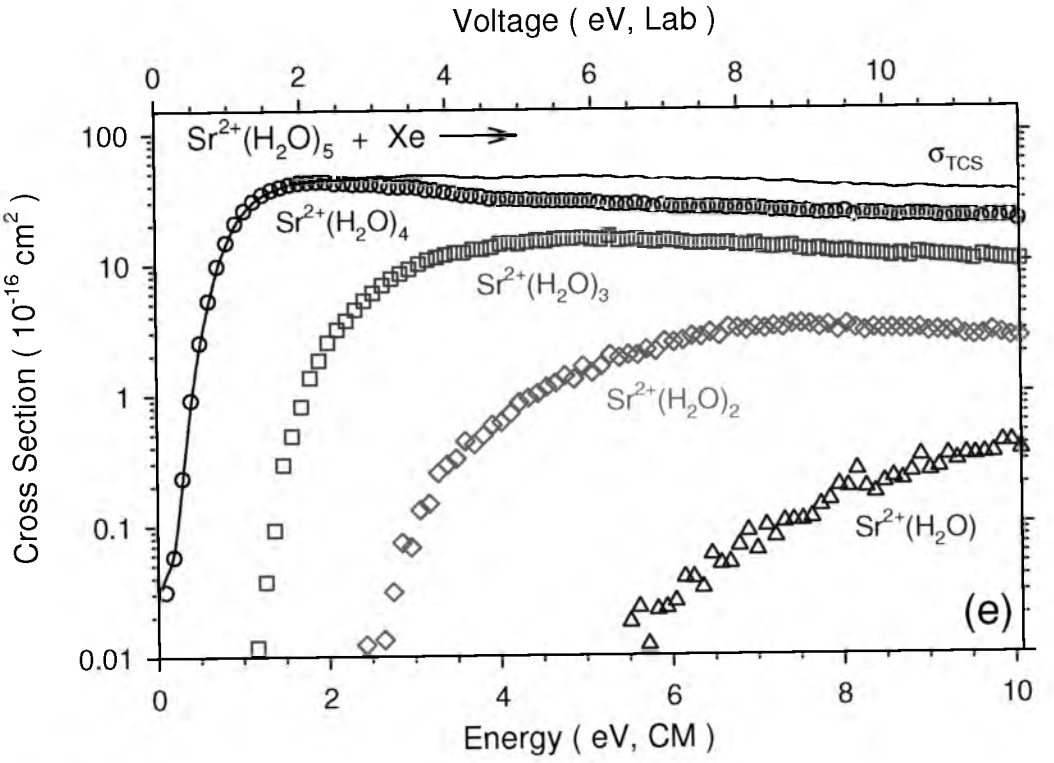

Figure 7.1. continued

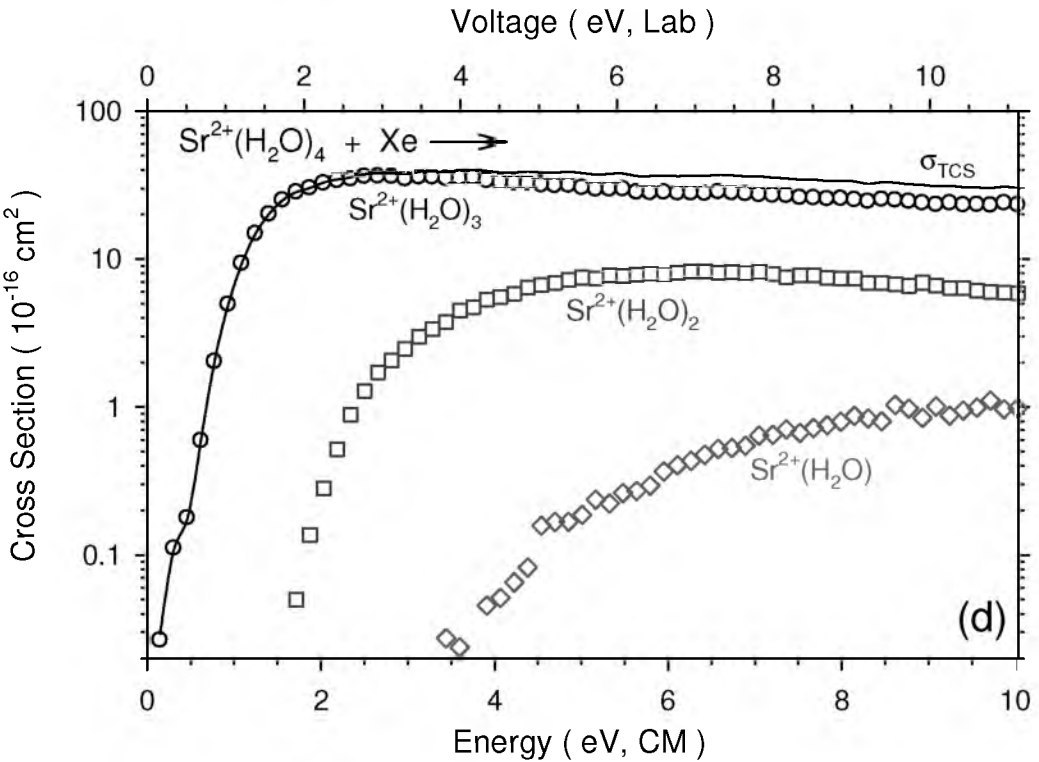
Voltage (eV, Lab)
0
2
4
6
8
10
100
10
1
0.1
Cross Section (10^-16 cm^2)
Sr2+(H2O)4 + Xe
σTCS
Sr2+(H2O)3
Sr2+(H2O)2
Sr2+(H2O)
(d)
0
2
4
6
8
10
Energy (eV, CM)

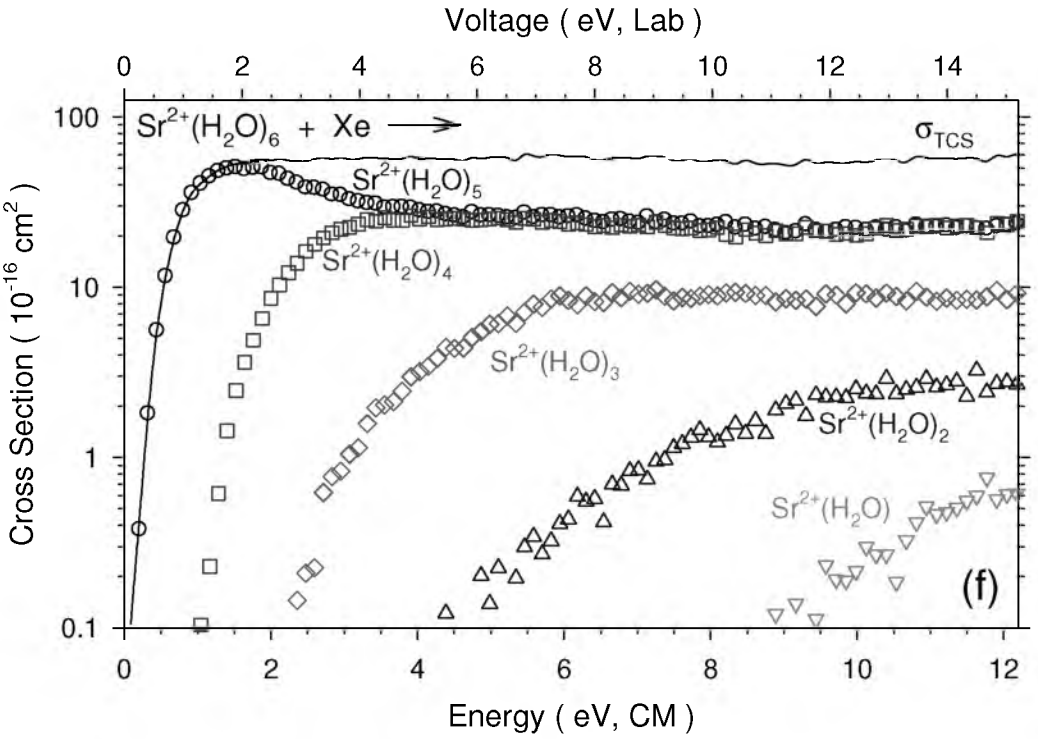

Figure 7.1. continued

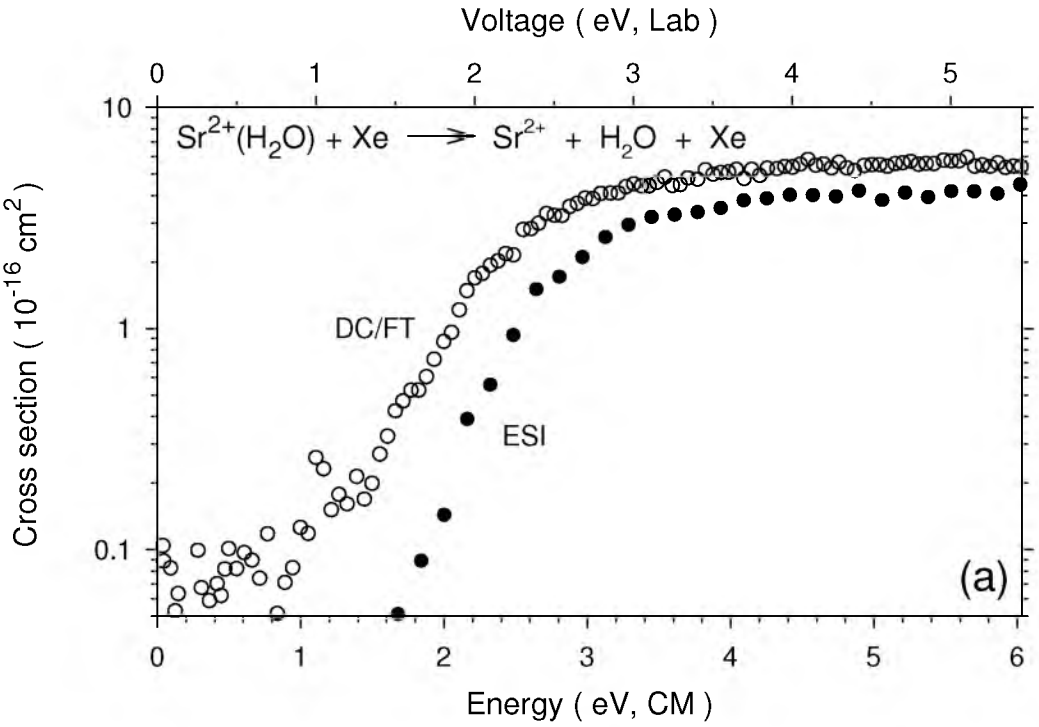

Figure 7.2. Comparison of total cross sections for collision-induced dissociation of $Sr^{2+}(H_2O)_x$ where x = 1 – 6 (parts a – f, respectively) with Xenon for ions generated with the ESI source (solid symbols) and DC/FT source (open symbols).

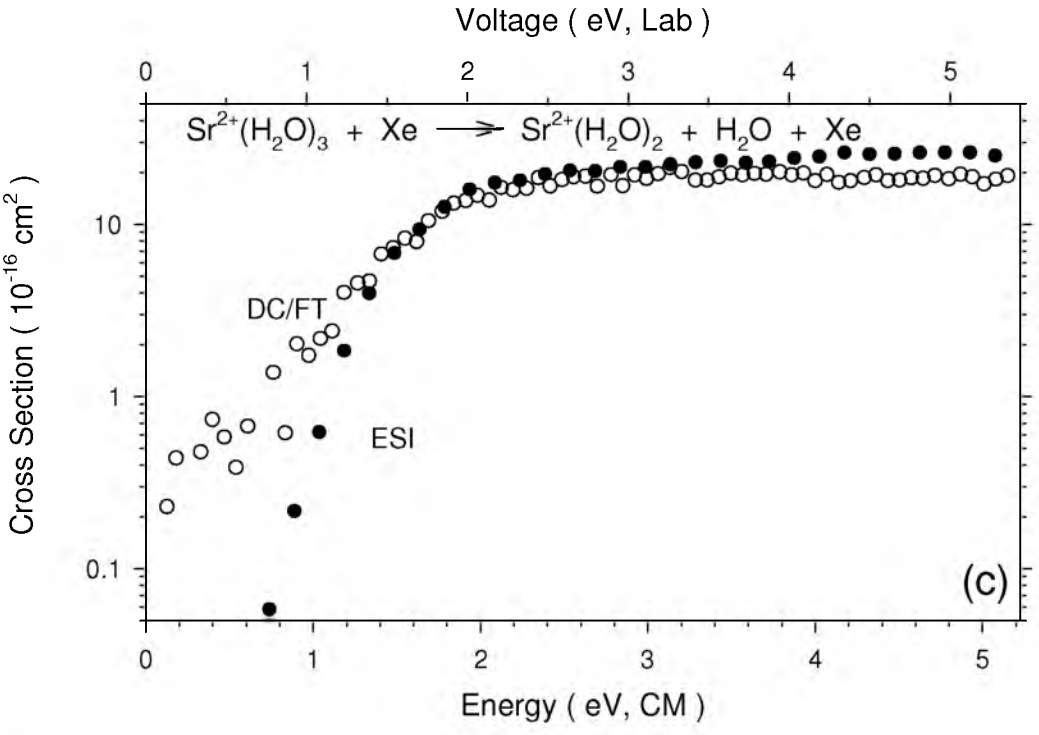

Figure 7.2. continued

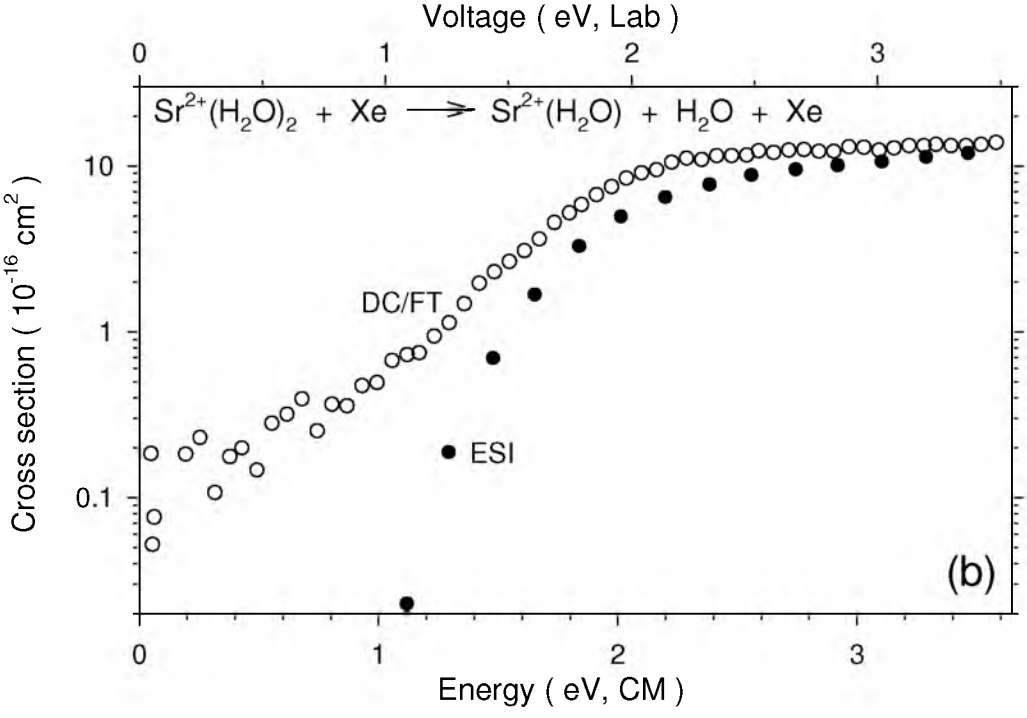
Voltage (eV, Lab)
0
1
2
3
$Sr^{2+}(H_2O)_2 + Xe \longrightarrow Sr^{2+}(H_2O) + H_2O + Xe$
10
1
0.1
Cross section (10^{-16} cm^2)
DC/FT
ESI
(b)
0
1
2
3
Energy (eV, CM)

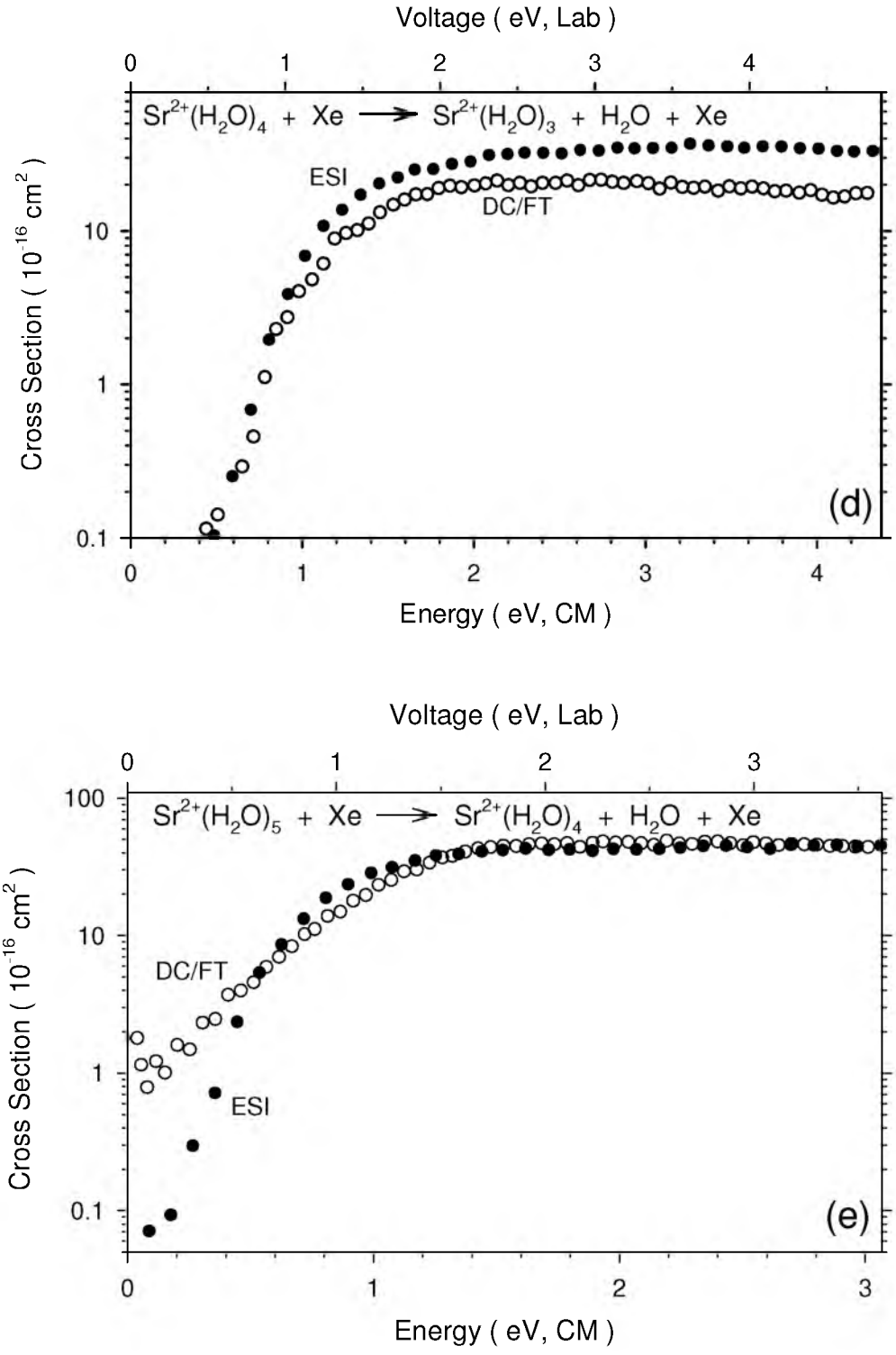

Figure 7.2. continued

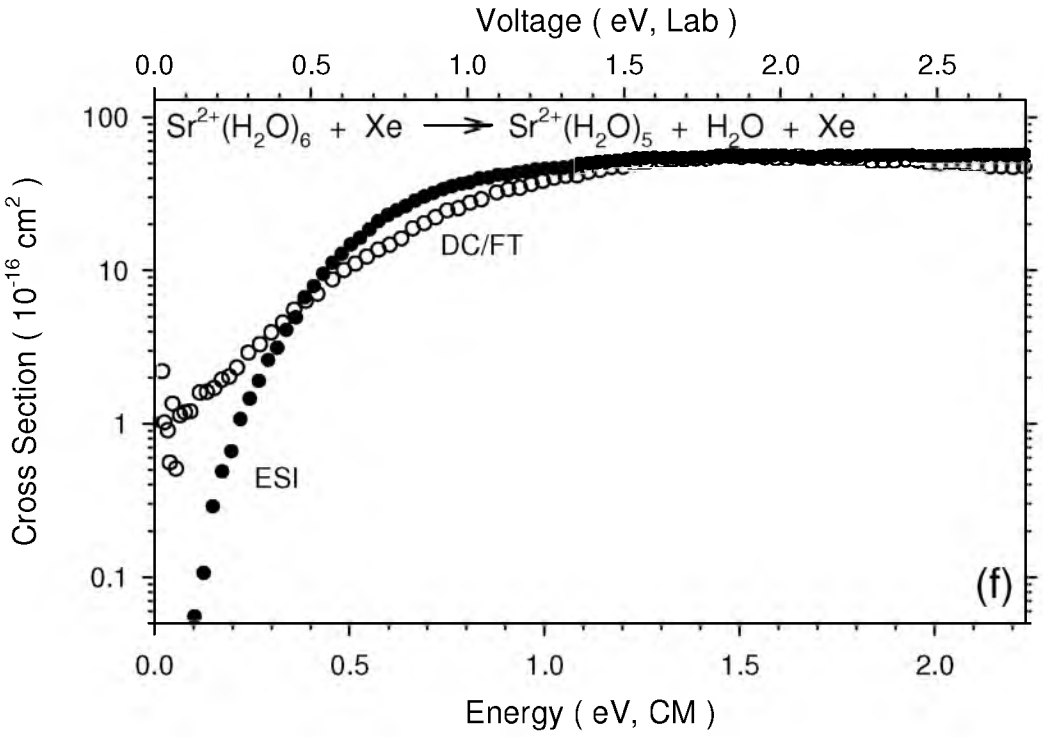

Figure 7.2. continued

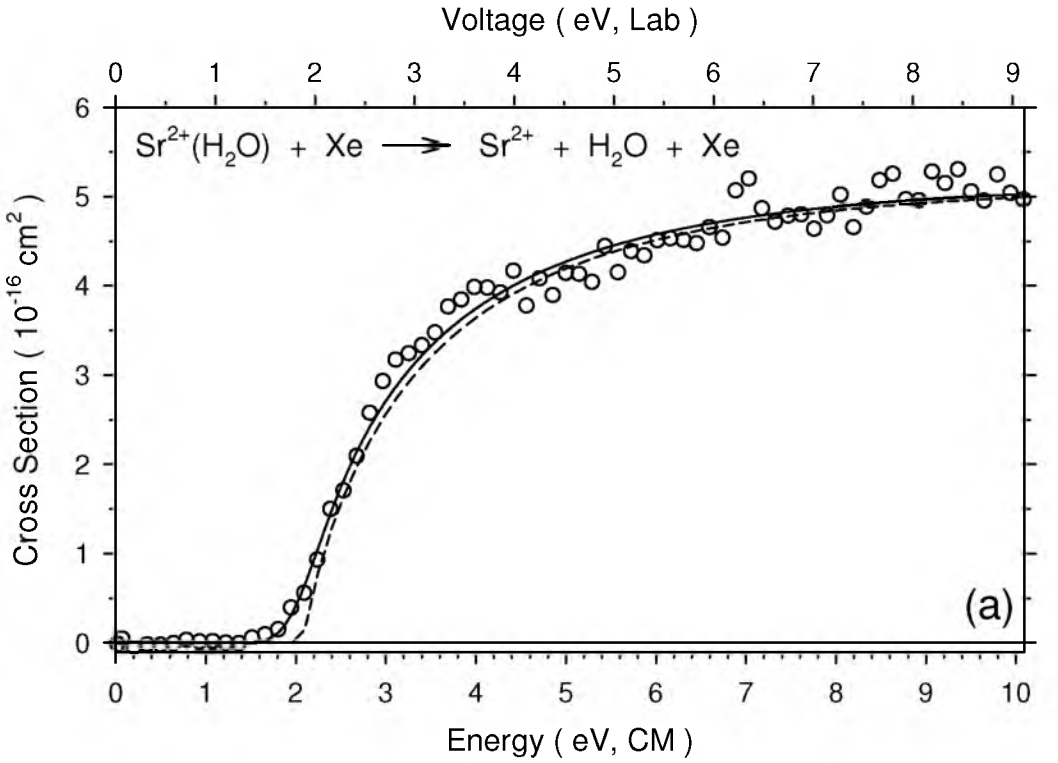

Figure 7.3. Zero pressure extrapolated cross sections for collision-induced dissociation of $Sr^{2+}(H_2O)_x$ where x = 1 – 6 (parts a – f, respectively) with Xenon in the threshold region as a function of kinetic energy in the center-of-mass frame (lower x-axis) and the applied laboratory frame voltage (upper x-axis). The solid lines show the best fit to the data using the model of Equation 2.5 convoluted over the neutral and ion kinetic and internal energy distributions. The dashed lines show the model cross sections in the absence of experimental kinetic energy broadening for reactions with an internal energy of 0 K.

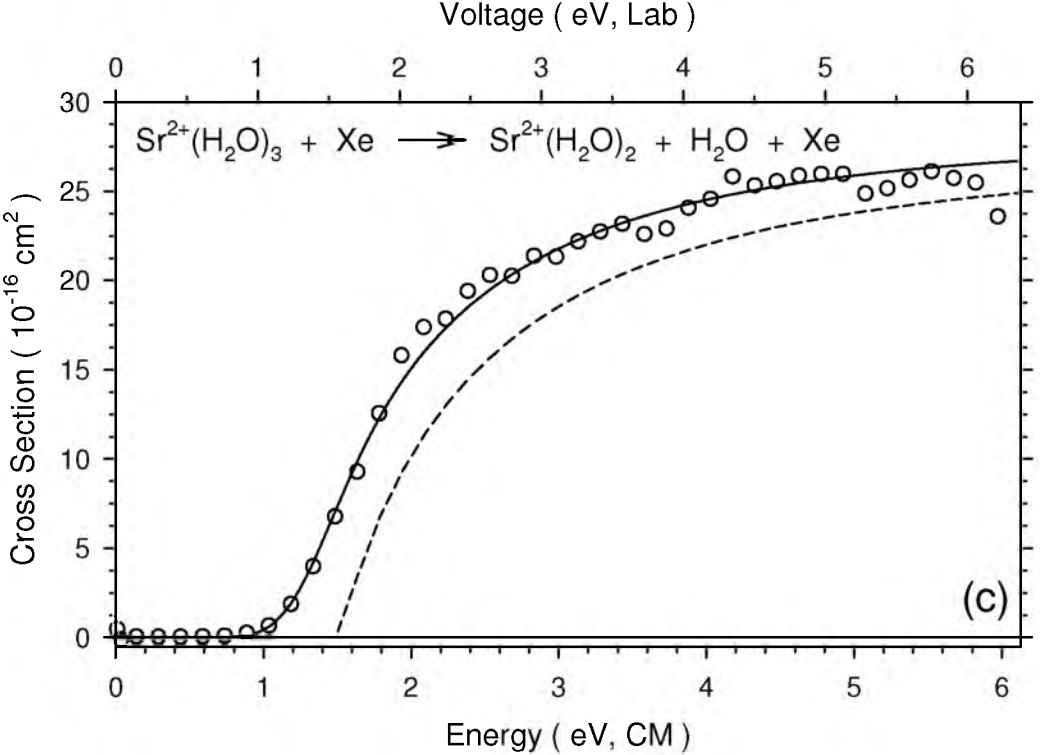

Figure 7.3. continued

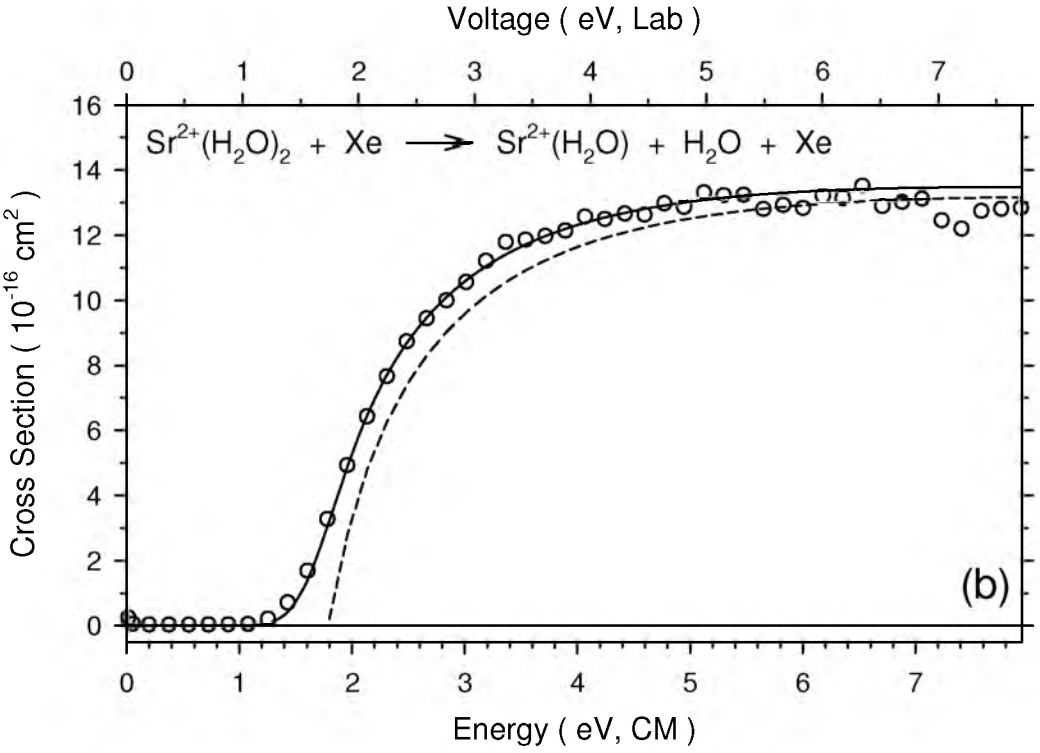
Voltage (eV, Lab)
0
1
2
3
4
5
6
7
16
14
12
10
8
6
4
2
0
Cross Section (10^-16 cm^2)
Sr2+(H2O)2 + Xe → Sr2+(H2O) + H2O + Xe
(b)
Energy (eV, CM)

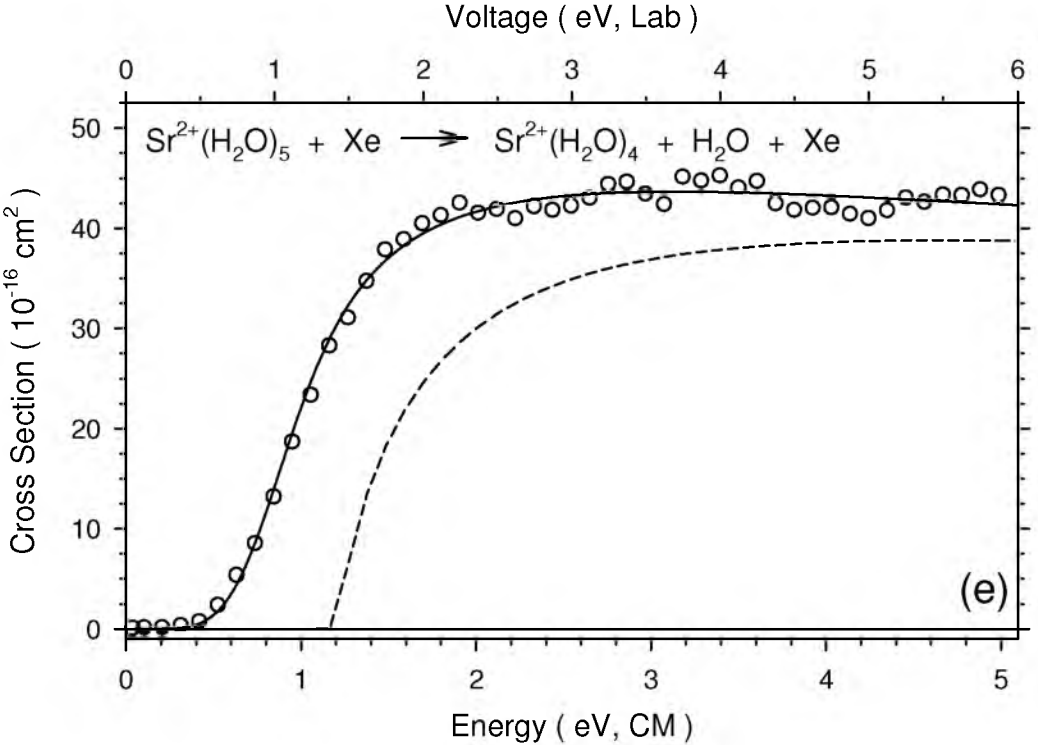

Figure 7.3. continued

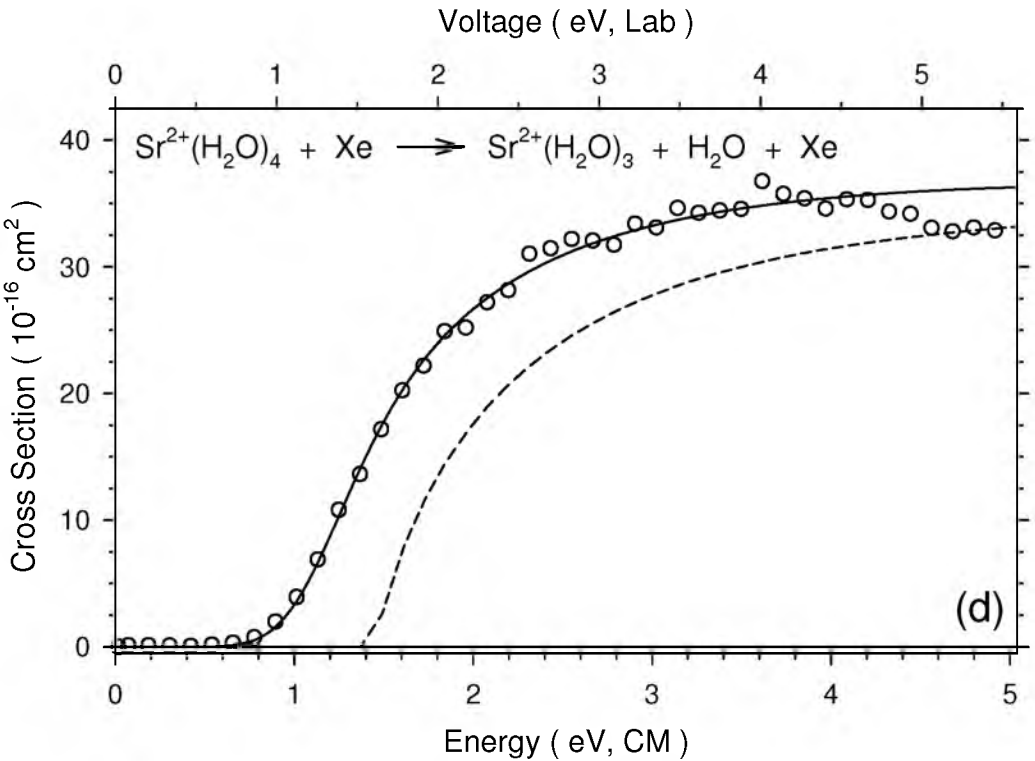
Voltage (eV, Lab)
0
1
2
3
4
5
40
30
20
10
0
Cross Section (10^-16 cm^2)
Sr2+(H2O)4 + Xe → Sr2+(H2O)3 + H2O + Xe
(d)
0
1
2
3
4
5
Energy (eV, CM)

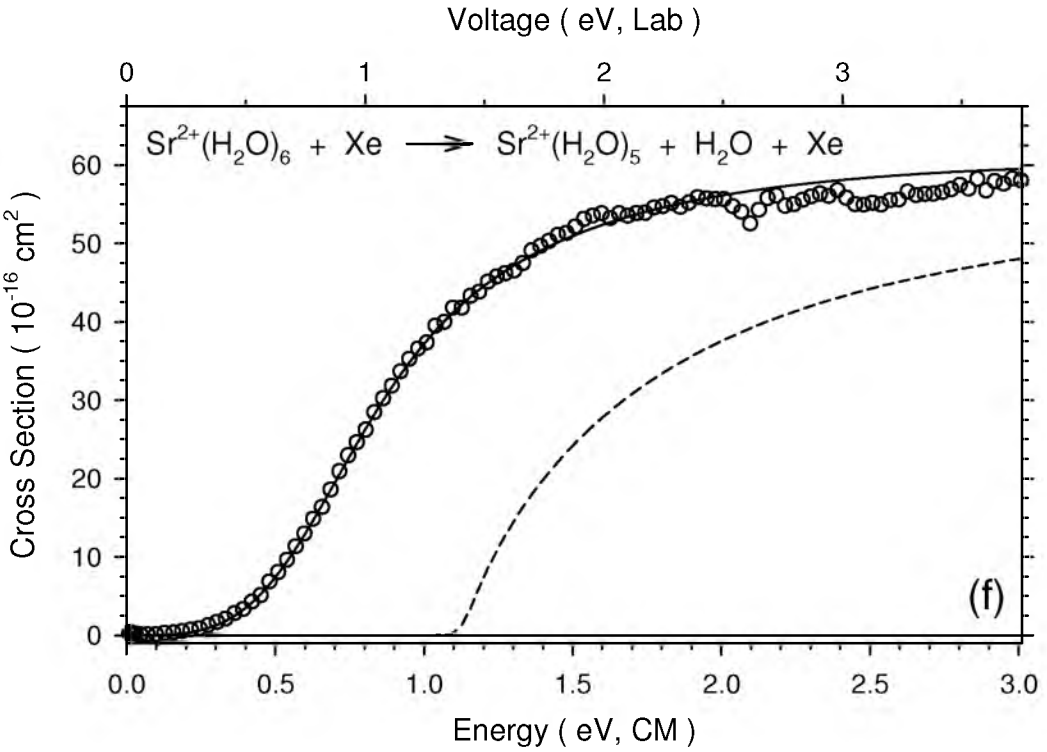

Figure 7.3. continued

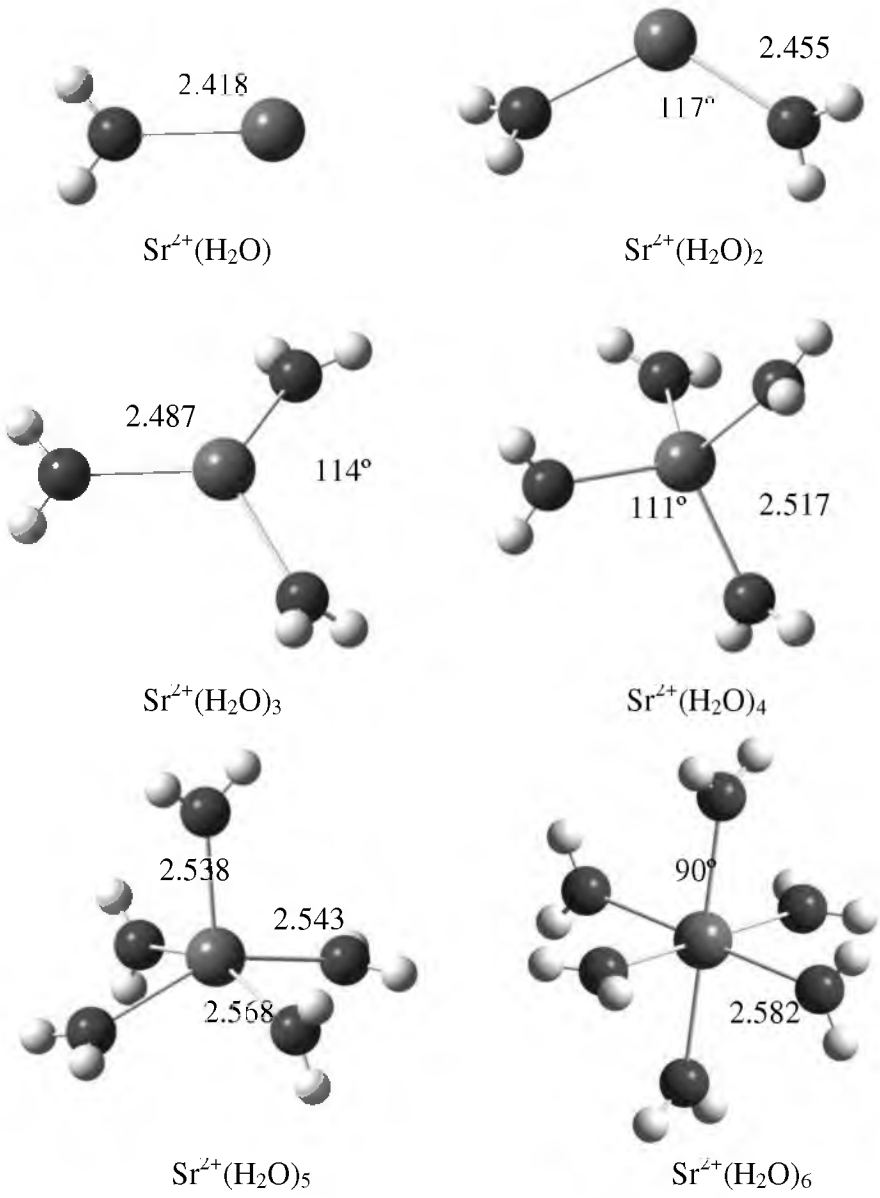

Figure 7.4. Structures for $Sr^{2+}(H_2O)_x$, where x = 1 – 6. Bond lengths (Å) and bond angles (degrees) shown are calculated at the B3LYP/Def2TZVP level.

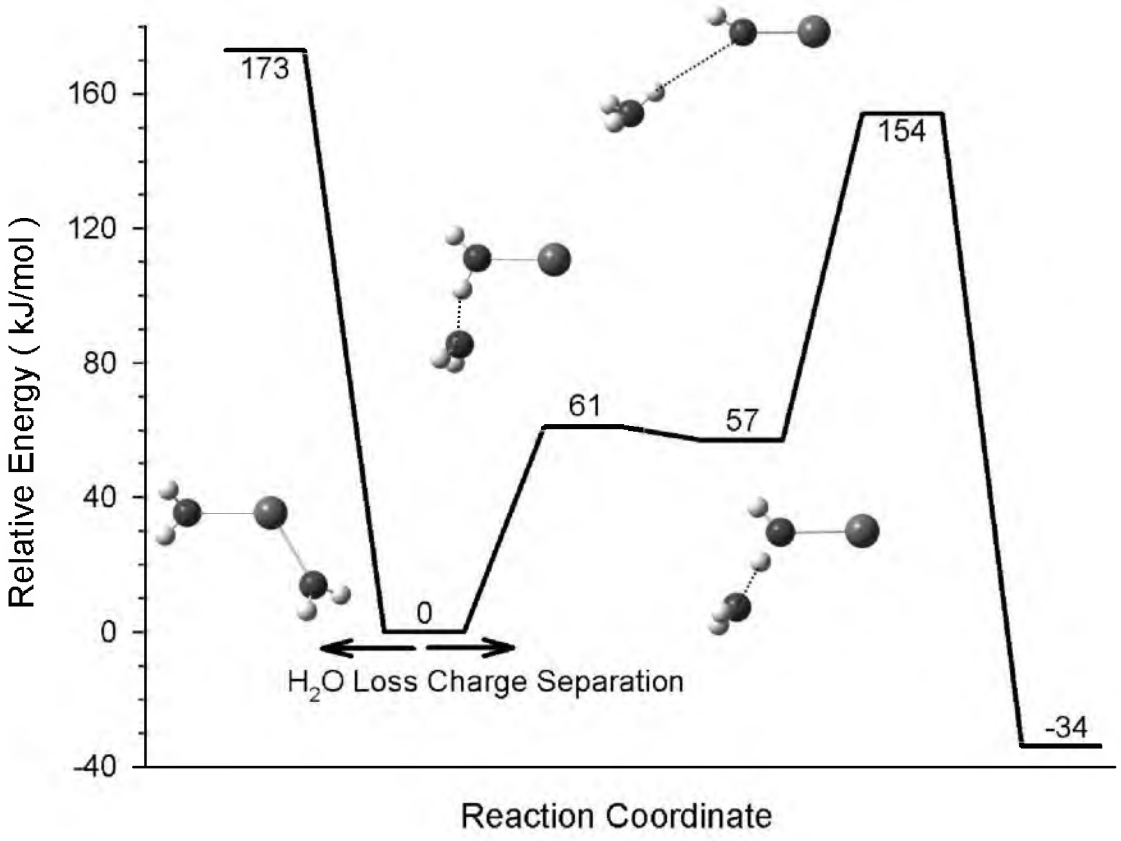

Figure 7.5. Reaction coordinates for water loss and charge separation pathways for $Sr^{2+}(H_2O)_2$ calculated at the B3LYP/Def2TZVPP level of theory including zero-point energy corrections. Hydrogen bonds shown as dashed lines.

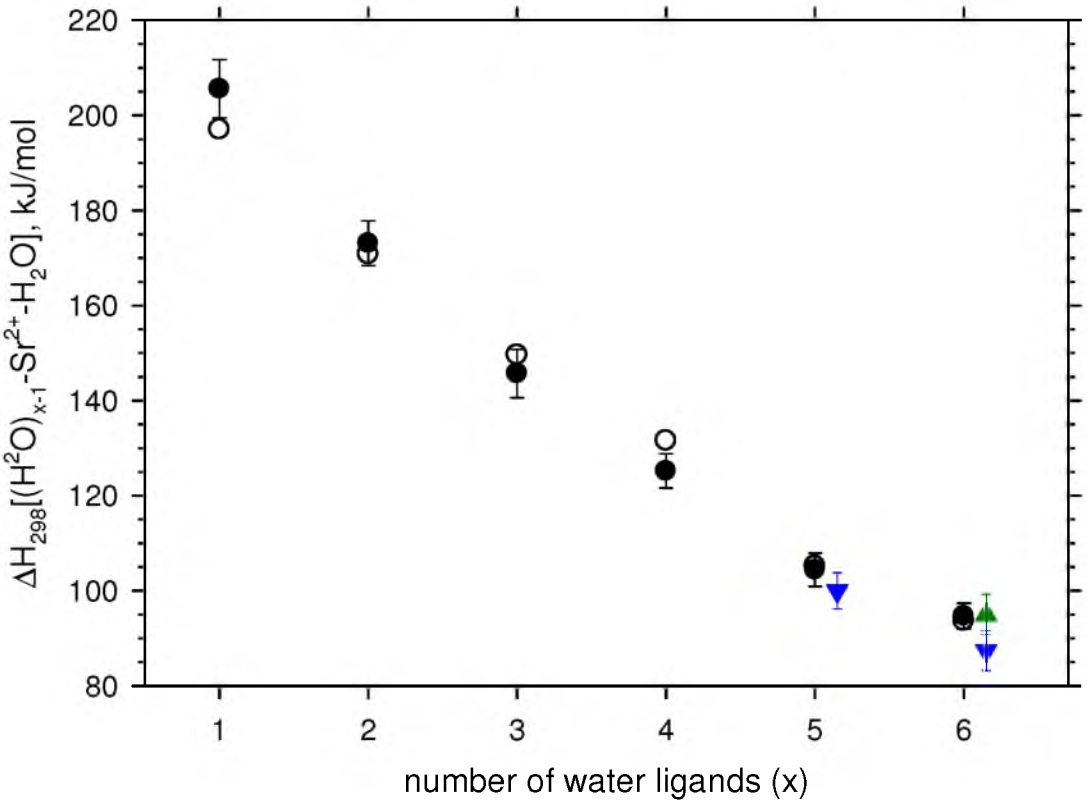

Figure 7.6. Comparison of present experimental (solid circles) and theoretical B3LYP/Def2TZVPP (open circles) bond enthalpies at 298 K. HPMS results from reference 3 (solid triangles) and BIRD results from reference 5 (solid inverted triangles) are also included.

Table 7.1 Parameters used to model primary dissociation process for collision-induced dissociation of $Sr^{2+}(H_2O)_x$ (x = 1 – 6)[a]

Reactant	Product	σ_0[b]	n[b]	E_0 (PSL) (eV)[b]	E_0 (eV)[c]
$Sr^{2+}(H_2O)$	Sr^{2+}	8 (1)	0.9 (0.1)	2.09 (0.06)	2.09 (0.06)
$Sr^{2+}(H_2O)_2$	$Sr^{2+}(H_2O)$	24 (2)	0.8 (0.1)	1.78 (0.05)	1.80 (0.06)
$Sr^{2+}(H_2O)_3$	$Sr^{2+}(H_2O)_2$	41 (3)	0.9 (0.1)	1.49 (0.05)	1.53 (0.06)
$Sr^{2+}(H_2O)_4$	$Sr^{2+}(H_2O)_3$	59 (3)	0.9 (0.1)	1.29 (0.04)	1.43 (0.04)
$Sr^{2+}(H_2O)_5$	$Sr^{2+}(H_2O)_4$	72 (4)	0.8 (0.1)	1.06 (0.04)	1.21 (0.05)
$Sr^{2+}(H_2O)_6$	$Sr^{2+}(H_2O)_5$	84 (3)	0.8 (0.1)	0.97 (0.03)	1.14 (0.04)

[a] Uncertainties are in parentheses.
[b] Parameters from modeling with Equation 2.5, where lifetime effects are included.
[c] Parameters from modeling with Equation 2.4, which excludes lifetime effects.

Table 7.2. Conversion between 0 K binding energies for H_2O loss from $Sr^{2+}(H_2O)_x$ (x = 1 – 6) to enthalpies and free energies at 298 K in kJ/mol[a]

Complex	ΔH_0[b]	ΔH_{298}-ΔH_0[c]	ΔH_{298}	$T\Delta S_{298}$[c]	ΔG_{298}
$Sr^{2+}(H_2O)$	201.3 (6.1)	4.3 (0.2)	205.6 (6.1)	28.5 (0.5)	177.1 (6.1)
$Sr^{2+}(H_2O)_2$	172.1 (4.6)	1.0 (0.2)	173.1 (4.7)	22.8 (1.2)	150.3 (4.8)
$Sr^{2+}(H_2O)_3$	144.2 (5.1)	1.5 (0.2)	145.7 (5.1)	36.3 (1.3)	109.4 (5.2)
$Sr^{2+}(H_2O)_4$	124.2 (3.6)	1.0 (0.2)	125.2 (3.6)	33.1 (1.3)	92.1 (3.9)
$Sr^{2+}(H_2O)_5$	102.6 (3.5)	1.8 (0.3)	104.4 (3.5)	41.5 (1.3)	62.9 (3.7)
$Sr^{2+}(H_2O)_6$	93.6 (2.7)	1.0 (0.3)	94.7 (2.7)	40.2 (1.3)	54.5 (3.0)

[a] Uncertainties are in parentheses.
[b] Experimental values from Table 7.1.
[c] Values were calculated using standard formulae and molecular constants calculated at the B3LYP/HW*/6-311+G(d,p) level. Uncertainties were determined by scaling the vibrational frequencies up and down by 10%.

Table 7.3. Experimental and theoretical 298 K bond enthalpies for H_2O loss from ground state $Sr^{2+}(H_2O)_x$ (x = 1 – 6) in kJ/mol

Experiment		x=1	2	3	4	5	6	
This work		206 ± 6	173 ± 5	146 ± 5	125 ± 4	104 ± 4	95 ± 3	
HPMS[a]							95 ± 4	
BIRD[b]						100 ± 4	87 ± 4	
Geometry[c]	Single point[d]	x=1	2	3	4	5	6	MAD[e]
B3LYP/HW*/ 6-311+G(d,p)	M06	195 (196)	167 (169)	148 (150)	131 (133)	111 (113)	100 (102)	6 ± 3 (7 ± 2)
	B3LYP	192 (192)	165 (166)	146 (148)	130 (131)	104 (106)	93 (95)	5 ± 5 (5± 5)
	B3P86	194 (195)	166 (167)	147 (149)	130 (132)	104 (106)	93 (95)	5 ± 4 (5 ± 4)
	MP2(full)	180 (186)	158 (163)	142 (148)	127 (134)	108 (116)	98 (109)	9 ± 9 (11 ± 6)
B3LYP/SD/ 6-311+G(d,p)	M06	195 (196)	167 (169)	149 (150)	131 (133)	112 (113)	100 (102)	6 ± 2 (7 ± 2)
	B3LYP	193 (193)	166 (167)	147 (149)	130 (132)	104 (106)	93 (95)	5 ± 5 (5 ± 4)
	B3P86	194 (195)	167 (168)	148 (150)	130 (132)	104 (106)	93 (95)	5 ± 4 (5 ± 4)
	MP2(full)	183 (188)	160 (166)	144 (151)	130 (137)	109 (117)	101 (110)	9 ± 8 (12 ± 5)
B3LYP/ Def2TZVP	M06	195 (198)	169 (172)	148 (151)	130 (133)	111 (114)	101 (105)	6 ± 3 (7 ± 4)
	B3LYP	197 (200)	171 (175)	150 (154)	132 (136)	105 (110)	94 (99)	4 ± 3 (6 ± 3)
	B3P86	197 (200)	171 (174)	149 (153)	131 (135)	105 (109)	93 (97)	4 ± 3 (5 ± 3)
	MP2(full)	188 (194)	166 (172)	147 (154)	132 (139)	110 (118)	100 (110)	8 ± 6 (11 ± 5)
BH&HLYP/ Def2TZVPP	BH&HLYP	199 (202)	166 (166)	151 (151)	132 (132)	105 (106)	95 (95)	4 ± 3 (4 ± 3)
GF[f]		198	174	156	141	116	106	10 ± 5
Klobukowski[g]		(181)	(166)	(154)	(137)			(12 ± 5)
BSP[h]		(187)	(168)	(152)				(8 ± 4)
KS[i]		(198)	(179)					(3 ± 3)

Table 7.3. continued

[a] Reference 3.
[b] Reference 5
[c] Level of theory for geometry optimization.
[d] Basis sets for single point energies are HW*/6-311+G(2d,2p), SD/6-311+G(2d,2p), or Def2TZVPP. Single point energies in parentheses do not include counterpoise corrections.
[e] Mean absolute deviations with respect to experimental binding enthalpies.
[f] Theoretical results from reference 10. Glendening and Feller
[g] Theoretical results from reference 11. Values corrected to 298 K.
[h] Theoretical results from reference 12. Values corrected to 298 K.
[i] Theoretical results from reference 13. Values corrected to 298 K.

Table 7.4. Relative 0 K energies of transition states, intermediates, and products for charge separation and water loss from $Sr^{2+}(H_2O)_2$[a]

Complex	HW*[b]	SD[c]	Def2TZVPP[d]
$Sr^{2+}(H_2O) + H_2O$	165, **162**	166, **165**	173, **170**
$Sr^{2+}(H_2O)_2$	0, **0**	0, **0**	0, **0**
TS1	60, **59**	60, **61**	61, **60**
INT (1,1)	56, **58**	57, **60**	57, **58**
TS[0+1]	165, **186**	160, **181**	154, **170**
$SrOH^+ + H_3O^+$	-13, **13**	-24, **4**	-34, **-14**

[a] B3LYP energies are in roman text. MP2(full) energies are in **bold text**.
[b] Single point energies calculated with the HW*/6-311+G(2d,2p) basis set using B3LYP/HW*/6-311+G(d,p) geometries and ZPE corrections.
[c] Single point energies calculated with the SD/6-311+G(2d,2p) basis set using B3LYP/SD/6-311+G(d,p) geometries and ZPE corrections.
[d] Single point energies calculated with the Def2TZVPP basis set using B3LYP/Def2TZVP geometries and ZPE corrections.

References

(1) Whitehouse, C. M.; Dreyer, R. N.; Yamashita, M.; Fenn, J. B. *Anal. Chem.* **1985**, *57*, 675.

(2) Yamashita, M.; Fenn, J. B. *J. Phys. Chem.* **1984**, *88*, 4451.

(3) Peschke, M.; Blades, A. T.; Kebarle, P. *J. Phys. Chem. A* **1998**, *102*, 9978.

(4) Blades, A. T.; Jayaweera, P.; Ikonomou, M. G.; Kebarle, P. *J. Chem. Phys.* **1990**, *92*, 5900.

(5) Rodriguez-Cruz, S. E.; Jockusch, R. A.; Williams, E. R. *J. Am. Chem. Soc.* **1999**, *121*, 8898.

(6) Wong, R. L.; Paech, K.; Williams, E. R. *Int. J. Mass Spectrom.* **2004**, *232*, 59.

(7) Carl, D. R.; Moision, R. M.; Armentrout, P. B. *Int. J. Mass Spectrom.* **2007**, *265*, 308.

(8) Schultz, R. H.; Armentrout, P. B. *Int. J. Mass Spectrom. Ion Proc.* **1991**, *107*, 29.

(9) *NIST Chemistry WebBook, NIST Standard Reference Database Number 69*; Linstrom, P. J.; Mallard, W. G., Eds.; National Institute of Standards and Technology: Gaithersburg MD, 20899, 2003; Vol. (http://webbook.nist.gov).

(10) Glendening, E. D.; Feller, D. *J. Phys. Chem.* **1996**, *100*, 4790.

(11) Klobukowski, M. *Can. J. Chem.* **1992**, *70*, 589.

(12) Bauschlicher, C. W.; Sodupe, M.; Partridge, H. *J. Chem. Phys.* **1992**, *96*, 4453.

(13) Kaupp, M.; Schleyer, P. V. *J. Phys. Chem.* **1992**, *96*, 7316.

(14) Carl, D. R.; Moision, R. M.; Armentrout, P. B. *J. Am. Soc. Mass Spectrom.* **2009**, *20*, 2312.

(15) Iceman, C.; Armentrout, P. B. *Int. J. Mass Spectrom.* **2003**, *222*, 329.

(16) Rodgers, M. T.; Armentrout, P. B. *J. Am. Chem. Soc.* **2000**, *122*, 8548.

(17) Moision, R. M.; Armentrout, P. B. *J. Phys. Chem. A.* **2002**, *106*, 10350.

(18) Moision, R. M.; Armentrout, P. B. *Phys. Chem. Chem. Phys.* **2004**, *6*, 2588.

(19) Moision, R. M.; Armentrout, P. B. *J. Phys. Chem. A.* **2006**, *110*, 3933.

(20) Amicangelo, J. C.; Armentrout, P. B. *J. Phys. Chem. A.* **2000**, *104*, 11420.

(21) Beyer, M.; Williams, E. R.; Bondybey, V. E. *J. Am. Chem. Soc.* **1999**, *121*, 1565.

(22) Shvartsburg, A. A.; Siu, K. W. M. *J. Am. Chem. Soc.* **2001**, *123*, 10071.

CHAPTER 8

COLLISION-INDUCED DISSOCIATION OF HYDRATED MAGNESIUM: EXPERIMENTAL AND THEORETICAL INVESTIGATION OF THE BINDING ENERGIES FOR $Mg^{2+}(H_2O)_x$ COMPLEXES (x = 2 – 10)

Abstract

The sequential bond energies of $Mg^{2+}(H_2O)_x$ complexes, where x = 2 – 10, are measured by threshold collision-induced dissociation (TCID) in a guided ion beam tandem mass spectrometer. From an electrospray ionization source that produces an initial distribution of $Mg^{2+}(H_2O)_x$ complexes where x = 7 – 10, complexes down to x = 3 are formed using an in-source fragmentation technique. Complexes smaller than $Mg^{2+}(H_2O)_3$ cannot be formed in this source because charge separation into $MgOH^+(H_2O)$ and H_3O^+ is a lower energy pathway than simple water loss from $Mg^{2+}(H_2O)_3$. The kinetic energy dependent cross sections for dissociation of $Mg^{2+}(H_2O)_x$ complexes, where x = 3 – 10, are examined over a wide energy range to monitor all dissociation products and are modeled to obtain 0 and 298 K binding energies. Analysis of both primary and secondary water molecule losses from each sized complex provides thermochemistry for the sequential hydration energies of Mg^{2+} for x = 2 – 10 and the first experimental values for x = 2 – 4. Additionally, the thermodynamic onsets leading to the charge separation products from $Mg^{2+}(H_2O)_3$ and $Mg^{2+}(H_2O)_4$ are determined for the first

time. Our experimental results for x = 3 – 7 agree well with quantum chemical calculations performed here and previously calculated binding enthalpies, as well as other experimental methods found in the literature. Present values for x = 8 – 10 are slightly lower than previous experimental results and theory, but overall within experimental uncertainties.

Introduction

The ability of ions to direct the aggregation of solvent is a crucial component of how those ions influence the properties of their solutions. In water, these factors control the acidity of aqueous solutions and constrain the local hydrogen bonding network. Therefore, the noncovalent interactions between ions and water molecules are important to understand from both analytical and fundamental points of view. Although the hydration of ions has been studied for many years, an experimental evaluation of the energetics of such phenomena, especially for the inner hydration shells of multiply charged ions, has only recently begun to be elucidated. As described in previous chapters, the hydration energies for the complete inner solvent shells for Ca^{2+} and Sr^{2+} have been determined utilizing guided ion beam tandem mass spectrometry (GIBMS).[1-3] Other hydration studies have been performed for the group 12 elements, Zn^{2+} and Cd^{2+},[4-7] as well as the transition metal Fe^{2+}.[8] In the present chapter, we further extend these studies to Mg^{2+}, providing hydration energies for $Mg^{2+}(H_2O)_x$ over the range of x = 2 – 10, including the first measurements of the thermochemistry for x = 2 – 4.

Hydrated alkaline earth metal dications are model systems for understanding solvation phenomena because of the closed shell character of the metal dications. Studies of such systems have been greatly aided by the facile generation of $M^{2+}(H_2O)_x$ complexes

using electrospray ionization (ESI).[9-14] For the $Mg^{2+}(H_2O)_x$ system, previous experimental work focused on thermochemistry includes equilibrium results from Kebarle and coworkers, who used high pressure mass spectrometry (HPMS),[11,12] and kinetic measurements from the Williams group, who used blackbody infrared dissociation (BIRD).[13,14] From these experimental studies, the bond dissociation energies (BDEs) for $Mg^{2+}(H_2O)_x$, x = 6 – 14 and x = 5 – 10, respectively, have been determined, leaving theoretical calculations to determine the bond energies for the remaining inner shell complexes (x = 1 – 4). In a related study, Williams and coworkers also found kinetic evidence for (6,0) and (4,2) isomers of $Mg^{2+}(H_2O)_6$.[15] This group also investigated $Mg^{2+}(H_2O)_x$ complexes, x = 6 – 32, via infrared multiple photon dissociation (IRMPD) action spectroscopy in the OH stretching region (2800 – 3800 cm^{-1}) in a Fourier transform ion cyclotron resonance (FT-ICR) mass spectrometer.[16] This study indicates that six water molecules bind directly to magnesium and that even with 32 water ligands, effects of the metal persist in influencing the structure of the outermost water molecules, in contrast to analogous complexes of the larger calcium and barium dications. More qualitative studies have examined the dissociation of the $Mg^{2+}(H_2O)_x$ complexes by charge separation into $MgOH^+(H_2O)_{x-y-1} + H^+(H_2O)_y$. Kebarle and coworkers[11] observed $MgOH^+(H_2O)$ as the largest magnesium hydroxide product ion complex, whereas Shvartsburg and Siu observed $MgOH^+(H_2O)_2$.[17] These observations were used to assign the so-called critical size (x_c), defined in these works as $Mg^{2+}(H_2O)_x$ complexes that do not dissociate exclusively by water loss, as 3 and 4, respectively. Using $Mg^{2+}(H_2O)_x$ complexes formed in a pick-up source, Stace and coworkers observed that under high-energy collision conditions (5 keV with air), their complexes dissociated

primarily by water loss, with contributions from the charge separation reaction, and small amounts of $Mg^+(H_2O)_{x-z}$ products formed by loss of $H_2O^+ + (z-1)\ H_2O$.[18] These dissociative charge transfer products are not observed in either the lower energy collision studies of Kebarle and coworkers, Shvartsburg and Siu, or in the present study. More recent studies by Chen and Stace have identified $Mg^{2+}(H_2O)_4$ as the smallest stable complex.[19]

Not surprisingly, much theoretical work has been performed to understand the binding of water molecules making up the inner and second hydration shells of magnesium dications and includes a diverse group of basis sets and levels of theory.[20-32] Because our data analysis requires reliable molecular parameters for the complexes in question, the present study provides an in-depth theoretical look at the structures and energetics of the $Mg^{2+}(H_2O)_x$ systems (x = 1 – 10), including a more comprehensive exploration of isomers where second shell water molecules hydrogen bond to the inner hydration shell. By comparing our experimental results with these theoretical calculations, we provide a more extensive understanding of the geometric structures of the inner and outer hydration shells. Significantly, there are limited theoretical studies that consider the reaction coordinate for the charge separation pathway, and these examine only $Mg^{2+}(H_2O)_2$ producing $MgOH^+ + H_3O^+$.[33,34] Because the charge separation process is actually observed at larger complex sizes, the present theoretical study is the first to examine experimentally relevant charge separation processes for comparison with those for water loss.

In the present work, we employ threshold collision-induced dissociation (TCID) in a GIBMS equipped with an ESI source to determine the binding enthalpies for

$Mg^{2+}(H_2O)_x$, where x = 2 – 10. The ESI source produces an initial distribution of $Mg^{2+}(H_2O)_x$ complexes with x = 7 – 10, and smaller $Mg^{2+}(H_2O)_x$ complexes, x = 3 – 6, are generated via an in-source fragmentation method,[35] described in Chapter 5. This procedure does not form complexes smaller than $M^{2+}(H_2O)_3$ complex because $Mg^{2+}(H_2O)_3$ preferentially charge separates into $MgOH^+(H_2O) + H_3O^+$ ions instead of losing a water ligand. Therefore, sequential modeling of the primary and secondary water losses from the TCID of $Mg^{2+}(H_2O)_3$ serves as the only means available for us to determine the binding enthalpy for the smallest $Mg^{2+}(H_2O)_x$ complexes. Sequential modeling has been shown to be a viable tool for extracting BDEs for $K^+(NH_3)_x$, where x = 1 – 4,[36] which have also been determined directly by TCID[37] and HPMS.[38] Sequential modeling has been useful in determining binding enthalpies for $Ca^{2+}(H_2O)_x$, x = 1 – 7 (Chapter 6),[39] $Zn^{2+}(H_2O)_x$,[4,5] x = 6 – 9, and $Cd^{2+}(H_2O)_x$, z = 4 – 11.[6,7] In addition to the dominant water loss channels, charge separation of the $Mg^{2+}(H_2O)_3$ and $Mg^{2+}(H_2O)_4$ species into $MgOH^+(H_2O) + H_3O^+$ and $MgOH^+(H_2O)_2 + H_3O^+$, respectively, are examined experimentally as a function of kinetic energy for the first time. For both the dehydration reactions and the charge separation processes, the thermodynamic onsets measured here are compared to theoretical calculations to provide additional insight into these reactions.

Results

Cross sections for collision-induced dissociation. The CID cross sections for $Mg^{2+}(H_2O)_x$, where x = 3 – 10, are shown in Figure 8.1 at Xe pressures of ~0.2 mTorr, which provides the greatest sensitivity for observing minor products. The primary

dissociation process for all complexes studied, except x = 3, is the loss of a single water molecule in Reaction 8.1.

$$Mg^{2+}(H_2O)_x + Xe \rightarrow Mg^{2+}(H_2O)_{x-1} + H_2O + Xe \quad (8.1)$$

Sequential water loss occurs at higher kinetic energies in all systems and could continue until the reactant is completely dehydrated to form Mg^{2+}, however, the $Mg^{2+}(H_2O)$ product ion was the smallest detectable product ion for all studied complexes, Figure 8.1.

In addition to water loss, a proton transfer/charge separation process from the $Mg^{2+}(H_2O)_3$ complex, Reaction 8.2, is observed in the CID of $Mg^{2+}(H_2O)_3$, $Mg^{2+}(H_2O)_4$, and $Mg^{2+}(H_2O)_5$ complexes, Figure 8.1, parts a – c, respectively.

$$Mg^{2+}(H_2O)_3 + Xe \rightarrow MgOH^+(H_2O) + H_3O^+ + Xe \quad (8.2)$$

In the CID of $Mg^{2+}(H_2O)_3$, Figure 8.1a, the thresholds for the $MgOH^+(H_2O)$ and H_3O^+ product cross sections are identical (as they must be) and have lower apparent thresholds (~0.8 eV) than the $Mg^{2+}(H_2O)_2$ product cross section (~1.7 eV). Despite being energetically favored, the magnitude of the charge separation cross section is smaller than that for water loss above ~2.5 eV, which clearly indicates the charge separation process is entropically disfavored. It should be noted that an unknown contamination was present in most data sets for the CID of the $Mg^{2+}(H_2O)_3$ complex (m/z 39), and produced products at both m/z 19 and m/z 21, which overlap with H_3O^+ and $Mg^{2+}(H_2O)$ products, respectively. The data shown in Figure 8.1a is a single data set in which this contamination was not present. Contributions from this contamination to the $Mg^{2+}(H_2O)$ and H_3O^+ product cross sections were removed by collecting the same product masses (m/z 21 and m/z 19, respectively) in the absence the in-source fragmentation voltage used

to produce $Mg^{2+}(H_2O)_3$ and subtracting suitable scaled cross sections from the $Mg^{2+}(H_2O)_3$.

Ideally, the magnitudes of the two charge separation products would be identical, but the $MgOH^+(H_2O)$ product cross section is about three times as large as the H_3O^+ product cross section below ~3 eV, Figure 8.1a, which must be attributed to incomplete collection of the lighter product. The magnitude differences between the two charge separation product cross sections have been highlighted previously for other $M^{2+}(H_2O)_x$ CID experiments.[2-8,39] Because the charge separation products pass over a large Coulombic barrier, they have a substantial kinetic energy release with the lighter product ion having a larger velocity. If this velocity exceeds the center-of-mass velocity, a portion of these ions will backscatter in the laboratory frame and are lost at the entrance to the octopole ion guide. Previous studies on other metals have demonstrated that alternative focusing conditions can be employed to more effectively collect the H_3O^+ product, with a resulting cross section that matches the $MOH^+(H_2O)$ product; however, such conditions sacrifice the overall reactant intensity, increase data collection times, and reduce signal-to-noise ratios. Therefore, in the data analysis below, the charge separation process is most accurately represented as the $MgOH^+(H_2O)$ cross section.

The formation of the $MgOH^+$ product channel observed in Figures 8.1a – 8.1c could potentially arise from a proton transfer/charge separation process from the x = 2 complex to form the $MgOH^+$ and H_3O^+ species. In Figure 8.1a, the H_3O^+ product channel exhibits a small increase near 5 eV that may be indicative of this charge separation process. Additionally, the sequential loss of a water molecule from the $MgOH^+(H_2O)$ may contribute to the $MgOH^+$ product channel, however, the onset of the

$MgOH^+$ product lies ~0.5 eV higher than the maximum in the $MgOH^+(H_2O)$ cross section. Thus, the primary reason for the decline in the $MgOH^+(H_2O)$ cross section is competition with the entropically favored water loss to form $Mg^{2+}(H_2O)_2$, as confirmed in the modeling below.

A second proton transfer/charge separation process, Reaction 8.3, is also observed in the CID of $Mg^{2+}(H_2O)_4$ and $Mg^{2+}(H_2O)_5$, Figures 8.1b and 8.1c.

$$Mg^{2+}(H_2O)_4 + Xe \rightarrow MgOH^+(H_2O)_2 + H_3O^+ + Xe \qquad (8.3)$$

A tail in the H_3O^+ cross section having the same energy dependence as the $MgOH^+(H_2O)_2$ cross section can be observed in the $Mg^{2+}(H_2O)_4$ system, but again with a smaller magnitude. The $MgOH^+(H_2O)_2$ product cross sections clearly have thresholds higher (> 1 eV in the apparent thresholds) than the competing $Mg^{2+}(H_2O)_3$ product cross sections and their relative magnitudes differ by a factor of over 200. These are clear indications that Reaction 3 is entropically and possibly energetically disfavored and therefore very inefficient.

It is worth noting that the formation of $Mg^{2+}(H_2O)_3$ (secondary water loss, m/z 39) from $Mg^{2+}(H_2O)_5$ (m/z 57) shows a low energy feature at ~1% magnitude between 1 and 2 eV, whereas the primary water loss product cross section for $Mg^{2+}(H_2O)_4$ exhibits no such feature, Figure 8.1c. This feature is attributed to a small amount of $K^+(H_2O)$ (m/z 57) that dissociates into K^+ (m/z 39). The $K^+(H_2O)$ contamination can be minimized by using freshly prepared electrospray solutions that are not handled directly. Collection of the $Mg^{2+}(H_2O)_5$ complex via the ^{26}Mg isotope (nominal mass m/z 58) would circumvent this isobaric contamination, but this is not feasible considering the ^{26}Mg isotope has 1/7 the intensity of the ^{24}Mg isotope species. Additionally, the formation of

these smaller $Mg^{2+}(H_2O)_x$ complexes via in-source fragmentation already utilizes low ion intensity to mitigate the formation of excited conformers present in the reactant ion beam as described in Chapter 5. To eliminate the small amount of K^+ contamination, our approach was to perform CID on the $K^+(H_2O)$ and subtract out the contribution from the K^+ product from the $Mg^{2+}(H_2O)_3$ cross section. This procedure is needed for the sequential modeling described below. Ostensibly, $K^+(H_2O)_y$ complexes could also contribute to other $Mg^{2+}(H_2O)_x$ complexes, where x is odd; however, other than $Mg^{2+}(H_2O)_5$, no evidence for such contamination was found.

Theoretical results of $Mg^{2+}(H_2O)_x$ for x = 1 – 10. For $Mg^{2+}(H_2O)_x$ complexes, where x = 1 – 4, B3LYP/6-311+G(2d,2p) (DFT) and MP2(full)/6-311+G(2d,2p) (MP2) levels of theory both predict the lowest energy conformations consist of water molecules bound directly to the Mg center, in agreement with previous theoretical results.[20-24,28,30,31] B3LYP/6-311+G(d,p) optimized geometries for x = 1 – 4 have C_{2v}, D_{2d}, D_3, and S_4 symmetries with Mg-O distances of 1.942, 1.958, 1.987, and 2.021 Å, respectively. Relative 0 K enthalpies and 298 K free energies are presented in Table 8.1 for the ground state (GS) and low-lying $Mg^{2+}(H_2O)_x$ structures for x = 3 – 10. Higher energy structures for x = 3 and 4 were found with (x-1,1) geometries and both single and double acceptor outer shell water ligands. The DFT [MP2] single point energies for (2,1)_D_A and (2,1)_2D_AA structures exceed the 298 K (3,0) GS structure by 89 [94] and 126 [124] kJ/mol, respectively, using the. Likewise, the (3,1)_D_A and (3,1)_2D_AA lie 65 [73] and 75 [80] kJ/mol, respectively, above the 298 K (4,0) GS structure. For the (2,1) species, the double acceptor structure distorts the inner shell water orientations drastically, raising its 0 K energy well above that of the single acceptor structure, whereas

for the (3,1) species, the distortion is less severe such that the AA and A structures are similar in energy at 0 K. At 298 K, the outer-shell single-acceptor water of the (x-1,1)_D_A structures behave as a free rotor, which results in a larger entropic contribution that lowers the free energy of these structures compared to the double acceptor water molecule in the (x-1,1)_2D_AA structure, which is locked into place.

The GS structure for $Mg^{2+}(H_2O)_5$ is a (5,0) structure with C_{2v} symmetry for both DFT and MP2 0 K enthalpies and 298 K free energies, as previously found.[22,24,28-31] The oxygen atoms of the (5,0) structure resemble a square pyramid with four base water molecules, r_{MgO} = 2.052 (2) and 2.105 (2) Å, and a single apex water molecule, r_{MgO} = 2.060 Å. If the inner shell includes only four inner shell water molecules, an outer shell water molecule can either be a single acceptor, (4,1)_D_A, or double acceptor, (4,1)_2D_AA, structure. Relative 0 K enthalpies predict the (4,1)_2D_AA structure is favored over the (4,1)_D_A structure by 3.1 [6.2] kJ/mol, but 298 K free energies predict the (4,1)_D_A structure is lower in energy by 3.6 [0.6] kJ/mol, again a consequence of the free rotor behavior of the single-acceptor second-shell water molecule.

DFT 298 K free energies predict a five water inner shell (5,y) for $Mg^{2+}(H_2O)_x$ complexes, where x = 6 – 10, although six water inner shell structures (6,y) are usually within thermal energies (k_BT = 2.5 kJ/mol) of the calculated GS complexes, Table 8.1. In contrast, MP2 298 K free energies clearly predict (6,y) GS structures with the lowest energy (5,y) structures lying 5 – 12 kJ/mol higher in energy. Both levels of theory place (4,2) structures at energies > 21 kJ/mol above the GS. Using IRMPD spectroscopy, Bush et al. have determined that $Mg^{2+}(H_2O)_6$ has the (6,0) structure with no evidence for bands associated with a second shell water molecule associated with a (5,1) or (4,2) structure.[16]

The spectra for larger complexes are also most consistent with (6,y) structures, such that the relative ordering of the MP2 structures appears to correspond most closely with the true experimental isomer distributions. This conclusion parallels that drawn previously for $Zn^{2+}(H_2O)_x$ complexes, where again IRMPD spectra are most consistent with MP2 predictions and are inconsistent with B3LYP predictions.[40] The remainder of this section will utilize the MP2 results exclusively. $Mg^{2+}(H_2O)_x$ GS and low-lying structures are presented in Figure 8.2 for x = 7 – 10.

For x = 6, the MP2 0 [298] K enthalpies predict a symmetrical (6,0) GS structure favored by 23 [5] kJ/mol, respectively, over the lowest energy five water molecule inner shell complex, (5,1)_2D_A_aA_b, where the subscripts indicate a (apex) or b (base) inner shell water molecules. The (6,0) structure has T_h symmetry with all Mg-O distances being 2.113 Å and hydrogens directed at oxygens on all adjacent water ligands. The single acceptor (5,1)_D_A_a structure lies 11.6 (13.6) kJ/mol above the (5,1)_2D_A_aA_b structure. Free energies for x = 6 complexes having a four water inner shell lie more than 36 kJ/mol above the GS structures, Table 8.1 Pavlov et al. found that a (4,2) structure was 18.4 kJ/mol above the (6,0) GS,[24] comparable to our B3LYP excitation energy of 21.6 kJ/mol, Table 8.1.

For $Mg^{2+}(H_2O)_7$, both a (6,1)_2D_AA and (6,1)_D_A complex were located as the only six inner shell structures, Figure 8.2, with the former being the GS (by 2.8 kJ/mol) at 0 K and the latter being the GS at 298 K (by only 0.2 kJ/mol) because of the near free rotation of the outer shell water. All (5,2) complexes lie more than 10 kJ/mol higher in free energy and (4,3) complexes lie >38 kJ/mol above the predicted GS structure. Pavlov et al. determined that the (7,0) structure was very high in energy, lying

63.2 kJ/mol above the GS.[24] For x = 8, the (6,2)_DD,2D_2AA (1) structure represents the lowest energy calculated structure. This structure optimizes with the oxygen atoms of both outer shell water molecules in the same plane as all atoms of the three inner shell water molecules to which they are bound, Figure 8.3. Two (6,2)_4D_2AA structures, designated as (1) and (2) lie within 3 kJ/mol of the (6,2)_DD,2D_2AA (1) structure. In the (6,2)_4D_2AA (2) structure, the outer shell water molecules lie directly across from another, whereas in the (6,2)_4D_2AA (1), they utilize adjacent pairs of inner shell water molecules, Figure 8.3. Four complexes having single acceptor water molecules in the second solvent shell lie 10 – 20 kJ/mol above the ground state at 0 K, but drop to 1 – 8 kJ/mol at 298 K. The lowest of these, (6,2)_3D_AA,A could only be localized using an ultrafine grid for the optimization. Two (6,2)_2D_2A structures differ in whether the outer shell waters lie across from one another (1), Figure 8.3, or on inner shell ligands that are perpendicular (2). All remaining (6,2) and all (5,3) complexes lie 11 – 25 kJ/mol above the MP2 GS.

At $Mg^{2+}(H_2O)_9$, the (6,3)_6D_3AA structure is the GS and has all inner shell water molecules donating one hydrogen bond, i.e., each outer shell water molecule binds to a separate pair of inner shell water ligands, Figure 8.4. The three lowest lying isomers are (6,3)_DD,4D_3AA (1), (6,3)_DD,3D_2AA,A, and (6,3)_2DD,2D_3AA (1) structures lying 2.4, 7.9, and 8.3 kJ/mol above the GS, Figure 8.4. The two 3AA structures bind to different sets of inner shell waters compared to the GS, leaving either one or two inner shell ligands uncoordinated, whereas the 2AA,A structure has one single acceptor in the second shell, thereby allowing more extensive hydrogen bonding among the inner shell waters. Other unique (6,y,z) structures lie 9 – 17 kJ/mol above the (6,3) MP2 GS and

(5,y,z) structures are more than 11 kJ/mol higher than the GS. For x = 10, the (6,4)_2DD,4D_4AA (1) structure is the MP2 GS structure. In this structure, two pairs of outer shell waters lie in planes perpendicular to one another, Figure 8.5. Three additional six water inner shell structures were located with 298 K free energies 3.8 – 9.6 kJ/mol above the GS structure and can be described by adding the tenth water to the (6,3)_6D_3AA structure. The tenth water can simply hydrogen bond to one of the single donor inner shell waters yielding (6,4)_DD,5D_3AA,A, or it can bridge between this position and one of the second shell waters forming (6,3.5,0.5)_DD,5D_2AA,AAD_A_1A_2, or bridge between two inner shell waters forming (6,4)_2DD,4D_4AA (2). Interestingly the (6,3.5,0.5) structure in which one water binds to both an inner and second shell ligand is isoenergetic with the GS at 0 K, but the extra constraint of the ring-like structure limits its entropy, such that it lies 9.6 kJ/mol above the (6,4) GS at 298 K. All (5,y,z) structures lie 10 kJ/mol higher than the GS, with the (5,5)_4DD,D_4A_bA_b,A_a, formed by adding the tenth water to the (5,4)_4DD_4A_bA_b structure at the apex inner shell water, being the lowest.

Thermochemical results for primary water loss from $Mg^{2+}(H_2O)_x$ complexes, x = 3 – 10. The total cross sections for dissociation of the $Mg^{2+}(H_2O)_x$ complexes by water loss, Reaction 8.1, and subsequent processes were modeled using Equations 2.4 and 2.5. The total cross sections are modeled because the cross sections for Reaction 8.1 are influenced by sequential dissociation of additional water molecules as shown in Figure 8.1. The optimum fitting parameters for modeling the primary water loss from the $Mg^{2+}(H_2O)_x$ complexes, where x = 3 – 10, are listed in Table 8.2. In all threshold analyses, the reactant isomer corresponds to the 298 K GS, which comprises the largest

population at thermal energies and the product isomer corresponds to the 0 K GS because our threshold analysis is dominated by the lowest 0 K enthalpy species.[4] GS structures used in these analyses correspond to those predicted by the MP2(full)/6-311+G(2d,2p) level of theory, which clearly results in a six water inner shell, for reasons noted above. The models of Equation 2.5 are compared to the zero-pressure extrapolated cross sections for all $x \geq 4$, as shown in Figure 8.6. For x = 3, individual pressure data sets are analyzed because there was no obvious pressure dependence observed and zero-pressure extrapolated cross sections are too noisy to adequately define the fitting parameters. In all cases, the model reproduces the total cross section for water loss over extended energy and magnitude ranges.

For x = 3 – 7, the data could be modeled accurately with Equation 2.4, which does not include lifetime effects. The difference in the threshold energies obtained using Equations 2.4 and 2.5 provides the kinetic shift, which ranges between 0.08 and 0.22 eV; however, no clear trend in these values is observed. For larger complexes, x = 8 – 10, the data could not be reproduced using Equation 2.4, which demonstrates that lifetime effects must be considered in order to obtain accurate thermochemistry.

Reaction thresholds for losing a single water molecule decrease with increasing size of the $Mg^{2+}(H_2O)_x$ complex for x = 3 – 10. Thresholds values in the range of x = 3 – 6 decrease sharply whereas x = 7 – 10 complexes exhibit a more gentle decrease. This suggests the formation of a second solvent shell once six water molecules bind to the Mg^{2+} center, in agreement with theory and the IR action spectroscopy results.[16]

Thermochemical results for competitive modeling of $Mg^{2+}(H_2O)_3$ and $Mg^{2+}(H_2O)_4$. In addition to the inner shell hydration energies of the $Mg^{2+}(H_2O)_x$ system,

it is of interest to determine the thermodynamic onsets for the rate-limiting TSs for the charge separation processes from $Mg^{2+}(H_2O)_3$, Reaction 8.2, and $Mg^{2+}(H_2O)_4$, Reaction 8.3. The product cross sections for $MgOH^+(H_2O)$ and $MgOH^+(H_2O)_2$ were modeled independently and in competition with water loss using Equation 2.5. Optimum fitting parameters for these models are also presented in Table 8.2.

Independent analysis of the water loss and charge separation pathways (modeled as the sum of all cross sections) for $Mg^{2+}(H_2O)_3$ produce 0 K reaction thresholds of 2.31 ± 0.13 eV and 1.53 ± 0.20 eV, respectively. With the competitive model, the charge separation cross section cannot be accurately reproduced using the computed vibrational frequencies for the rate-limiting TS[1+1] of the charge separation pathway unless relative scaling factors, $\sigma_{0,j}$ in Equation 2.5, for the two channels are different by factors of 10^6 - 10^{10}. Competitive analysis using unscaled frequencies results in thresholds values of 2.32 ± 0.03 eV and 1.78 ± 0.20 eV for water loss and charge separation, respectively, with the latter being 0.25 eV higher than the corresponding independent analysis. We have previously suggested that such a nonphysical scaling factor may indicate inaccurate transition state frequencies.[5,41] In this case, the scaling factor suggests that TS[1+1] is too loose or the TS for water loss is too tight, where the latter conclusion is at odds with the phase space limit already used. To produce a more physically realistic representation of the competition, the vibrational frequencies below 650 cm^{-1} of TS[1+1], which are most likely to be inaccurately determined, are scaled up. When these frequencies are multiplied by a factor of 6.2 – 8.3, a $\sigma_{0,j}$ scaling factor near unity is obtained and the competitive analysis is able to reproduce both cross sections from threshold to 5 eV with high fidelity, as shown in Figure 8.7a. This model demonstrates that the decline in the

$MgOH^+(H_2O)$ cross section is a result of competition with the entropically favored water loss channel. The 0 K reaction threshold for the charge separation pathway is determined as 1.12 ± 0.13 eV, 0.41 eV lower than for independent analysis, which is consistent with the tighter TS, and the threshold for the water loss pathway remains nearly the same as the independent analysis, slightly increasing from 2.31 ± 0.13 eV to 2.34 ± 0.15 eV. These same competitive product channels are also observed in the CID of $Mg^{2+}(H_2O)_4$, where independent analysis of the secondary water loss reveals a threshold of 4.06 ± 0.16 eV, which decreases to 3.89 ± 0.12 eV when competition with $MgOH^+(H_2O)$ is considered, resulting in a competitive shift of 0.17 ± 0.20 eV, Table 8.2 and Figure 8.7b. In this competitive analysis, frequencies of TS[1+1] were scaled between 1.0 – 1.3 in order to increase the cross section scaling factors to near unity.

The zero-pressure extrapolated cross section for the charge separation process from $Mg^{2+}(H_2O)_4$ into $MgOH^+(H_2O)_2$ and H_3O^+ ions over TS[2+1], Reaction 8.3, was modeled independently (not shown) and in competition with the primary water loss, Figure 8.7c. In this case, because of the small magnitude of the $MgOH^+(H_2O)_2$ cross section (0.1 $Å^2$ maximum), accurate energy-dependent cross sections could only be obtained at higher Xe pressures. In this analysis, the vibrational frequencies less than 800 cm^{-1} for the rate-limiting TS of the charge separation pathway from $Mg^{2+}(H_2O)_4$, TS[2+1], were scaled by 1.2, such that the cross section scaling factor for charge separation would approach unity. In this system, independent and competitive analyses yield nearly identical thresholds for both channels, as might be expected given the very small charge separation cross section. Interestingly, both analyses also indicate that the threshold for charge separation lies slightly below that for water loss, which differs from

the conclusion drawn from apparent thresholds. Indeed, the mere observation of these charge separation products is some indication that this entropically favored channel must compete energetically.

Thermochemical results for sequential modeling. Thermochemical results utilizing the sequential model[36] are presented in Table 8.3 for x = 3 – 10 and a representative example of the model is provided in Figure 8.8 for x = 6. The sequential model reproduces the primary and secondary cross sections from threshold energies to ~5 eV. For $Mg^{2+}(H_2O)_3$ and $Mg^{2+}(H_2O)_4$, competition with the charge separation pathway is not included as the results of the previous section indicate that it does not affect the thresholds for the water loss channel in the primary analysis. The differences between the primary and secondary thresholds, shown in brackets in Table 8.3, provide a second independent measurement of the bond dissociation energy (BDE) for $Mg^{2+}(H_2O)_{x-1}$ dissociating to $Mg^{2+}(H_2O)_{x-2} + H_2O$ and is referred to as a secondary BDE. Secondary BDEs typically have small uncertainties (0.01 – 0.08 eV for x = 4 – 10) despite using results from multiple data sets because many systematic uncertainties in the measurements cancel for these relative measurements.[36] The uncertainty in the secondary BDE obtained from the $Mg^{2+}(H_2O)_3$ system is much larger because of the very small magnitude of the $Mg^{2+}(H_2O)$ cross section and the complications associated with removing contributions from the unknown contamination.

Table 8.3 also includes primary BDEs from Table 8.2 for comparison to these secondary BDEs. The σ_0, E_0, and n values of Equation 2.5 from modeling the total cross sections of $Mg^{2+}(H_2O)_x$ complexes, Table 8.2, are nearly identical to those in Table 8.3, with analogous E_0 values within 0.01 eV for x = 5 – 10. For these complexes, secondary

BDEs are slightly larger than the primary BDEs with differences of 0.02 – 0.14 eV. For the smallest complexes, x = 3 and 4, the σ_0, E_0, and n values from modeling the total cross sections, Table 8.2, no longer agree well with the sequential modeling results in Table 8.3, with analogous E_0 values differing by 0.11 – 0.23 eV. For these cases, the secondary reactions occur at sufficiently high energies that the shape of the cross section (as parameterized by n in Equation 2.5) cannot reproduce the high energy region while maintaining the integrity of the fit in the threshold for the primary water loss. To fit these higher energy ranges, the parameter n must decrease, which concomitantly results in a higher primary threshold value. Alternatively, the primary thresholds for x = 3 and 4 can be kept fixed at their optimum values from Table 8.2, while all other parameters were allowed to optimize. This procedure shows slightly larger secondary thresholds for x = 3 (by 0.12 eV) and 4 (by 0.05 eV) compared to allowing all parameters to optimize, Table 8.3. In addition, the secondary BDE value for x = 4 and possibly x = 3 is affected by competition with the charge separation pathway, which introduces a competitive shift of 0.17 ± 0.20 eV, as determined above from the analysis of secondary water loss with and without competition with the charge separation pathway in the CID of x = 4. This competitive shift reduces the secondary BDEs from 2.66 ± 0.06 and 2.71 ± 0.05 eV to 2.49 ± 0.21 and 2.54 ± 0.21 eV, respectively, within experimental uncertainty of the 2.31 ± 0.13 eV primary value. For dissociation of $Mg^{2+}(H_2O)_2$ to $Mg^{2+}(H_2O)$, there is no primary value available for comparison. The secondary BDEs obtained by the two different treatments are similar, ranging from 2.66 ± 0.37 – 2.78 ± 0.41 eV, suggesting that this result is a reasonable estimate of the true BDE within the uncertainty. An additional check of this value is provided by analysis of the primary and secondary cross

sections for data that are contaminant free but measured only at high pressure, which means it could be shifted to lower energies. This yields a secondary BDE of 2.55 eV, well within the uncertainty of our best value for x = 2.

Conversion of 0 K hydration energies to 298 K. To convert our 0 K hydration energies to enthalpies and free energies at 298 K, H_{298} - H_0 and $T\Delta S_{298}$ values are calculated with a rigid rotor/harmonic oscillator approximation using the rotational constants and vibrational frequencies calculated at the B3LYP/6-311+G(d,p) level of theory. The uncertainties in these values are determined by scaling the vibrational frequencies up and down by 10%. These conversion factors are used to calculate ΔH_{298} and ΔG_{298} values in Table 8.4 for both the primary and secondary BDEs, which are compared to previous theoretical calculations and experimental results. It should be realized that some of the low-lying vibrational frequencies correspond to torsional motions of the water ligands (hindered rotations) such that their treatment as harmonic oscillators may not be completely accurate. Such differences may explain why the theoretical entropies of Table 8.4 are considerably lower than experimentally determined $T\Delta S_{298}$ values from HPMS equilibrium[12] experiments for x = 6, 8, and 9, differing by 13, 16, and 15 kJ/mol, respectively; however, values for x = 7 and 10 differ only by 0.4 and -4 kJ/mol. Alternatively, such differences could be attributed to populations in the HPMS reactant chamber of low-lying x and x-1 conformations containing five inner shell waters. This seems plausible given that calculated $T\Delta S_{298}$ values for the (5,y) structures of x = 6 – 10 complexes are 33, 54, 40, 39, and 30 kJ/mol, leading to differences from the HPMS values of 3, 23, 5, 7, and 3 kJ/mol.

Theoretical bond enthalpies. Theoretical bond enthalpies for losing a single water molecule from the 298 K GS $Mg^{2+}(H_2O)_x$ structures are listed in Table 8.5 and were calculated from B3LYP and MP2(full) levels of theory using a 6-311+G(2d,2p) basis set and B3LYP/6-311+G(d,p) optimized geometries. Zero-point energies and thermal corrections to 298 K with and without counterpoise corrections (cp) for basis set superposition errors are included. Unlike $Ca^{2+}(H_2O)_x$ results for x = 1 – 6 where B3LYP and B3P86 produced nearly identical binding energies, the energetic differences for magnesium are noticeable. B3LYP energies are larger by 8 [19], 6 [14], and 2 [6] kJ/mol for x = 1 – 3, respectively, nearly identical for x = 4 and lower by 3 [5 – 7] kJ/mol for x = 5 and 6 compared to B3P86 [MP2(full)] energies. B3P86 energies for x = 7 – 10 complexes are larger than corresponding B3LYP energies by 2 – 3 kJ/mol whereas MP2(full) results show < 1 kJ/mol difference. B3P86 energies are not included in Table 8.5. Counterpoise corrections are 2 – 4 kJ/mol for both DFT methods (average of 3 ± 1 kJ/mol), but 6 – 13 kJ/mol for MP2(full) (average of 9 ± 2 kJ/mol) with the largest BSSE determined for $Mg^{2+}(H_2O)_6$.

A split-level basis set treatment was also pursued for geometry optimizations and subsequent single point energies for x = 1 – 6 complexes using Dunning's aug-cc-pVTZ basis set for water molecules and the cc-pCVTZ basis set for magnesium. The cc-pCVTZ, basis set includes extra functions designed for core-core and core-valence correlation. The combination of these basis sets is denoted as pCVTZ. Correlation has been shown to be important in accurately describing the binding energies for $Ca^{2+}(H_2O)$ and $Ca^{2+}(H_2O)_2$ in Chapter 6 compared to a strictly Pople-style basis set treatment. BSSEs are typically less than 2 kJ/mol for DFT methods employing the pCVTZ basis set,

whereas MP2(full) corrections are still larger, 5 – 10 kJ/mol. DFT/pCVTZ binding enthalpies are 9, 5, and 4 kJ/mol larger than their DFT/6-311+G(2d,2p) counterparts for x = 1 – 3 complexes, respectively, whereas x = 4 – 6 differ by less than 2 kJ/mol. MP2(full)/pCVTZ energies predicted tighter binding energies by 13, 9, 7, 6, 4, and 4 kJ/mol for x = 1 – 6 compared to analogous MP2(full)/6-311+G(2d,2p) results. Only B3LYP/pCVTZ results are provided in Table 8.5.

Literature calculations. An extensive number of theoretical investigations have been conducted in the literature for $Mg^{2+}(H_2O)_x$, where x = 1 – 6, employing numerous levels of theory and basis set treatments.[20-32] As many of these results are similar to one another and to the present calculations, only a few of these studies are highlighted below. Glendening and Feller (GF) calculated hydration energies for $Mg^{2+}(H_2O)_x$, x = 1 – 6, employing a MP2(FC)/6-31+G(d)//RHF/6-31+G(d) level of theory.[22] For the geometry optimization and single point energy calculations, correlation of the inner-shell 1s electrons of O and 1s, 2s, and 2p electrons of Mg was neglected in the MP2(FC) treatment. ZPE, thermal, and BSSE corrections were included in this study with their final values. GF demonstrated that their values gave very similar trends to previous calculations of Klobukowski,[20] Bauschlicher et al.[21] and Kaupp and Schleyer.[32] Not surprisingly, we find that their values are very similar to the MP2(full) values calculated here, lying in between our values with and without cp corrections. Pavlov et al.[24] have determined geometries for $Mg^{2+}(H_2O)_x$ complexes where x = 1 – 8 with B3LYP using a Hay/Wadt ECP treatment for magnesium and a LANL2DZ basis set for O and H, followed by single point energy calculations that include ZPE corrections at the B3LYP/6-311+G(2d,2p) level. For x = 1 – 6, all waters bind directly to Mg^{2+} and

secondary solvent shell structures for x = 7 and 8 presented are identical to our lowest energy (6,1)_2D_AA and (6,2)_DD,2D_2AA (1) complexes, described above. Their binding energies do not include counterpoise corrections, and therefore are very similar to our B3LYP values without cp corrections once their values have been adjusted to 298 K using thermal corrections calculated here. Recent theoretical calculations by Rao et al. have determined sequential BDEs of $Mg^{2+}(H_2O)_x$ complexes, where x = 1 – 6 using an identical protocol as described in Chapter 6 for $Ca^{2+}(H_2O)_x$ complelxes.[31] Geometry optimizations and frequency calculations were first performed at the B3LYP/6-31G(d) level of theory to locate minimum energy conformations. The lowest energy conformations were then subjected to further optimizations at the B3LYP/6-311++G(d,p) level of theory followed by single point energies calculated at several levels with the highest being the CCSD(T)/6-311++G(d,p) level of theory. G3 calculations were also reported in this study. Despite including counterpoise corrections to their BDEs, the authors did not include ZPE or thermal corrections. As a result, we performed additional geometry and frequency calculations (scaled by 0.989) at the B3LYP/6-311++G(d,p) level of theory and adjusted their BDEs to 298 K to allow for comparison to our theoretical results. In addition, the geometry determined by Rao et al. for $Mg^{2+}(H_2O)_6$ differs from the ground state structure determined here (as well as most previous theoretical studies). As discussed above, we find that the lowest energy structure has a highly symmetric T_h geometry that maximizes inner shell hydrogen bonding (hydrogen atoms of all water molecules are directed towards oxygen atoms on adjacent water molecules), whereas the $Mg^{2+}(H_2O)_6$ structure optimized by Rao et al. has D_3 symmetry, which allows hydrogen-hydrogen repulsions. At the B3LYP/6-311++G(d,p) level, the T_h

structure is 15.1 kJ/mol lower in energy at 0 K than the D_3 structure. Overall, once these adjustments are made, the values from this work are again similar to those presented here for the B3LYP and MP2(full). The Rao et al. CCSD(T) results are slightly lower than our MP2(full)/6-311+G(2d,2p) results by an average of 4 ± 3 kJ/mol.

Charge separation channels. $Mg^{2+}(H_2O)_3$ undergoes charge separation to form $MgOH^+(H_2O)$ and H_3O^+ in Reaction 8.2 and has a lower apparent threshold than the $Mg^{2+}(H_2O)_2$ product cross section, Figure 8.1a. Charge separation also takes place from the $Mg^{2+}(H_2O)_4$ complex to form $MgOH^+(H_2O)_2$ and H_3O^+ products in Reaction 8.3, however, the $MgOH^+(H_2O)_2$ product cross section has a higher apparent threshold than the $Mg^{2+}(H_2O)_3$ product cross section and is smaller by over two orders of magntitude, Figures 8.1b and 8.1c. We have previously defined the critical size (x_c) for a $M^{2+}(H_2O)_x$ system as the complex size at which charge separation becomes the lower energy pathway compared to simple ligand loss.[35] Thus, these observations suggest that the critical size for hydrated magnesium complexes is $x_c = 3$. However, our data analysis of the charge separation process for $x = 4$ indicates it has a similar but slightly lower threshold (by 0.04 eV) compared to water loss, Table 8.2. The small magnitude of the $MgOH^+(H_2O)_2$ cross section makes this measurement somewhat tenuous, although the mere observation of the entropically disfavored $MgOH^+(H_2O)_2$ product ion indicates that the threshold for Reaction 8.3 must be close to that for Reaction 8.1, if not lower. This observation echoes the findings for $Ca^{2+}(H_2O)_3$ and $Sr^{2+}(H_2O)_2$ data presented in Chapters 6 and 7, respectively. Therefore, a critical size of $x_c = 4$ for the $Mg^{2+}(H_2O)_x$ system cannot be discounted. The assignment of $x_c = 3$ agrees with the conclusions of Chen and Stace[19] and Kebarle and coworkers,[11] whereas $x_c = 4$ agrees with Shvartsburg

and Siu.[17] In the latter two studies, the authors assigned the critical value on the basis of $MgOH^+(H_2O)_{xc-1}$ being the largest magnesium hydroxide cation observed, thereby assuming that H_3O^+ was formed concomitantly, as verified experimentally here. In contrast, Chen and Stace assigned the critical size on the basis of their observation that the minimum number of water molecules required to stabilize Mg^{2+} against spontaneous charge separation was four. This conclusion is in direct conflict with our observation that $Mg^{2+}(H_2O)_3$ requires energy to undergo charge separation, Figure 8.1a. The difference in observations can probably be reconciled if the pick-up/electron ionization source used to generate the $Mg^{2+}(H_2O)_x$ complexes yields relatively hot ions.

The theoretical reaction coordinates for charge separation from $Mg^{2+}(H_2O)_3$ and $Mg^{2+}(H_2O)_4$ are calculated at the B3LYP/6-311+G(d,p) level of theory and shown in Figure 8.9, parts a and b, respectively. The charge separation process involves transferring a water molecule from the inner solvent shell through TS1 to the second solvent shell, where it binds through a single hydrogen bond forming the (x-1,1) intermediate (INT). As the products separate, a proton is transferred to the second solvent shell water molecule, thereby allowing formation of two singly charged ions that separate from one another over a large Coulombic barrier at TS[x-2 + 1].[33] TS[1+1] and TS[2+1] are found to have separations between the incipient products of r_{OH} = 3.21 and 3.55 Å, respectively, with imaginary frequencies of 72 and 62 cm^{-1}, respectively. Table 8.6 provides relative energies for the TSs, intermediates, and products of the charge separation and water loss pathways for the $Mg^{2+}(H_2O)_3$ and $Mg^{2+}(H_2O)_4$ ground state structures calculated at the B3LYP, B3P86, and MP2(full) levels with a 6-311+G(2d,2p) basis set using the B3LYP/6-311+G(d,p) geometries and frequencies for zero point

energy corrections. For charge separation from $Mg^{2+}(H_2O)_3$, B3LYP and B3P86 energies of the trihydrate complex are nearly identical to the sum of energies for $MgOH^+(H_2O)$ and H_3O^+ products whereas MP2(full) calculations predicts the trihydrate is lower in energy by 11 kJ/mol with respect to the charge separation products. All levels of theory predict the $Mg^{2+}(H_2O)_4$ complex is 32 – 45 kJ/mol lower in energy than the $MgOH^+(H_2O)_2 + H_3O^+$ products.

Discussion

Comparison between present primary and secondary experimental values. Trends in the experimental 298 K binding enthalpies are shown in Figure 8.10. The secondary binding enthalpies are consistently larger than the corresponding primary BDEs for x = 3 – 9, with a MAD of 7 ± 5 kJ/mol. Primary and secondary binding enthalpies differ by 2 – 7 kJ/mol for x = 4, 5, and 7 – 9, well within experimental uncertainties, whereas larger differences (14 kJ/mol) are found for x = 3 and 6. The results for x = 3 agree within combined uncertainties whereas the x = 6 values do not overlap. Overall, the primary BDEs are believed to be inherently more reliable than the secondary BDEs because the kinetic and internal energy distributions of the associated energized molecule are better characterized, whereas statistical assumptions are needed to provide this information for the secondary dissociation processes. Clearly, the secondary bond enthalpies represent accurate upper limits for the binding enthalpies for x = 3 – 9. In that regard, the secondary BDE for x = 2 can also be viewed as an upper limit, but shifting it down by 7 ± 5 kJ/mol would have little influence on the final value given the already large uncertainty.

Comparison between present and literature experimental values. The binding enthalpies for $Mg^{2+}(H_2O)_x$ complexes have previously been reported for x = 6 – 14 and x = 5 – 10 using equilibrium[11,12] and kinetic[13,14] approaches, respectively. These results are included in Table 8.5 and Figure 8.10 along with the present experimental primary and secondary binding enthalpies. For x = 5, our primary bond enthalpy is nearly 10 kJ/mol larger than the BIRD result, but within the combined experimental uncertainties. Our primary value for x = 6 agrees quite well with both HPMS and BIRD results, with the secondary value being ~12 kJ/mol higher. We observe a relatively large decrease in binding enthalpies between x = 6 and 7 of 27 [38] kJ/mol from primary [secondary] modeling. The former value is slightly larger than the changes determined by HPMS (18 kJ/mol), but agrees well with the BIRD result (23 kJ/mol). Our second solvent shell BDEs (x = 7 – 10) show similar values for x = 7 and 8, a drop of 8 kJ/mol for x = 9, and another drop of 19 kJ/mol to x = 10. A very similar pattern is observed in the BIRD values except these values are uniformly 7 ± 2 kJ/mol higher than the present results. The binding enthalpies from HPMS are also higher but by less systematic amounts, 11 ± 7 kJ/mol. Such differences are comparable to those observed for x = 7 – 9 complexes of $Ca^{2+}(H_2O)_x$,[3,39] with differences of 9 ± 5 kJ/mol (BIRD) and 5 ± 3 kJ/mol (HPMS). One possible explanation for these systematic shifts is that the $H_{298} - H_0$ thermal adjustments applied here are inaccurate for the second shell water molecules.

Comparison between present experimental and theoretical values for x = 1 – 6. The primary and secondary experimental bond enthalpies are compared with B3LYP/6-311+G(2d,2p) [B3LYP/pCVTZ] and MP2(full)/6-311+G(2d,2p) values in Table 8.5 and Figure 8.10. Figure 8.10 shows that the overall pattern in the binding

energies is the same for both experimental determinations made here as well as for theory. For the inner shell complexes, x = 3 – 6, the agreement between the primary binding enthalpies and the calculated BDEs is excellent with MADs of 3 ± 2 [4 ± 1] and 5 ± 5 kJ/mol. Primary bond enthalpies for x = 7 – 10 are lower than calculated energies by 2 – 15 kJ/mol and increase the MADs for x = 3 – 10 to 6 ± 5 (B3LYP) and 7 ± 5 kJ/mol (MP2) when they are taken into account. Similar differences in the ability of theory to reproduce the first and second hydration shells were observed for $Ca^{2+}(H_2O)_x$ complexes.[39] The MAD of the secondary BDEs with respect to the theoretical results for x = 2 – 6 are larger, 14 ± 12 [14 ± 15] and 10 ± 9 kJ/mol, but decrease to 9 ± 3 [7 ± 3] and 7 ± 8 kJ/mol if the secondary BDE for x = 2 is excluded from the MAD comparison. For the second solvent shell, x = 7 – 9, secondary bond enthalpies are lower than calculated energies by 0 – 12 kJ/mol with MADs of 5 ± 6 and 5 ± 5 kJ/mol. Overall, the secondary bond enthalpies for x = 2 – 9 have MADs compared to theory of 11 ± 11 [14 ± 15] and 8 ± 8 kJ/mol, which are larger than those for the primary bond enthalpies, although if the value for x = 2 is excluded, these decrease to 7 ± 4 [7 ± 3] and 6 ± 6 kJ/mol, within 3 kJ/mol of the analogous primary MADs of 6 ± 5 [4 ± 1] and 7 ± 5 kJ/mol. Overall, the various levels of theory considered here provide comparable agreement with experiment for both the inner and outer shell hydration enthalpies. The addition of core polarization has only a small effect over the range of x = 4 – 6 complexes, with larger increases for x = 1 – 3. For $Ca^{2+}(H_2O)_x$ complexes, pCVTZ basis sets are larger for x = 1 and 2 compared to the Pople-style basis sets using the same level of the theory.[39] We point out that that the larger discrepancies between theory and

experiment for the second solvent shell compared to the first solvent shell may be a reflection of the inherent inaccuracies of the theoretical treatment of hydrogen bonding.

The theoretical results can also be compared to the HPMS[11,12] and BIRD results. B3LYP (MP2) results have MADs compared to the HPMS results for x = 6 – 10 of 7 ± 3 (9 ± 2) kJ/mol, slightly better than a comparison of our primary values over the same range, with MADs of 9 ± 5 (10 ± 5) kJ/mol. For the BIRD results of x = 5 – 10, the MADs are 4 ± 2 (6 ± 5) kJ/mol, whereas they are 8 ± 5 (9 ± 5) kJ/mol for our primary values over the same range.

Comparison with theoretical results from the literature. As noted above, results from the literature are essentially reproduced by the present calculations. Our B3LYP results match those of Pavlov et al.[24] (MAD compared to primary experimental BDEs of 5 kJ/mol for x = 3 – 8 versus 4 kJ/mol for the present B3LYP values). Our MP2 results essentially reproduce values from Glendening and Feller[22] (MAD of 9 kJ/mol for x = 3 – 6 versus 5 kJ/mol here with cp corrections and 14 kJ/mol without) and the CCSD(T) results of Rao et al.[31] (MAD of 5 kJ/mol for x = 3 – 6 versus 5 kJ/mol here). Hence the only values added to Table 8.5 from the literature are the G3 results from Rao et al.,[31] which can be seen to overestimate both the primary and secondary experimental bond enthalpies by large amounts (MADs of 17 – 20 kJ/mol). Clearly, G3 theory, which was not calibrated using any systems like the present non-covalent hydration systems, is not an accurate method of calculating this type of thermochemistry. G3 was also found to overbind in the $Ca^{2+}(H_2O)_x$ system, although with smaller discrepancies.[39]

Comparison of experimental and theoretical values for charge separation. The thermodynamic onsets associated with the rate limiting transition state TS[1+1] and

TS[2+1] for charge separation were determined by modeling the $MgOH^+(H_2O)_x$ product cross sections independently and competitively with water loss from the $Mg^{2+}(H_2O)_3$ and $Mg^{2+}(H_2O)_4$ complexes, respectively, with results compiled in Table 8.6. For x = 4, the independent and competitive analyses yield similar thresholds for charge separation near 174 kJ/mol that agree nicely with the rate limiting TS[2+1] located at 180 (DFT) and 190 (MP2) kJ/mol. Furthermore, theory finds these thresholds lie 0 – 3 kJ/mol below those for simple water loss, in agreement with the experimental differences of 4 ± 6 kJ/mol. For x = 3, theory and experiment agree that the threshold for charge separation lies well below that for water loss. We believe that the best measurement of the energy for TS[1+1] comes from analysis of the total cross section, 148 ± 19 kJ/mol, with the results from competitive fits shifting both up (172 ± 12 kJ/mol) and down (108 ± 13 kJ/mol) depending on the details of additional scaling assumptions needed to reproduce the competition. This value agrees reasonably well with the theory values of 162 – 169 kJ/mol. All levels of theory predict charge separation over TS[1+1] is favored over water loss by 61 – 69 kJ/mol, Table 8.6. These findings are within experimental uncertainties of the measured differences of 75 ± 18 kJ/mol from independent modeling and 53 ± 9 kJ/mol from one of the competitive models that did not include frequency scaling.

The theoretical results for $Mg^{2+}(H_2O)_3$ can also be compared to measurements of Chen and Stace regarding the average kinetic energy release upon separation to $MgOH^+(H_2O) + H_3O^+$.[19] Their measurement of 209 kJ/mol is somewhat above the reverse barriers calculated here, 158 – 162 kJ/mol (Table 8.6), or the maximum experimental value of 171 ± 12 kJ/mol (which presumes that the product asymptote of 1 kJ/mol is correct). Note that addition of the 209 kJ/mol value to the calculated product

asymptotes puts the energy of TS[1+1] at 210 – 220 kJ/mol, which is still below that for water loss. but with an energy difference that is inconsistent with our experimental measurements. These differences could reflect inaccuracies in the calculated TS[1+1] barrier height or the product asymptotic energy, or could indicate that excess energy in the original complex makes its way into the kinetic energy release of these products.

Conclusions

The kinetic energy dependent cross sections for $Mg^{2+}(H_2O)_x$ where x = 3 – 10 are measured by threshold collision-induced dissociation using a guided ion beam mass spectrometer equipped with an electrospray ionization source. The ESI source produces an initial distribution of $Mg^{2+}(H_2O)_x$ ions, where x = 7 – 10, having suitable ion intensities for TCID studies. Smaller $Mg^{2+}(H_2O)_x$ complexes, where x = 3 – 6, are accessed using an in-source fragmentation technique that takes place in the high pressure region of the rf-only hexapole ion guide.[35] $Mg^{2+}(H_2O)_2$ and $Mg^{2+}(H_2O)$ complexes cannot be produced in this manner because the charge separation process that forms $MgOH^+(H_2O)$ and H_3O^+ ions is a lower energy process compared to water loss from $Mg^{2+}(H_2O)_3$. Experimental results confirm this observation and demonstrate that the critical size complex[5] is certainly $x_c \geq 3$ for the $Mg^{2+}(H_2O)_x$ system, with $x_c = 4$ being a distinct possibility.

The dominant process taking place for all $Mg^{2+}(H_2O)_x$ complexes is the loss of a single water molecule. Charge separation processes are observed once the $Mg^{2+}(H_2O)_4$ and $Mg^{2+}(H_2O)_3$ complexes are reached. For $Mg^{2+}(H_2O)_4$, the magnitude of the product cross section for charge separation is about 200 times smaller than the $Mg^{2+}(H_2O)_3$ product cross section. Experimental results and theoretical calculations indicate these

processes are energetically similar, but charge separation is entropically disfavored, which explains why the $Mg^{2+}(H_2O)_3$ complex can be generated with the in-source fragmentation technique. Experimental results and theoretical calculations of the charge separation process from $Mg^{2+}(H_2O)_3$ indicate that charge separation is energetically favored over water loss, which is consistent with the relative apparent thresholds of the charge separated products with respect to water loss in the CID of $Mg^{2+}(H_2O)_3$. Here, these cross sections differ by only about a factor of four in magnitude, with the entropically favored water loss channel dominating again at higher energies.

In an attempt to determine the hydration energies for the complete inner shell of the $Mg^{2+}(H_2O)_x$ system, secondary binding enthalpies for $Mg^{2+}(H_2O)_x$ complexes, where $x = 2 - 9$, were determined by analyzing the primary and secondary water losses in the CID of $x = 3 - 10$ using a sequential model.[36] These secondary results are consistently larger than corresponding primary results for all x (by an average of 7 ± 5 kJ/mol, comparable to the average experimental uncertainty of 9 ± 3 kJ/mol), suggesting they are most conservatively regarded as upper limits. In the case of the BDE for $x = 2$, which is available only from analysis of the secondary dissociation, the experimental value is somewhat below theory, however, they agree within the larger uncertainties associated with this value, a consequence of the very small cross section for production of $Mg^{2+}(H_2O)$ and an unknown contamination.

The present TCID work determines the first experimental hydration energies for $Mg^{2+}(H_2O)_2$ to $Mg^{2+}(H_2O)_4$. Our experimental hydration energies for $Mg^{2+}(H_2O)_5$ to $Mg^{2+}(H_2O)_{10}$ are in reasonable agreement with available thermochemistry from HPMS[11,12] and BIRD[13,14] studies although the present value for $x = 5$ is slightly higher

and those for x = 8 – 10 are slightly lower, but still within the combined experimental uncertainties in most cases. The present experimental hydration energies for the inner shell complexes, where x = 3 – 6, are in good agreement with theoretical bond enthalpies calculated at the B3LYP/6-311+G(2d,2p)//B3LYP/6-311+G(d,p) and MP2(full)/6-311+G(2d,2p)//B3LYP/6-311+G(d,p) levels of theory. Values for the second shell agree nicely for x = 7 but are lower for x = 8 – 10, just outside of experimental uncertainty. Additionally, the thermodynamic onsets of the rate limiting TSs for charge separation from $Mg^{2+}(H_2O)_3$ and $Mg^{2+}(H_2O)_4$ have been measured experimentally for the first time and are comparable to the theoretical values.

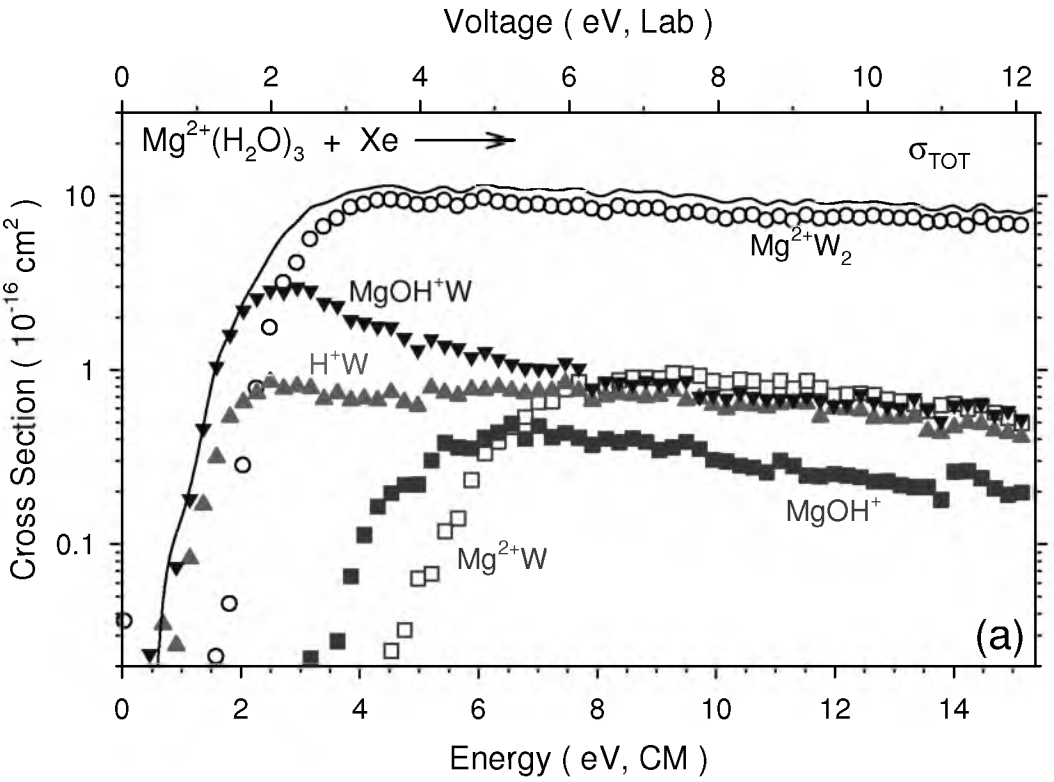

Figure 8.1. Cross sections for collision-induced dissociation of $Mg^{2+}(H_2O)_x$, where x = 3 – 10 (a – h, respectively) with Xenon (~0.2 mTorr) as a function of kinetic energy in the center-of-mass frame (lower x-axis) and applied voltage in the laboratory frame (top x-axis). W = H_2O.

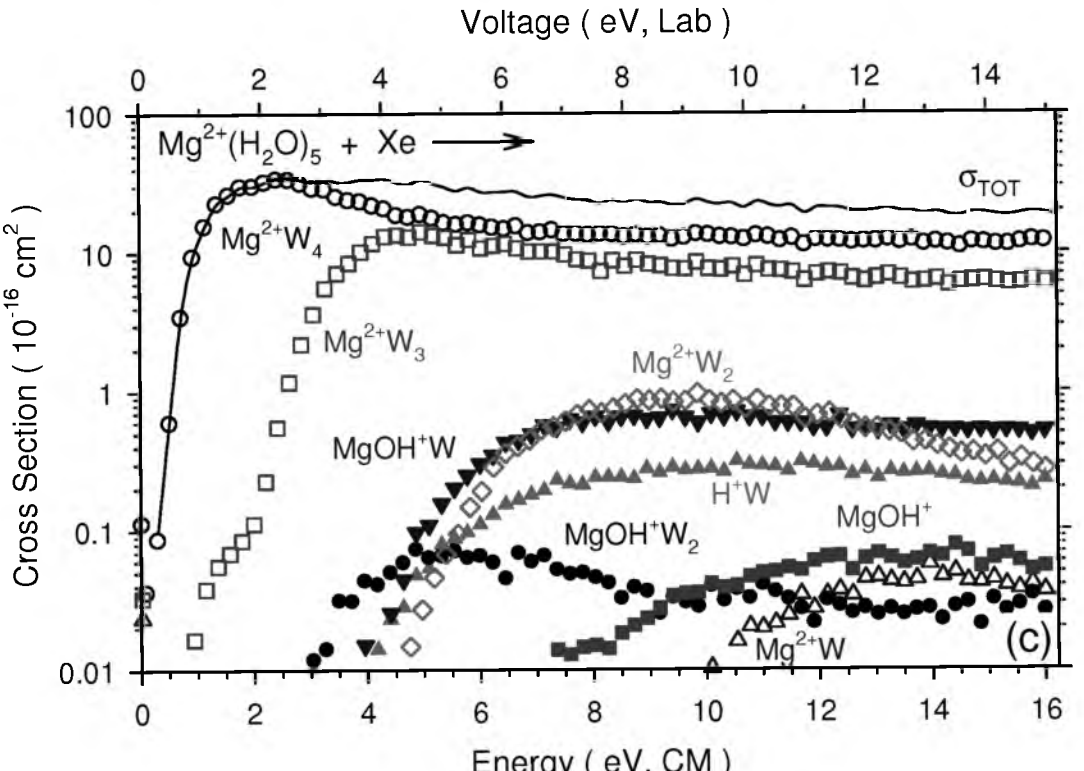

Figure 8.1. continued

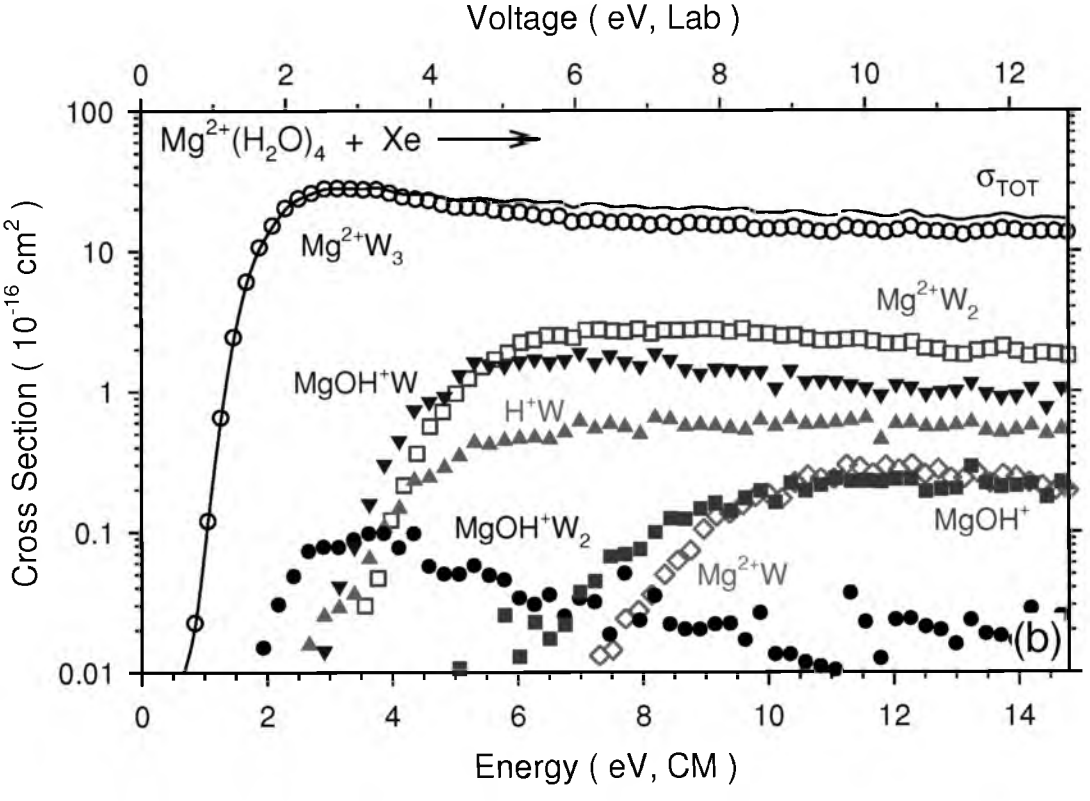
Voltage (eV, Lab)
0
2
4
6
8
10
12
100
10
1
0.1
0.01
Cross Section (10^-16 cm^2)
Mg2+(H2O)4 + Xe
σTOT
Mg2+W3
Mg2+W2
MgOH+W
H+W
MgOH+W2
MgOH+
Mg2+W
(b)
0
2
4
6
8
10
12
14
Energy (eV, CM)

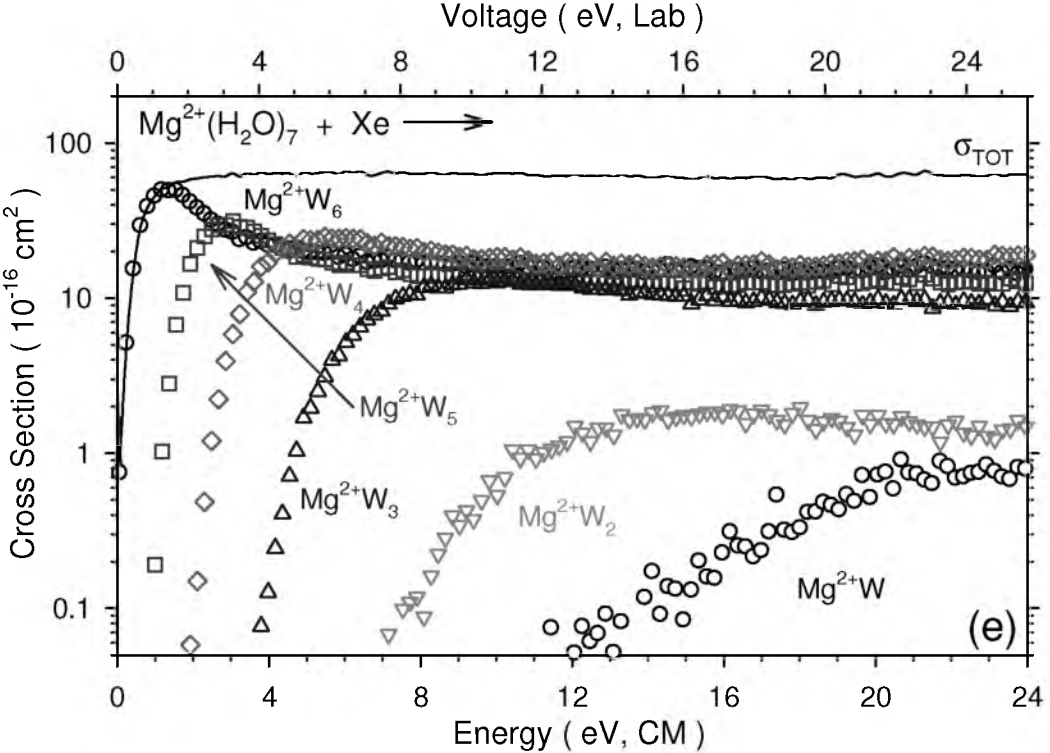

Figure 8.1. continued

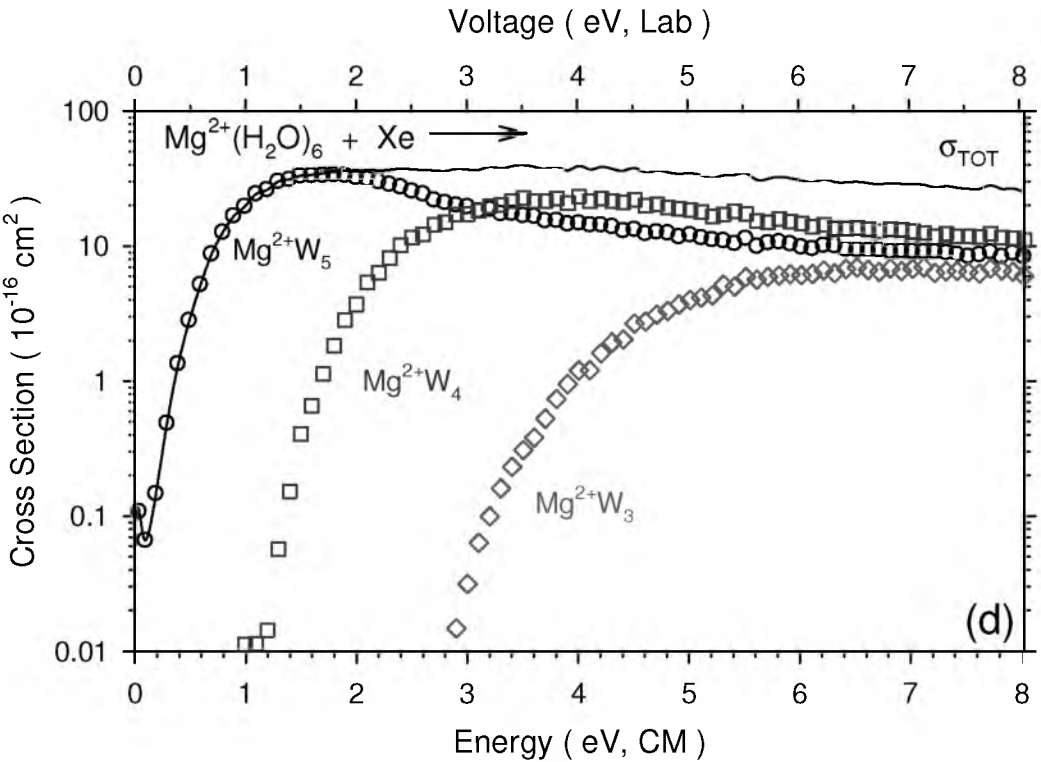
Voltage (eV, Lab)
0
1
2
3
4
5
6
7
8
100
10
1
0.1
0.01
Cross Section (10^-16 cm^2)
Mg2+(H2O)6 + Xe
σTOT
Mg2+W5
Mg2+W4
Mg2+W3
(d)
Energy (eV, CM)

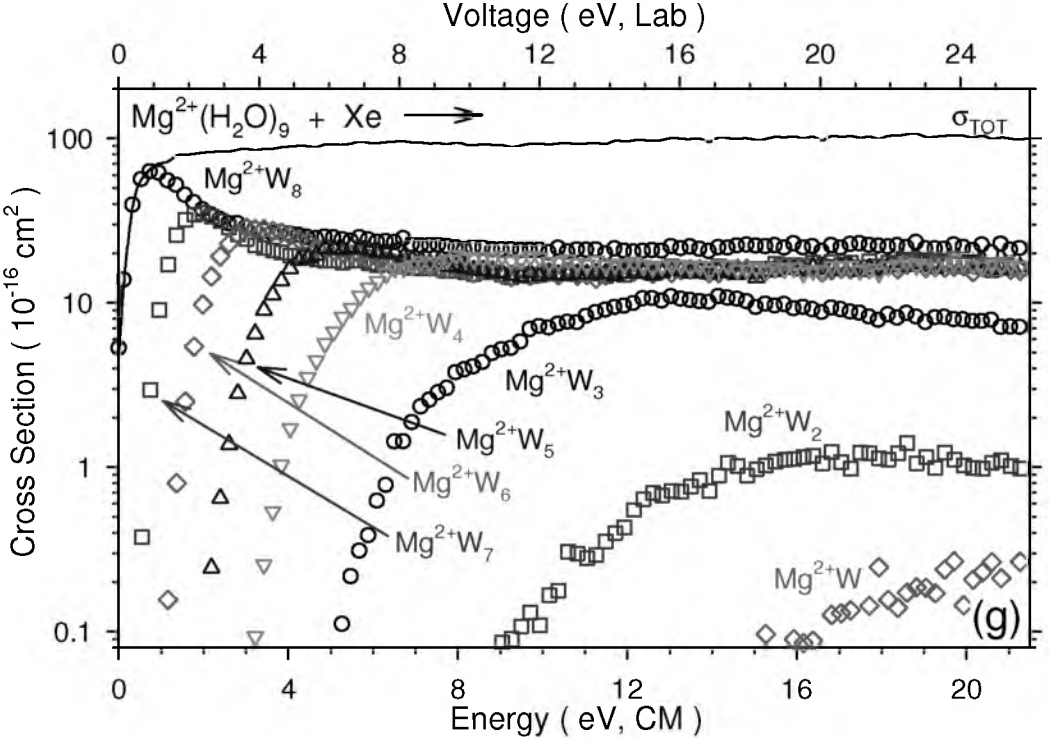

Figure 8.1. continued

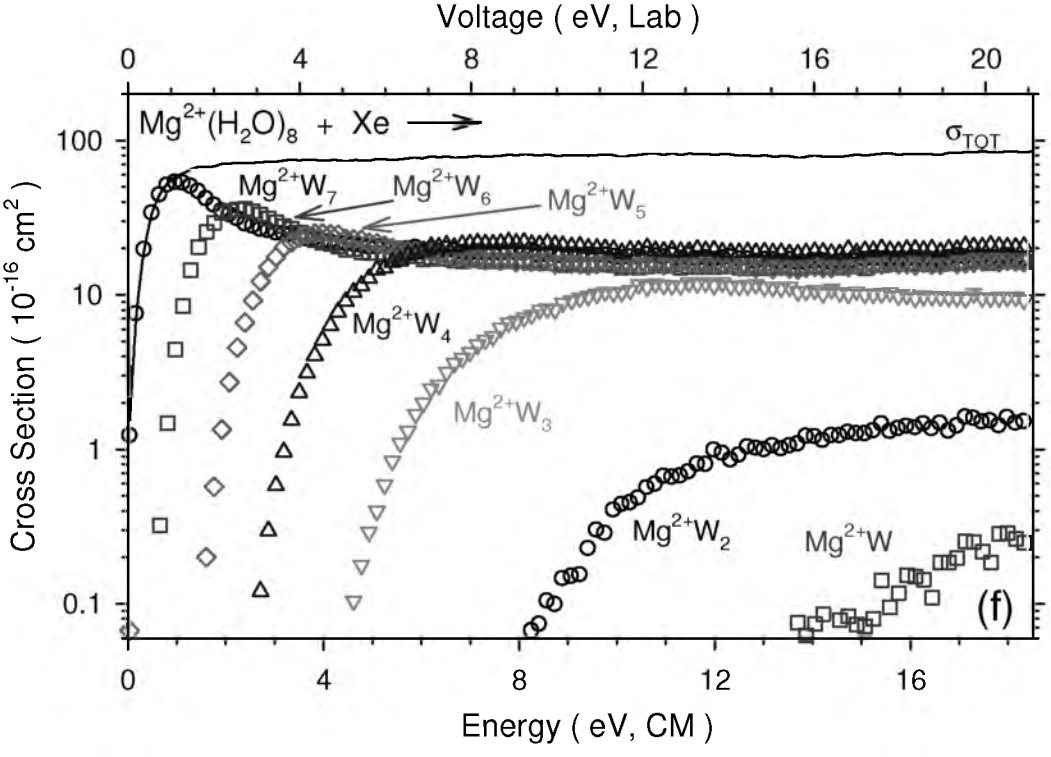
Voltage (eV, Lab)
0
4
8
12
16
20
$Mg^{2+}(H_2O)_8$ + Xe
σ_{TOT}
$Mg^{2+}W_7$
$Mg^{2+}W_6$
$Mg^{2+}W_5$
$Mg^{2+}W_4$
$Mg^{2+}W_3$
$Mg^{2+}W_2$
$Mg^{2+}W$
(f)
Cross Section (10^{-16} cm^2)
100
10
1
0.1
0
4
8
12
16
Energy (eV, CM)

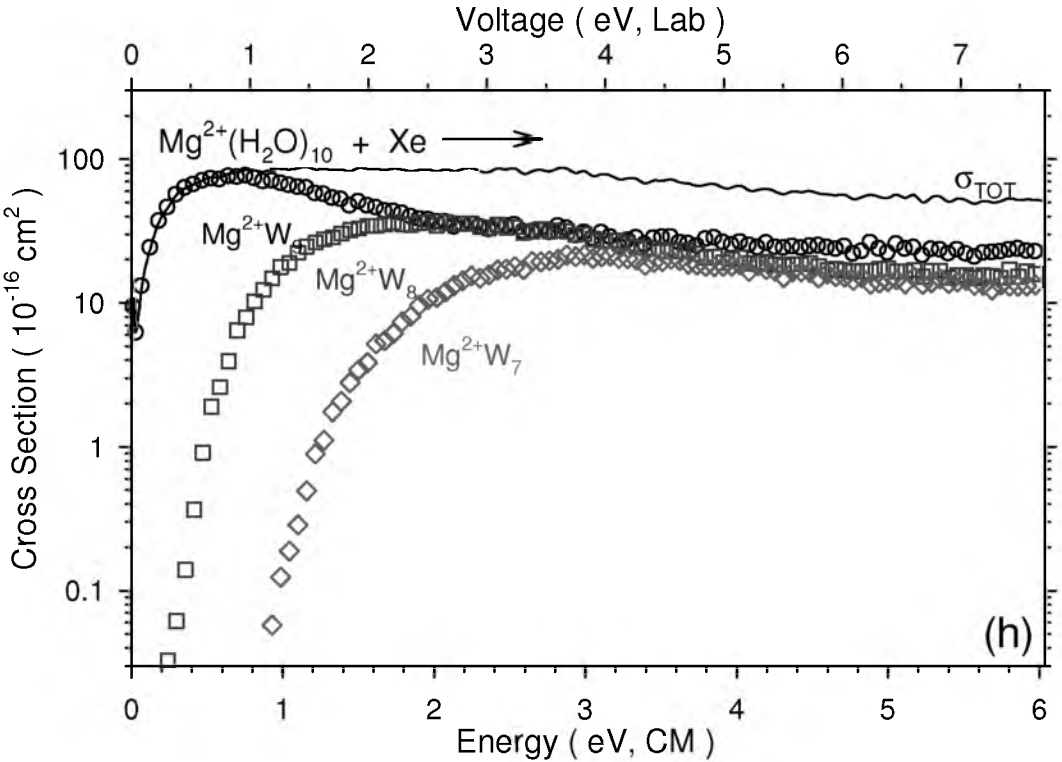

Figure 8.1. continued

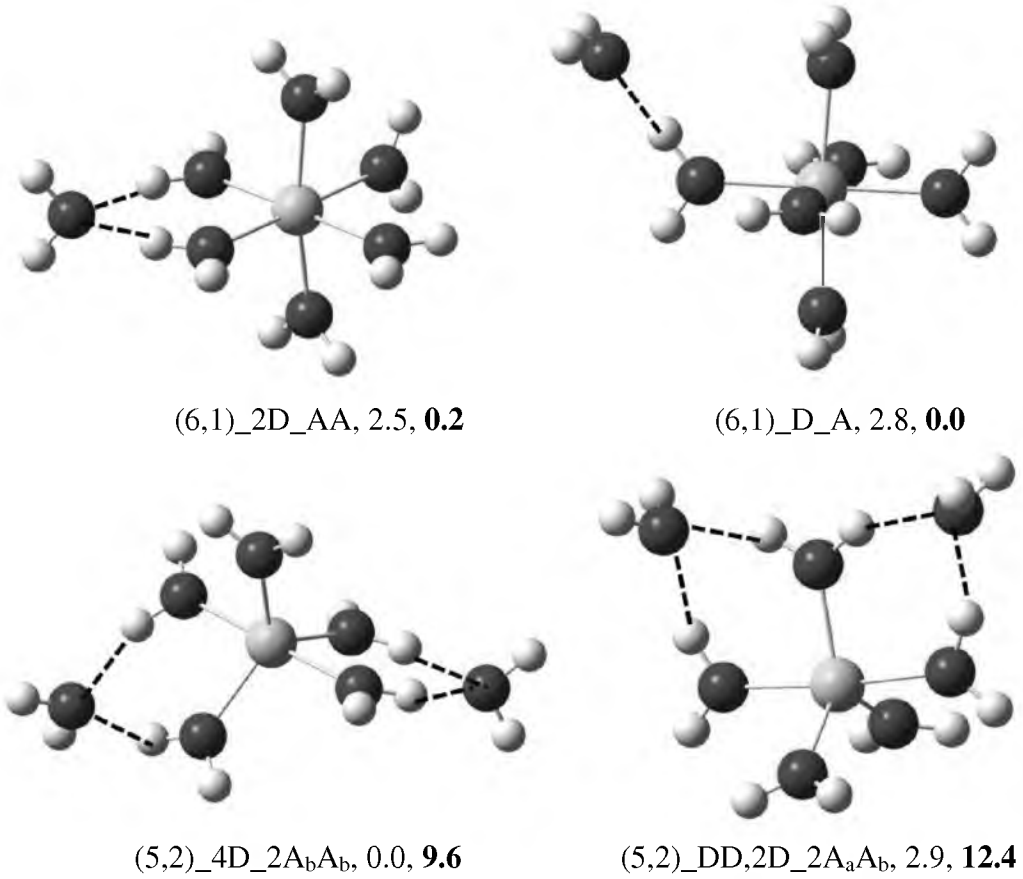

Figure 8.2. Ground-state and low-lying geometries of $Mg^{2+}(H_2O)_7$. Hydrogen bonds are shown as dashed lines. The relative B3LYP/6-311+G(2d,2p)//B3LYP/6-311+G(d,p) (roman) and MP2(full)/6-311+G(2d,2p)//B3LYP/6-311+G(d,p) (**bold**) 298 K free energies (kJ/mol) from Table 8.1 are provided.

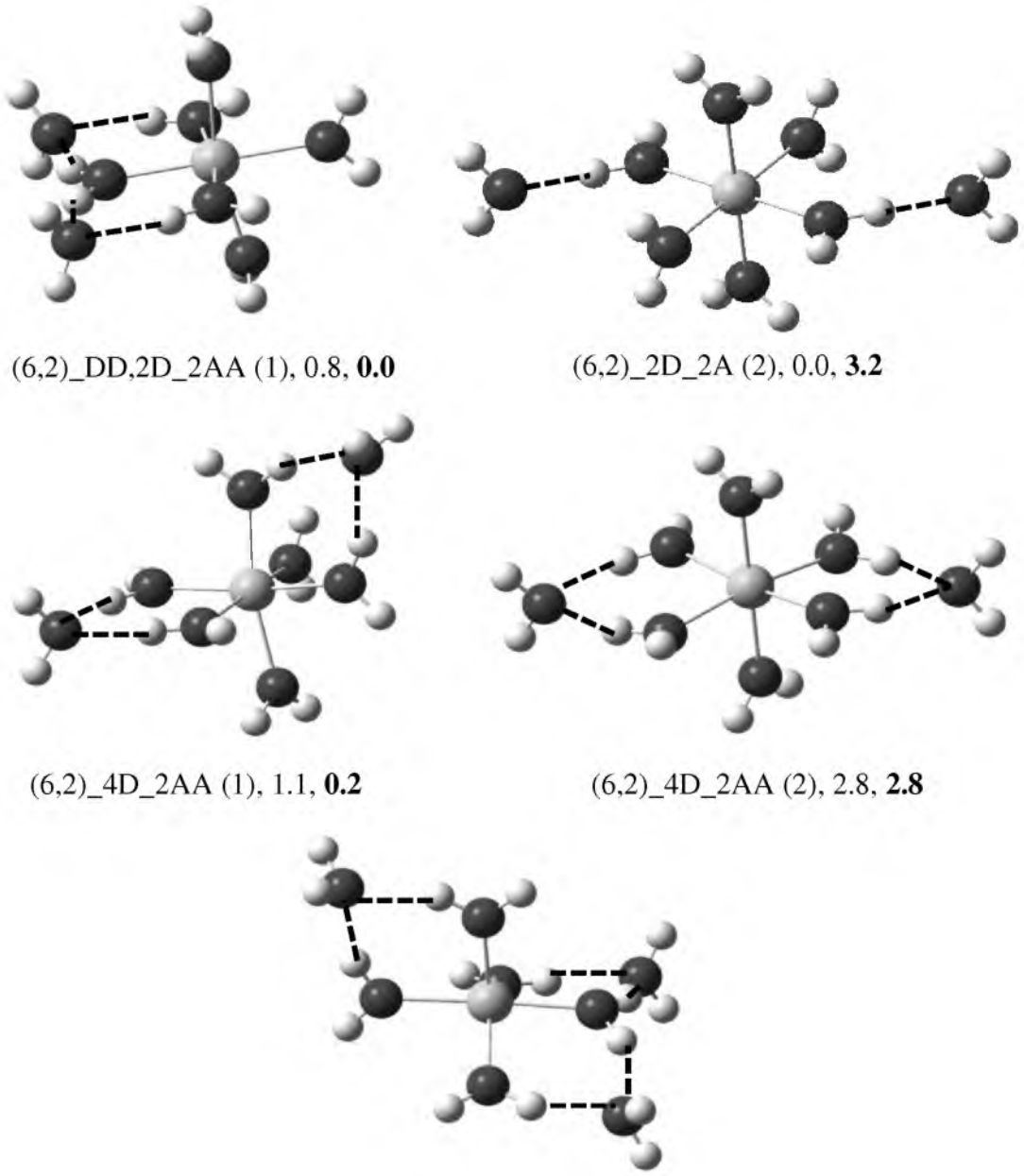

Figure 8.3. Ground-state and low-lying geometries of $Mg^{2+}(H_2O)_8$. Hydrogen bonds are shown as dashed lines. The relative B3LYP/6-311+G(2d,2p)//B3LYP/6-311+G(d,p) (roman) and MP2(full)/6-311+G(2d,2p)//B3LYP/6-311+G(d,p) (**bold**) 298 K free energies (kJ/mol) from Table 8.1 are provided.

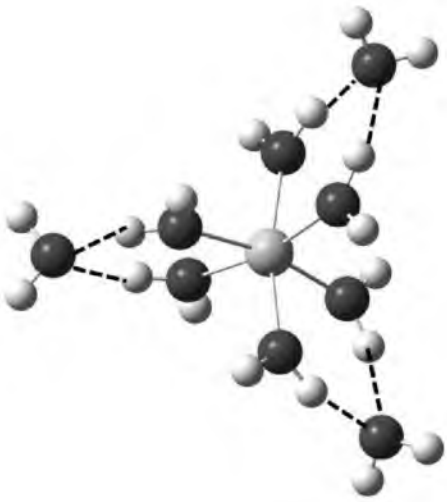

(6,3)_6D_3AA, 0,6, **0.0**

(6,3)_DD,4D_3AA (1), 3.1, **2.4**

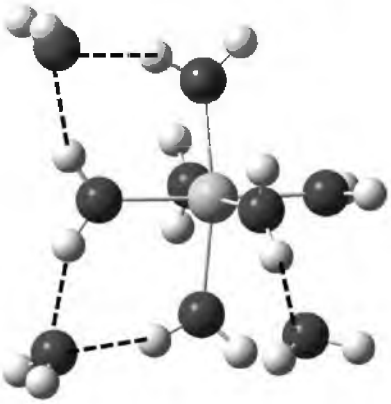

(6,3)_DD,3D_2AA,A, 6.9, **7.9**

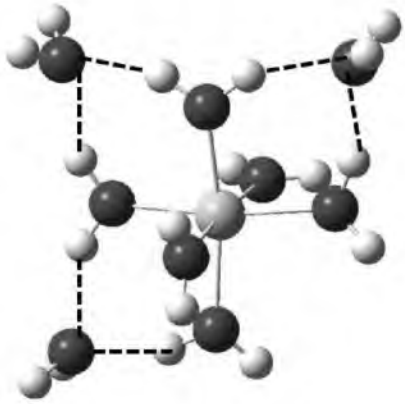

(6,3)_2DD,2D_3AA (1), 9.0, **8.3**

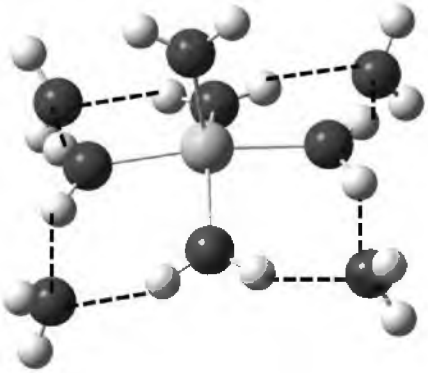

(5,4)_4DD_4A_bA_b, 0.0, **10.9**

Figure 8.4. Ground-state and low-lying geometries of $Mg^{2+}(H_2O)_9$. Hydrogen bonds are shown as dashed lines. The relative B3LYP/6-311+G(2d,2p)//B3LYP/6-311+G(d,p) (roman) and MP2(full)/6-311+G(2d,2p)//B3LYP/6-311+G(d,p) (**bold**) 298 K free energies (kJ/mol) from Table 8.1 are provided.

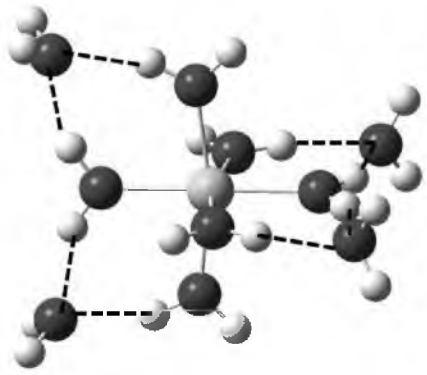

(6,4)_2DD,4D_4AA (1), 3.7, **0.0**

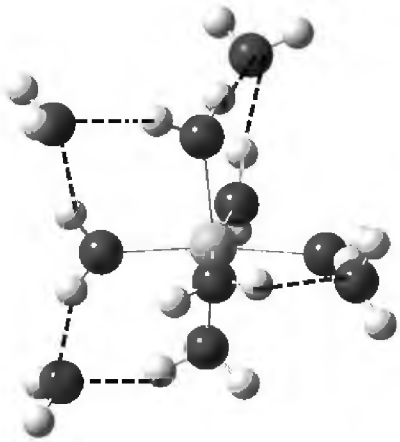

(6,4)_2DD,4D_4AA (2), 12.7, **7.5**

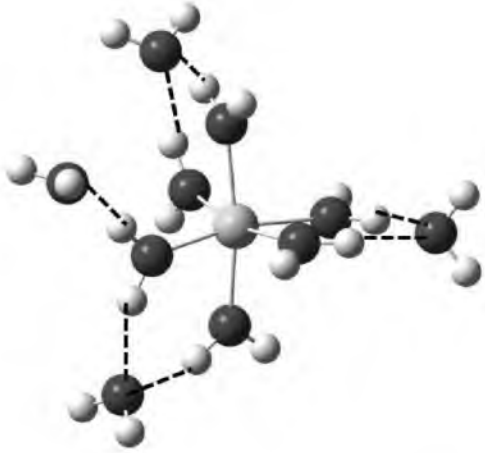

(6,4)_DD,5D_3AA,A, 7.3, **3.8**

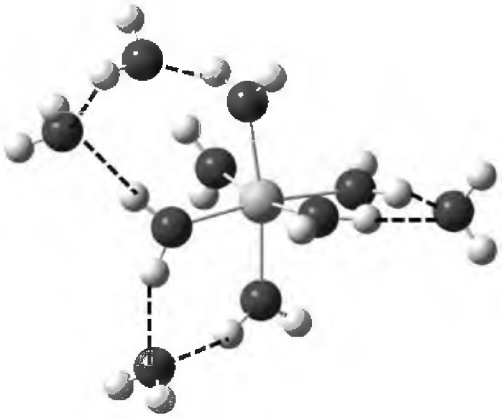

(6,3.5,0.5)_DD,5D_2AA,AAD_A_1A_2, 15.9, **9.6**

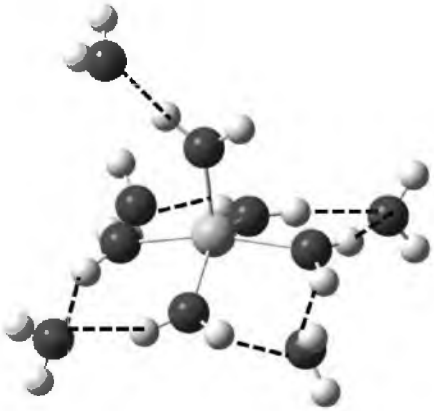

(5,5)_4DD,D_4A_bA_b,A_a, 0.0, **9.7**

Figure 8.5. Ground-state and low-lying geometries of $Mg^{2+}(H_2O)_{10}$. Hydrogen bonds are shown as dashed lines. The relative B3LYP/6-311+G(2d,2p)//B3LYP/6-311+G(d,p) (roman) and MP2(full)/6-311+G(2d,2p)//B3LYP/6-311+G(d,p) (**bold**) 298 K free energies (kJ/mol) from Table 8.1 are provided.

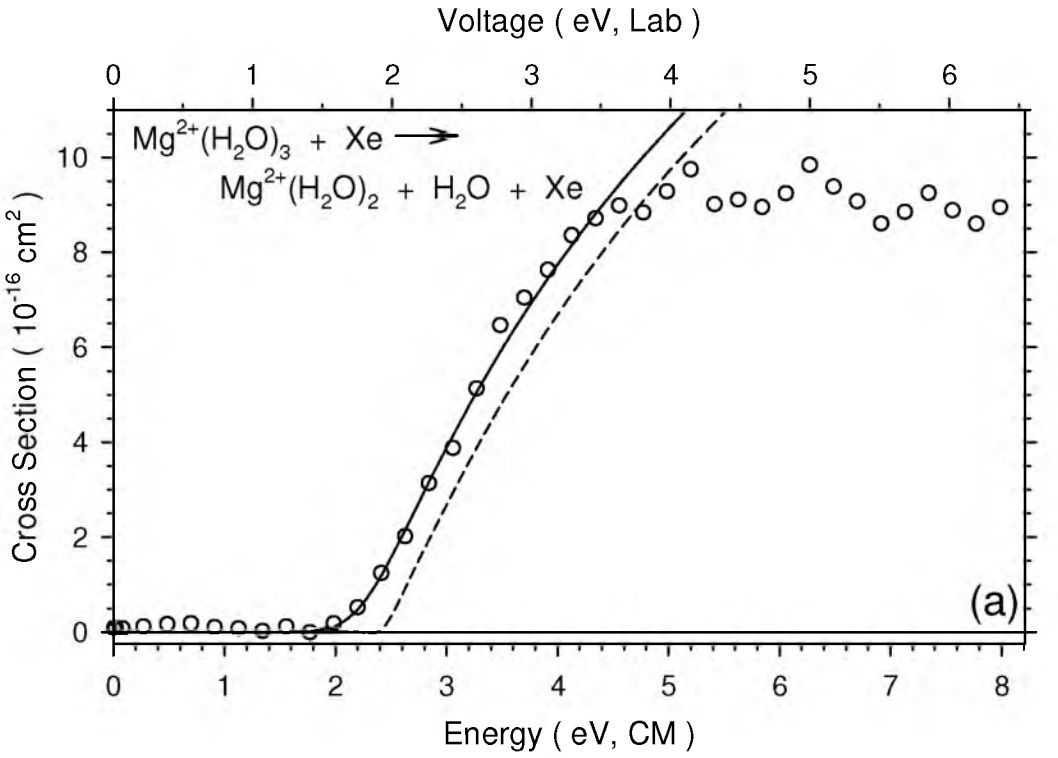

Figure 8.6. Analysis of the low pressure (x = 3) and zero-pressure extrapolated (x = 4 – 10) cross sections for single water molecule loss from collision-induced dissociation of $Mg^{2+}(H_2O)_x$, where x = 3 – 10 (parts a – h, respectively) with Xenon as a function of kinetic energy in the center-of-mass frame (lower x-axis) and applied voltage in the laboratory frame (top x-axis). The solid lines show the best fit to the data using the model convoluted over the neutral and ion kinetic energy and internal energy distributions of the reactants. The dashed lines show the model cross sections in the absence of experimental kinetic energy broadening for reactants at 0 K.

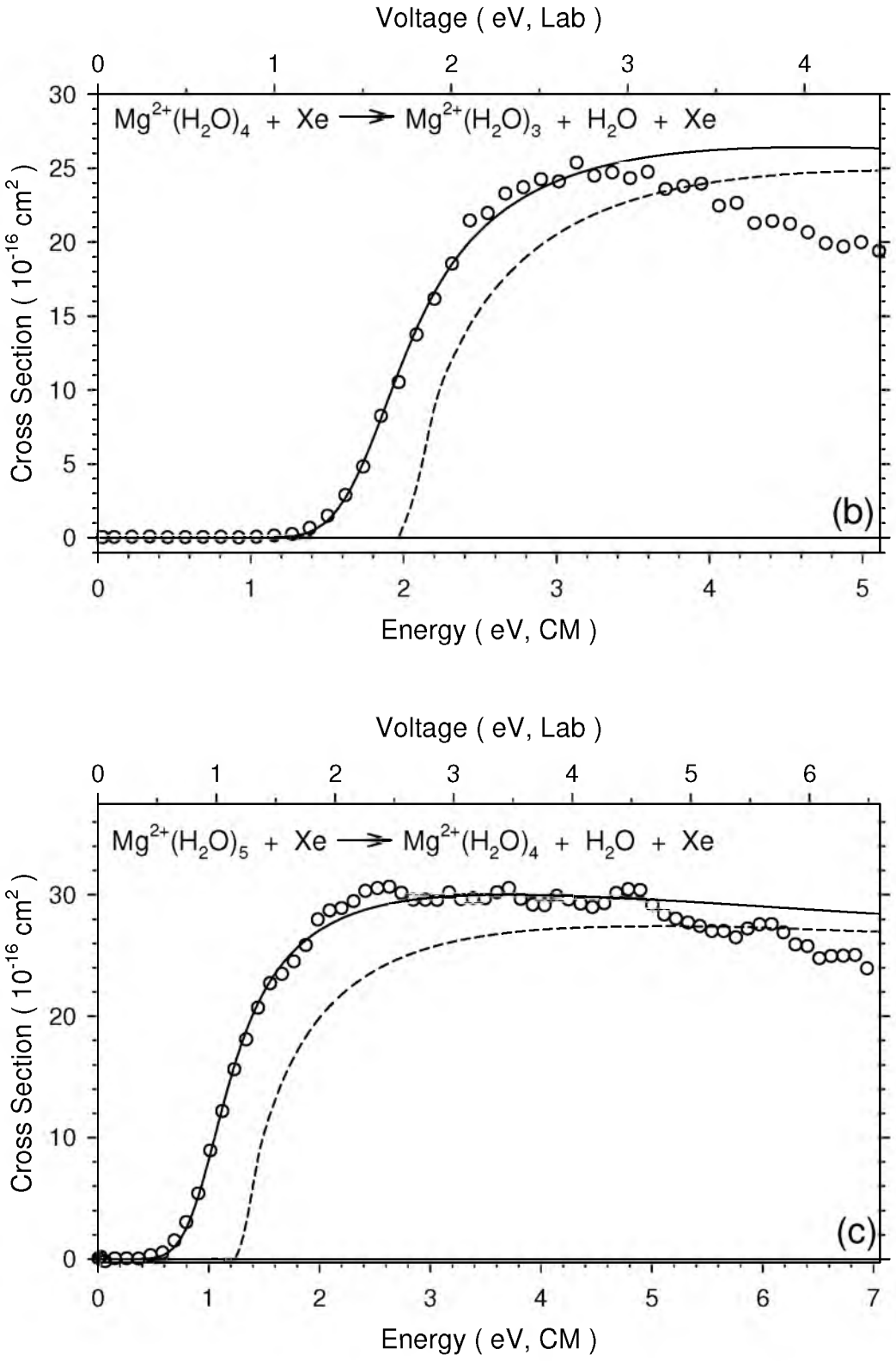

Figure 8.6. continued

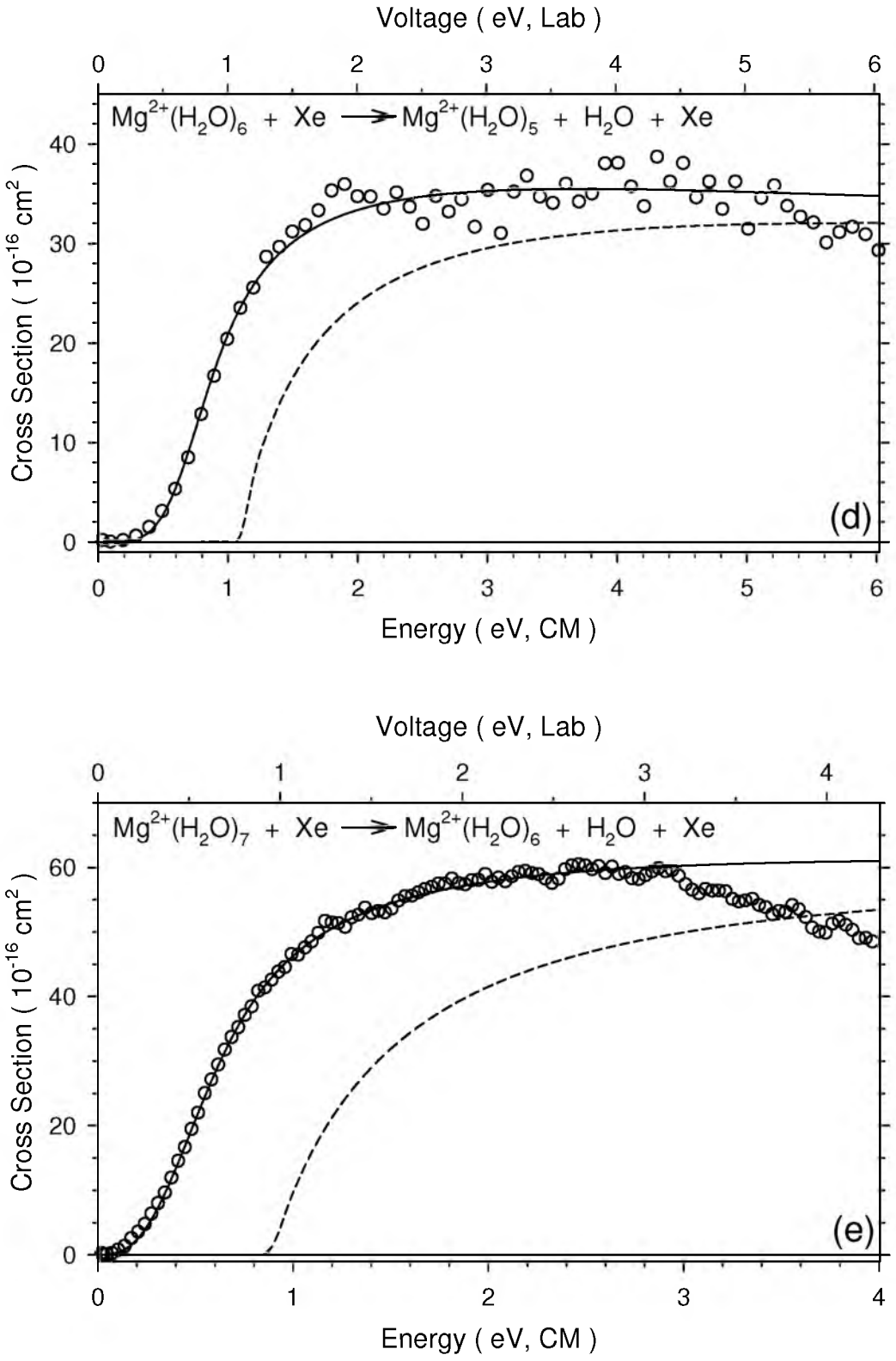

Figure 8.6. continued

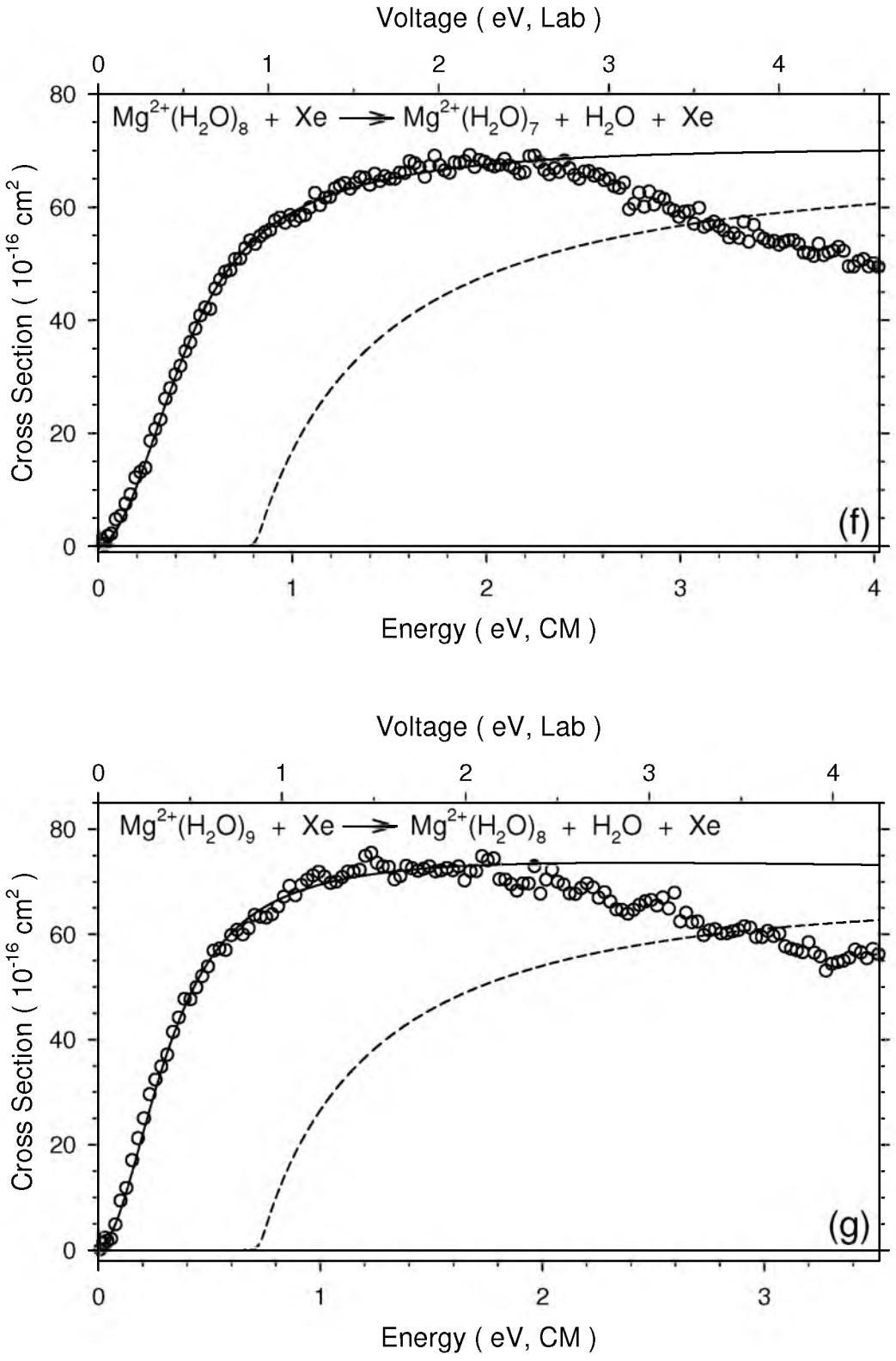

Figure 8.6. continued

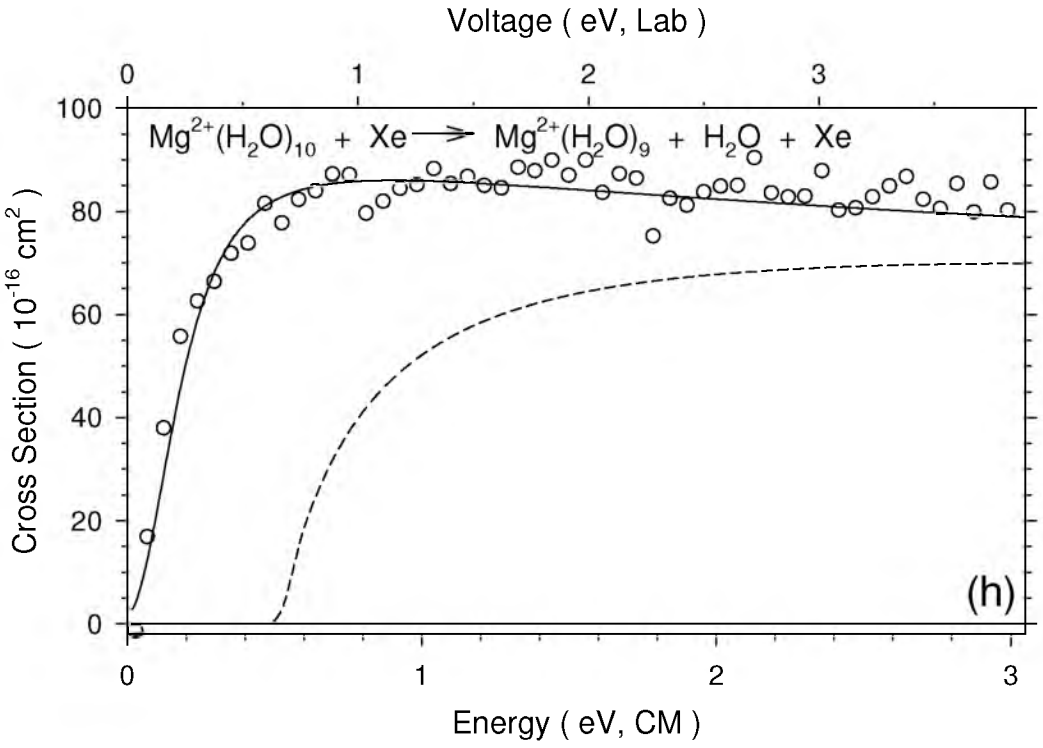

Figure 8.6. continued

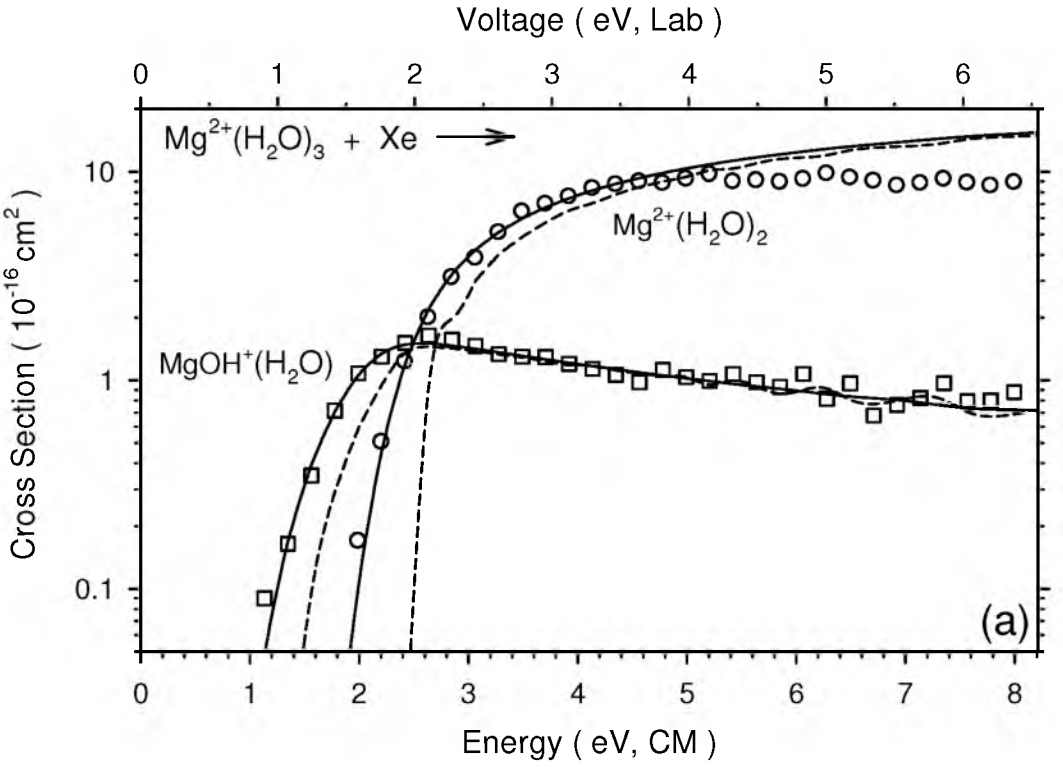

Figure 8.7. Competitive analysis of the high pressure (x = 3) and zero-pressure extrapolated (x = 4) product cross sections for the primary and secondary (if applicable) water loss (open circles) and the associated charge separation process (open squares) from the collision-induced dissociation of $Mg^{2+}(H_2O)_x$, where x = 3 (part a) and 4 (part b and c) with Xenon as a function of kinetic energy in the center-of-mass frame energy (lower x-axis) and applied laboratory frame voltage (upper x-axis). The solid lines show the best fit to the data using the competitive model convoluted over the neutral and ion kinetic and internal energy distributions. The dashed lines show the model cross sections in the absence of experimental kinetic energy broadening for reactions with an internal energy of 0 K.

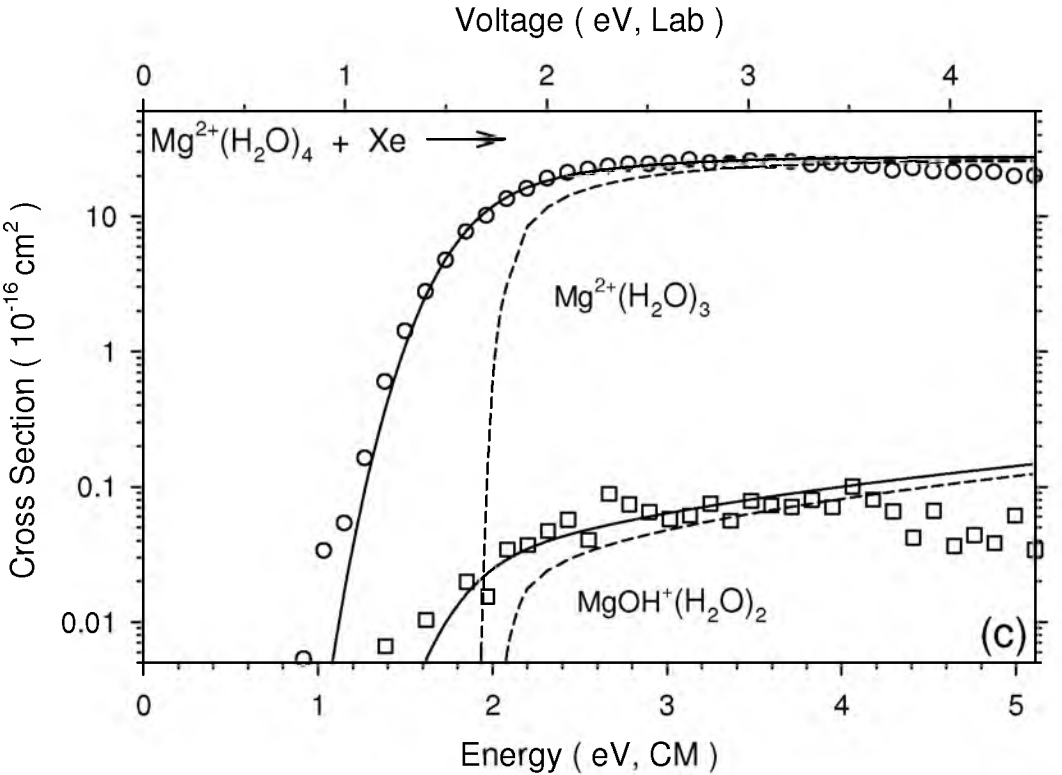

Figure 8.7 continued

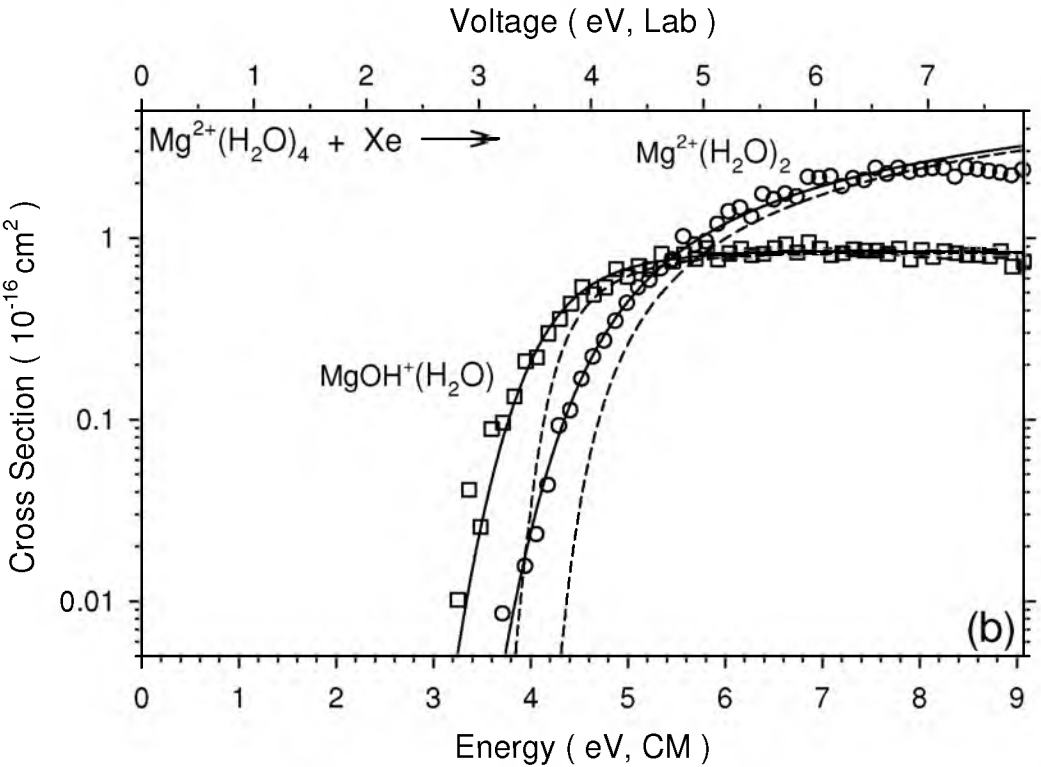
Voltage (eV, Lab)
0
1
2
3
4
5
6
7
Mg2+(H2O)4 + Xe
Mg2+(H2O)2
MgOH+(H2O)
Cross Section (10-16 cm2)
1
0.1
0.01
(b)
0
1
2
3
4
5
6
7
8
9
Energy (eV, CM)

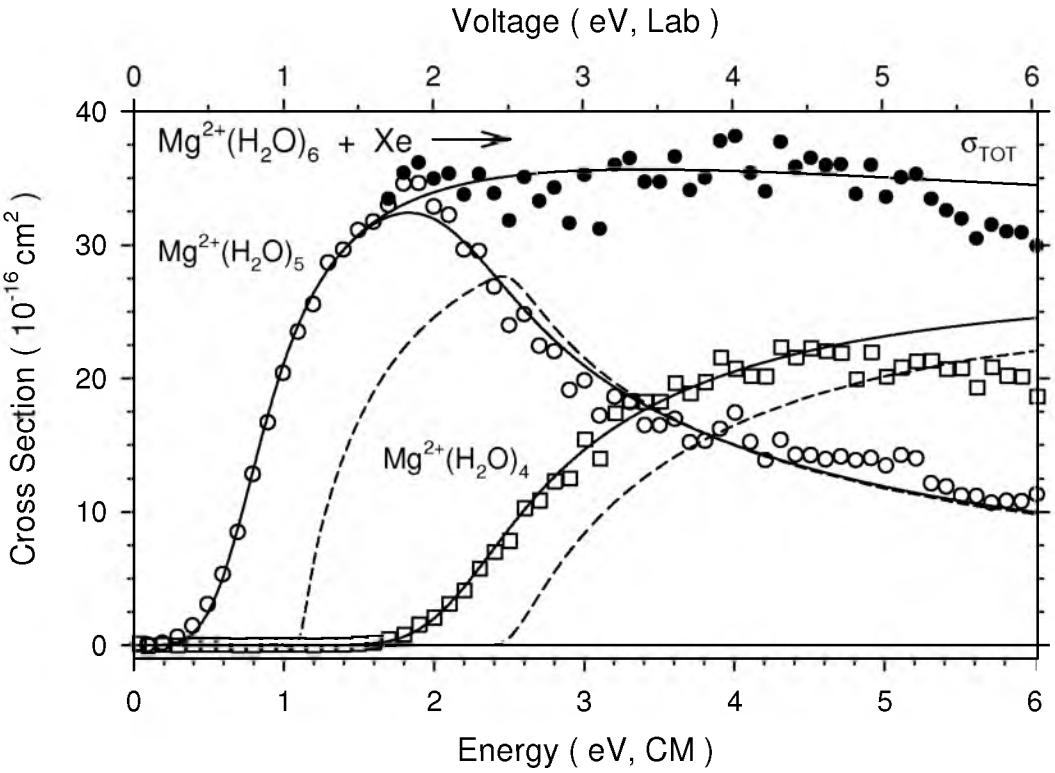

Figure 8.8. Sequential model analysis of the zero-pressure extrapolated cross sections for the primary (open circles) and secondary (open squares) water losses, and the total cross section (solid circles) from the collision-induced dissociation of $Mg^{2+}(H_2O)_6$ with Xenon as a function of kinetic energy in the center-of-mass frame (lower x-axis) and applied laboratory frame voltage (upper x-axis). The solid lines show the best fit to the data using the sequential model convoluted over the neutral and ion kinetic and internal energy distributions. The dashed lines show the model cross sections in the absence of experimental kinetic energy broadening for reactions with an internal energy of 0 K.

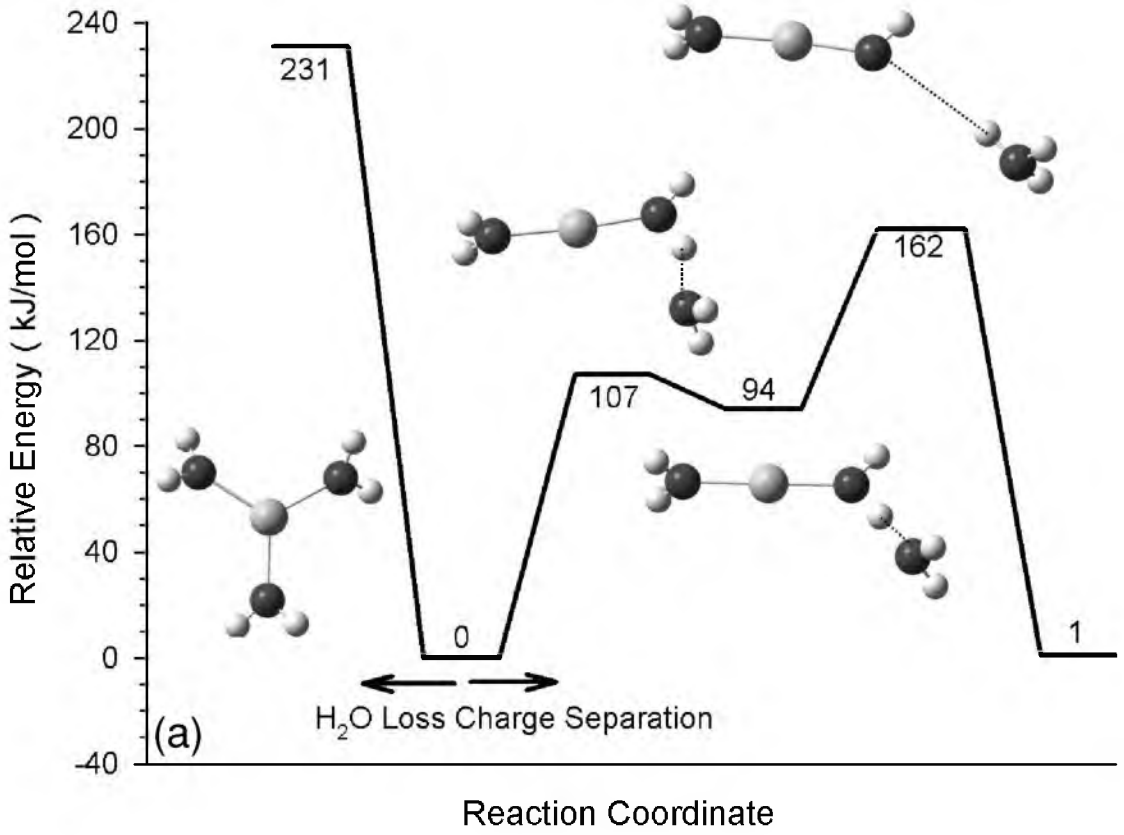

Figure 8.9. Reaction coordinates for water loss and charge separation pathways for $Mg^{2+}(H_2O)_3$ and $Mg^{2+}(H_2O)_4$ calculated at the B3LYP/6-311+G(2d,2p) level of theory (parts a and b, respectively). Relative energies (kJ/mol) include zero-point energy corrections for all stationary structures. Hydrogen bonds shown as dashed lines.

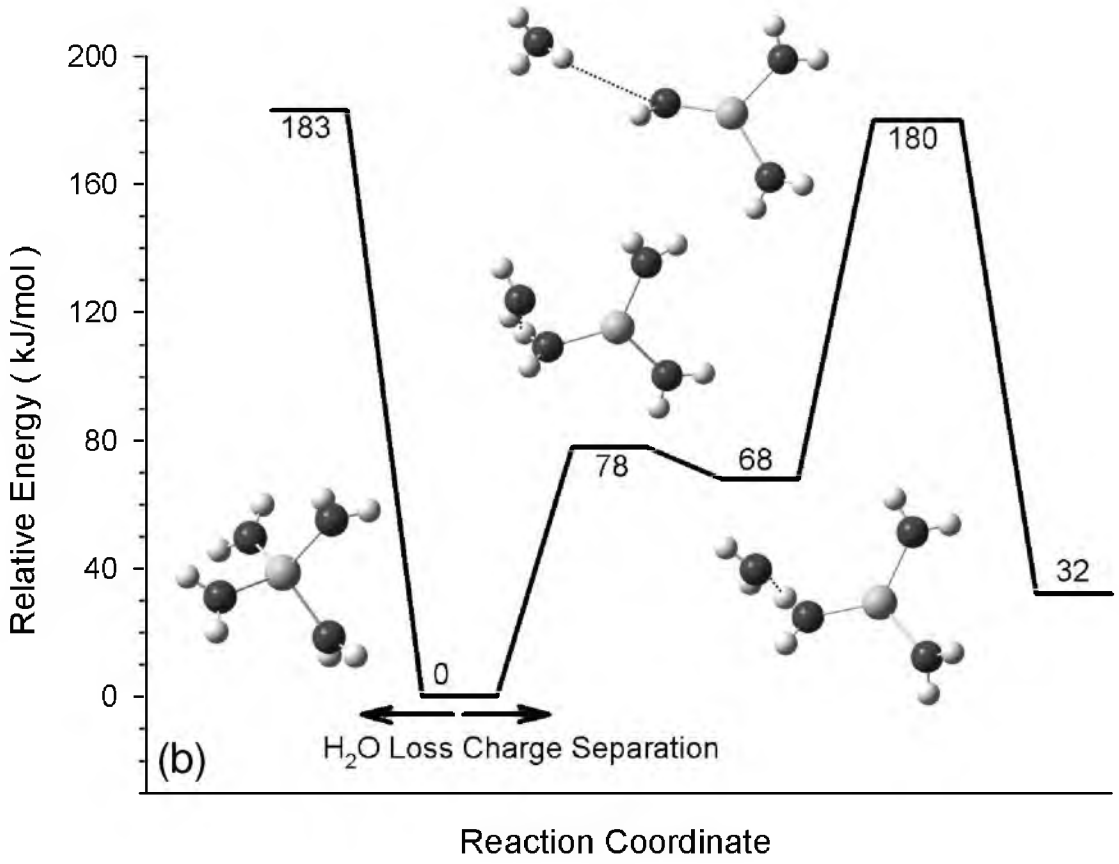

Figure 8.9. continued

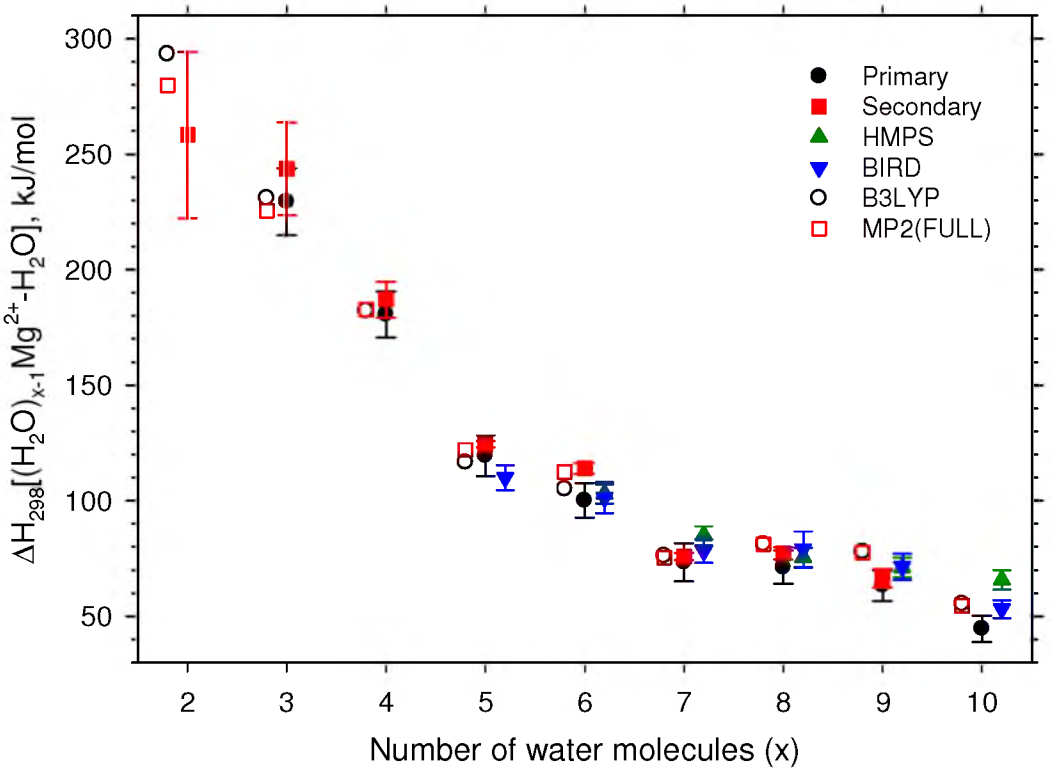

Figure 8.10. Comparison of experimental primary (solid circles) and secondary (solid squares) and theoretical B3LYP/6-311+G(2d,2p)//B3LYP/6-311+G(d,p) (open circles) and MP2(full)/6-311+G(2d,2p)//B3LYP/6-311+G(d,p) (open squares) bond dissociation energies in kJ/mol at 298 K. HPMS results from reference 12 (solid triangles) and BIRD results from references 13 and 14 (solid inverted triangles) are also included.

Table 8.1. Relative calculated enthalpies (ΔH_0) and free energies (ΔG_{298}) in kJ/mol for $Mg^{2+}(H_2O)_x$ isomers[a]

x	Complex name	B3LYP[b]	MP2[b]	Pavlov[c]
3	**(3,0)**	**0.0 (0.0)**	**0.0 (0.0)**	**0.0**
	(2,1)_D_A	93.5 (88.8)	98.3 (93.5)	
	(2,1)_2D_AA	123.4 (126.3)	120.8 (123.7)	
4	**(4,0)**	**0.0 (0.0)**	**0.0 (0.0)**	**0.0**
	(3,1)_D_A	68.2 (64.6)	76.7 (73.1)	
	(3,1)_2D_AA	71.2 (75.4)	75.6 (79.8)	
5	**(5,0)**	**0.0 (0.0)**	**0.0 (0.0)**	**0.0**
	(4,1)_D_A	18.2 (11.3)	30.6 (23.7)	18.0
	(4,1)_2D_AA	15.1 (14.9)	24.4 (24.3)	15.1
6	**(6,0)**	**0.0** (6.1)	**0.0** (**0.0**)	**0.0**
	(5,1)_2D_A_aA_b	11.0 (**0.0**)	22.6 (5.4)	15.5
	(5,1)_D_A_a	19.8 (10.7)	34.2 (19.0)	20.5
	(4.2)_4D_2AA	23.6 (21.6)	44.9 (36.7)	18.4
7	**(6,1)_2D_AA**	4.1 (2.5)	**0.0** (0.2)	**0.0**
	(6,1)_D_A	5.2 (0.6)	2.8 (**0.0**)	4.2
	(5,2)_4D_2A_bA_b	**0.0 (0.0)**	7.8 (9.6)	
	(5,2)_DD,2D_2A_aA_b	4.1 (2.9)	11.8 (12.4)	
	(4,3)_4D_AA,2A	25.4 (12.9)	49.0 (38.3)	
	(7,0)			63.2
8	**(6,2)_DD,2D_2AA (1)**	1.1 (0.8)	**0.0 (0.0)**	**0.0**
	(6,2)_4D_2AA (1)	2.3 (1.1)	1.2 (0.2)	
	(6,2)_3D_AA,A	9.1 (-0.2)	10.1 (1.0)	
	(6,2)_4D_2AA (2)	8.3 (2.8)	8.0 (2.8)	
	(6,2)_2D_2A (1)	11.5 (0.0)	14.5 (3.2)	
	(6,2)_2D_2A (2)	11.9 (1.8)	14.6 (4.7)	
	(6,2)_DD_2A	19.4 (6.1)	20.5 (7.5)	
	(5,3)_DD,4D_2A_bA_b,A_aA_b	**0.0 (0.0)**	11.6 (11.9)	

Table 8.1. continued

x	Complex name	B3LYP[b]	MP2[b]	Pavlov[c]
9	**(6,3)_6D_3AA**	**0.0** (0.6)	**0.0 (0.0)**	
	(6,3)_DD,4D_3AA (1)	3.2 (3.1)	3.1 (2.4)	
	(6,3)_DD,3D_2AA,A	13.2 (6.9)	14.8 (7.9)	
	(6,3)_2DD,2D_3AA (1)	11.1 (9.0)	11.0 (8.3)	
	(5,4)_4DD_4A$_b$A$_b$	2.8 (**0.0**)	14.3 (10.9)	
10	**(6,4)_2DD,4D_4AA (1)**	2.3 (3.7)	**0.0 (0.0)**	
	(6,4)_DD,5D_3AA,A	3.8 (7.3)	1.6 (3.8)	
	(6,4)_2DD,4D_4AA (2)	4.5 (12.7)	0.6 (7.5)	
	(6,3.5,0.5)_DD,5D_2AA,AAD_A$_1$A$_2$	5.0 (15.9)	**0.0** (9.6)	
	(5,5)_4DD,D_4A$_b$A$_b$,A$_a$	**0.0 (0.0)**	11.0 (9.7)	

[a] Relative ΔG_{298} are in parentheses. Bold structures represent ground state structures.
[b] Single point energies calculated using 6-311+G(2d,2p) basis set from B3LYP/6-311+G(d,p) geometries including zero point energy corrections.
[c] B3LYP/6-311+G(2d,2p)//B3LYP/LANL2DZ theoretical values taken from reference 24.

Table 8.2. Optimized parameters for analysis of $Mg^{2+}(H_2O)_x$ CID cross sections[a]

x	Reactant	Product	σ_0[b]	n[b]	E_0 (eV)[c]	E_0 (PSL,eV)[b]	ΔS_{1000} (J mol^{-1} K^{-1})[b]
3	(3,0)	(2,0)	15 (4)	1.3 (0.2)	2.40 (0.12)	2.31 (0.13)	50 (9)
	(3,0)	TS[1+1]	8 (4)	1.5 (0.2)	1.67 (0.20)	1.53 (0.20)	33 (3)
	(3,0)[d]	(2,0)	2.5e7 (x100)	1.2 (0.1)		2.32 (0.03)	50 (28)
		TS[1+1]	13 (1)			1.78 (0.12)	33 (3)
	(3,0)[d,e]	(2,0)	16 (5)	1.2 (0.2)		2.34 (0.15)	50 (9)
		TS[1+1]	13 (23)			1.12 (0.13)	-158 (11)
4	(4,0)	(3,0)	65 (7)	0.6 (0.2)	2.06 (0.12)	1.84 (0.11)	37 (9)
	(4,0)	TS[2+1]	0.20 (0.11)	0.6 (0.6)	2.17 (0.42)	1.80 (0.32)	35 (1)
	(4,0)[d,f]	(3,0)	66 (7)	0.6 (0.2)		1.85 (0.10)	37 (9)
		TS[2+1]	48 (40)			1.81 (0.11)	1 (2)
	(4,0)	(2,0)	3.0 (0.7)	1.6 (0.3)		4.06 (0.16)	47 (9)
	(4,0)	TS[1+1]	4.3 (0.8)	0.8 (0.2)		3.34 (0.16)	18 (1)
	(4,0)[d,g]	(2,0)	5 (1)	1.3 (0.2)		3.89 (0.12)	46 (9)
		TS[1+1]	4 (11)			3.15 (0.30)	-2 (17)
5	(5,0)	(4,0)	52 (7)	0.7 (0.1)	1.32 (0.11)	1.20 (0.09)	63 (9)
6	(6,0)	(5,0)	54 (8)	0.8 (0.1)	1.09 (0.11)	1.01 (0.08)	80 (9)
7	(6,1)_2D_AA	(6,0)	73 (11)	0.9 (0.2)	0.94 (0.09)	0.73 (0.08)	26 (9)
8	(6,2)_DD,2D_2AA	(6,1)	78 (8)	1.0 (0.2)	NR	0.70 (0.07)	72 (9)
9	(6,3)_6D_3AA	(6,2)[h]	82 (11)	0.9 (0.2)	NR	0.61 (0.07)	75 (9)

Table 8.2. continued

x	Reactant	Product	σ_0[b]	n[b]	E_0 (eV)[c]	E_0 (PSL,eV)[b]	ΔS_{1000} (J mol^{-1} K^{-1})[b]
10	(6,4)_2DD,4D_4AA	(6,3)[i]	98 (5)	0.8 (0.2)	NR	0.46 (0.06)	7 (9)

[a] Uncertainties, in parentheses, are reported as two standard deviations (2σ).
[b] Parameters from Equation 2.5, which includes RRKM theory to account for lifetime effects.
[c] Threshold energies from Equation 2.4, which excludes lifetime effects. NR denotes cross sections that could not be accurately reproduced with this model.
[d] Competitive dissociation model.
[e] Frequencies below 650 cm^{-1} in TS[1+1] were multiplied by a factor of 6.2 – 8.3.
[f] Frequencies below 800 cm^{-1} in TS[2+1] were multiplied by a factor of 1.2.
[g] Frequencies below 800 cm^{-1} in TS[1+1] were multiplied by a factor of 1.0 – 1.3.
[h] (6,2)_DD,2D_2AA.
[i] (6,3)_6D_3AA.

Table 8.3. Optimized parameters for analysis of $Mg^{2+}(H_2O)_x$ CID cross sections using the sequential model[a]

x	Reactant	Product	σ_0	n	E_0 (eV)[b]	E_0 (PSL,eV)[c]
3	(3,0)[d]	(2,0)	21 (6)	0.8 (0.1)	2.54 (0.14)	2.31 (0.13)
		(1,0)	10 (1)		5.19 (0.41)	
					[2.66 (0.37)]	
	(3,0)[e]	(2,0)	15 (5)	0.9 (0.2)	2.32 (0.13)	2.31 (0.13)
		(1,0)	8 (2)		5.09 (0.41)	
					[2.78 (0.41)]	
4	(4,0)[d]	(3,0)	78 (13)	0.3 (0.1)	1.95 (0.10)	1.84 (0.11)
		(2,0)	27 (4)		4.61 (0.11)	4.15 (0.17)
					[2.66 (0.06)]	[2.31 (0.13)]
	(4,0)[e]	(3,0)	63 (12)	0.5 (0.1)	1.83 (0.10)	1.84 (0.11)
		(2,0)	23 (3)		4.54 (0.10)	4.15 (0.17)
					[2.71 (0.05)]	[2.31 (0.13)]
5	(5,0)	(4,0)	52 (6)	0.7 (0.1)	1.20 (0.09)	1.20 (0.09)
		(3,0)	45 (4)		3.11 (0.10)	3.04 (0.14)
					[1.91 (0.08)]	[1.84 (0.11)]
6	(6,0)	(5,0)	54 (7)	0.8 (0.1)	1.02 (0.08)	1.01 (0.08)
		(4,0)	49 (4)		2.27 (0.08)	2.21 (0.12)
					[1.25 (0.01)]	[1.20 (0.09)]
7	(6,1)_2D_AA	(6,0)	73 (11)	1.0 (0.2)	0.73 (0.09)	0.73 (0.08)
		(5,0)	72 (6)		1.88 (0.08)	1.74 (0.11)
					[1.15 (0.02)]	[1.01 (0.08)]
8	(6,2)_DD,2D_2AA	(6,1)	79 (8)	1.0 (0.2)	0.70 (0.09)	0.70 (0.07)
		(6,0)	74 (3)		1.45 (0.09)	1.43 (0.11)
					[0.75 (0.02)]	[0.73 (0.08)]
9	(6,3)_6D_3AA	(6,2)[f]	84 (9)	1.0 (0.2)	0.61 (0.08)	0.61 (0.07)
		(6,1)	75 (6)		1.37 (0.09)	1.31 (0.10)
					[0.76 (0.03)]	[0.70 (0.07)]

Table 8.3. continued

x	Reactant	Product	σ_0	n	E_0 (eV)[b]	E_0 (PSL,eV)[c]
10	(6,4)_2DD,4D_4AA	(6,3)[g]	97 (5)	0.8 (0.2)	0.45 (0.09)	0.46 (0.06)
		(6,2)[f]	72 (10)		1.09 (0.12)	1.07 (0.09)
					[0.64 (0.04)]	[0.61 (0.07)]

[a] Uncertainties, in parentheses, are reported for two standard deviations (2σ).
[b] Values in brackets are the differences between primary and secondary thresholds, with uncertainties determined directly from the sequential models.
[c] Experimental values from Table 8.2.
[d] Allow all parameters to optimize.
[e] Primary E_0 fixed to Table 8.2 value.
[f] (6,2)_DD,2D_2AA.
[g] (6,3)_6D_3AA.

Table 8.4. Conversion of 0 K bond dissociation energies to 298 K enthalpies and free energies in kJ/mol for water loss from $Mg^{2+}(H_2O)_x$, where x = 2 – 10. Uncertainties in parentheses.

Reactant	Product	ΔH_0 (Primary)[a] ΔH_0 (Secondary)	$\Delta H_{298} - \Delta H_0$[b]	ΔH_{298} (Primary) ΔH_{298} (Secondary)	$T\Delta S_{298}$[b]	ΔG_{298} (Primary) ΔG_{298} (Secondary)
(2,0)	(1,0)		2.0 (0.2)		34.3 (0.7)	
		256.3 (36.0)		258.3 (36.0)		224.0 (36.0)
(3,0)	(2,0)	226.2 (14.5)[c]	3.2 (0.3)	229.4 (14.5)	39.9 (0.7)	189.5 (14.5)
		240.4 (20.1)[d]		243.6 (20.1)		203.7 (20.1)
(4,0)	(3,0)	178.3 (10.0)[c]	2.4 (0.3)	180.7 (10.0)	36.7 (0.7)	144.0 (10.0)
		184.7 (7.8)		187.1 (7.8)		150.4 (7.8)
(5,0)	(4,0)	116.1 (8.8)	3.4 (0.3)	119.5 (8.8)	43.7 (0.7)	75.8 (8.8)
		121.0 (1.4)		124.4 (1.4)		80.7 (1.6)
(6,0)	(5,0)	97.4 (7.5)	2.7 (0.3)	100.1 (7.5)	49.4 (0.8)	50.7 (7.5)
		111.3 (2.4)		114.0 (2.4)		64.6 (2.5)
(6,1)_2D_AA	(6,0)	70.3 (8.2)	3.0 (0.2)	73.3 (8.2)	32.0 (0.6)	41.3 (8.2)
		72.8 (1.6)		75.8 (1.6)		43.8 (1.7)
(6,2)_DD,2D_2AA	(6,1)	67.4 (7.2)	3.8 (0.3)	71.2 (7.2)	45.3 (0.6)	25.9 (7.2)
		73.4 (2.6)		77.2 (2.6)		31.9 (2.7)
(6,3)_6D_3AA	(6,2)[e]	59.0 (6.7)	4.3 (0.3)	63.3 (6.7)	45.9 (0.6)	17.4 (6.7)
		62.1 (4.0)		66.4 (4.0)		20.5 (4.1)
(6,4)_2DD,4D_4AA	(6,3)[f]	44.1 (5.7)	0.5 (0.2)	44.6 (5.7)	27.8 (0.7)	16.9 (5.7)

Table 8.4. continued

[a] Experimental values from Tables 8.2 and 8.3.
[b] Values calculated from the vibrations and rotations calculated at the B3LYP/ 6-311+G(d,p) level. Uncertainties determined by scaling the frequencies up and down by 10%.
[c] Competitive analysis.
[d] Secondary BDE value from Table 8.3 adjusted downward with the 16.4 ± 19.3 kJ/mol competitive shift determined from analysis of secondary water loss in x = 4, see text.
[e] (6,2)_DD,2D_2AA.
[f] (6,3)_6D_3AA.

Table 8.5. Comparison of experimental 298 K primary and secondary BDEs with theoretical and literature values from the CID of $Mg^{2+}(H_2O)_x$, where x = 3 – 10

x	ΔH_{298}[a] primary	ΔH_{298}[a] secondary	HPMS[b]	BIRD[c]
1				
2		258 ± 36		
3	229 ± 15	244 ± 20		
4	181 ± 10	187 ± 8		
5	120 ± 9	124 ± 2		110 ± 5
6	100 ± 8	114 ± 2	103 ± 4	101 ± 7
6,1	73 ± 8	76 ± 2	85 ± 4	78 ± 5
6,2	71 ± 7	77 ± 3	75 ± 4	79 ± 8
6,3	63 ± 7	66 ± 4	71 ± 4	71 ± 6
6,4	45 ± 6		66 ± 4	53 ± 4
MADs[g]				
Primary		7	10	7
Secondary	7		7	7
HPMS	10	7		5
BIRD	7	7	5	
B3LYP				

Table 8.5. continued

x	B3LYP[d,e]	B3LYP/ pCVTZ[e]	MP2[d,e]	G3[f]
1	339 (341)	348 (348)	319 (325)	337
2	293 (297)	298 (299)	280 (289)	299
3	231 (234)	235 (236)	225 (234)	240
4	182 (185)	184 (185)	183 (192)	198
5	117 (120)	115 (116)	122 (133)	138
6	105 (109)	105 (106)	113 (125)	131
6,1	76 (79)		75 (84)	
6,2	81 (84)		81 (90)	
6,3	78 (81)		78 (86)	
6,4	55 (58)		54 (63)	
MADs[g]				
Primary	6 (9)	4 (5)	7 (16)	20
Secondary	11 (11)	14 (13)	8 (13)	17
HPMS	7 (8)		9 (11)	
BIRD	4 (6)	4 (6)	6 (15)	29
B3LYP	(3)	4 (4)	5 (10)	16

[a] Experimental values from Table 8.4.
[b] Experimental values taken from reference 12.
[c] Experimental values taken from references 13 and 14.
[d] Single point energies use 6-311+G(2d,2p) basis set. Geometry optimizations at B3LYP/6-311+G(d,p) level of theory.
[e] Values in parentheses do not include counterpoise corrections.
[f] G3 theoretical values taken from reference 31. Adjusted for ZPE and thermal effects here.
[g] Mean absolute deviations.

Table 8.6. Comparison of 0 K transition state energies and water loss bond energies in kJ/mol to theoretical results for $Mg^{2+}(H_2O)_3$ and $Mg^{2+}(H_2O)_4$

Complex	B3LYP[a]	B3P86[a]	MP2(full)[a]	Experiment[b]
$Mg^{2+}(H_2O)_2 + H_2O$	231	228	230	223 ± 13[c], 224 ± 3[d,e]
				226 ± 15[d,f]
TS1	107	102	108	
INT (2,1)	94	87	98	
TS[1+1]	162	163	169	148 ± 19[c], 172 ± 12[d,e]
				108 ± 13[d,f]
$MgOH^+(H_2O) + H_3O^+$	1	1	11	
$Mg^{2+}(H_2O)_3 + H_2O$	183	183	190	178 ± 10[c]
				178 ± 10[d,f]
TS1	78	75	83	
INT (3,1)	68	64	76	
TS[2+1]	180	181	190	173 ± 31[c]
				174 ± 11[d,f]
$MgOH^+(H_2O)_2 + H_3O^+$	32	33	45	

[a] Single point energies calculated with 6-311+G(2d,2p) basis set using B3LYP/6-311+G(d,p) geometry optimizations (ZPE corrections included).
[b] Values taken from Table 8.2.
[c] Single channel analysis.
[d] Competitive analysis.
[e] No scaling of charge separation frequencies.
[f] Charge separation frequencies scaled.

References

(1) Carl, D. R.; Armentrout, P. B. *J. Phys. Chem. A* **2012**, *116*, 3802.

(2) Carl, D. R.; Chatterjee, B. K.; Armentrout, P. B. *J. Chem. Phys.* **2010**, *132*, 44303.

(3) Carl, D. R.; Moision, R. M.; Armentrout, P. B. *Int. J. Mass Spectrom.* **2007**, *265*, 308.

(4) Cooper, T. E.; Carl, D. R.; Armentrout, P. B. *J. Phys. Chem. A* **2009**, *113*, 13727.

(5) Cooper, T. E.; Armentrout, P. B. *J. Phys. Chem. A* **2009**, *113*, 13742.

(6) Cooper, T. E.; Armentrout, P. B. *Chem. Phys. Lett.* **2010**, *486*, 1.

(7) Cooper, T. E.; Armentrout, P. B. *J. Chem. Phys.* **2011**, *134*, 114308.

(8) Hofstetter, T. E.; Armentrout, P. B. *J. Phys. Chem. A* **2013**, in press.

(9) Whitehouse, C. M.; Dreyer, R. N.; Yamashita, M.; Fenn, J. B. *Anal. Chem.* **1985**, *57*, 675.

(10) Yamashita, M.; Fenn, J. B. *J. Phys. Chem.* **1984**, *88*, 4451.

(11) Blades, A. T.; Jayaweera, P.; Ikonomou, M. G.; Kebarle, P. *J. Chem. Phys.* **1990**, *92*, 5900.

(12) Peschke, M.; Blades, A. T.; Kebarle, P. *J. Phys. Chem. A* **1998**, *102*, 9978.

(13) Rodriguez-Cruz, S. E.; Jockusch, R. A.; Williams, E. R. *J. Am. Chem. Soc.* **1999**, *121*, 8898.

(14) Wong, R. L.; Paech, K.; Williams, E. R. *Int. J. Mass Spectrom.* **2004**, *232*, 59.

(15) Rodriguez-Cruz, S. E.; Jockusch, R. A.; Williams, E. R. *J. Am. Chem. Soc.* **1999**, *121*, 1986.

(16) Bush, M. F.; O'Brien, J. T.; Prell, J. S.; Wu, C.-C.; Saykally, R. J.; Williams, E. R. *J. Am. Chem. Soc.* **2009**, *131*, 13270.

(17) Shvartsburg, A. A.; Siu, K. W. M. *J. Am. Chem. Soc.* **2001**, *123*, 10071.

(18) Barran, P. E.; Walker, N. R.; Stace, A. J. *J. Chem. Phys.* **2000**, *112*, 6173.

(19) Chen, X.; Stace, A. J. *Chem. Commun.* **2012**, *48*, 10292.

(20) Klobukowski, M. *Can. J. Chem.* **1992**, *70*, 589.

(21) Bauschlicher, C. W.; Sodupe, M.; Partridge, H. *J. Chem. Phys.* **1992**, *96*, 4453.

(22) Glendening, E. D.; Feller, D. *J. Phys. Chem.* **1996**, *100*, 4790.

(23) Markham, G. D.; Glusker, J. P.; Bock, C. L.; Trachtman, M.; Bock, C. W. *J. Phys. Chem.* **1996**, *100*, 3488.

(24) Pavlov, M.; Siegbahn, P. E. M.; Sandstrom, M. *J. Phys. Chem. A* **1998**, *102*, 219.

(25) Pye, C. C.; Rudolph, W. W. *J. Phys. Chem. A* **1998**, *102*, 9933.

(26) Martínez, J. M.; Pappalardo, R. R.; Marcos, E. S. *J. Am. Chem. Soc.* **1999**, *121*, 3175.

(27) Petrie, S.; Radom, L. *Int. J. Mass Spectrom.* **1999**, *192*, 173.

(28) Dudev, T.; Lim, C. *J. Phys. Chem. A* **1999**, *103*, 8093.

(29) Markham, G. D.; Glusker, J. P.; Bock, C. W. *J. Phys. Chem. B* **2002**, *106*, 5118.

(30) Merrill, G. N.; Webb, S. P.; Bivin, D. B. *J. Phys. Chem. A* **2003**, *107*, 386.

(31) Rao, J. S.; Dinadayalane, T. C.; Leszczynski, J.; Sastry, G. N. *J. Phys. Chem. A* **2008**, *112*, 12944.

(32) Kaupp, M.; Schleyer, P. v. R. *J. Phys. Chem.* **1992**, *96*, 7316.

(33) Beyer, M.; Williams, E. R.; Bondybey, V. E. *J. Am. Chem. Soc.* **1999**, *121*, 1565.

(34) Peschke, M.; Blades, A. T.; Kebarle, P. *Int. J. Mass Spectrom.* **1999**, *185/186/187*, 685.

(35) Carl, D. R.; Moision, R. M.; Armentrout, P. B. *J. Am. Soc. Mass Spectrom.* **2009**, *20*, 2312.

(36) Armentrout, P. B. *J. Chem. Phys.* **2007**, *126*, 234302.

(37) Iceman, C.; Armentrout, P. B. *Int. J. Mass Spectrom.* **2003**, *222*, 329.

(38) Castleman Jr., A. W. *Chem. Phys. Lett.* **1978**, *53*, 560.

(39) Carl, D. R.; Armentrout, P. B. *J. Phys. Chem. A,* **2012**, *116*, 3802.

(40) Cooper, T. E.; O'Brien, J. T.; Williams, E. R.; Armentrout, P. B. *J. Phys. Chem. A* **2010**, *114*, 12646.

(41) Heaton, A. L.; Armentrout, P. B. *J. Am. Soc. Mass Spectrom.* **2009**, *20*, 852.

CHAPTER 9

INFRARED MULTIPLE PHOTON DISSOCIATION SPECTROSCOPY OF CATIONIZED METHIONINE: EFFECTS OF ALKALI-METAL CATION SIZE ON GAS-PHASE CONFORMATION

Abstract

The gas-phase structures of alkali-metal cation complexes of the amino acid methionine (Met) as well as protonated methionine are investigated using infrared multiple photon dissociation (IRMPD) spectroscopy utilizing light generated by a free electron laser. Spectra of Li^+(Met) and Na^+(Met) are similar and relatively simple, whereas the spectra of K^+(Met), Rb^+(Met), and Cs^+(Met) include distinctive new bands. Measured IRMPD spectra are compared to spectra calculated at the B3LYP/6-311+G(d,p) level of theory to identify the conformations present in the experiment studies. For Li^+ and Na^+ complexes, the only conformation present is a charge-solvated, tridentate structure that binds the metal cation to the amine and carbonyl groups of the amino acid backbone and the sulfur atom of the side chain, [N,CO,S]. In addition to the [N,CO,S] conformer, bands corresponding to alkali metal cation binding to a bidentate zwitterionic structure, [CO_2^-], are clearly present for the K^+, Rb^+, and Cs^+ complexes. Theoretical calculations of the lowest energy conformations of Rb^+ and Cs^+ complexes suggest that the experimental spectra could also include contributions from tridentate

[COOH,S] and bidentate [COOH] charge-solvated structures. For H^+(Met), the IRMPD action spectrum is reproduced by multiple low energy [N,CO,S] conformers, in which the protonated amine group hydrogen bonds to the carbonyl oxygen atom and the sulfur atom of the amino acid side chain. These [N,CO,S] conformers only differ in their side chain orientations.

Introduction

Fundamental interactions between biologically relevant metal ions and small molecules can have a profound effect on the function of complex biological processes. For example, the interactions between potassium ions and sulfur-containing amino acid methionine (Met) in the outer pore region of inward rectifying K^+ (Kir) ion channels are an important controlling factor in the selective passage of monocations.[1] Recently, the pairwise interactions between Met with the alkali metal cations, Li^+, Na^+, and K^+ have been investigated using guided ion beam mass spectrometry.[2] Quantitative bond dissociation energies were determined and found to be consistent with theoretical values predicted for the ground state conformations, charge-solvated structures involving tridentate bonding of the metal ion to the amide and carbonyl groups of the amino acid backbone and the side chain sulfur atom, [N,CO,S], for Li^+ and Na^+. For Li^+(Met) and Na^+(Met), the [N,CO,S] ground state lies well below (> 10 kJ/mol) any other conformations such that quantitative measurements are sufficient to determine the identity of the complexes formed experimentally.[2] Calculations indicate that the energy differences between the ground state and low-lying conformations decrease as the metal cations become heavier. For example, MP2(full) calculations predict a ground state of [N,CO,S] for K^+(Met), but density functional theory calculations indicate the ground state

is bidentate with K^+ bound to the carboxylate moiety of the zwitterionic [CO_2^-] conformation and the NH_3^+ group hydrogen bonds to the side chain sulfur atom.[2] At both levels of theory, the [N,CO,S] and [CO_2^-] conformers are separated by less than 3 kJ/mol. Low energy conformations are likely present for Rb^+ and Cs^+ complexed to Met as well. As such, threshold collision-induced dissociation measurements are unable to distinguish between small differences in conformational energy.

Infrared multiple photon dissociation (IRMPD) action spectroscopy can be used to examine the presence of specific conformations as a function of metal cation size. Previous IRMPD studies on M^+(Ser)[3] and M^+(Thr)[4] have found that the $M^+ = Li^+$ and Na^+ complexes are bound in a tridentate [N,CO,OH] conformer, whereas spectra for $M^+ = K^+$ and Rb^+ include evidence of bidentate [COOH] conformations. Additionally, the spectra for Cs^+ serine and threonine complexes also include contributions from a zwitterionic [CO_2^-] conformer. A similar progression is seen for M^+(Cys), however the zwitterionic [CO_2^-] contributes to the IRMPD spectra for $M^+ = K^+$ and Rb^+ as well.[5] For M^+(Arg), the transition from ground state charge-solvated to zwitterionic conformation occurs at Na^+(Arg).[6] The IRMPD action spectra of M^+(Asn) maintain the charge-solvated tridentate [N,CO,CO] conformation throughout the alkali cation series, but also includes spectral contributions from the [COOH,CO] conformer for K^+(Asn) to Cs^+(Asn).[7] A similar progression is seen in IRMPD studies of M^+(Gln).[8] M^+(Trp)[9], M^+(Lys)[10], M^+(Asp)[11], M^+(Glu)[11], and M^+(His)[12] complexes transition from solely tridentate to contributions of tridendate and bidentate conformers as the metal ion becomes heavier, but still maintain charge-solvated complexes. In the present study, we examine whether such trends are influenced by having a side-chain with a sulfur-containing functional

group, which tends to bind metal cations at different angles compared to analogous ether functional groups.[2] Thus, we measure the IRMPD action spectra for dissociation of M^+(Met) complexes, where $M^+ = Li^+$, Na^+, K^+, Rb^+, Cs^+, and H^+. The conformations are identified by comparing the experimental action spectra to IR spectra predicted by quantum chemical calculations of the low-lying structures of the M^+(Met) complexes optimized at the B3LYP/6-311+G(d,p) level of theory.

Experimental Details

Mass spectrometry and photodissociation spectroscopy. A 4.7 T Fourier transform ion cyclotron resonance (FTICR) mass spectrometer was used in these experiments and has been described in detail elsewhere.[13-15] Tunable radiation for the photodissociation experiments is generated by the free electron laser for infrared experiments (FELIX).[16] For the present experiments, spectra were recorded over the wavelength range 19.4 μm to 5.5 μm corresponding to a frequency range of 520 to1820 cm^{-1}. Pulse energies were around 50 mJ/macropulse of 5 μs duration, although they fell off to about 20 mJ toward the blue edge of the scan range. Complexes were irradiated for 2.5 seconds, which corresponds to interaction with approximately 12 macropulses. The full width at half maximum bandwidth of the laser was typically 0.5% of the central wavelength. Methionine was obtained from Aldrich. Cationized amino acids were formed by electrospray ionization using a Micromass Z-Spray source from a solution of 1 mM Met and 1 mM alkali-metal chloride (or 1 mM acetic acid for H^+(Met)) in 70%:30% MeOH:H_2O. Solution flow rates were about 10 μL/min and the electrospray needle was held at a voltage of 3250 V. Ions were accumulated in a hexapole trap for about four seconds prior to being injected into the ICR cell via an rf octopole ion guide.

Electrostatic switching of the dc bias of the octopole, where a dc bias voltage is superimposed on the full length of all octopole rods, results in there being no change in the dc electric field along the axis of the ion guide.[15] This decelerates the ions exiting the octopole such that they can be captured in the ICR cell without a gas pulse and collisional heating of the ions is avoided.[15]

Results

Theoretical results. The low-lying structures found for all M^+(Met) complexes are illustrated by those for Rb^+(Met) in Figure 9.1. The nomenclature used to identify different structural isomers is identical to that described previously for the CID study of alkali-metal asparagine complexes[7] and differs somewhat from that utilized in the CID study of Met complexes.[2] Briefly, conformations of M^+(Met) are identified by their metal binding site (or protonation site) in brackets, followed by a description of the methionine orientation by a series of five dihedral angles. These dihedral angles start with the carboxylic acid hydrogen atom (or analogous proton attached to the NH_2 group for zwitterionic structures) to define the H-O-C-C dihedral angle and proceeds along the molecule to the terminal methyl group of the amino acid side chain (O-C-C-C, C-C-C-C, C-C-C-S, and C-C-S-C). The dihedral angles are distinguished as cis (c, for angles between 0° and 50°), gauche (g, 50° – 135°) and trans (t, 135° – 180°). Previously, we designated the conformations somewhat less completely by designating the HOCO angle followed by the last three side chain dihedrals, C-C-C-C, C-C-C-S, and C-C-S-C. In all cases, the HOCO and HOCC bond angles are the inverse of one another, i.e., c versus t, and the last three dihedral angles are identical. Descriptions of these structures have been provided for the cases of $M^+ = Li^+$, Na^+, and K^+ previously.[2]

Relative 0 K energies and 298 K free energies with respect to the ground-state structures calculated at three different levels of theory are given in Table 9.1 for the M^+(Met) complexes. Because the relative Gibbs free energies at 298 K are more relevant in describing the experimental distributions, these values are used throughout the discussion below. The overall trends in relative 298 K free energies calculated at the B3LYP, B3P86, and MP2(full) levels of theory are shown in Figure 9.2. Conversion from 0 K bond energies to 298 K free energies is accomplished using the rigid rotor/harmonic oscillator approximation with rotational constants and vibrational frequencies calculated at the B3LYP/6-311+G(d,p) and B3LYP/HW*/6-311+G(d,p) levels. Three to four side-chain orientations were optimized for each distinct type of conformation, but only the lowest of these are plotted in Figure 9.2 for each level of theory. For the most part, the calculated IR spectra of the various side-chain orientations are very similar, such that a comparison with the lowest energy conformer is sufficient for identification; however, in the comparison between calculated and observed photodissociation spectra, any spectral differences among these orientations will be discussed. Therefore, higher energy orientations that make up at least 1% of the ion population are included in Table 9.1. This corresponds to an excitation free energy of ~12 kJ/mol above the ground state.

The charge-solvated, tridentate [N,CO,S] conformation is the lowest energy conformation for Li^+(Met) and Na^+(Met). For K^+(Met), Rb^+(Met), and Cs^+(Met), the [N,CO,S] conformer is low-lying, 0 – 8, 1 – 10, and 5 – 13 kJ/mol, respectively, higher in energy than the calculated ground-state conformer. The zwitterionic [CO_2^-] conformation lies > 20 kJ/mol higher than the [N,CO,S] ground state for Li^+(Met),

however, as the metal cation becomes larger, the energetic difference between the [N,CO,S] and [CO_2^-] conformers decreases to 2 – 8 kJ/mol at Na^+(Met) and the two structures become nearly isoenergetic with one another at K^+(Met) through Cs^+(Met), with excitation energies of 0 – 8, -1 – 10, and -1 – 13 kJ/mol, respectively, Figure 9.2. The [COOH] conformer, the charge-solvated analogue of the zwitterionic [CO_2^-] structure, starts 58 – 71 kJ/mol higher than the ground state for Li^+(Met). As the metal cation becomes larger, the energy of the [COOH] conformer with respect to the ground state quickly decreases, but remains higher in energy than the [CO_2^-] conformation. For Li^+(Met), the [CO_2^-]/[COOH] difference is 38 – 43 kJ/mol, but decreases to 24 – 26, ~13, and ~4 kJ/mol for M^+(Met), $M^+ = Na^+$, K^+, and Rb^+, respectively. For Cs^+(Met), the difference drops to 0.3 – 1.9 kJ/mol. The charge-solvated, tridentate [COOH,S] conformation lies 19 – 23 kJ/mol above [N,CO,S] at Na^+(Met). For Li^+(Met), this structure collapses to the bidentate [CO,S]. At the MP2 level of theory, the [COOH,S] conformer becomes the lowest energy state for Rb^+(Met) and Cs^+(Met), lying 2 and 6 kJ/mol, respectively, below [CO_2^-], but the DFT calculations indicate the opposite order, with [COOH,S] lying 3 – 5 and 0 – 1 kJ/mol, respectively, above [CO_2^-]. Overall, the 298 K free energies of the [N,CO,S], [CO_2^-], [COOH], and [COOH,S] conformers all lie within 10 and 13 kJ/mol of one another for Rb^+(Met) and Cs^+(Met), respectively.

The [CO_2^-,S] conformer, the zwitterionic analogue of the charge-solvated [COOH,S] conformer, lies 11 – 14 kJ/mol above the [COOH,S] structure for Na^+(Met); however as the metal cation becomes larger, the difference between these two tridentate structures increases eventually reaching a difference of 31 – 32 kJ/mol at Cs^+(Met). The charge-solvated, tridentate [N,OH,S] conformer lies 30 – 35 kJ/mol above the [N,CO,S]

ground state for Li^+(Met) and remains fairly high in energy, only getting to within 20 – 28 kJ/mol of the [N,CO,S] conformer for Cs^+(Met). The charge-solvated bidentate [N,CO] conformer is 27 – 36 kJ/mol higher than the tridentate [N,CO,S] ground state at Li^+(Met), but the difference between these two types of complexes decreases with larger cations, differing by 1 – 8 kJ/mol at Cs^+(Met). Similar behavior is also observed for the charge-solvated, bidentate [CO,S] structure.

The [CO_2^-] and [COOH] conformers differ only in the position of the hydrogen atom shared by the carboxylic acid and amino groups, which moves only by 0.88 Å for Li^+(Met) to 0.75 Å for Cs^+(Met) for the ctggg orientation. Therefore, we also located the transition states (TSs) between these conformers using the synchronous transit-guided quasi-newton (STQN) method[17] at the B3LYP/6-311+G(d,p) ($M^+ = Li^+$, Na^+, and K^+) and B3LYP/HW*/6-311+G(d,p) ($M^+ = Rb^+$ and Cs^+) levels. Single point energies were calculated for this TS at the three levels listed above using the 6-311+G(2d,2p) basis set for $M^+ = Na^+$ and K^+ and HW*/6-311+G(2d,2p) basis set for $M^+ = Rb^+$ and Cs^+. 0 K energies for these TSs with ZPE corrections are 37 – 43, 18 – 24, 9 – 14, 3 – 7, and 1 – 5 kJ/mol higher in energy than the [CO_2^-] ctggg conformers for $M^+ = Li^+$, Na^+, K^+, Rb^+, and Cs^+, respectively. When compared to the energies of the [COOH] ctggg conformer, the TS is 3 kJ/mol lower for $M^+ = Li^+$, 4 – 8 kJ/mol lower for $M^+ = Na^+$, 2 – 7 kJ/mol lower for $M^+ = K^+$, 4 kJ/mol lower to 1 kJ/mol higher for $M^+ = Rb^+$, and 2 kJ/mol lower to 3 kJ/mol higher for $M^+ = Cs^+$. Therefore, once ZPEs are included, the [COOH] ctggg conformer of Li^+(Met), Na^+(Met), and K^+(Met) collapses to the lower energy zwitterionic [CO_2^-] ctggg with no barrier to proton transfer, whereas for Rb^+(Met) and Cs^+(Met),

small barriers for proton transfer of ~1 and ~3 kJ/mol, respectively, are calculated at the B3LYP and MP2(full) levels, but no barrier is found at the B3P86 level.

In order to more completely evaluate the utility of the HW* basis sets for the heavier Rb^+ and Cs^+ metal cations, relative free energies at 298 K for their complexes with Met were also calculated utilizing the Def2TZVP basis sets at the B3LYP, B3P86, and MP2(full) levels of theory, Table 9.2. Overall, the relative free energies using the Def2TZVP basis sets change very little compared to the results of the HW*/6-311+G(2d,2p) basis set. For Rb^+(Met), DFT energies from both treatments agree that the [CO_2^-] conformer is the lowest energy structure. MP2(full) calculations using the HW* and Def2TZVP basis sets predict that a [COOH,S] conformer is the lowest energy conformer. The MP2(full) energies using the HW* basis set predict the [CO_2^-], [N,CO,S], and [COOH,S] conformers lie within 2 kJ/mol of one another for HW* and less than 0.5 kJ/mol with the Def2TZVP basis set. For all basis sets, [CO_2^-], [N,CO,S], [COOH], and [COOH,S] conformers lie within 10 kJ/mol of one another.

For Cs^+(Met), the B3P86 level of theory with the HW* basis set maintains that the [CO_2^-] structure is the lowest energy complex, whereas the B3LYP and MP2(full) levels of theory calculate a [COOH,S] conformer as the lowest energy state. Additionally, all levels of theory with the Def2TZVP basis set determine the [COOH,S] conformer to be the lowest energy structure. For both basis sets, all three levels of theory predict that the [N,CO,S] conformer lies 5 – 13 kJ/mol above the lowest energy conformation. The [COOH] conformer lies 0 – 4 kJ/mol above the [CO_2^-] conformer at all levels of theory.

The vibrational frequencies calculated using the HW*/6-311+G(d,p) and Def2TZVP basis sets are identical within about 2 cm^{-1} for the Rb^+(Met) and Cs^+(Met) complexes. These results further indicate that the HW* calculations are adequate to describe relative energies and vibrational frequencies for the M^+(Met) set of systems.

Finally, all levels of theory predict the [N,CO,S] tgtgg conformer is the lowest energy structure of the H^+(Met) system, Table 9.1. Additional [N,CO,S] orientations lie within ~3 kJ/mol of the tgtgg conformer. The [N,OH,S] analogues lie 11 – 16 kJ/mol higher with respect to the analogous [N,CO,S] conformers at all levels of theory.

IRMPD action spectroscopy. Photodissociation spectra of Met complexed with Li^+, Na^+, K^+, Rb^+, Cs^+, and H^+ were examined. Photodissociation resulted in the loss of the intact ligand leaving the atomic metal cation for the Na^+, K^+, Rb^+, and Cs^+(Met) complexes. This result is consistent with collision-induced dissociation (CID) results for Na^+(Met) and K^+(Met).[2] For the complexes of K^+, Rb^+, and Cs^+, Figure 9.3 shows IRMPD action spectra taken from the relative intensity of the M^+ product cation as a function of laser wavelength. For Na^+(Met), the results shown in Figure 9.3 correspond to the depletion spectrum of the reactant complex as the Na^+ ion was difficult to collect in the FTICR and no other photodissociation products were observed for the Na^+(Met) system. Because of these difficulties, the Na^+(Met) spectrum only spans 900 to 1800 cm^{-1}.

For Li^+(Met), the CID spectra exhibit four low energy channels corresponding to the loss of NH_3, NH_3 + CO, C_3H_8S, and C_3H_8S + H_2O.[2] The first two dissociation pathways were also observed in the IRMPD spectrum for Li^+(Met) and have the greatest intensity upon photodissociation. Two additional channels consisting of the loss of H_2O

+ CO and CH_3SH were also observed in the IRMPD spectrum, but these decomposition pathways encompass less than 10% of the photodissociation signal. The sum of these four decomposition pathways is shown as the IRMPD action spectrum in Figure 9.3. For most bands, deamination (loss of NH_3) is two to three times more intense than the loss of NH_3 + CO, which is expected as deamination is the lowest energy decomposition pathway in the CID spectra of Li^+(Met). However, these two dissociation pathways have the same intensity for bands at 1445 and 1595 cm^{-1}.

For H^+(Met), the IRMPD spectrum shown in Figure 9.3 comprises the sum of the decomposition pathways corresponding to the loss of NH_3, H_2O + CO, H_2O + CO + NH_3, H_2O + CO + CH_3SH, and H_2O + CO + NH_3 + C_2H_2. All of these decomposition pathways are consistent with observed products in the CID spectra of H^+(Met) produced by electrospray ionization[18] and fast atom bombardment.[19] The deamination channel is five times more intense than the loss of H_2O + CO throughout the spectrum. The latter three channels make up approximately 5% of the product intensities from photodissociation.

Comparison of the IRMPD spectra in Figure 9.3 shows that the features observed in the Li^+(Met) spectrum are retained for all of the metal cation complexes, but that new spectral features begin to appear for K^+(Met). The major band at 1716 cm^{-1} shifts to the blue (higher frequencies) as the metal cation becomes heavier whereas the bands at 1160 and 1015 cm^{-1} shift to the red (lower frequencies). Spectral features at 735, 1085, and 1595 cm^{-1} remain largely unchanged as the size of the metal ion increases. The band at 1445 cm^{-1} for Li^+(Met) red shifts to 1430 cm^{-1} in Na^+(Met), and the photodissociation signal in this frequency range increases substantially for K^+(Met), Rb^+(Met), and

Cs^+(Met). A new band emerges at 1670 cm^{-1} for K^+(Met) and Rb^+(Met), but is less distinct for Cs^+(Met). These progressions suggest multiple conformers are now present in the IRMPD spectra for the K^+, Rb^+, and Cs^+ complexes. Of considerable interest here is that the spectra for K^+(Met), Rb^+(Met), and Cs^+(Met) are virtually identical. In contrast, the IRMPD action spectrum for H^+(Met) closely resembles a broadened version of the Li^+(Met) spectrum, with the exception that the highest frequency band blue shifts to 1770 cm^{-1} and there is a distinct peak at 865 cm^{-1}.

Discussion

Comparison of experimental and theoretical IR spectra for Li^+(Met). Figure 9.4 shows the experimental IRMPD action spectrum along with calculated IR spectra for the seven distinct conformers of Li^+(Met). In making these comparisons, it should be remembered that the calculated IR intensities may not correspond exactly with the action spectrum because the latter is a multiple photon process, whereas the theoretical IR spectra are based on single photon absorption. Given this information, it is clear that the bands predicted by the [N,CO,S] tgcgt conformer correspond well with the observed spectrum and have comparable relative intensities. All major bands are present with comparable theoretical and experimental frequencies. Alternative side-chain orientations of the [N,CO,S] conformer are sufficiently low in energy (Table 9.1) that they could also contribute to the experimental spectrum. According to the relative free energies in Table 9.1, the tgcgg conformer could comprise 8 – 11% with the other two conformers contributing less than 2% presuming an equilibrium distribution at room temperature. No other distinct low-lying conformers are predicted to the experimental spectrum.

The band observed at 1716 cm^{-1} corresponds to the carbonyl stretch, which explains its large intensity. The CO stretch predicted by the [N,CO,S]tgcgt conformer at 1705 cm^{-1} agrees with the observed band, but is red shifted by ~10 cm^{-1}. The three higher energy [N,CO,S] conformers have comparable CO stretching frequencies at 1708 (tgcgg), 1712 (tgggt), and 1711 (tgggg) cm^{-1}. Interaction with the lithium cation results in a red shift of this band with respect to free Met, calculated as 1758 and 1782 cm^{-1} depending on the specific conformation. The observed band at 1595 cm^{-1} has the largest deviation with the calculated spectra for the [N,CO,S] tgcgt conformer, which has a band predicted at 1624 cm^{-1} (a frequency essentially invariant for the other orientations). This band describes the bending motion of the NH_2 group and its predicted position is largely unaffected compared to ~1627 cm^{-1} band for neutral Met. Such deviations between experiment and theory have been observed for NH_2 bending modes in other systems[3,4,20,21] and are believed to result from strong anharmonic effects. The peaks observed at 1445, 1160, 1015, 740, 680, and 610 cm^{-1} are well represented by the spectra calculated for the [N,CO,S] conformer. The band at 1445 cm^{-1} is a conglomerate of vibrations corresponding to HCH bends in the amino acid side chain. The band at 1160 cm^{-1} is primarily associated with bending of the H-O-C angle of the carboxylic acid moiety. This is one of the few bands where the spectra of the various [N,CO,S] conformers differ somewhat. The observed band corresponds particularly well with the calculated ground state tgcgt conformer, as this has the most intensity at 1163 cm^{-1} with a shoulder at 1183 cm^{-1}. The shape of the band predicted for the tgcgg conformer is also similar to the observed spectra with a strong band at 1163 and shoulder at 1186 cm^{-1}. The tgggt orientation has a single strong band at 1173 cm^{-1} with a shoulder at 1148 cm^{-1}

and the tgggg orientation has two bands of equal intensity at 1164 and 1174 cm^{-1}. The profiles of these latter two bands do not agree as well with the observed spectrum, consistent with them making only small contributions to the observed spectrum. The [N,CO,S] spectra have predicted bands at 1021 – 1033 cm^{-1}, the NH_2 wagging motion, which is slightly blue shifted with respect to an observed peak at 1015 cm^{-1}. Observed peaks at 610, 680, and 740 cm^{-1} correspond to wagging motions of the carboxylic acid hydrogen atom and match the predicted spectra for all [N,CO,S] conformers well. Broad and weak bands observed at 800 – 900 cm^{-1} and 1250 – 1350 cm^{-1} are also consistent with predicted bands in the [N,CO,S] spectra. Finally, there is a weak band observed at 1080 cm^{-1} that could correspond to a weak band in the [N,CO,S] calculated spectra associated with synchronous C-C and C-N bond stretches.

It is quite clear that the observed spectrum for Li^+(Met) does not include any contributions from the zwitterionic [CO_2^-] and [CO_2^-,S] conformers. The intense carbonyl stretch predicted at 1620 and 1656 cm^{-1}, respectively, is much lower in frequency compared to free Met and the observed spectrum. Additionally, the broad bands at 1250 – 1500 cm^{-1} in the predicted zwitterionic spectra are inconsistent with the experimental spectrum. There does not appear to be any contribution from the [N,OH,S] tgggt conformer either. Compared to the [N,CO,S] calculated spectrum, this conformation has minimal diagnostic bands. The CO stretch (1835 cm^{-1}) is considerably blue shifted with respect to the observed band at 1716 cm^{-1}, but lies beyond the frequency range for the experimental spectrum. The major band predicted at 1029 cm^{-1} overlaps with the predicted band at 1030 cm^{-1} in the [N,CO,S] spectrum. Therefore, the bands at 577, 649, and 707 cm^{-1} corresponding to the wagging motion of the acid hydrogen atom

are the most diagnostic bands and do not match the observed spectrum. Although the predicted spectrum for the [N,CO] tgtgt conformer has a number of similarities to that for [N,CO,S] tgcgt, we can dismiss any contribution from the [N,CO] tgtgt conformation for Li^+(Met). First, the carbonyl stretch of the bidentate conformation (1690 cm^{-1}) is red shifted with respect to the observed band at 1716 cm^{-1} and calculated frequency of 1705 – 1712 cm^{-1} in the [N,CO,S] conformation. Second, the predicted spectrum shows a low-frequency shoulder for the band at 1160 cm^{-1}, which is not observed. Finally, the predicted profile for the observed band at 1015 cm^{-1} matches that predicted for the NH_2 wagging motion in the [N,CO,S] tgcgt and tgcgg conformations at 1030 – 1033 cm^{-1}, with a weaker low frequency shoulder and a steep profile at higher frequencies, in contrast to the relative intensities of these bands in the [N,CO] tgtgt spectrum. Similarly, the [CO,S] and [COOH] spectra do not reproduce the experimental spectrum with any fidelity. Overall, the experimental IRMPD action spectrum can be explained completely by the calculated spectra of the ground state [N,CO,S] tgcgt and tgcgg conformers.

Comparison of experimental and theoretical IR spectra for Na^+(Met). The Na^+(Met) spectrum is very similar to the Li^+(Met) spectrum over the available range of 900 to 1800 cm^{-1}, Figure 9.3. Subtle differences with respect to the action spectrum of Li^+(Met) are present and include a blue shift in the band at 1716 cm^{-1} to 1734 cm^{-1} and bands that red shift from 1015 cm^{-1} to 1000 cm^{-1}, 1160 cm^{-1} to 1140 cm^{-1}, and 1445 cm^{-1} to 1430 cm^{-1}. Bands located at 1080 and 1595 cm^{-1} are unaffected. Comparison of the experimental spectrum with the theoretical spectra for Na^+(Met) is shown in Figure 9.5. As for Li^+(Met), the predicted [N,CO,S] tgcgt spectrum shows a close correspondence to the limited observed spectrum for Na^+(Met). Notably, the predicted carbonyl stretch

frequency shifts to higher frequency by 16 cm^{-1} from Li^+(Met) to Na^+(Met), in agreement with the experimental observation. Likewise the NH_2 bending band at 1595 cm^{-1} is predicted not to shift from Li^+(Met) to Na^+(Met), consistent with experiment. Overall, the predicted spectra for the [N,CO,S] conformers of Li^+(Met) and Na^+(Met) accurately represent the changes observed with metal cation identity.

The major peaks observed in the Na^+(Met) depletion spectrum at 1735, 1430, 1140, and 1000 cm^{-1} were also observed in the Na^+ product ion spectrum (not shown); however, the weak bands observed at 1650, 1595, and 1080 cm^{-1} in the depletion spectrum were not present in the Na^+ product ion spectrum. The weak band at 1650 cm^{-1} cannot be described by the [N,CO,S] tgcgt conformer, but could correspond to an antisymmetric carboxylate stretch for the zwitterionic [CO_2^-] ctggg and cgtgg conformers calculated to lie at 1639 cm^{-1}. It is possible that the experimental spectrum could contain the [CO_2^-] ctggg and cgtgg conformers, which are calculated to lie 2 – 11 kJ/mol above the [N,CO,S] tgcgt ground state, Table 9.1. One might anticipate that the presence of the [CO_2^-] conformer would also lead to a signal increase near 1440 cm^{-1}; however, the low intensity of the 1650 cm^{-1} band suggests that this would be hidden by the spectral features already present from [N,CO,S]. If the relative intensities of the bands at 1734 and 1650 cm^{-1} are reliable indicators of the relative populations of the two conformers (and this may not be the case for the reasons noted above), then the [CO_2^-] conformer would represent ~7% of the signal present (consistent with an excitation energy of 6.4 kJ/mol at 298 K).

Comparison of experimental and theoretical IR spectra for K^+(Met) and Rb^+(Met). Figures 9.6 and 9.7 show the experimental IRMPD action spectrum of

K^+(Met) and Rb^+(Met) compared with theoretical predictions for the seven lowest energy distinct conformations. Compared to the experimental spectra for Li^+(Met) and Na^+(Met), the IRMPD spectrum of K^+(Met) retains the same bands, but new features are present, Figure 9.3. The spectrum for Rb^+(Met) is very similar to that for K^+(Met), having the same number of new bands compared to the Li^+(Met) and Na^+(Met) spectra. These new bands could be attributed to new conformers present or could be attributed to improved sensitivity by more facile dissociation from this weakly bound system. However, in no case do the new experimental bands correspond to previously unobserved peaks in the predicted spectrum for [N,CO,S]. Hence, there is no indication that enhanced sensitivity can explain the new features.

New bands in the observed spectrum of K^+(Met) [Rb^+(Met)] occur at 875 [880], 960 [955], 1225 [1230], 1405 [1395], and 1670 [1670] cm^{-1}. The band at 1430 [1430] cm^{-1} has grown in intensity with respect to Na^+(Met) and a broad low frequency shoulder is now present. Overall, a comparison between the K^+(Met) and Rb^+(Met) spectra with those of Li^+(Met) and Na^+(Met) shows a considerable increase in photodissociation in the region from 750 to 1400 cm^{-1}. The [N,CO,S] conformers may still be present as the predicted carbonyl stretch of 1724 – 1730 [1731 – 1737] cm^{-1} agrees well with the corresponding band observed at 1735 [1742] cm^{-1}; however, carbonyl stretches of the [COOH] (1733 [1743] cm^{-1}) and [CO,S] (1732 [1739] cm^{-1}) conformers are equally consistent. The frequencies for the bending mode of the NH_2 group in the [N,CO,S] spectra (1618 – 1626 [1618 – 1624] cm^{-1}) are still blue shifted by ~30 cm^{-1} with respect to the observed band at ~1595 [1590] cm^{-1}, consistent with observations for Li^+(Met) and Na^+(Met). The intense calculated band at 1149 –1152 [1143 – 1148] cm^{-1} corresponding

to the C-O-H bending mode of the [N,CO,S] conformer matches the observed spectrum for K^+(Met) [Rb^+(Met)] well. Likewise, the wagging motions of the acidic hydrogen atom at 730 [735] and below 700 cm^{-1} in the observed K^+(Met) [Rb^+(Met)] spectrum are also well characterized in the calculated spectra for the [N,CO,S] conformer. These bands demonstrate the presence of the [N,CO,S] conformer as it and the higher energy [N,CO] are the only conformers with bands in this frequency range. Bands observed at 960 [955], 1100 [1090], and the shoulder at 1430 [1430] cm^{-1} could also have contributions from the [N,CO,S] conformer.

A prominent new peak at 1670 [1670] cm^{-1} in the observed spectra for K^+(Met) [Rb^+(Met)] indicates the presence of the zwitterionic [CO_2^-] conformer. Calculated spectra for these conformers indicate this band appears at 1649 – 1650 [1660 – 1661] cm^{-1} for K^+(Met) [Rb^+(Met)]. The appearance of this new peak is accompanied by the band observed at 1405 [1395] cm^{-1} along with a broad shoulder to the red. These new bands can be attributed to the intense band calculated at 1417 – 1423 [1408 – 1413] cm^{-1} in the predicted spectra for the three [CO_2^-] conformers along with several bands extending from 1225 [1230] to 1405 [1395] cm^{-1}. Bands observed at 875 [880] and 1100 [1090] cm^{-1} can also be described by bands calculated in all [CO_2^-] spectra.

Overall, the experimental spectra for K^+(Met) and Rb^+(Met) are adequately represented by contributions from the [N,CO,S] and [CO_2^-] conformers. This is consistent with calculations for K^+(Met), which indicate that any other conformers lie at least 7 kJ/mol higher in energy, Table 9.1. Thus, at 298 K, contributions from [COOH,S] conformations are calculated to be <6% and those for any other conformer are <1%. For Rb^+(Met), both the [COOH,S] and [COOH] conformers lie low enough in energy (0 – 8

and 3 – 10 kJ/mol, respectively, Table 9.1) to potentially contribute to the ion population. Indeed, the broad band observed at 1405 [1395] cm^{-1} for K^+(Met) [Rb^+(Met)] could have contributions from the intense bands at 1378 – 1386 [1374 – 1389] cm^{-1} for the [COOH,S] conformers, which are attributed to the C-O-H bending mode. The relative intensities of the peaks observed at 875 [880] and 960 [955] cm^{-1} are also consistent with similar bands in the calculated spectra of the [COOH,S] cgggg and cgggt conformations, but notably not of the highest energy cgcgg orientation. Discounting the presence of the [COOH,S] conformers is the fact that the calculated carbonyl stretches (1750 – 1756 [1756 – 1763] cm^{-1}) are blue shifted by 15 – 20 cm^{-1} with respect to the observed band at 1735 [1742] cm^{-1}, in contrast to the red shift of ~15 cm^{-1} observed for this band in the Li^+(Met) and Na^+(Met) spectra. There are no high frequency shoulders in this region of the observed spectra that would be consistent with the presence of considerable amounts of both the [N,CO,S] and [COOH,S] conformers, although minor amounts of the latter would lead to simple broadening of this peak, which is possibly consistent with the data. In contrast, the carbonyl stretches at 1733 – 1735 [1743 – 1745] cm^{-1} for the [COOH] conformers agree well with the CO stretch observed in the IRMPD spectra and would simply overlap the contribution from the [N,CO,S] conformer present. These three [COOH] conformers lie within 4 kJ/mol of one another for K^+(Met) and Rb^+(Met), Table 9.1. These conformers also have an intense peak predicted at 1403 [1404 – 1410] cm^{-1} that could correspond to the observed peak at 1405 [1395] cm^{-1}. The [COOH] conformer has no additional distinctive bands that allow its presence to be verified. In conclusion, we can confidently attribute the observed spectra of K^+(Met) and Rb^+(Met) to

dissociation from [N,CO,S] and [CO_2^-] conformers, but cannot rule out contributions from [COOH,S] and [COOH] conformers.

Comparison of experimental and theoretical IR spectra for Cs^+(Met). Figure 9.8 shows the IRMPD action spectrum of Cs^+(Met) with theoretical predictions for seven low-energy distinct conformers. All of the spectral features for K^+(Met) and Rb^+(Met) are still present in the Cs^+(Met) spectrum, Figure 9.3, with the only differences being increases in relative intensity between 700 – 900 and 1200 – 1400 cm^{-1}. Therefore, all of the comparisons between the observed spectrum and the predicted spectra mentioned in the previous section are still viable. Both [N,CO,S] tgcgt and [CO_2^-] conformers appear to contribute to the observed spectra with intensity changes indicating that there is more [CO_2^-] compared to [N,CO,S], consistent with the changes in the relative energies calculated as a function of metal cation. The presence of [COOH] and [COOH,S] conformers is again possible, although the peak corresponding to the carbonyl stretch provides no strong indications that these latter conformers are present.

Comparison of experimental and theoretical IR spectra for H^+(Met). Figure 9.9 shows the IRMPD action spectrum of H^+(Met) with theoretical predictions for three low-energy conformations. The H^+(Met) complex is unique among all the systems investigated here as the proton is covalently bound to the amine group of the amino acid backbone. Only two spectra are shown for the four low energy [N,CO,S] conformations described in Table 9.1 as the calculated IR spectra are identical for tgtgg and tgtgt orientations and for tgggg and tgggt orientations. The calculated spectrum for the [N,OH,S] tgtgg conformation is also shown for comparison. The experimental spectrum exhibits bands at 1775, 1560, 1455, 1330, 1230, 1155, 1050, 975, 865, 710, 620, and 580

cm^{-1}. The observed peak at 1775 cm^{-1} corresponds to the carbonyl stretch. The peaks at 1560 and 1455 cm^{-1} correspond to the NH_3 bending and NH_3 umbrella motions, respectively. Observed bands at 1330 and 1230 cm^{-1} correspond to wagging motions of the alpha carbon hydrogen atom and CH_2 groups of the amino acid side chain. The H-O-C bending motion is represented by the peak observed at 1155 cm^{-1}. The peak at 975 cm^{-1} corresponds to elongation of the C-C and C-N bonds in the backbone, while the band at 865 cm^{-1} corresponds to the NH_2 rocking motion. The three peaks at 710, 620, and 580 cm^{-1} are wagging motions of the acidic hydrogen atom.

The IRMPD action spectrum is well described by the [N,CO,S] calculated spectra. The H^+(Met) carbonyl stretch in the observed spectrum (1775 cm^{-1}) is reproduced extremely well by the [N,CO,S] spectra (1768 – 1770 cm^{-1}), whereas the CO stretch is blue shifted nearly 45 cm^{-1} (1820 cm^{-1}) for the [N,OH,S] tgtgg conformer. Therefore, it is unlikely that the observed spectrum includes any contribution from the [N,OH,S] conformers, consistent with their calculated relative energies (Table 9.1), which would predict <0.5% population at 298 K. This peak is red shifted compared to the neutral ligand by much less than any of the metal cation complexes, consistent with a more delocalized charge in the H^+(Met) complex. The bending and umbrella motions of the NH_3 group in the calculated spectra for H^+(Met) are blue shifted with respect to the observed peaks at 1455 and 1560 cm^{-1}. This further illustrates that the single photon calculations cannot adequately describe the multiple photon spectra for umbrella or bending motions of the amine group. The broad peak spanning 1375 – 1500 cm^{-1} in the observed spectrum is a conglomerate of the bands corresponding to the umbrella motions at 1470 – 1475 cm^{-1} for the [N,CO,S] conformations, as well as the band at 1390 cm^{-1}.

The calculated spectra predict a band associated with the H-O-C bending mode at 1160 cm^{-1}, which agrees with the 1155 cm^{-1} peak in the observed spectrum. The large shoulder located at frequencies below the 1155 cm^{-1} peak is reproduced by the shoulder of the tgggg/tgggt calculated spectrum, which indicates that these higher energy orientations are definitely present. The observed spectrum from 580 to 1000 cm^{-1} is reproduced quite well by the [N,CO,S] calculated spectra. The band at 865 cm^{-1} with a low frequency shoulder is consistent with the presence of both tgtgg/tgtgt and tgggg/tgggt orientations. The largest discrepancy in the low frequency region is the calculated band at 640 cm^{-1} is blue shifted with respect to the observed peak at 620 cm^{-1}. As noted above, the 865 cm^{-1} band in the H^+(Met) spectrum, which corresponds to the rocking motion of the NH_2 group, does not appear in the Li^+(Met) spectrum, Figure 9.3. This is because the strong tridentate interaction of the lithium ion effectively quenches this rocking motion from occurring, whereas the bidentate interactions of the proton allow it.

Overall comparison. We can now provide a more global comparison of the main features in all five spectra in Figure 9.3. The predicted frequencies for the CO stretch of the [N,CO,S]tgcgt conformer change from 1705 cm^{-1} for Li^+(Met), 1721 cm^{-1} for Na^+(Met), 1728 cm^{-1} for K^+(Met), 1736 cm^{-1} for Rb^+(Met), and 1739 cm^{-1} for Cs^+(Met) (1732 cm^{-1} for the tgggg orientation), in agreement with the observed blue shift in the experimental spectra from 1716 cm^{-1} for Li^+(Met), 1734 cm^{-1} for Na^+(Met), 1735 cm^{-1} for K^+(Met), and 1742 cm^{-1} for both Rb^+(Met) and Cs^+(Met). The CO stretch of the [COOH] conformers shows a similar shift with metal cation, changing from 1733 – 1735 cm^{-1} for K^+, 1743 – 1745 cm^{-1} for Rb^+, and 1746 – 1749 cm^{-1} for Cs^+; however, because these bands are blue shifted compared to the [N,CO,S] conformer, appreciable contributions of

the [COOH] conformers would be expected to lead to larger blue shifts in the experimental spectrum than observed. Likewise, the CO stretch for the [COOH,S] conformers, 1750 – 1756 cm^{-1} for K^+, 1747 – 1763 cm^{-1} for Rb^+, and 1753 – 1764 cm^{-1} for Cs^+, is blue shifted even further, again suggesting that this species does not make major contributions to the experimental spectrum. The observed band at 1158 cm^{-1} in the Li^+(Met) spectrum red shifts to 1145 cm^{-1} for Cs^+(Met). This shift is consistent with that predicted for the in-plane COH bending motion of [N,CO,S] tgcgt conformers with predicted frequencies of 1168 cm^{-1} for Li^+(Met), 1160 cm^{-1} for Na^+(Met), 1152 cm^{-1} for K^+(Met), 1148 cm^{-1} for Rb^+(Met), and 1145 cm^{-1} for Cs^+(Met). Although the band at 1595 cm^{-1} is not accurately predicted because of its anharmonicity, this band does not shift with metal cation identity, in agreement with the predictions for the [N,CO,S] tgcgt conformers. No shifts are predicted for the broad band at 1430 cm^{-1}, which becomes a high frequency shoulder in the spectra for K^+(Met) – Cs^+(Met). Likewise the bands at about 730 cm^{-1} observed in all the spectra are predicted to red shift somewhat, from 738 to 724 cm^{-1} in going from Li^+(Met) to Cs^+(Met). The good agreement in these trends provides further evidence that the [N,CO,S] tgcgt conformer is present for all the IRMPD action spectra in Figure 9.3.

The antisymmetric CO stretch of the [CO_2^-] conformers first appears in the IRMPD action spectrum for Na^+(Met) at 1650 cm^{-1} and blue shifts to 1670 cm^{-1} for both K^+(Met) and Rb^+(Met). This band is not as well defined for Cs^+(Met), but the photodissociation signal at similar frequencies can only be described by the presence of [CO_2^-] conformations. The predicted bands of all [CO_2^-] conformers agree well with the observed bands and are predicted to shift from 1639 to 1661 cm^{-1} in going from Na^+(Met)

to Rb^+(Met). The umbrella motions of the NH_3 group in the [CO_2^-] conformers are predicted at 1417 – 1426 cm^{-1} for K^+(Met), 1408 – 1417 cm^{-1} for Rb^+(Met), and 1402 – 1411 cm^{-1} for Cs^+(Met). This decrease in frequencies with heavier metal ion is consistent with the IRMPD action spectra for K^+(Met), Rb^+(Met), and Cs^+(Met) with peaks located at 1405, 1395, and 1390 cm^{-1}, respectively, Figure 9.3, with a consistent shift to lower frequencies compared to experiment of ~15 cm^{-1}.

The theoretical results for Rb^+(Met) and Cs^+(Met) indicate that the [COOH,S] and [COOH] conformers are low-energy structures and could be present in the IRMPD action spectra. These conformers have intense bands predicted near 1400 cm^{-1}, corresponding to the C-O-H bending motion, which are the most diagnostic bands in their calculated spectra. This motion is largely unaffected with increasing cation size for both conformers. For the [COOH,S] conformers, this motion is predicted at 1378 – 1386 cm^{-1} for K^+(Met), 1374 – 1389 cm^{-1} for Rb^+(Met), and 1377 – 1386 cm^{-1} for Cs^+(Met). These predicted frequencies do lie closer to the observed peaks at 1405, 1395, and 1390 cm^{-1} for K^+(Met), Rb^+(Met), and Cs^+(Met), respectively, than the frequencies corresponding to the umbrella motion of the NH_3 group in the [CO_2^-] conformers, but the frequencies increase as the metal gets heavier for the cgggg orientation and change very little for cgggt and cgcgg orientations instead of the red shift experimentally observed. Likewise, the C-O-H bending modes of the [COOH] conformers are predicted to occur at 1403 cm^{-1} for K^+(Met), 1404 – 1410 cm^{-1} for Rb^+(Met), and 1405 – 1407 cm^{-1} for Cs^+(Met). Because the observed bands at ~1400 cm^{-1} are broad in these three spectra, contributions from these two conformations cannot be eliminated.

Conclusions

The IRMPD action spectra of cationized methionine in the region of 550 – 1800 cm^{-1} have been obtained for complexes with Li^+, Na^+, K^+, Rb^+, Cs^+, and H^+. Comparison of these experimental spectra with IR spectra calculated at the B3LYP/6-311+G(d,p) and B3LYP/HW*/6-311+G(d,p) levels of theory allow the conformations likely to be present in the experiment to be identified. For the H^+(Met) system, the IRMPD spectrum is characterized by four [N,CO,S] conformers that differ only in their side-chain orientation and deviate little in energy (within 4 kJ/mol). For the alkali metal cationized systems, these comparisons suggest that the charge-solvated [N,CO,S] conformer is the only structure present in the IRMPD action spectrum for Li^+(Met) and Na^+(Met), consistent with it being the clear ground-state conformation according to theory. This species remains a contributor for all metal cations studied. Contributions from the [CO_2^-] conformer, which becomes the ground state according to DFT calculations as the metal cation gets heavier, clearly manifest themselves for K^+(Met), Rb^+(Met), and Cs^+(Met). Theory suggests that [COOH,S], the ground state conformer for Rb^+(Met) and Cs^+(Met) according to MP2(full) calculations, and [COOH] conformers should also be present for Rb^+(Met) and Cs^+(Met). The experimental IRMPD action spectra cannot eliminate the presence of these conformers, but do not require their presence to be reproduced. The photodissociation spectra of K^+(Met), Rb^+(Met), and Cs^+(Met) have very similar spectral features and are considerably more complex than IRMPD spectra of K^+, Rb^+, and Cs^+ bound to other amino acids.[3,4,6-9,11,12] Zwitterionic [CO_2^- contributions for these larger metals are also observed for cysteine, the other sulfur-containing amino acid, bound to alkali metal cations.[5]

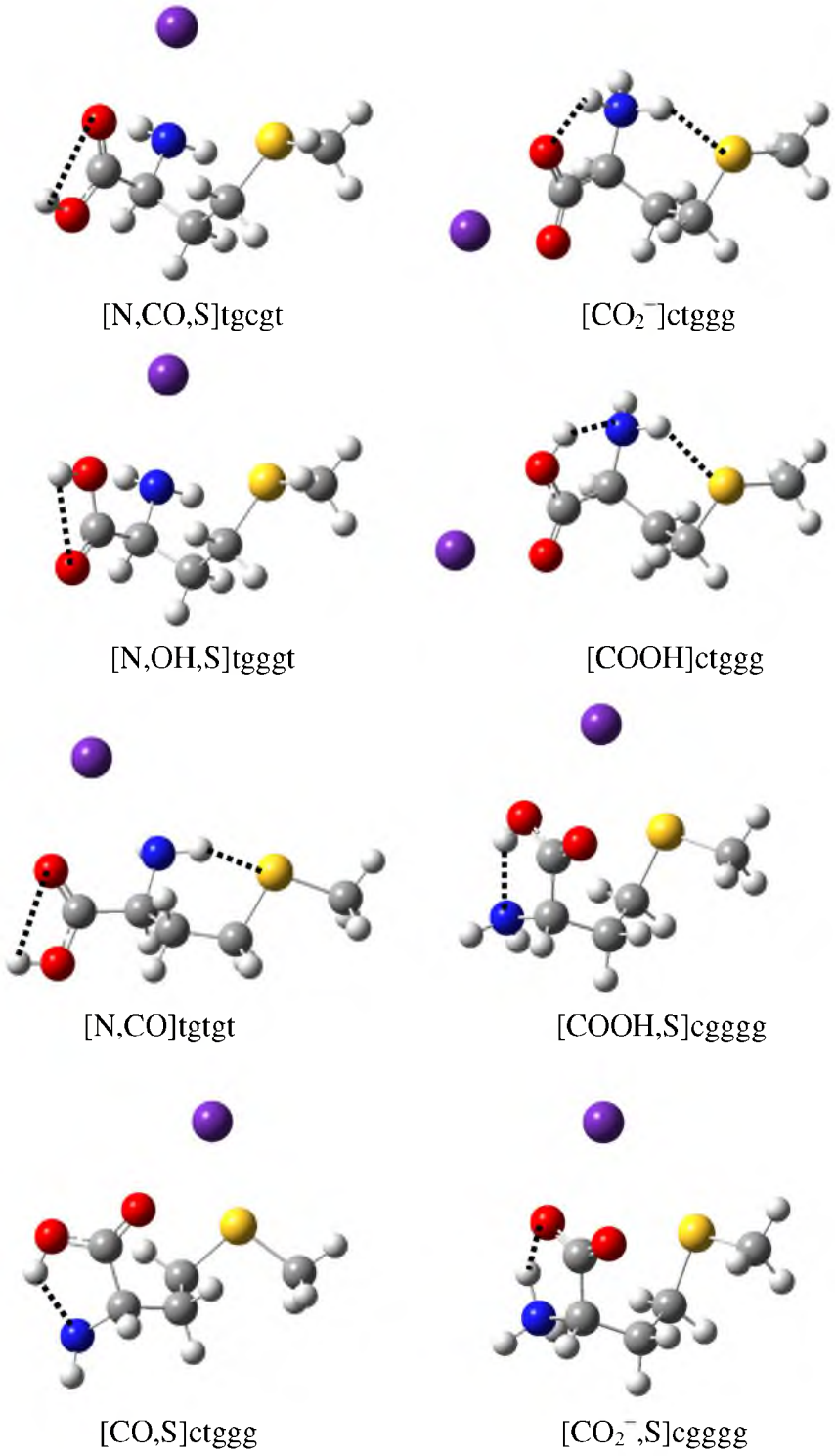

Figure 9.1. Structures of the Rb^+(Met) complexes calculated at the B3LYP/HW*/6-311+G(d,p) level of theory. Hydrogen bonds indicated by dashed lines.

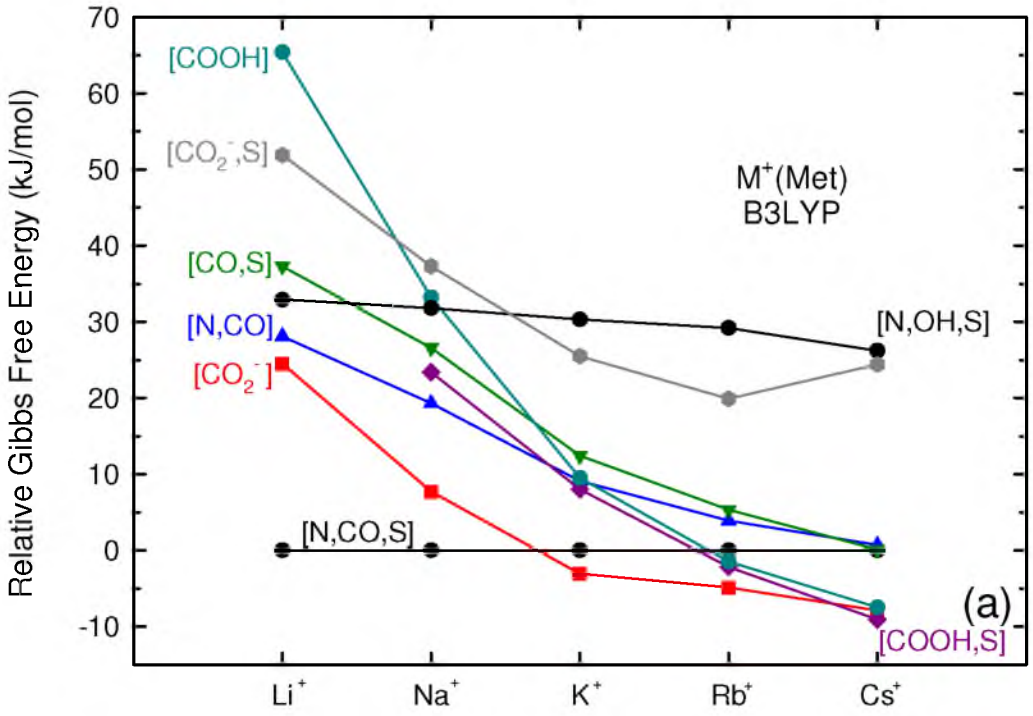

Figure 9.2. 298 K free energies (kJ/mol) from Table 9.1 calculated at the B3LYP, B3P86, and MP2(full) levels of theory (parts a – c, respectively) of eight conformations of M^+(Met) complexes as a function of the alkali-metal cation relative to the energy of the [N,CO,S] conformer. The relative energy of the [CO_2^-,S] structure is higher than expected for Cs^+ because the orientation preferred for Li^+ to Rb^+ collapses to a high energy [CO_2^-] structure.

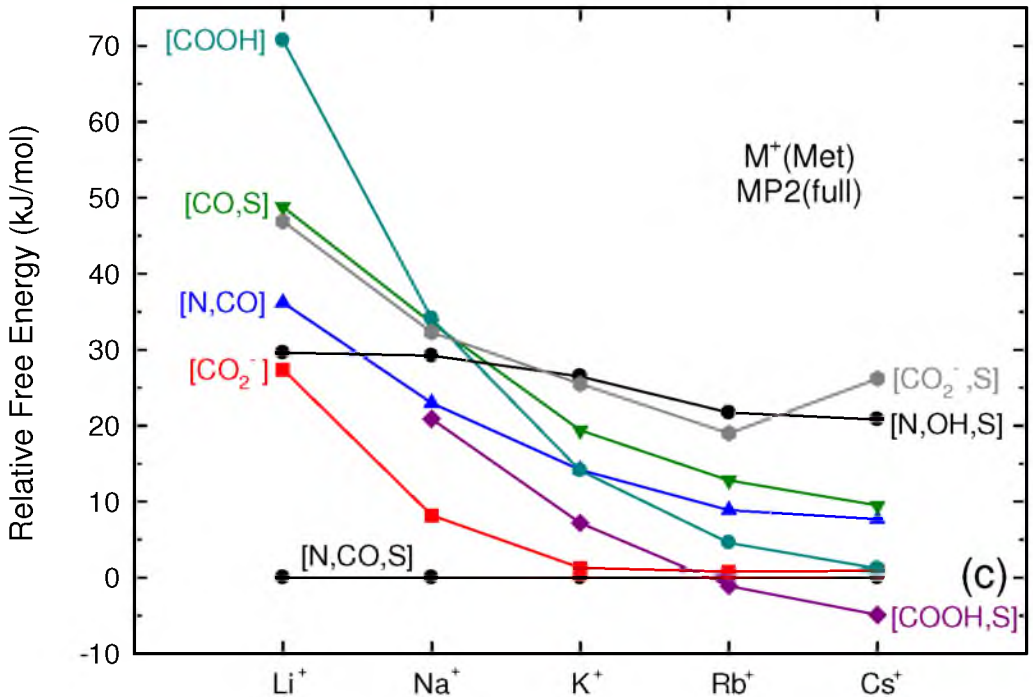

Figure 9.2. continued

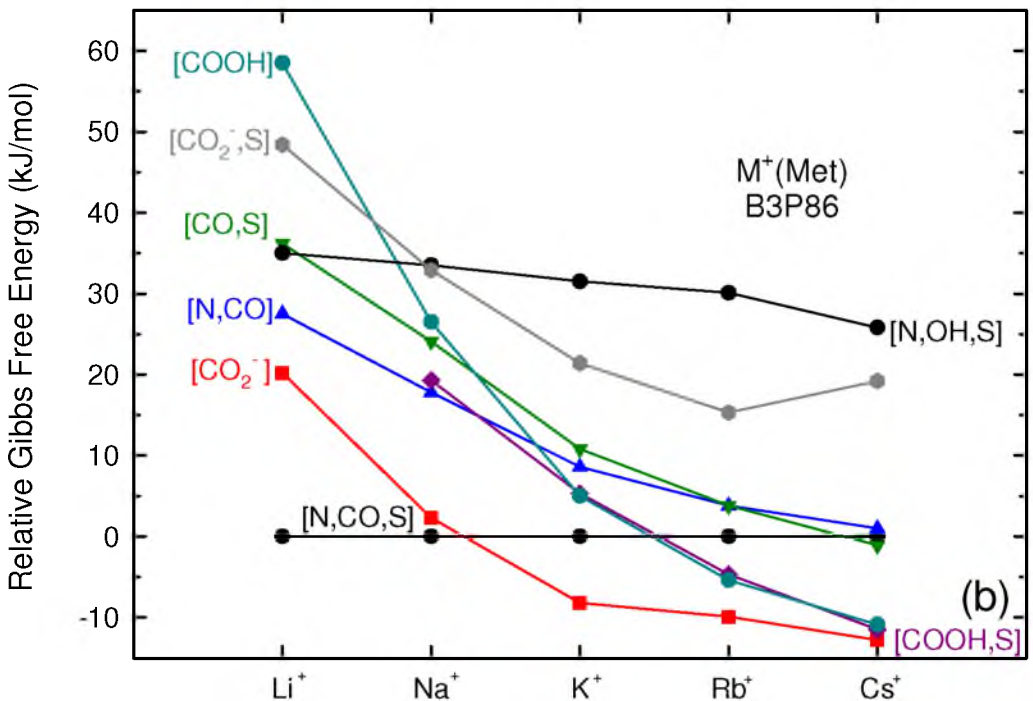
Relative Gibbs Free Energy (kJ/mol)
60
50
40
30
20
10
0
-10
[COOH]
[CO2-,S]
[CO,S]
[N,CO]
[CO2-]
[N,CO,S]
M+(Met)
B3P86
[N,OH,S]
(b)
[COOH,S]
Li+
Na+
K+
Rb+
Cs+

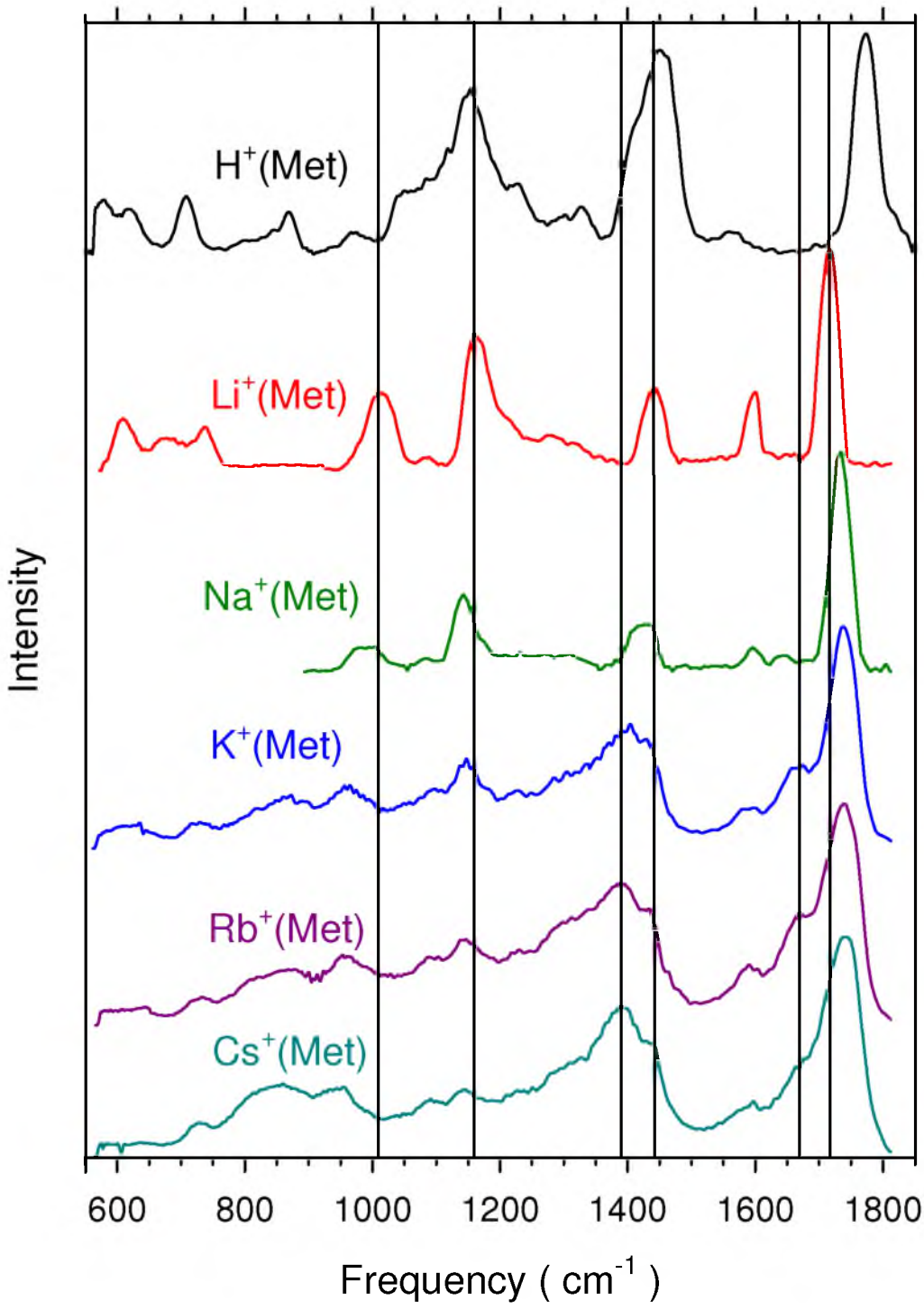

Figure 9.3. IRMPD action spectra of M^+(Met) complexes, where $M^+ = H^+$, Li^+, Na^+, K^+, Rb^+, and Cs^+.

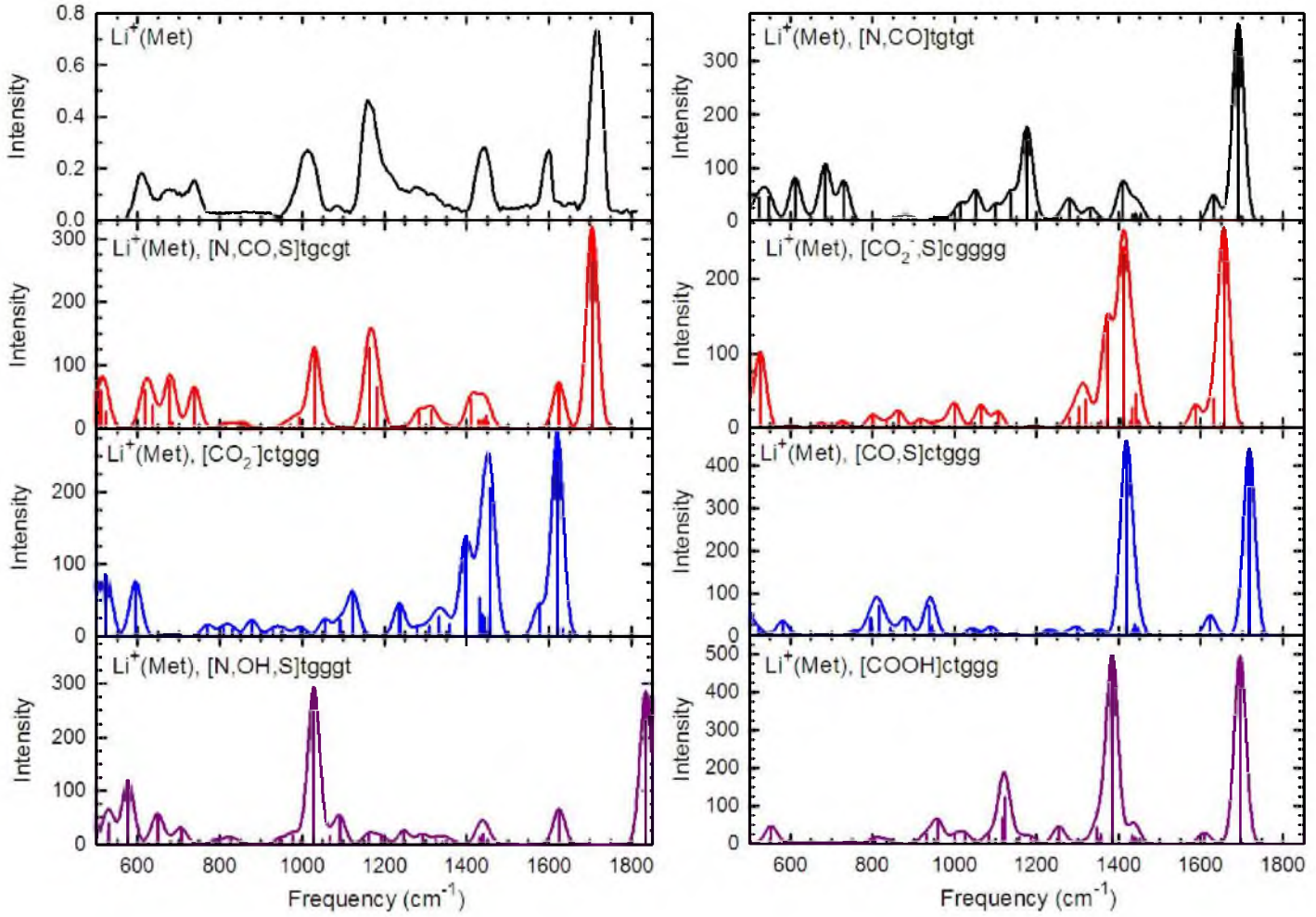

Figure 9.4. Comparison of the experimental IRMPD action spectrum for Li^+(Met) with IR spectra predicted at the B3LYP/6-311+G(d,p) level of theory for seven conformations.

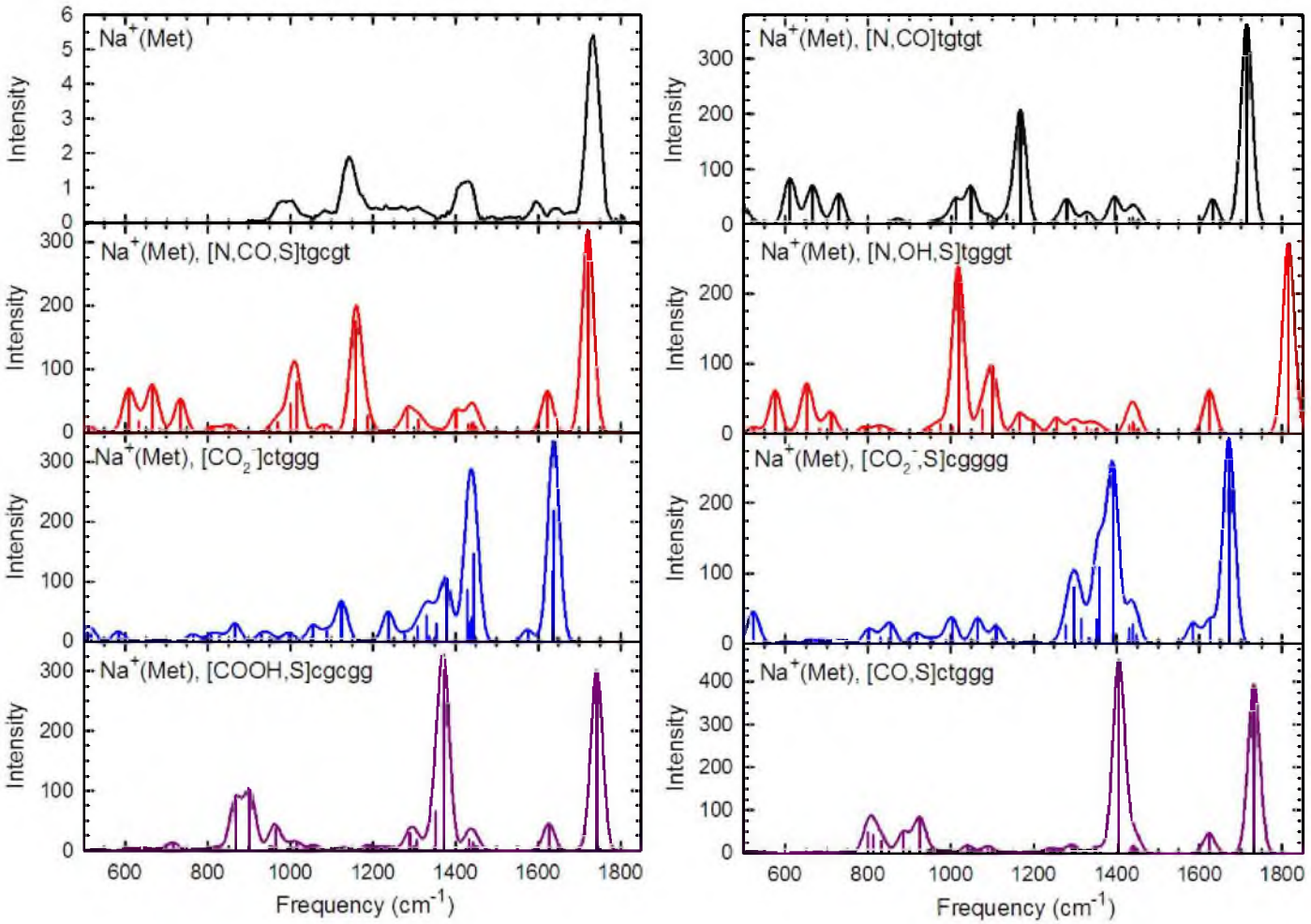

Figure 9.5. Comparison of the experimental IRMPD action spectrum for Na^+(Met) with IR spectra predicted at the B3LYP/6-311+G(d,p) level of theory for seven conformations.

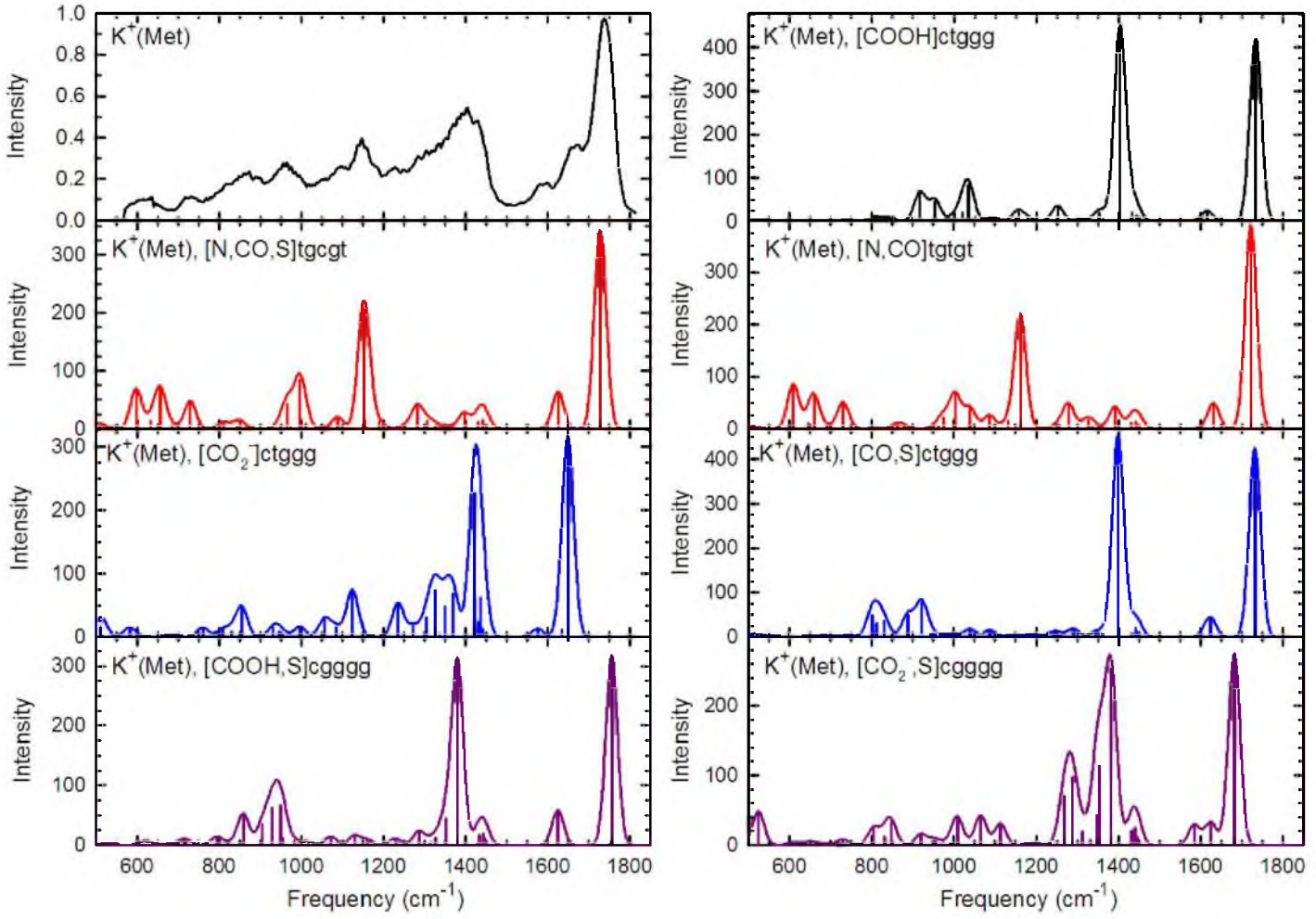

Figure 9.6. Comparison of the experimental IRMPD action spectrum for K^+(Met) with IR spectra predicted at the B3LYP/6-311+G(d,p) level of theory for seven conformations.

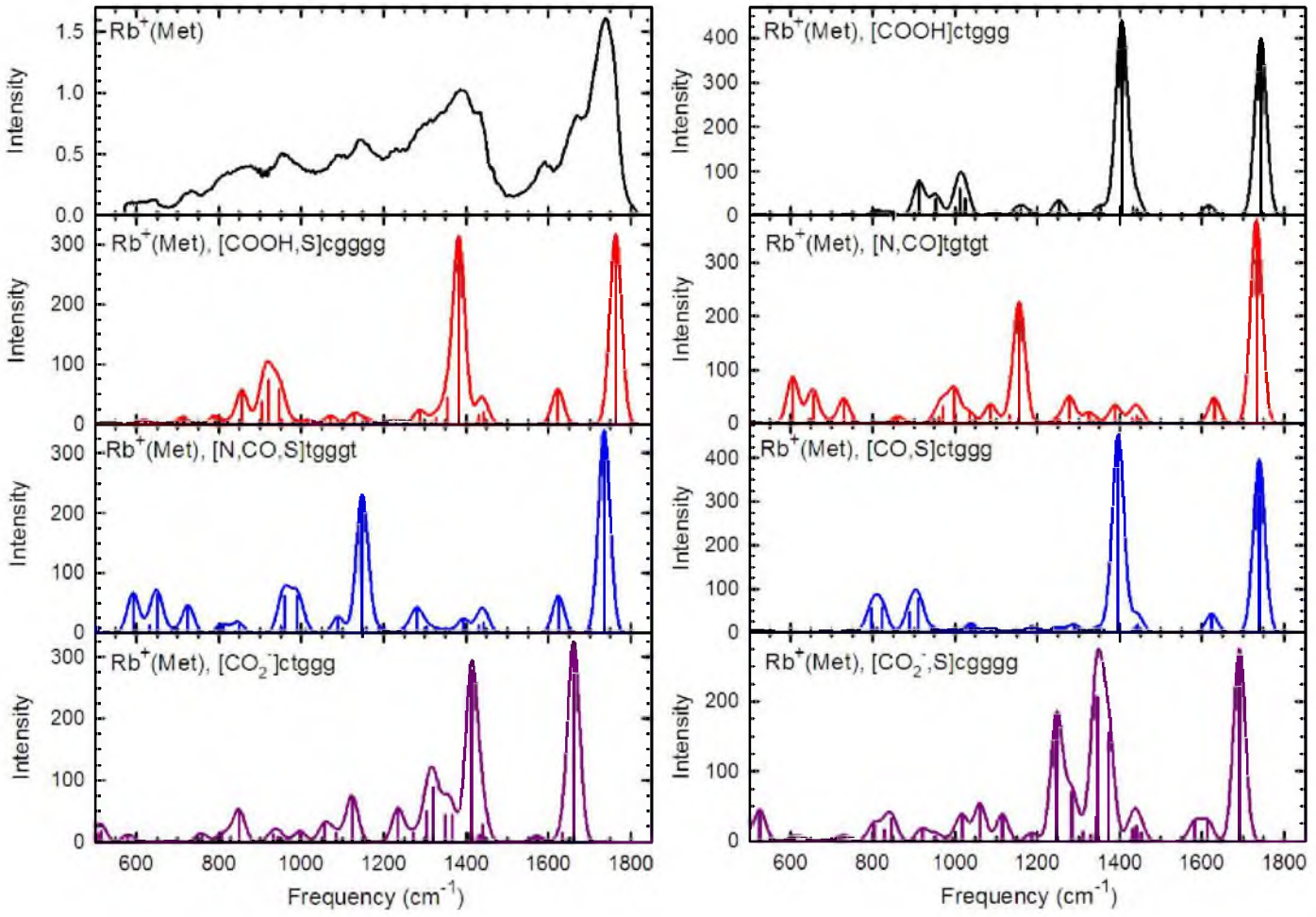

Figure 9.7. Comparison of the experimental IRMPD action spectrum for Rb^+(Met) with IR spectra predicted at the B3LYP/HW*/6-311+G(d,p) level of theory for seven conformations.

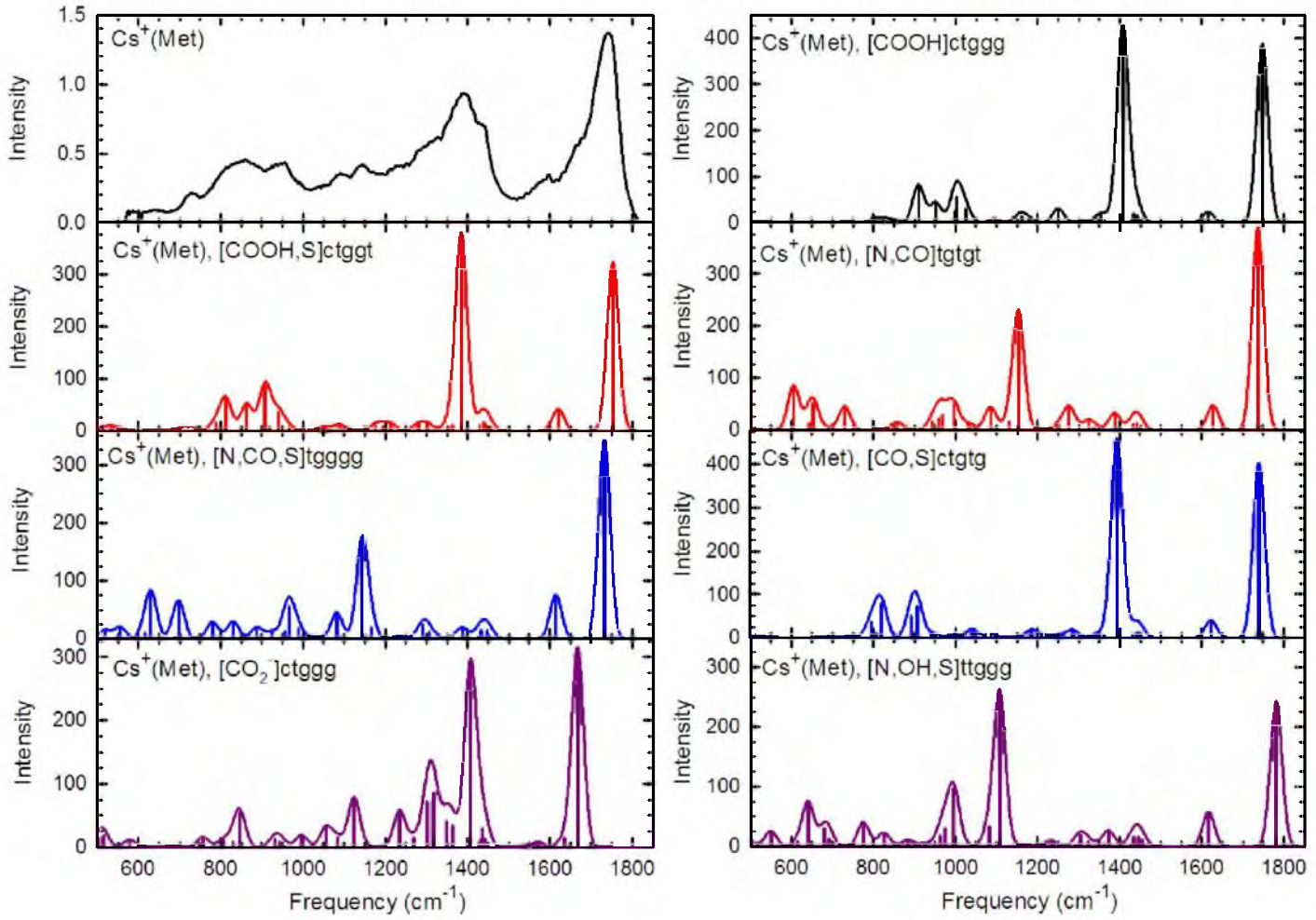

Figure 9.8. Comparison of the experimental IRMPD action spectrum for Cs^+(Met) with IR spectra predicted at the B3LYP/HW*/6-311+G(d,p) level of theory for seven conformations.

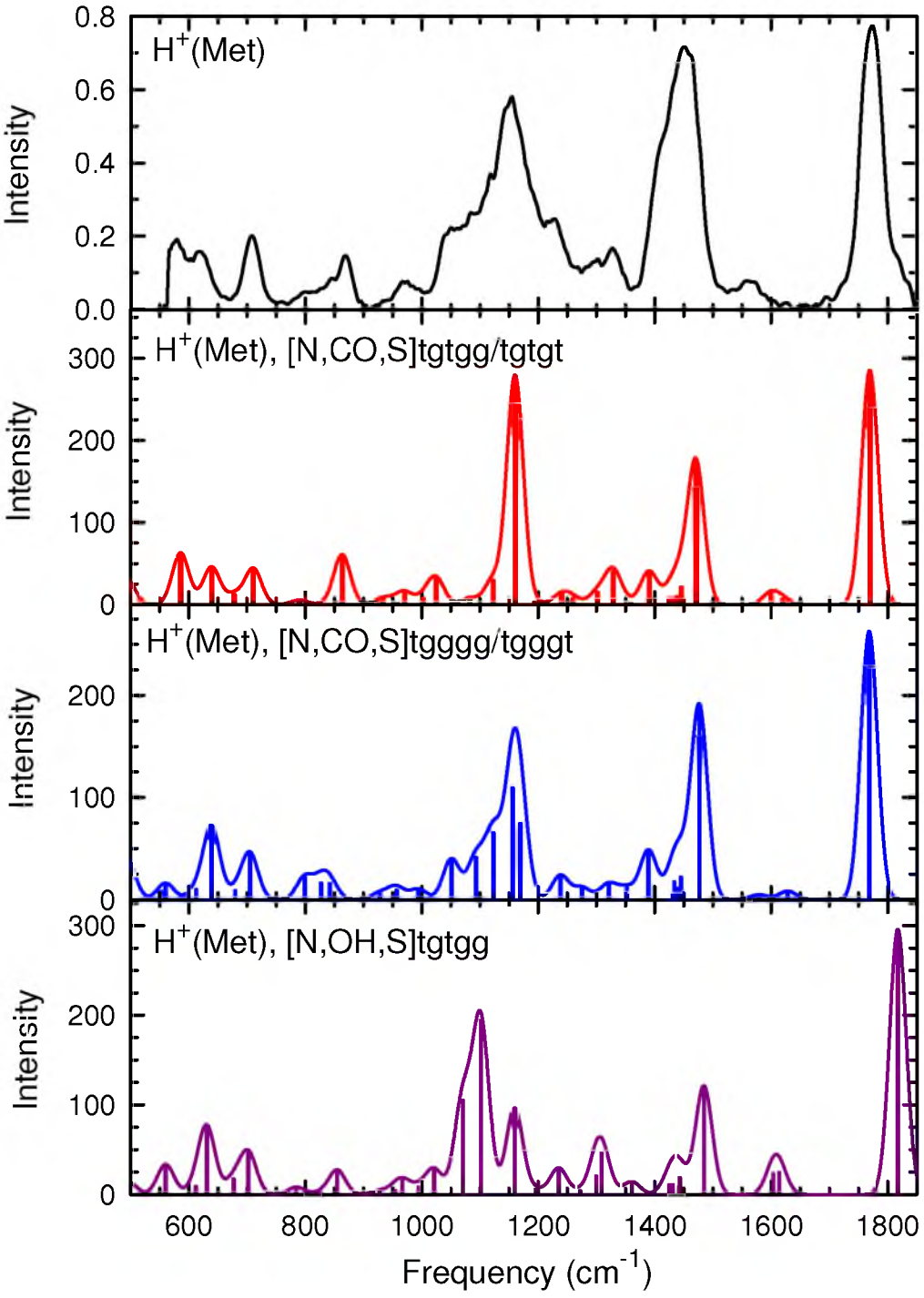

Figure 9.9. Comparison of the experimental IRMPD action spectrum for H^+(Met) with IR spectra for two of the four lowest energy [N,CO,S] conformers and the lowest energy [N,OH,S] conformer predicted at the B3LYP/6-311+G(d,p) level of theory.

Table 9.1. Relative energies at 0 K and free energies at 298 K (kJ/mol) of low-lying conformers of cationized Met.

Complex	Structure	B3LYP	B3P86	MP2(full)
Li^+(Met)	[N,CO,S]tgcgt	**0.0 (0.0)**	**0.0 (0.0)**	**0.0 (0.0)**
	[N,CO,S]tgcgg	6.1 (6.0)	6.3 (6.2)	5.2 (5.1)
	[N,CO,S]tgggt	11.2 (10.8)	11.2 (10.8)	11.6 (11.2)
	[N,CO,S]tgggg	12.9 (12.2)	12.9 (12.3)	12.4 (11.7)
	[CO_2^-]ctggg	27.4 (24.5)	23.1 (20.2)	30.3 (27.4)
	[N,CO]tgtgt	31.9 (28.1)	31.4 (27.5)	40.0 (36.2)
	[N,OH,S]tgggt	33.5 (32.9)	35.6 (35.0)	30.1 (29.6)
	[CO,S]ctggg	40.5 (37.3)	39.4 (36.2)	52.0 (48.8)
	[CO_2^-,S]cgggg	52.2 (51.9)	48.6 (48.4)	47.2 (46.9)
	TS[CO_2^-,COOH]	68.0 (64.5)	60.2 (56.7)	73.0 (69.5)
	[COOH]ctggg	70.6 (65.4)	63.6 (58.5)	75.8 (70.7)
	[COOH,S]cgggg[b]			
Na^+(Met)	[N,CO,S]tgcgt	**0.0 (0.0)**	**0.0 (0.0)**	**0.0 (0.0)**
	[N,CO,S]tgcgg	7.3 (7.1)	7.6 (7.4)	6.8 (6.6)
	[N,CO,S]tgggt	8.7 (8.6)	8.6 (8.5)	8.1 (8.0)
	[CO_2^-]ctggg	10.1 (7.7)	4.6 (2.3)	10.5 (8.2)
	[CO_2^-]cgtgg	10.3 (7.9)	5.6 (3.2)	13.3 (10.9)
	[N,CO,S]tgggg	12.2 (11.9)	11.6 (11.3)	9.4 (9.1)
	[CO_2^-]ctggt	12.8 (10.3)	7.6 (5.1)	14.8 (12.3)
	[N,CO]tgtgt	23.3 (19.3)	21.8 (17.8)	27.1 (23.0)
	[COOH,S]cgcgg	29.3 (23.4)	25.2 (19.3)	26.8 (20.9)
	[CO,S]ctggg	29.3 (26.6)	26.8 (24.1)	36.2 (33.5)
	[N,OH,S]tgggt	32.6 (31.8)	34.3 (33.5)	29.9 (29.2)
	TS[CO_2^-,COOH]	33.3 (30.7)	23.0 (20.4)	34.3 (31.7)
	[COOH]ctggg	37.8 (33.2)	31.0 (26.5)	38.7 (34.1)
	[CO_2^-,S]cgggg	37.9 (37.3)	33.6 (32.9)	32.9 (32.3)

Table 9.1. continued

Complex	Structure	B3LYP	B3P86	MP2(full)
K^+(Met)	[CO_2^-]ctggg	**0.0 (0.0)**	**0.0 (0.0)**	1.7 (1.3)
	[CO_2^-]cgtgg	0.7 (0.4)	1.5 (1.2)	5.0 (4.2)
	[CO_2^-]ctggt	2.6 (0.9)	2.8 (1.2)	5.5 (3.5)
	[N,CO,S]tgcgt	2.7 (3.1)	7.8 (8.2)	**0.0 (0.0)**
	[N,CO,S]tgggt	9.3 (9.9)	14.4 (15.0)	5.4 (5.5)
	[N,CO,S]tgcgg	10.1 (10.3)	15.3 (15.6)	7.1 (7.0)
	[N,CO,S]tgggg	10.8 (12.7)	14.8 (16.6)	3.3 (4.7)
	[COOH,S]cgggt	12.6 (11.1)	15.1 (13.5)	10.0 (8.1)
	[COOH,S]cgcgg	13.0 (13.1)	15.3 (15.4)	8.5 (8.2)
	[COOH,S]cgggg	13.1 (13.0)	15.1 (14.9)	7.8 (7.2)
	TS[CO_2^-,COOH]	13.5 (13.0)	9.4 (8.9)	15.2 (14.3)
	[N,CO]tgtgt	15.2 (12.2)	19.9 (16.8)	17.6 (14.2)
	[COOH]ctggg	15.4 (12.6)	16.0 (13.2)	17.3 (14.1)
	[CO,S]ctggg	18.1 (15.5)	21.6 (19.0)	22.4 (19.4)
	[CO_2^-,S]cgggg	29.3 (28.6)	30.2 (29.6)	24.6 (23.5)
	[N,OH,S]tgggt	34.1 (33.4)	40.4 (39.7)	29.2 (28.0)
Rb^+(Met)	[CO_2^-]ctggg	***0.0 (0.0)***	***0.0 (0.0)***	*1.7 (1.9)*
	[CO_2^-]cgtgg	*0.9 (0.6)*	*1.8 (1.5)*	*5.3 (5.3)*
	[CO_2^-]ctggt	*2.5 (1.6)*	*2.8 (1.9)*	*5.8 (5.1)*
	[N,CO,S]tgcgt	*5.0 (4.9)*	*10.0 (9.9)*	*0.9 (1.1)*
	[COOH]ctggg	*6.4 (3.4)*	*7.5 (4.5)*	*8.4 (5.7)*
	[COOH]cgtgg	*6.5 (3.9)*	*7.8 (5.2)*	*10.6 (8.3)*
	[COOH,S]cgggt	*6.6 (2.7)*	*9.1 (5.2)*	*3.9 (0.4)*
	[COOH,S]cgcgg	*6.7 (5.7)*	*9.3 (8.3)*	*2.0 (1.3)*
	[COOH,S]cgggg	*7.2 (5.6)*	*9.4 (7.8)*	*1.4* ***(0.0)***
	TS[CO_2^-,COOH]	*7.4 (6.8)*	*3.3 (2.7)*	*8.8 (8.5)*
	[COOH]ctggt	*9.2 (5.7)*	*10.5 (7.0)*	*12.8 (9.7)*

Table 9.1. continued

Complex	Structure	B3LYP	B3P86	MP2(full)
Rb^+(Met)	[N,CO,S]tgggg	*10.1 (11.7)*	*13.9 (15.5)*	***0.0** (1.9)*
	[N,CO,S]tgggt	*10.6 (10.7)*	*15.6 (15.7)*	*4.5 (4.9)*
	[N,CO,S]tgcgg	*12.3 (10.5)*	*17.5 (15.7)*	*8.2 (6.7)*
	[N,CO]tgtgt	*12.5 (8.8)*	*17.4 (13.7)*	*13.3 (10.0)*
	[CO,S]ctggg	*13.0 (10.2)*	*16.5 (13.7)*	*16.4 (13.9)*
	[CO_2^-,S]cgggg	*28.7 (24.8)*	*29.1 (25.2)*	*23.7 (20.1)*
	[N,OH,S]ttggg	*34.0 (36.7)*	*37.9 (40.5)*	*19.9 (22.8)*
Cs^+(Met)	[CO_2^-]ctggg	***0.0** (1.2)*	***0.0 (0.0)***	*3.2 (5.8)*
	[CO_2^-]cgtgg	*1.1 (4.2)*	*1.8 (3.6)*	*7.6 (11.9)*
	[COOH]cgtgg	*1.3 (1.6)*	*3.0 (2.1)*	*7.4 (9.0)*
	[COOH]ctggg	*1.5 (1.6)*	*3.1 (1.9)*	*4.7 (6.1)*
	[COOH,S]ctggt	*2.5 **(0.0)***	*5.0 (1.3)*	*1.2 **(0.0)***
	[CO_2^-]cgggt	*2.8 (4.3)*	*3.1 (3.3)*	*7.6 (10.4)*
	[COOH,S]cgcgg	*3.2 (4.7)*	*6.0 (6.3)*	*0.2 (3.0)*
	[COOH]ctggt	*4.0 (1.9)*	*5.9 (2.5)*	*9.3 (8.4)*
	[COOH,S]cgggg	*4.2 (4.8)*	*6.7 (6.0)*	*0.4 (2.4)*
	TS[CO_2^-,COOH]	*4.7 (6.5)*	*0.7 (1.3)*	*7.7 (10.9)*
	[N,CO,S]tgcgt	*7.2 (9.1)*	*12.2 (12.8)*	*3.7 (7.0)*
	[N,CO,S]tgggg	*9.3 (12.9)*	*13.2 (15.6)*	***0.0** (4.9)*
	[CO,S]ctgtg	*9.4 (9.2)*	*13.1 (11.7)*	*13.3 (14.4)*
	[N,CO]tgtgt	*11.0 (9.8)*	*16.2 (13.8)*	*12.5 (12.6)*
	[N,CO,S]tgggt	*11.6 (13.2)*	*16.6 (16.9)*	*6.3 (9.1)*
	[N,CO,S]tgcgg	*12.0 (10.4)*	*16.9 (14.0)*	*9.0 (8.7)*
	[CO_2^-,S]cgcgg	*30.1 (32.2)*	*31.1 (32.0)*	*27.7 (31.1)*
	[N,OH,S]ttggg	*32.9 (37.6)*	*36.7 (40.1)*	*19.8 (25.7)*

Table 9.1. continued

Complex	Structure	B3LYP	B3P86	MP2(full)
H^+(Met)	[N,CO,S]tgtgg	**0.0 (0.0)**	**0.0 (0.0)**	**0.0 (0.0)**
	[N,CO,S]tgggg	2.6 (3.0)	2.0 (2.4)	0.4 (0.8)
	[N,CO,S]tgtgt	2.7 (1.9)	3.1 (2.3)	3.9 (3.1)
	[N,CO,S]tgggt	3.6 (3.3)	3.2 (2.9)	2.5 (2.2)
	[N,OH,S]tgtgg	15.4 (12.7)	16.6 (13.9)	14.5 (11.8)
	[N,OH,S]ttggg	17.2 (17.4)	17.7 (17.9)	13.7 (13.9)
	[N,OH,S]tgtgt	17.5 (13.9)	19.2 (15.6)	17.9 (14.2)
	[N,OH,S]ttggt	18.9 (17.9)	19.8 (18.8)	16.5 (15.5)

[a] Free energies in parentheses. All values calculated at the level of theory indicated using the 6-311+G(2d,2p) or HW*/6-311+G(2d,2p) basis set with geometries and zero-point energies calculated at the B3LYP/6-311+G(d,p) or B3LYP/HW*/6-311+G(d,p) level of theory. Values in italics specify the HW* basis set treatment of the metal.
[b] The [COOH,S] conformer for Li^+(Met) collapses to [CO,S].

Table 9.2. Relative free energies at 298 K (kJ/mol) of low-lying conformations of cationized Met calculated using different basis set.

Complex	Structure	HW*/6-311+G(2d,2p)	Def2TZVP
Rb^+(Met)	[CO_2^-]ctggg	**0.0, 0.0,** 1.9	**0.0, 0.0,** 0.5
	[N,CO,S]tgcgt	4.9, 9.9, 1.1	2.5, 7.3, 0.2
	[COOH]ctggg	3.4, 4.5, 5.7	4.5, 5.3, 7.2
	[COOH,S]cgggt	2.7, 5.2, 0.4	4.1, 6.3, **0.0**
	[COOH,S]cgggg	5.6, 7.8, **0.0**	6.5, 8.4, 1.4
	[N,CO]tgtgt	8.8, 13.7, 10.0	7.8, 12.5, 11.1
	[CO,S]ctggg	10.2, 13.7, 13.9	9.4, 12.7, 13.7
	[CO_2^-,S]cgggg	24.8, 25.2, 20.1	23.3, 23.3, 15.4
	[N,OH,S]ttggg	36.7, 40.5, 22.8	35.7, 39.6, 24.8
Cs^+(Met)	[CO_2^-]ctggg	1.2, **0.0**, 5.8	3.4, 1.1, 7.5
	[COOH]ctggg	1.6, 1.9, 6.1	5.6, 4.8, 11.8
	[COOH,S]ctggt	**0.0**, 1.3, **0.0**	**0.0, 0.0, 0.0**
	[N,CO,S]tgcgt	9.1, 12.8, 7.0	9.0, 11.3, 8.7
	[CO,S]ctgtg	9.2, 11.7, 14.4	11.6, 13.0, 18.0
	[N,CO]tgtgt	9.8, 13.8, 12.6	11.6, 14.3, 17.8
	[CO_2^-,S]cgcgg	32.2, 32.0, 31.1	32.9, 31.3, 28.6
	[N,OH,S]ttggg	37.6, 40.1, 25.7	39.4, 40.9, 30.2

[a] Values listed are calculated at the B3LYP, B3P86, and MP2(full) levels of theory using the indicated basis set. Geometries and zero-point energies were calculated at the B3LYP/HW*/6-311+G(d,p) and B3LYP/Def2TZVP levels of theory.

References

(1) Wischmeyer, E.; Doring, F.; Karschin, A. *FEBS Lett.* **2000**, *466*, 115.

(2) Armentrout, P. B.; Gabriel, A.; Moision, R. M. *Int. J. Mass Spectrom.* **2009**, *283*, 56.

(3) Armentrout, P. B.; Rodgers, M. T.; Oomens, J.; Steill, J. D. *J. Phys. Chem. A* **2008**, *112*, 2248.

(4) Rodgers, M. T.; Armentrout, P. B.; Oomens, J.; Steill, J. D. *J. Phys. Chem. A* **2008**, *112*, 2258.

(5) Citir, M.; Stennett, E. M. S.; Oomens, J.; Steill, J. D.; Rodgers, M. T.; Armentrout, P. B. *Int. J. Mass Spectrom.* **2010**, *297*, 9.

(6) Forbes, M. W.; Bush, M. F.; Polfer, N. C.; Oomens, J.; Dunbar, R. C.; Williams, E. R.; Jockusch, R. A. *J. Phys. Chem. A* **2007**, *111*, 11759.

(7) Heaton, A. L.; Bowman, V. N.; Oomens, J.; Steill, J. D.; Armentrout, P. B. *J. Phys. Chem. A* **2009**, *113*, 5519.

(8) Bush, M. F.; Oomens, J.; Saykally, R. J.; Williams, E. R. *J. Phys. Chem. A* **2008**, *112*, 8578.

(9) Polfer, N. C.; Oomens, J.; Dunbar, R. C. *Phys. Chem. Chem. Phys.* **2006**, *8*, 2744.

(10) Bush, M. F.; Forbes, M. W.; Jockusch, R. A.; Oomens, J.; Polfer, N. C.; Saykally, R. J.; Williams, E. R. *J. Phys. Chem. A* **2006**, *111*, 7753.

(11) O'Brien, J. T.; Prell, J. S.; Steill, J. D.; Oomens, J.; Williams, E. R. *J. Phys. Chem. A* **2008**, *112*, 10823.

(12) Citir, M.; Hinton, C. S.; Oomens, J.; Steill, J. D.; Armentrout, P. B. *J. Phys. Chem. A* **2012**, *116*, 1532.

(13) Valle, J. J.; Eyler, J. R.; Oomens, J.; Moore, D. T.; van der Meer, A. F. G.; von Heldon, G.; Meijer, G.; Hendrickson, C. L.; Marschall, A. G.; Blakney, G. T. *Rev. Sci. Instrum.* **2005**, *76*, 023103.

(14) Polfer, N. C.; Oomens, J. *Phys. Chem. Chem. Phys.* **2007**, *9*, 3804.

(15) Polfer, N. C.; Oomens, J.; Moore, D. T.; von Helden, G.; Meijer, G.; Dunbar, R. C. *J. Am. Chem. Soc.* **2006**, *128*, 517.

(16) Oepts, D.; van der Meer, A. F. G.; van Amersfoort, P. W. *Infrared Phys. Technol.* **1995**, *36*, 297.

(17) Peng, C. Y.; Schlegel, H. B. *Israel J. Chem.* **1994**, *33*, 449.

(18) Armentrout, P. B., Unpublished Results, University of Utah, Department of Chemistry.

(19) Dookeran, N. N.; Yalcin, T.; Harrison, A. G. *J. Mass Spectrom.* **1996**, *31*, 500.

(20) Oomens, J.; Moore, D. T.; Meijer, G.; von Helden, G. *Phys. Chem. Chem. Phys.* **2004**, *6*, 710.

(21) Sinclair, W. E.; Pratt, D. W. *J. Chem. Phys.* **1996**, *105*, 7942.